LOW-TEMPERATURE SINTERING AND FABRICATION RESEARCH OF CERAMICS AND NUMERICAL SIMULATION ON ELASTIC, PRESSURE DROP AND HEAT TRANSFER PROPERTIES OF OPEN CELL FOAMS

A Dissertation

presented to

the Faculty of the Graduate School

at the University of Missouri-Columbia

In Partial Fulfillment

of the Requirements for the Degree

Doctor of Philosophy

---

by

ZHENGWEI ANDREW NIE

Dr. Yuyi Lin, Dissertation Supervisor

DECEMBER 2016

The undersigned, appointed by the dean of the Graduate School, have examined the dissertation entitled

LOW-TEMPERATURE SINTERING AND FABRICATION RESEARCH OF CERAMICS AND NUMERICAL SIMULATION ON ELASTIC, PRESSURE DROP AND HEAT TRANSFER PROPERTIES OF OPEN CELL FOAMS

presented by Zhengwei Andrew Nie, a candidate for the degree of doctor of philosophy, and hereby certify that, in their opinion, it is worthy of acceptance.

Professor Yuyi Lin

Professor Frank Feng

Professor Robert A. Winholtz

Professor Jian Lin

Professor Stephen Montgomery-Smith

Dedication

This dissertation is dedicated to my family, especially my parents, Changge Nie and Xiangyun Lv, who have always loved me unconditionally and whose good examples have taught me to work hard for the things that I aspire to achieve. I am truly thankful for having you in my life.

Columbia, MO US

October 10, 2016

ACKNOWLEDGEMENTS

I would like to express my sincere gratitude to my advisor Dr. Yuyi Lin for his continuous guidance and support during my Ph.D. study.

Besides my advisor, I also would like to give great gratitude to the rest of my committee members: Dr. Frank Feng, Dr. Robert A. Winholtz, Dr. Jian Lin, and Dr. Stephen Montgomery-Smith, for their insightful comments and suggestions.

I would like to thank Dr. Feixue Wang, who is a professor at Yanshan University, China, for his help in experimental studies and thank Dr. Guoliang Huang for using his lab's computer workstation to do numerical simulations.

I am also grateful to all my friends, colleagues, professors, and staffs of Department of Mechanical and Aerospace Engineering for their support and help driving me to complete my Ph.D. study successfully.

Last but not least, I would like to express my most profound gratitude to my family for providing me with unconditional love, unfailing support, and continuous encouragement throughout my years of study and through the process of research. This accomplishment would not have been possible without them.

TABLE OF CONTENTS

LIST OF FIGURES

LIST OF TABLES

ABSTRACT

Three zinc titanate compounds have been confirmed to exist in the ZnO-TiO_2 system, namely, Zn_2TiO_4 (cubic), $ZnTiO_3$ (hexagonal) and $Zn_2Ti_3O_8$ (cubic). Due to its relatively low sintering temperature and excellent microwave dielectric properties, moreover, for the low cost of its raw materials, ZnO-TiO_2 ceramics has been considered to be a promising candidate for low temperature co-fired ceramics (LTCC), and then more and more interesting has been paid in the investigation of its structure, sintering behavior and microwave dielectric properties in recent years. The first chapter of this dissertation, vanadium pentoxide (V_2O_5) was chosen as a sintering aid to lower the sintering temperature of the ZnO–TiO_2 system. The advantage of V_2O_5 is that it has a lower melting point, around 680 ℃. Solid V_2O_5 would become liquid phase during the sintering process, which can facilitate the densification of ceramics. The ZnO–TiO_2 ceramics was prepared by the conventional mixed-oxide method. Cermets made from ceramics and copper (Cu) was prepared using the powder metallurgy method. The effect of V_2O_5 on the sintering behavior of ZnO–TiO_2 ceramics and cermets was studied as a function of additive percentage and sintering temperature.

Porous ceramics is one of the frequently used materials for a variety of applications, including the filtration of molten metals, high-temperature thermal insulation, support for catalytic reactions, filtration of particulates from diesel engine exhaust gases, filtration of hot corrosive gases in various industrial processes, and lightweight structural materials. Many different preparation methods for porous ceramics have been studied over the past decade, such as polymeric foam replication, starch consolidation casting, and gel casting,

etc. The second chapter of this work, porous alumina ceramics with different porosity were fabricated by two different methods. The first one combined the starch consolidation process with the gel-casting process using corn starch as the pore-forming agent and also as the binder. The other one used hollow microspheres as the pore-forming agent. No relative studies using hollow microspheres as the pore-forming agent is reported in the literature so far. For both of two methods, the bulk density, porosity, and microstructure of the obtained alumina ceramics were studied.

Open cell foams, as one type of porous materials, are nowadays commercially used in modern biomedical and technical applications. One of the main biomedical interests is the reconstruction of the human body by the implantation of scaffolds. Other important fields of foam applications are engineering applications, such as filtering and catalysis, etc. The third chapter in this dissertation, we wish to model foam structures that have a roughly uniform cell size, but which are still random and isotropic. A non-periodic, evenly spaced, and isotropic arrangement of seed points is, therefore, necessary. A method for the generation of random foam structures, based on Laguerre-Voronoi tessellations of randomly packed spheres with log-normal volume distribution, was proposed. This model could give the study of the variation coefficient effect on the geometric and topological properties of foams. To evaluate the generated model in this work, a series of parameters were discussed, such as the average number of faces per foam cell, porosity, and specific surface area, etc.

Since the microstructures of open cell foams are normally of order mm in size and can be easily identified, it is desirable to establish the relationship between the microstructure and the macroscopic mechanical properties of foams. The fourth chapter in

this work, a three dimensional random Laguerre-Voronoi foam model was developed to investigate the elastic properties of open cell ceramic foams. A size sensitivity study was first performed to determine the appropriate number of cells to be included in each foam specimen and the suitable number of specimens to be used in statistical analysis. This was followed by a finite element analysis to calculate the effective Young's modulus, shear modulus, and Poisson ratio of the foams. Finally, the results obtained in this work were compared with some results in the literature. A few conclusions on the models and the obtained results are summarized in the final part.

Open cell foam structures exhibit specific properties such as high specific surface area, high porosity (60%–95%), low density, favorable mechanical, thermal and corrosion resistance. They are well suited to serve as compact heat exchangers, reaction catalyst support, flow stabilizers or filters. High porosities enable a considerable reduction of the pressure drop along the catalyst bed even at high flow rates; also, the solid ligaments (or struts) in open cell foams allow the continuous connection of the different catalyst domains which increase the effective thermal conductivity of the entire system without thermal breaking points. The last chapter of this dissertation investigated the pressure drop and heat transfer through open cell foams. A pressure drop correlation with a universal form was developed based on theoretical grounds and the tortuosity of open cell foams was taken into account for the pressure drop. The developed correlation was then validated using numerical simulations on pressure drop properties of aluminum foam structures of pore densities between 10 ppi and 50 ppi and porosities from 70% to 95%, with the commercial CFD analysis package: ANSYS Fluent. The numerical results for pressure drop were compared with the prediction by the theoretical correlation. The results showed that the

pressure drop of foams increased with increasing pore density and decreasing porosity. The numerical results were consistent with the prediction of the theoretical correlation. Permeability and friction factor of foams were also evaluated. For the low Reynolds number range, friction factor scaled as $1/Re$ at lower Reynolds numbers, while at higher Reynolds numbers, the non-linear term began to dominate because of the inertial effects. Then the computed interstitial heat transfer coefficients were investigated. The heat transfer coefficient increased with the air velocity and the heat transfer coefficient increased when the porosity increases at constant pore density. At constant porosity the heat transfer coefficient increased when increasing the pore density. Furthermore, a correlation was given to derive the hydraulic diameter from the ppi number.

Finally, this dissertation stated that with additive manufacturing techniques, e.g., SLS and EBM, it is possible to control the morphological and geometrical parameters of foam structures with a high degree of reproducibility and vary these properties in a controlled manner and it is possible to perform computational design for open cell foams with defined flow properties using the Laguerre-Voronoi model developed in Chapter 3 and Chapter 4 of this work.

CHAPTER 1 LOW-TEMPERATURE SINTERING OF ZnO-TiO_2 CERAMICS

1.1 Introduction

Zinc titanate (ZnO–TiO_2) has been used as pigments and catalysts since the phase diagram and the characterization of the ZnO–TiO_2 system have been studied by Dulin et al. [1], Bartram et al. [2] and Yamaguchi et al. [3] last century. The ZnO–TiO_2 system includes three compounds: $Zn_2Ti_3O_8$ (cubic), $ZnTiO_3$ (hexagonal) and Zn_2TiO_4 (cubic) [4, 5]. In recent years, the ZnO–TiO_2 system has been of considerable interest to the microwave dielectric ceramics industry since pure $ZnTiO_3$, in the ZnO–TiO_2 system, possesses good microwave dielectric properties and features relatively low-cost raw materials [6, 7]. Namely, it has high dielectric constant $\epsilon_r \approx 19$, high quality factor, $Q \approx 3000$ (at 10 GHz), and low as close as possible to zero temperature coefficient of resonant frequency, $\tau_f \approx -55$ ppm/℃ [8]. Table 1.1 shows the dielectric properties of ZnO–TiO_2 with different composition under different sintering temperature in the literature. Thus, the ZnO–TiO_2 system ceramics is regarded as one of the most promising candidates for gas sensor [9] (for example, sensor for CO, ethanol, etc.) and microwave resonator [10]. ZnO–TiO_2 ceramics in most of known studies, which have been employed for the present applications, have been usually fabricated by employing the high sintering temperature, which is usually between 1100–1500 ℃. [11]. High temperature processing hence forbids the use of cheaper base metals, e.g., Cu, Ag, as an electrode, instead of noble metals like Pd, Pt, Mo, or Ni, which is currently employed. It increases the manufacturing cost, both in terms of money and energy. Hence, it is of prime importance to lower the sintering

temperature of the dielectrics in order to replace the noble metals by base metals as an electrode. This substitution is an indispensable condition for producing low temperature co-fired ceramics (LTCC) devices which imposes to use silver as electrodes [12, 13]. Remembering the melting point of silver (961 ℃.), obtaining a sintering temperature lower than this value is the technological challenge that will allow to produce cheaper, performer and more miniaturize devices. Moreover, with the development of electronic chip components, the demand for reducing energy consumption has been promoting the study of LTCC, especially research into the sintering of the $ZnO–TiO_2$ ceramics [14-18]. In principle, two basic approaches can be adopted to reduce the sintering temperature of ceramics: (1) the addition of glass phase or crystalized materials to act as densification promoter (owing to the formation of a liquid phase to improve species diffusion); (2) the using liquid phase processing (e.g., sol–gel method) or grinding system in order to reduce the grain size of the powder, which in turn enhances the reactivity of the final powder.

Table 1.1 Dielectric properties of $ZnO–TiO_2$ ceramics in [19]

Composition	Sintering temperature (℃)	Density (g/cm^3)	ϵ_r	Q at 10 GHz	τ_f (ppm/℃)
$ZnO–TiO_2$	1200	4.59	30	2500	+25
$ZnO–TiO_2$	920	4.39	19	3000	-55
$ZnO–TiO_2$	1100	5.00	15	200	28
$ZnO–1.1TiO_2$	920	4.53	27	4400	+6
$1.1ZnO–TiO_2$	1100	4.70	24	3000	-13

The second point is not often privileged in an industrial environment because of the high cost of the precursors and of the complexity of the liquid phase processing. The first point, i.e. the sintering of dielectric materials with glass addition have already been

successfully developed in several microwave dielectric systems, e.g. $(Zr,Sn)TiO_4$, $ZnO–Nb_2O_5–TiO_2$, $(Ca,Mg)TiO_3$, $BaO–Nb_2O_3–TiO_2$ [20-26].

Zhang et al. presented that the density of $ZnO–TiO_2$ ceramics increased up to 98% of theoretical density through sintering at 900 °C for 3 hours with 2.0 wt.% $ZnO–B_2O_3–SiO_2$ [17]; Kim et al. noted that zinc titanates can be sintered at lower than 900 °C with less than 5 wt.% glass frit as the sintering aid [20]; Kim et al. clarified that densities of higher than 94% of the theoretical density have been obtained for the $ZnO–TiO_2$ system when it was sintered at 875 °C for 4 hours with a small amount of B_2O_3 additives (less than 1 wt.%) [27]. Table 1.2 shows the results on low-temperature sintering of $ZnO–TiO_2$ ceramics in the literature.

Table 1.2 Results on low-temperature sintering of $ZnO–TiO_2$ ceramics in the literature

Ceramics	Sintering aid	Sintering temperature (°C)	Phase composition[#]	Relative density (%)	Reference
$ZnO–TiO_2$	$K_2O–ZnO–B_2O_3–SiO_2$	920	ZT	85	[19]
$ZnO–TiO_2$ +0.25 TiO_2	B_2O_3	880	ZT+T	94	[27]
$1ZnO–1.2TiO_2$	$ZnO–B_2O_3–SiO_2$	900	ZT+T	97	[17]
$ZnO–TiO_2$	$CuO + B_2O_3$	900	Z_2T+T	96.5	[6]
$ZnO–TiO_2$	Bi_2O_3	1000	Z_2T+T	95	[28]

#: T, ZT, and Z_2T are TiO_2, $ZnTiO_3$, and Zn_2TiO_4, respectively.

Liquid-phase sintering is a frequently used method to realize ceramics densification under low-temperature sintering. To this end, the selected sintering aids are mostly oxide which possesses low melting point [14, 29]. In this study, vanadium pentoxide (V_2O_5) was chosen as a sintering aid to lower the sintering temperature of the $ZnO–TiO_2$ system. The advantage of V_2O_5 is that it has a lower melting point, around 680 ℃. Solid V_2O_5 would become liquid phase during the sintering process, which can facilitate the densification of

ceramics. The ZnO–TiO_2 ceramics was prepared by the conventional mixed-oxide method. Cermets made from ceramics and copper (Cu) was prepared using the powder metallurgy method. The effect of V_2O_5 on the sintering behavior of ZnO–TiO_2 ceramics and cermets was studied as a function of additive percentage and sintering temperature. The properties of these two materials made in this work were investigated. The prospect of applying three-dimensional printing technology using ZnO–TiO_2 ceramics and cermets as raw materials was also discussed.

1.2 Experimental procedures

The ceramics raw powders were prepared by the conventional mixed-oxide method. Reagent-grade raw powders of ZnO (Alfa Aesar Co., USA) and TiO_2 (Alfa Aesar Co., USA) with purities higher than 99.9% were chosen as raw materials. The raw powders were weighed with the mole ratio of ZnO:TiO_2/2:1, and then mixed using ball mill with beads (2–3 mm in diameter) for 24 hours. Both jar and milling beads are made of agate while milling medium is deionized water. The mixed materials were then dried in an electric oven at a temperature of 80 ℃ and sieved using a 120-mesh sieve. The mixed materials were pre-sintered at 800 ℃ for 4 hours in Al_2O_3 crucible. V_2O_5 powders were added after pre-sintering and before the second ball-milling. To granulate ground powders, 5 wt.% polyvinyl alcohol (PVA) solution was added as a binder and milled again for 1 hour. Powders were then compacted by using a single-axial cold press under a pressure of 200 MPa. Shaped specimens of 13 mm in diameter and 6 mm in thickness were obtained. The sintering process was done in an electric heating furnace and the sintering temperature was from 800 ℃ to 1300 ℃ at a heating rate of 5 ℃/min. The specimens were held in an

Al_2O_3 crucible and an argon atmosphere sintering environment. Specimens stayed in 500 ℃ for 2 hours to eliminate PVA, were heated to set the temperature at the same heating rate and stayed at such temperature for another 4 hours, after which time the specimens were cooled to room temperature in the furnace. The block diagrams of the process are shown in Figure 1.1 and Figure 1.2. Figure 1.3 shows the specimens made in this study.

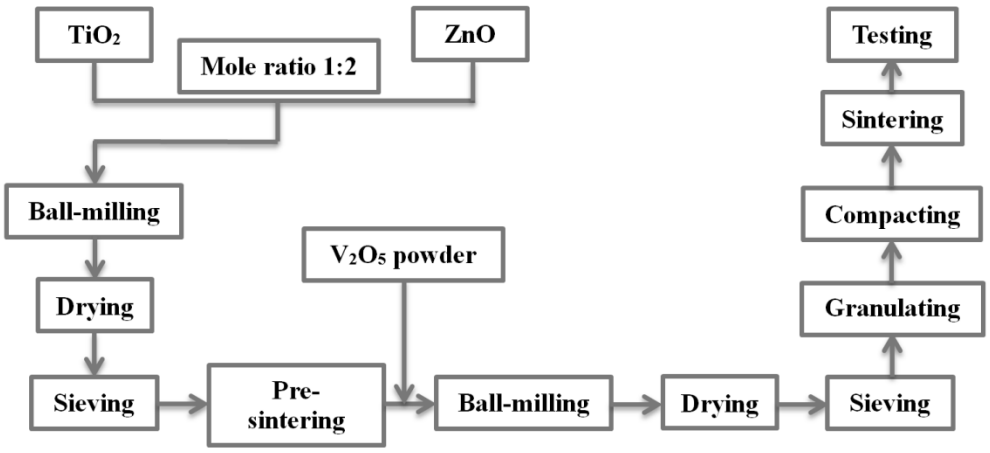

Figure 1.1 Block diagram for ceramics preparation

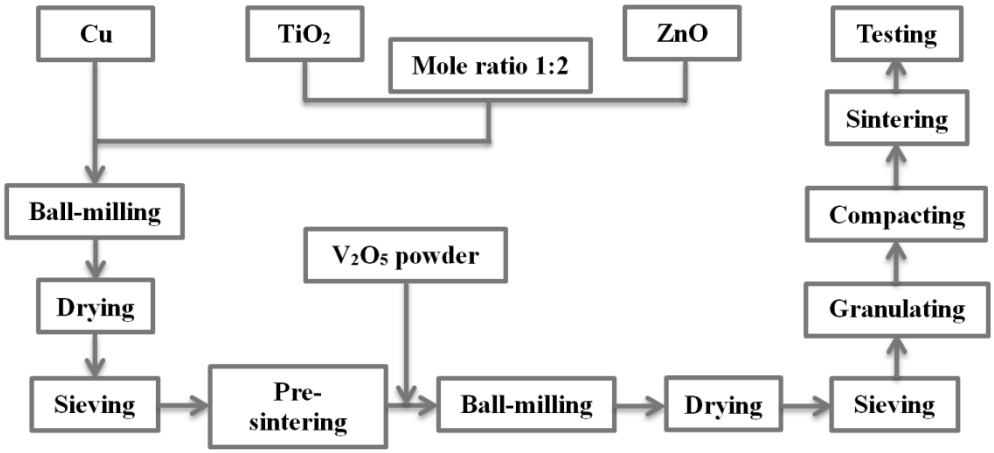

Figure 1.2 Block diagram for cermets preparation

(a) (b)

Figure 1.3 Specimens made of (a) ZnO and TiO_2, (b) ZnO, TiO_2, and Cu in this study

1.3 Results and discussion

1.3.1 ZnO–TiO_2 system

The bulk densities of ZnO–TiO_2 ceramics under different sintering temperatures is profiled in Figure 1.4. The densities were measured by Archimedes technique. This figure shows that ceramics with approximate 95% theoretical density (theoretical density=5.14 g/cm^3, estimated from the XRD pattern of phase $ZnTiO_3$) is attained when the sintering temperature is around 1200 ℃. The density of ZnO–TiO_2 ceramics rapidly increased from around 950 ℃, which states that the specimens started densification at about 950 ℃. Thus, the ceramics density was almost unchanged when the sintering temperature was below 950 ℃. The temperature barrier the sintering needs to overcome is at around 950 ℃. When the sintering temperature was between 1100 ℃ and 1300 ℃, the density of ceramics increased only slightly.

Figure 1.5 shows that the hardness of ZnO–TiO_2 ceramics related to sintering temperature. Comparing Figure 1.5 with Figure 1.4, the relationship between hardness and

the sintering temperature presents the same trend as that between density and the sintering temperature since higher sintering temperatures (the range of sintering temperature is 800–1300 ℃ in this study) can be very helpful in getting well-sintered ceramics, which possesses better densification and higher hardness. As shown in Figure 1.5, the hardness of $ZnO–TiO_2$ ceramics sintered at a temperature of more than 1000 ℃ could reach to 650 HV. Ceramics at this hardness have good machining properties and possible broader applications.

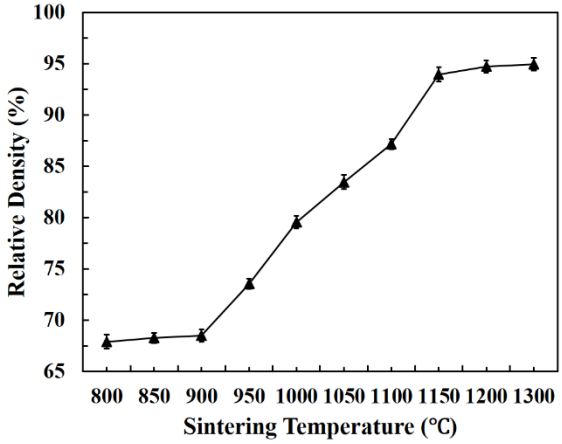

Figure 1.4 Relative densities of $ZnO–TiO_2$ ceramics related to sintering temperature

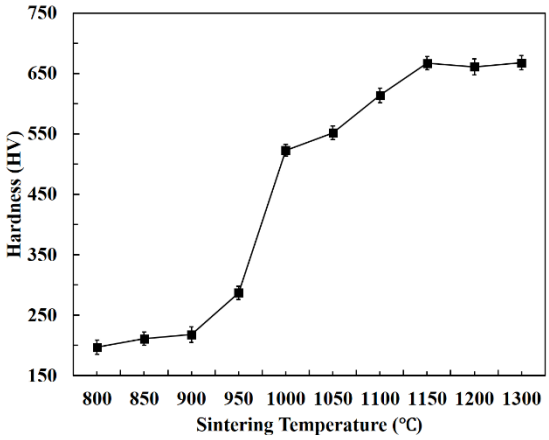

Figure 1.5 Hardness of $ZnO–TiO_2$ ceramics related to sintering temperature

Figure 1.6 illustrates the relationship between the bulk densities of ZnO–TiO_2 ceramics and the amount of V_2O_5 additive at different sintering temperatures. As presented in Figure 1.6, the density of ZnO–TiO_2 ceramics using V_2O_5 as the sintering aid, compared to using pure ZnO–TiO_2 ceramics, apparently increased below 950 ℃. The density of ZnO–TiO_2 ceramics can attain 95% theoretical density between 900 ℃ and 920 ℃. The 90%, 92%, 95%, and 90% of theoretical density of ZnO–TiO_2 ceramics added 0.5, 1, 2, and 4 wt.% sintering aid were abtained at 920, 920, 900, and 920 ℃, respectively. With 0.5 and 4.0 wt.% V_2O_5 aid, the density increased along with the increase of the sintering temperature and became saturated. However, for the ceramics with 1–2 wt.% V_2O_5 aid, the densities of the specimens initially increased along with increasing sintering temperatures, reached a maximum, and then decreased. When the amount of V_2O_5 aid is up to 2 wt.%, the density of ZnO–TiO_2 ceramics first increases and then dramatically decreases. This phenomenon may be explained by following. V_2O_5 has a low melting point, about 680 ℃. A liquid phase was formed in the sintering process, the existence of which can improve material transfer rate and the sintering rate of the ceramics body, and thus making ZnO–TiO_2 ceramics to denser at a lower sintering temperature. The amount of V_2O_5 ranging from 1.0 wt.% to 2.0 wt.%, V_2O_5 formed a liquid phase which was very helpful in increasing the density of the ceramics body when increasing the sintering temperature. However, more than 2 wt.% V_2O_5 addition and higher sintering temperatures resulted in excess pores occurring due to the evaporation of the V_2O_5, which in turn, reduced the density of the ZnO–TiO_2 ceramics. When the amount of V_2O_5 is less than 1 wt.% the liquid phase that V_2O_5 formed is not enough to improve sintering. Therefore, the 2 wt.% V_2O_5 addition can make ZnO–TiO_2 ceramics realize more than 90 % densification between 900–

920 ℃. V_2O_5 is a good sintering aid in lowering sintering temperatures of ZnO–TiO_2 ceramics. The hardness of specimens with the 2 wt.% V_2O_5 addition at different sintering temperatures is shown in Figure 1.7. For the ZnO–TiO_2 ceramics with the 2 wt.% V_2O_5 addition, the hardness values increased along with an increase of the sintering temperature and then attained a stable value, which is approximately 560 HV.

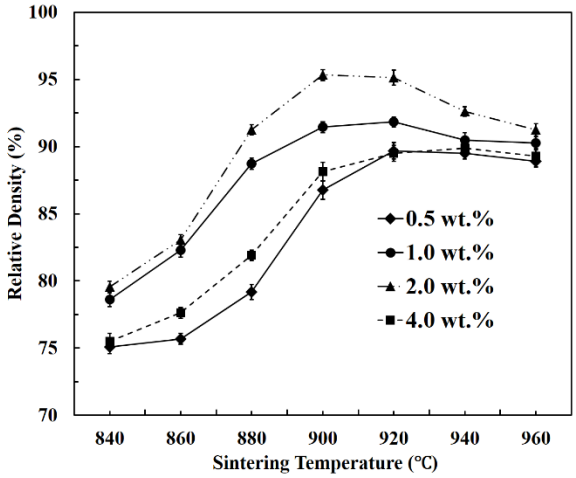

Figure 1.6 Relative densities of ZnO–TiO_2 ceramics as a function of amount of V_2O_5 and sintering temperature

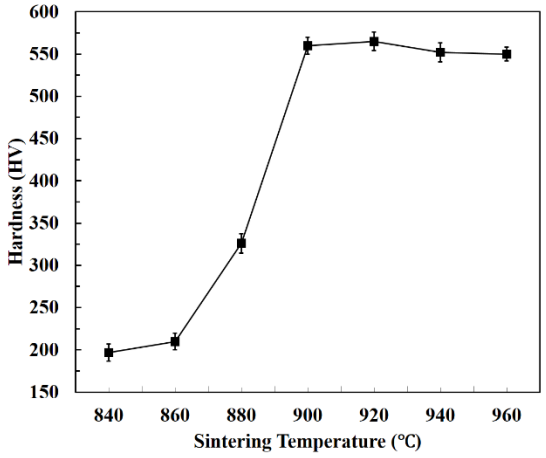

Figure 1.7 Hardness of ZnO–TiO_2 ceramics added 2 wt.% V_2O_5 addition related to sintering temperature

Figure 1.8 shows (a) the XRD patterns of ZnO–TiO_2 specimens sintered at 900 ℃ with 0.5 wt.%, 1 wt.%, 2 wt.%, and 4 wt.% V_2O_5 as the sintering aid, and (b) without V_2O_5 sintered at different temperatures. For all the specimens sintered at 900 ℃ for 4 hours, rutile (TiO_2) and hexagonal $ZnTiO_3$ were formed. The hexagonal phase was retained when the sintering temperature was less than 900 ℃. As shown in Figure 1.8, the Zn_2TiO_4 phase has been synthesized at this sintering temperature with excess rutile solubility. The form of Zn_2TiO_4 was not influenced by the amount of V_2O_5 at 900 ℃. Thus, the Zn_2TiO_4 was stable when the sintering temperature was less than 950 ℃. These results indicate that the addition of V_2O_5 lowered the temperature of phase transition from that of hexagonal $ZnTiO_3$ to cubic Zn_2TiO_4. Figure 1.8 also shows that there is no any other impurity phase formed in all specimens. This suggests that V_2O_5 may have formed a solid solution with the principal phase, may have entered into the principal lattice, or may have evaporated away.

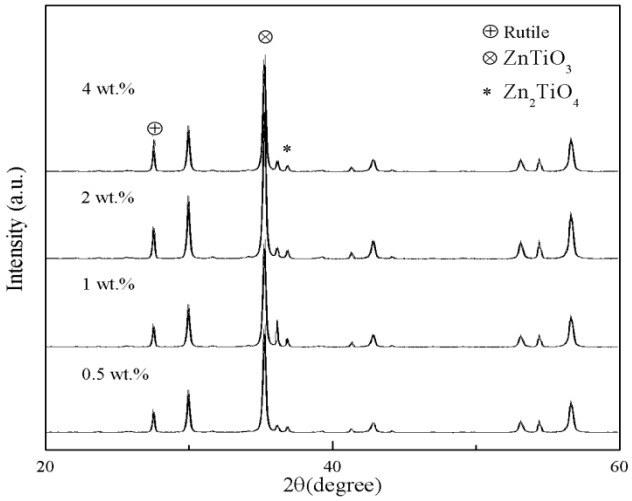

(a)

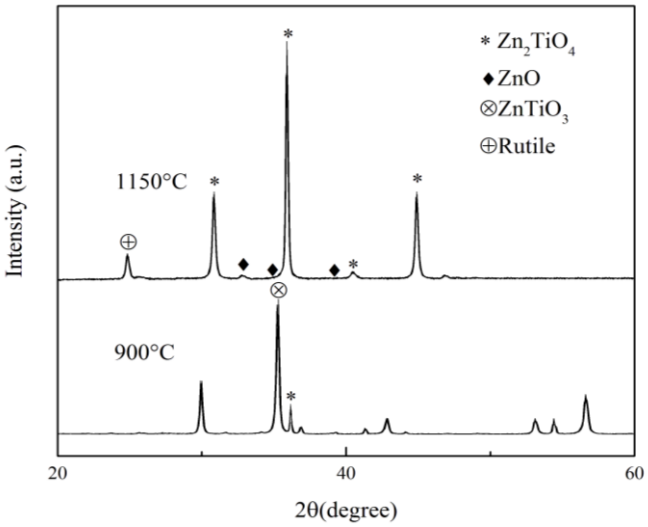

(b)

Figure 1.8 (a) XRD patterns of ZnO–TiO_2 ceramics sintered with V_2O_5 at 900 ℃, and (b) without V_2O_5 at different temperatures

SEM micrographs of ZnO–TiO_2 ceramics sintered at 880 ℃ and 900 ℃ for 4h without V_2O_5 and with 2 wt.% V_2O_5 are shown in Figure 1.9. From Figure 1.9 (a) and (b), basically, ZnO–TiO_2 sintered at 880 ℃ and 900 ℃ without V_2O_5 could not obtain good ceramics having high relative density, which has been stated in Figure 1.4. On the other hand, the ceramics have traces of liquid phase sintering when sintered with 2 wt.% V_2O_5. Based on the XRD results, the larger grains are Zn_2TiO_4 and the smaller ones are uncombined rutile. From Figure 1.9 (c) and (d), the small agglomeration of white grain in the specimens sintered at 880 ℃ can be observed, which is rather large in some areas. However, there is no such agglomeration in specimens sintered at 900 ℃. Both size and number of the pores in all specimens significantly decreased when the sintering temperature increased, which also proves that the addition of V_2O_5 improved the grain growth of ZnO–TiO_2 ceramics.

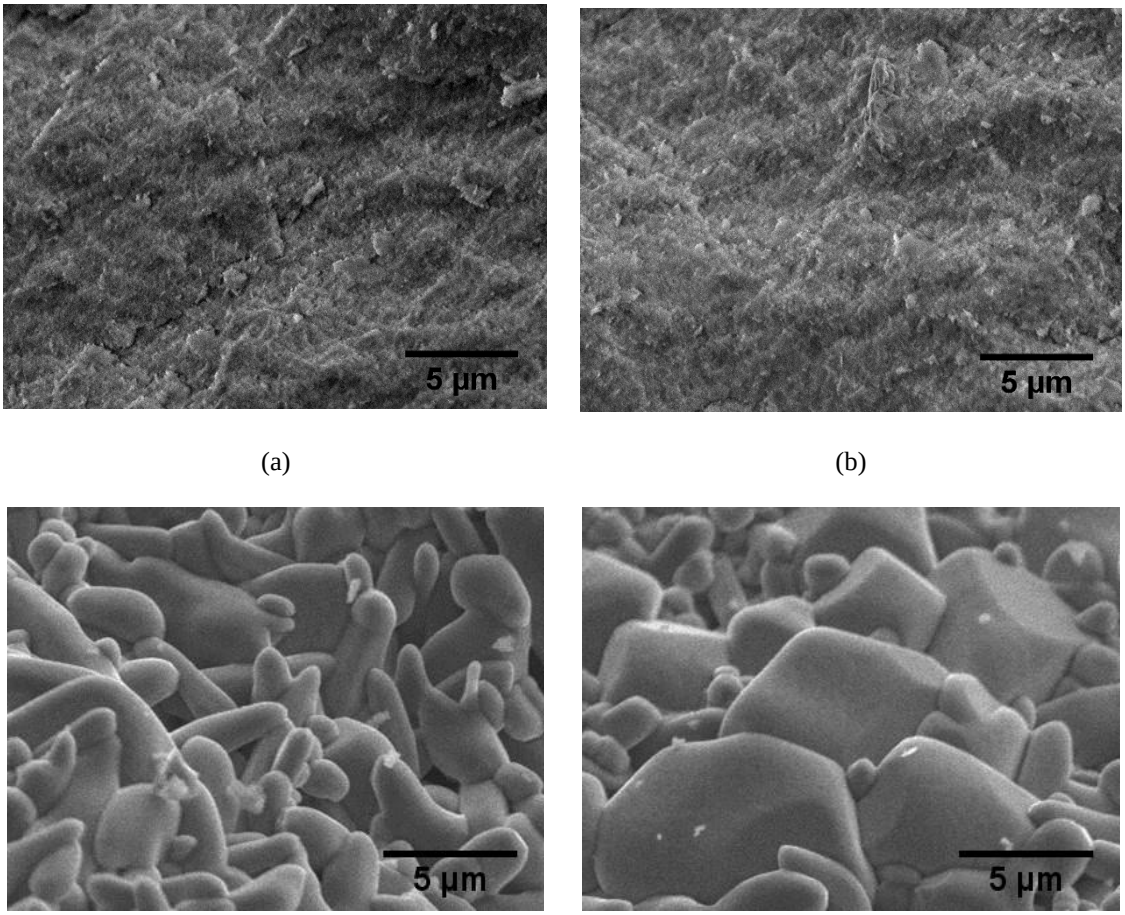

Figure 1.9 SEM micrographs of ZnO–TiO_2 ceramics sintered for 4 hours at (a) 880 ℃ and (b) 900 ℃ without V_2O_5, (c) 880 ℃ and (d) 900 ℃ with 2 wt.% V_2O_5

1.3.2 ZnO–TiO_2+Cu system

In this study**,** the cermets made from ZnO–TiO_2 ceramics and copper (Cu) was prepared using powder metallurgy method. The amount of V_2O_5, sintering aid, is 2 wt.% based on that of ZnO–TiO_2 system.

The relative density curve of cermets as a function of the amount of Cu at different sintering temperature for 4 hours is shown in Figure 1.10. The theoretical density was calculated by lattice parameters which can be determined using XRD patterns and atomic

masses. The melting point of copper is 1083.4 ℃. In order to prevent Cu from being extruded from the specimen, the highest sintering temperature is 1000 ℃ in this study. The density curve can be divided into three stages: (1) <880 ℃; (2) 880–960 ℃; (3) >960 ℃. When the cermets were sintered below 880 ℃, its density increased slowly. The density of cermets increased significantly between 880 ℃and 960 ℃, and almost stayed the same above 960 ℃. The density of cermets can reach 90% theoretical density when the sintering temperature is higher than 960 ℃. The above facts indicate that when the sintering temperature is below 880 ℃, the densification of cermets is difficult to attain since sintering hasn't crossed the temperature barrier. The densification of cermets mainly occurs from 880 ℃ to 960 ℃. Figure 1.11 shows the cermets specimen with 80 wt.% Cu after sintering.

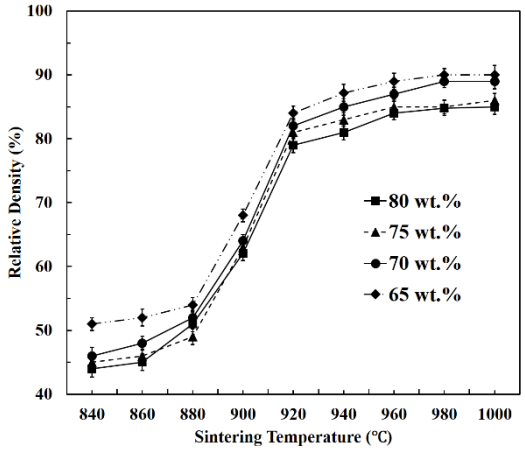

Figure 1.10 Relative densities of cermets as a function of amount of Cu and sintering temperature

Figure 1.11 Cermets specimen with 80 wt.% Cu after sintering

Figure 1.12 presents that the hardness of cermets with 80 wt.% Cu varies with sintering temperatures. As shown in Figure 1.10, the relationship between hardness of cermets and sintering temperature was same as that between relative density of cermets and sintering temperature as illustrated in Figure 1.10 was revealed. The reason is that cermets can be sintered well at a higher sintering temperature (the range of sintering temperature of cermets in this study is 840–1000 ℃), which possesses nearly complete densification and higher hardness. Figure 1.12 shows that the hardness of cermets sintered at a temperature of more than 1000 ℃ could reach to 130 HV. Such hardness is only 19% of that of ZnO–TiO_2 ceramics added 2 wt.% V_2O_5 addition since the amount of Cu in the cermets up to 80 wt.%. However, the hardness of cermets made in this study is higher than that of common pure copper.

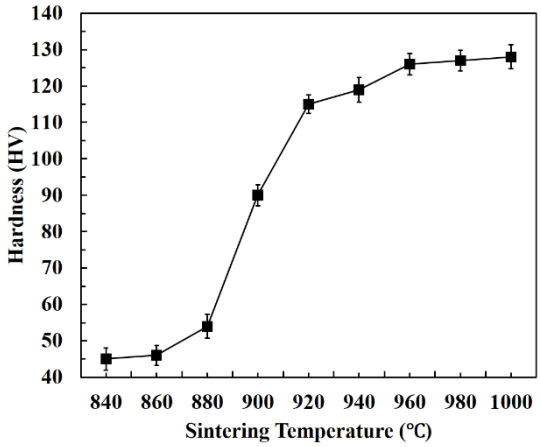

Figure 1.12 Hardness of cermets with 80 wt.% Cu as a function of sintering temperature

SEM micrographs of the cermets made of ZnO–TiO_2 ceramics and 80 wt.% Cu with the addition of 2 wt.% V_2O_5 sintered at 880 ℃, 900℃, and 920 ℃ for 4h are shown in Figure 1.13. The phase structure of the cermets has lots of pores and the grains did not grow and are quite loose, as shown in Figure 1.13 (a). However, densification and grain growth can be observed for the specimens sintered at 900℃ and 920 ℃, as shown in Figure 1.13 (b) and (c).Also, it can be seen that the densification of ceramics sintered at 900℃ is better than that of 920 ℃. According to the density results above in this study, the densification of specimens added V_2O_5 as the sintering aid has begun, but was not completed when sintered at 880 ℃. And the ceramics conversion reactions have completed when sintered at 920 ℃. Thus, the SEM results agreed with the analysis above in this study. Comparing the SEM micrographs and density analysis results, V_2O_5 can improve the ceramics conversion reactions in cermets made of ZnO–TiO_2 ceramics and Cu and can lower its sintering temperature.

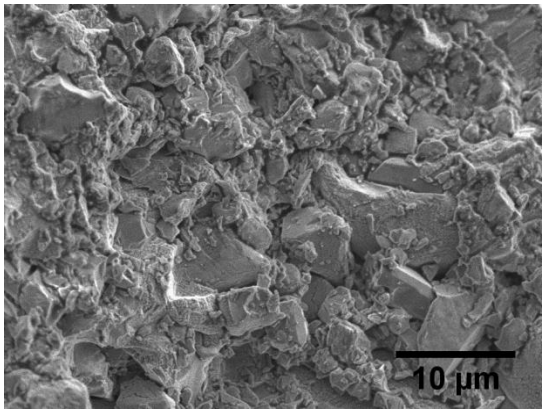

(a)

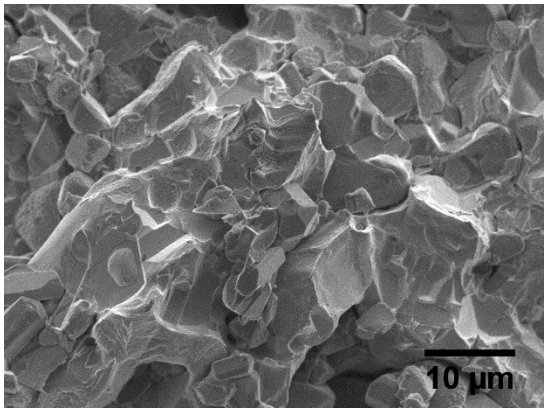

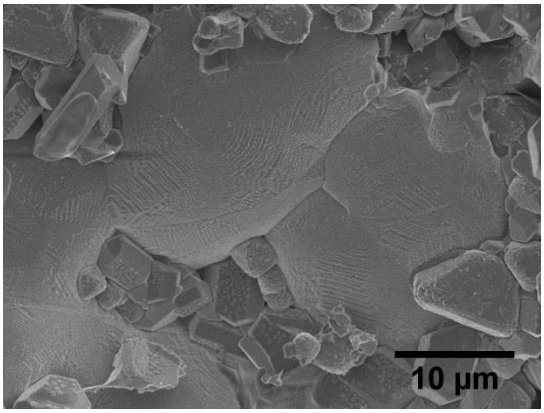

(b) (c)

Figure 1.13 SEM micrographs of cermets made of ZnO–TiO_2 ceramics and 80 wt.% Cu sintered for 4 hours with 2 wt.% V_2O_5 addition at (a) 880 ℃, (b) 900 ℃, and (c) 920 ℃

1.3.3 Application prospect

Most previous work with respect to ZnO–TiO_2 system attempted to apply the theory of the system to microwave dielectric ceramics or LTCC. However, no study applying the ZnO–TiO_2 system to three dimensional printing (3DP) has been previously reported. It has been demonstrated that 3DP has the capability of fabricating complex 3D structures which can be made from a variety of materials, including ceramics, metals, and polymers with an array of unique geometries and enabling small quantities of customized goods to be

produced at relatively low costs [30-32]. The authors will attempt to use the $ZnO–TiO_2$ ceramics and cermets made in this study as a raw material for a further study on three dimensional printing: what will happen to 3DP products when going through sintering and how can we improve the machining properties of the products after sintering.

1.4 Conclusions

The effect of V_2O_5 as the sintering aid on the density and hardness of $ZnO–TiO_2$ ceramics and cermets made of $ZnO–TiO_2$ ceramics and copper were investigated. The density of $ZnO–TiO_2$ ceramics was increased up to 95% of theoretical density with an additive of 2 wt.% V_2O_5 at low sintering temperature: 900–920 ℃, for 4 hours. With the additional of more V_2O_5, the density was reduced since many large pores were formed due to the evaporation of the excess liquid phase of the sintering aid. The hardness of $ZnO–TiO_2$ ceramics added 2 wt.% V_2O_5 addition sintered at a 920 ℃ for 4 hours could reach to 560 HV. For the cermets made of $ZnO–TiO_2$ ceramics and copper, up to 90% of theoretical density can be obtained when the sintering temperature is 960 ℃ for 4 hours. The hardness of cermets made of $ZnO–TiO_2$ ceramics and 80 wt.% Cu can reach 130 HV, which is higher than that of common pure copper. Based on the facts in this study, the prospective applications using $ZnO–TiO_2$ ceramics and cermets made of $ZnO–TiO_2$ ceramics and copper as raw materials of 3DP would be very attractive.

REFERENCES

[1] Dulln, F. and D. Rase, *Phase Equilibria in the System ZnO—TiO_2.* Journal of the American Ceramic Society, 1960. **43**(3): p. 125-131.

[2] BARTRAM, S.F. and R.A. SLEPETYS, *Compound Formation and Crystal Structure in the System ZnO-TiO_2.* Journal of the American Ceramic Society, 1961. **44**(10): p. 493-499.

[3] Yamaguchi, O., et al., *Formation and transformation of $ZnTiO_3$.* Journal of the American Ceramic Society, 1987. **70**(5).

[4] Chang, Y.-S., et al., *Synthesis and characterization of zinc titanate nano-crystal powders by sol–gel technique.* Journal of crystal growth, 2002. **243**(2): p. 319-326.

[5] Chang, Y.-S., et al., *Synthesis, formation and characterization of $ZnTiO_3$ ceramics.* Ceramics International, 2004. **30**(8): p. 2183-2189.

[6] Li, B., et al., *Low-fired microwave dielectrics in ZnO-TiO_2 ceramics doped with CuO and B_2O_3.* Journal of Materials Science: Materials in Electronics, 2002. **13**(7): p. 415-418.

[7] Wang, Y.-R., S.-F. Wang, and Y.-M. Lin, *Low temperature sintering of (Zn_{1-x}, Mg_x) TiO_3 microwave dielectrics.* Ceramics International, 2005. **31**(7): p. 905-909.

[8] Li, E., et al., *Low temperature sintering of low-loss $ZnTiO_3$ microwave dielectric ceramics with Zn–B–Si glass.* Journal of Alloys and Compounds, 2015. **647**: p. 866-872.

[9] Obayashi, H., Y. Sakurai, and T. Gejo, *Perovskite-type oxides as ethanol sensors.* Journal of Solid State Chemistry, 1976. **17**(3): p. 299-303.

[10] Kim, H.T., et al., *Low-Fired (Zn, Mg) TiO_3 Microwave Dielectrics.* Journal of the American Ceramic Society, 1999. **82**(12): p. 3476-3480.

[11] Chaouchi, A., et al., *Effects of additives on the sintering temperature and dielectric properties of $ZnTiO_3$ based ceramic.* Ceramics international, 2007. **33**(2): p. 245-248.

[12] Scrantom, C.Q., *LTCC Technology: Where We are and Where We're Going*, in *MCM C/Mixed Technologies and Thick Film Sensors*. 1995, Springer. p. 77-87.

[13] Scrantom, C.Q. and J.C. Lawson. *LTCC technology: where we are and where we're going. II.* in *Technologies for Wireless Applications, 1999. Digest. 1999 IEEE MTT-S Symposium on*. 1999. IEEE.

[14] Liu, X.-c., et al., *Progress in the Stuty of ZnO-TiO_2 Microwave Dielectric Ceramics.* ELECTRONIC COMPONENTS AND MATERIALS, 2005. **24**(6): p. 47.

[15] Jantunen, H., et al., *Compositions of $MgTiO_3$–$CaTiO_3$ ceramic with two borosilicate glasses for LTCC technology.* Journal of the European Ceramic Society, 2000. **20**(14): p. 2331-2336.

[16] Santhaveesuk, T., et al., *Zn_2TiO_4 Nanostructures Prepared by Thermal Oxidation Method.* Advanced Materials Research, 2008. **55-57**: p. 641-644.

[17] Zhang, Q., et al., *Sintering and microwave dielectric properties of LTCC-zinc titanate multilayers.* Materials Letters, 2005. **59**(8): p. 880-884.

[18] Liu, Z.-C., et al., *Sintering and Phase Transition of $0.25CuO$–$0.75MoO_3$ Doped ZnO–TiO_2 Microwave Dielectric Ceramics.* J. Inorg. Mater, 2009. **24**(4): p. 712-716.

[19] Golovchansky, A., H.T. Kim, and Y. Kim, *Zinc titanates dielectric ceramics prepared by sol-gel process.* Journal of the Korean Physical Society, 1998. **32**: p. S1167-S1169.

[20] Kim, H., J. Byun, and Y. Kim, *Microstructure and microwave dielectric properties of modified zinc titanates (I).* Materials research bulletin, 1998. **33**(6): p. 963-973.

[21] Chang, Y.-S., et al., *Synthesis and characterization of zinc titanate doped with magnesium.* Solid State Communications, 2003. **128**(5): p. 203-208.

[22] Chaouchi, A., et al., *Low temperature sintering of $ZnTiO_3/TiO_2$ based dielectric with controlled temperature coefficient.* Journal of the European Ceramic Society, 2007. **27**(7): p. 2561-2566.

[23] Liu, X., et al., *Low-temperature sintering and phase transition of zinc titanate ceramics with V_2O_5 and B_2O_3 addition.* Journal of Alloys and Compounds, 2007. **436**(1-2): p. 285-289.

[24] Wang, L., et al., *Low-temperature synthesis of $ZnTiO_3$ nanopowders.* Journal of Crystal Growth, 2009. **311**(3): p. 611-614.

[25] Kim, H., J. Byun, and Y. Kim, *Microstructure and microwave dielectric properties of modified zinc titanates (II).* Materials research bulletin, 1998. **33**(6): p. 975-986.

[26] Huang, G., et al., *Low-temperature sintering and microwave dielectric properties of (Zr, Sn) TiO_4 ceramics.* Materials Science and Engineering: B, 2003. **99**(1): p. 416-420.

[27] Kim, H.T., et al., *Low-Temperature Sintering and Microwave Dielectric Properties of Zinc Metatitanate-Rutile Mixtures Using Boron.* Journal of the American Ceramic Society, 1999. **82**(11): p. 3043-3048.

[28] Chen, H.-C., et al., *Effect of bismuth addition on sintering behavior and microwave dielectric properties of zinc titanate ceramics.* Journal of electronic materials, 2005. **34**(1): p. 119-124.

[29] Eom, J.-H., et al., *Microstructure and properties of porous silicon carbide ceramics fabricated by carbothermal reduction and subsequent sintering process.* Materials Science and Engineering: A, 2007. **464**(1-2): p. 129-134.

[30] Lu, K. and W.T. Reynolds, *3DP process for fine mesh structure printing.* Powder technology, 2008. **187**(1): p. 11-18.

[31] Utela, B., et al., *A review of process development steps for new material systems in three dimensional printing (3DP).* Journal of Manufacturing Processes, 2008. **10**(2): p. 96-104.

[32] Berman, B., *3-D printing: The new industrial revolution.* Business horizons, 2012. **55**(2): p. 155-162.

CHAPTER 2 FABRICATION OF POROUS ALUMINA CERAMICS IN TWO DIFFERENT WAYS

2.1 Introduction

Porous ceramics is one of the frequently used materials for a variety of applications, including the filtration of molten metals, high-temperature thermal insulation, support for catalytic reactions, filtration of particulates from diesel engine exhaust gases, filtration of hot corrosive gases in various industrial processes, and lightweight structural materials [1-5]. The advantages of using porous ceramics in these applications are usually the high melting point, tailored electronic properties, high corrosion, and wear resistance in combination with the features gained by the replacement of solid material by voids in the component. Such features include low thermal mass, low thermal conductivity, controlled permeability, high surface area, low density, high specific strength, and low dielectric constant. Many different preparation methods for porous ceramics have been studied over the past decade, such as polymeric foam replication, starch consolidation casting, and gel casting, etc.

2.1.1 Polymeric foam replication

Yao et al. prepared the reticulated porous silicon carbide ceramics using polymeric foam replication by a recoating technique. Reticulated porous ceramics (RPCs) are highly porous ceramics (70–95%) with an open, three-dimensional network structure. The most common applications of the RPCs are molten metal and diesel engine exhaust filters, catalyst supports due to their high permeability, resistance to chemical attack and structural uniformity [6-8].

The ‘‘polymeric sponge’’ process [7], invented by Schwartzwalder and Somers [9]. In the method, green RPCs consisting of a few filled cells were fabricated by coating a polyurethane sponge with a thixotropic slurry. In order to remove excess slurry from the sponge, centrifuging or passing through preset rollers is the commonly used technique. RPCs produced by this process are of low strength and fracture toughness since very thin struts of the ceramic structure may remain and triangular pores exist after the organic sponge is burned out, making them sensitive to structural stresses and limiting their structural applications [10]. Several techniques have been tried to improve the slurry coverage [11, 12]. A second coating of the slurry may be applied to fill in any flaws or thin areas in the first coating. As suggested by Schwartzwalder and Somers [9] and Brown and Green [13], the second coat may be directly applied on the dried original coating. The dried body including the sponge substrate is difficult to recoat by dipping since dipping can wash away some of the previously deposited ceramic coatings and weaken the structure. At the same time, the recoat slurry floated by gravity will lead to filled cells, especially near the bottom portion of the part. Zhu et al. [14] developed a new recoating method. First, the green body prepared by preset roller method is preheated to produce a reticulated preform with enough handling strength after the sponge is burnt out. Then, the preform was recoated by a thinner slurry using the centrifugal method. This technique greatly improved the mechanical properties of RPCs.

Wen et al. [15] prepared porous ceramics with controllable pore size using natural clay and silica as starting materials and organic polymer sponge as a template. Table 2.1 shows the bulk chemical composition of the natural clay used here; LOI refers to weight loss after ignition at 1000 °C. Figure 2.1 shows that sintered samples with decreasing

porosities from A through F. All the samples have a reticular structure with open cells. The cells are linked together by solid 3D skeletons forming connected open channels, allowing fluid access and to a limited degree even fluid flow. The cell sizes of each porous ceramic sample depend on the cell sizes of the organic polymer sponge templates used.

Table 2.1 Chemical composition of the natural clay [15]

	SiO_2	Al_2O_3	Fe_2O_3	TiO_2	CaO	MgO	K_2O	Na_2O	LOI	Total
wt.%	70.63	16.96	0.54	0.03	0.45	1.00	1.95	0.31	8.13	100.00

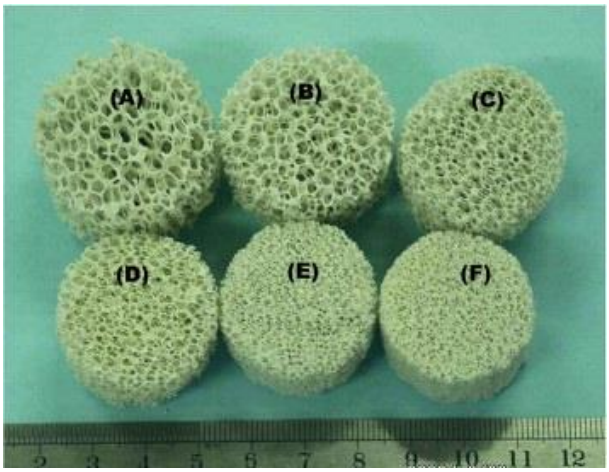

Figure 2.1 Morphology of the prepared porous silica ceramics with different pore sizes (A: 5.7 mm pore size and 78 vol.% porosity, B: 5.3 mm pore size and 77.8 vol.% porosity, C: 4.4 mm pore size and 77.3 vol.% porosity, D: 3.2 mm pore size and 76.2 vol.% porosity [15]

2.1.2 Starch consolidation casting (SCC)

The use of pore-forming agents is one of the frequently used methods to produce porous ceramics with controlled microstructure (porosity and pore size) [2, 16]. During heating up to the final firing temperature of the ceramics, these pore-forming agents are burnt out, leaving void pores in the ceramic. Among the various pore-forming agents, those

of biological origin, in particular, starch, have gained a prominent position. They are cheap, non-toxic, environmentally friendly and exhibit defect free burnout between approximately 300 and 600 °C [17, 18]. A specific advantage for porous ceramics is the fact that the pore size can be controlled by choosing the appropriate starch type and that the pore size distribution is in most cases sufficiently narrow to make technological process control efficient [19]. The pore sizes achievable with commercial starch types ranging from ~5 µm in rice starch to ~50 µm in potato starch [18].

Starch grains are normally white, dense and water-insoluble at room temperature. Most starches consist of mixtures of two polysaccharide types, a linear one, amylose, and a highly branched one, amylopectin. Amylose gives the starch its gelling property in aqueous suspensions. The glucose units that build up the polymeric chains in starch expose a lot of hydroxyl groups and, therefore, give a strong hydrophilic character to starch granules, as shown in Figure 2.2 [20]. These have some favorable characteristics such as good thickening, stabilizing, membrane-forming and gelling properties.

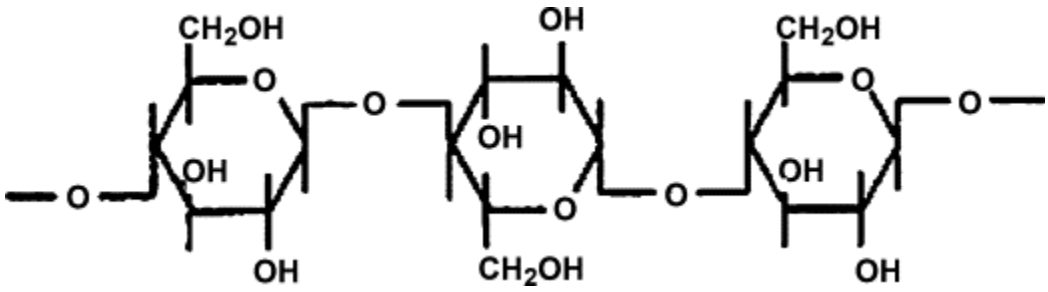

Figure 2.2 Starch as a polymer consisting of condensed glucose units [20]

SCC is based on the ability of starch to swell and finally gelatinize in water at elevated temperature (60–80 °C), so that ceramic green samples can be formed from suspensions in impermeable molds (usually metal molds) [19, 21-24]. As the starch

granules or particles swell they will also act as a binder adding strength to the consolidated body, which enables demolding prior to drying. After burn-out of the starch and sintering of the ceramic matrix, a material is obtained with a porosity corresponding to the original amount, shape and size of the starch particles [20].

Gregorová et al. presented that the porous alumina ceramics between 25 and 50% porosity were produced by SCC and the limits of pore size and porosity were discussed [19, 22, 25]. In addition, Sepulveda et al. made open cell hydroxyapatite (HA) foams with relative porosities from 72 to 90% [26]. Colombo et al. obtained the macrocellular and microcellular silicon carbide open cell ceramics using sacrificial template technique. Macrocellular structures with cell sizes ranging from 100–600 μm were synthesized by a foaming approach. Microcellular structures with a cell size of around 8 μm were fabricated using polymer microbeads as sacrificial templates [27].

Among the methods aforementioned, polymeric foam replication and sacrificial templates are the processing routes used for the production of macroporous ceramics exhibiting pore size (d) larger than 50 nm; additionally, direct foaming also used for the preparation of macroporous ceramics as shown in Figure 2.3 [2]. While starch consolidation casting and gel-casting are used to produce the micro- (d < 2 nm) and mesoporous (2 nm < d < 50 nm) ceramics [2].

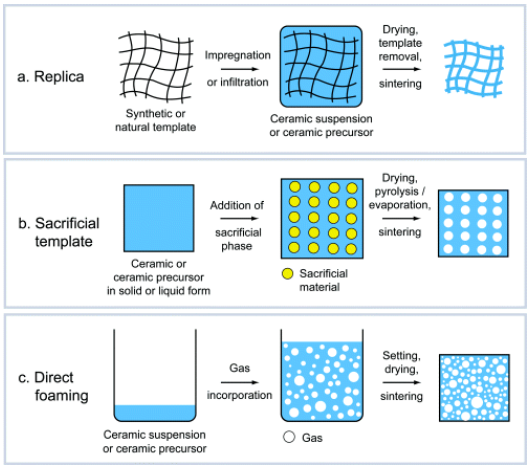

Figure 2.3 Scheme of possible processing routes used for the production of macroporous ceramics [2]

Each of these routes mentioned above has its own disadvantages, e.g., the mechanical properties of the ceramics prepared by the polymeric foam replication are poor because of the drawbacks of the pyrolysis process and its pore sizes are limited to macro scale and millimeter scale. In order to fabricate porous ceramics without drawbacks mentioned above, some studies developed procedures combining these techniques to produce ceramics with improved properties that could not be obtained by a single technique. Ramay et al. reported that the macro porous hydroxyapatite scaffolds, which possessed an open, uniform, and interconnected porous structure with a pore size of 200–400 μm and a compressive yield strength of 5 MPa, by combining the replication method with the gel-casting method [23]. Mao et al. developed a new technique to make ceramics with hierarchical pore structure using starch consolidation casting and foaming methods [28].

In this work, porous alumina ceramics with different porosity were fabricated by two different methods: the first one combined the starch consolidation process with the gel-casting process using corn starch as the pore-forming agent and also as the binder. The

other one used hollow microspheres as the pore-forming agent. No relative studies using hollow microspheres as the pore-forming agent is reported in the literature so far. For both of two methods, the bulk density, porosity, and microstructure of the obtained alumina ceramics were studied.

2.2 Alumina ceramics fabrication with corn starch

In this study, porous alumina ceramics with different porosity were fabricated by combining the starch consolidation process with the gel-casting process using corn starch as the pore-forming agent and the binder. The bulk density, porosity, and microstructure of the obtained alumina ceramics were studied. Moreover, a relationship between the total porosity of alumina ceramics after sintering and corn starch content was obtained. The relation between the linear shrinkage of porous alumina ceramics and the starch content also was discussed. Finally, the compressive strength of the sintered samples was measured.

2.2.1 Theory

SCC is based on the ability of starch to swell in water at elevated temperature and thus to absorb water from aqueous ceramic suspensions. This behavior enables the preparation of ceramic green bodies by casting starch-containing ceramic suspensions into impermeable molds and heating the system up to approximate 807 ℃. The swelling starch compresses the ceramic powder and at the same time dewaters the suspension. In combination with the subsequent rheological changes, this transforms the initially viscous

suspension into an elastic (more or less rigid) ceramic green body. After some time, this green body can be taken out of the mold (demolded) and subsequently dried and fired.

The relative volumetric swelling ϵ of starch granules (with V being the volume after swelling and V_0 the volume before swelling) is related to the diameter of the swollen starch granules D (more precisely, its volume-weighted arithmetic mean) by the following equation:

$$\epsilon = \frac{V - V_0}{V_0} = \left(\frac{D}{D_0}\right)^3 - 1 \tag{2.1}$$

where D_0 is the diameter of the dry starch granule (before swelling). The swelling kinetics has a sigmoidal time dependence which may conveniently be fitted with the three-parameter so-called logistic model [24]:

$$\epsilon = \frac{a}{1 + bexp(-ct)} \tag{2.2}$$

where t is the time in minutes (includes heating and swelling time) and a, b, c are adjustable fit parameters (empirical fit parameters without physical meaning). When ceramic powder particles are present in addition to starch, like in a ceramic suspension, the swelling starch granules push the ceramic particles (which are much smaller than the starch granules) aside and press them into a dense "random close packed" or "maximally random jammed" structure [29]. For monodisperse spheres the maximum packing density of such a system is approximate 64% and a similar value may be adopted as an estimate for moderately polydisperse systems of isometric particles. However, it is ascertained that in many cases the swelling factor (ratio of swollen diameter to initial diameter) cannot attain its maximum value since the excess water present in the suspension will be exhausted

before this value is attained. Based on elementary geometrical considerations the maximum relative volumetric swelling of the starch is given by the following relationship [24]:

$$\epsilon^* = \frac{(\phi_0^{max} - \phi_0) \cdot (1 - \phi_S)}{\phi_0^{max} \phi_0 \phi_S} \tag{2.3}$$

where ϕ_0 is the volume fraction of ceramic powder in water (without starch), ϕ_0^{max} maximum value (typically around 0.64) and ϕ_S the nominal starch content in the suspension (i.e. the volume fraction of starch related to the solids content without water). After measuring the unconstrained swelling kinetics (in water), the time dependence of the relative volumetric swelling can be fitted using the logistic model and the minimum time needed for the consolidation step in the constrained system can be predicted with this equation [24]:

$$t_{min} = -\frac{ln\left(\frac{a - \epsilon^*}{b\epsilon^*}\right)}{c} \tag{2.4}$$

The sum of the final porosity of a ceramic body and its volumetric shrinkage after firing equals the initial porosity (before firing). Under the assumption of isotropic and uniform microstructures, the volumetric shrinkage of a ceramic body is related to its linear shrinkage σ_L (measured in one direction):

$$\sigma_V = \sigma_L^3 - 3\sigma_L^2 + 3\sigma_L \tag{2.5}$$

2.2.2 Experimental procedure

As ceramics' raw materials, alumina powder (main size less than 0.5 μm, A16SG, Alcoa Inc., New York City, USA) was chosen as received in this study. Alumina nanopowder (40–80 nm, gamma-phase > 99%, Alfa Aesar Co., Ward Hill, USA) was used as a sintering additive. The 5 wt.% polyvinyl alcohol (PVA) solution was added as an

adhesive agent. Commercially available corn starch (density=1.6 g/cm^3, Hodgson Mill Inc., Effingham, USA) was selected as the pore-forming agent and binder. The corn starch in this study received no pre-processing. Figure 2.4 and Figure 2.5 show the micrographs, and size distributions of corn starch, respectively and it can be observed that the mean diameter of corn starch is between 12.9 μm and 15.0 μm [30].

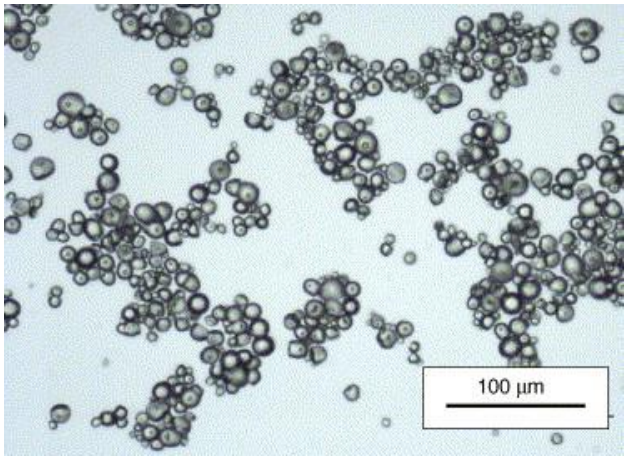

Figure 2.4 Optical micrograph of corn starch chose in this study [30]

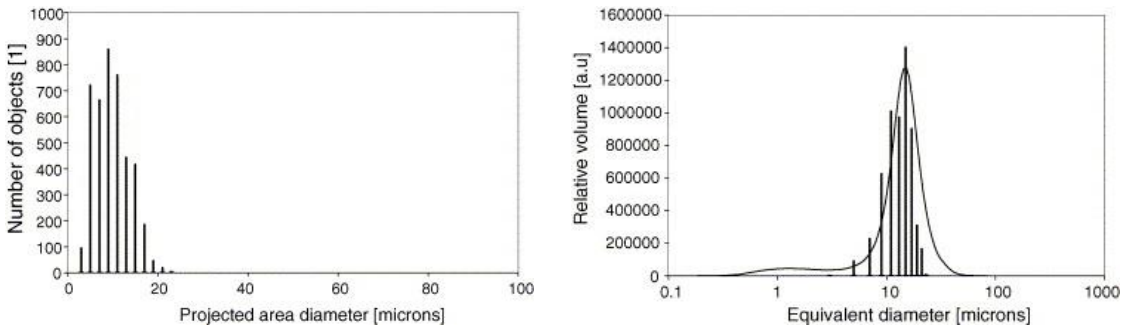

(a) (b)

Figure 2.5 (a) Number-weighted size distributions, and (b) volume-weighted size distributions [30]

The micron scale alumina powder and alumina nanopowder were combined with the weight ratio of 95%/5%, and then mixed using a ball mill with beads (2-3 mm in

diameter) for 8 hours. Both jar and milling beads consisted of agate while milling medium is deionized water. The 5 wt.% polyvinyl alcohol (PVA) solution was added to the alumina suspension. PVA has an excellent adhesive property which could help sample molding during the molding process and can undergo pyrolysis above 200 ℃. Amounts of 0–50% corn starch mixed with the stabilized alumina suspension were then measured by the volume fraction of raw ceramics powders. 0.5 wt.% commercial dispersant for Al_2O_3 (Dolapix CE64, Zschimmer & Schwarz Inc., Milledgeville, USA) also added with the corn starch. The resulting mixtures were prepared to a slurry with 15 vol.% solid loading, including Al_2O_3 powders, starch, PVA, and dispersant and then were agitated using an electromagnetic stirrer at room temperature for 24 hours. The slurry was then subjected to de-aeration to remove undesired entrapped bubbles. After that, the slurry was agitated and heated on the electromagnetic stirrer at 80 ℃ for 1 hour. This process was based on the swelling and absorbing ability of starch in the aqueous ceramics suspensions after heating to around 80 ℃ [19]. The slurry was then dried in an oven at 60 ℃ for 2–3 days. Figure 2.6 shows the mechanism of the preparation process of the green body. The dried powders were compacted under 100 MPa into samples of 16 mm-diameter and 10 mm-thickness, as shown in Figure 2.7. The compacted samples were then sintered in an air environment at atmospheric pressure in an electric heating furnace. After sintering all samples were cut to a size of 12 mm-diameter and 4 mm-thickness. The compressive strength was tested with a cross head speed of 0.05 mm/min on an Instron 3369 Testing Machine. Eight samples were utilized to obtain average values and standard deviations.

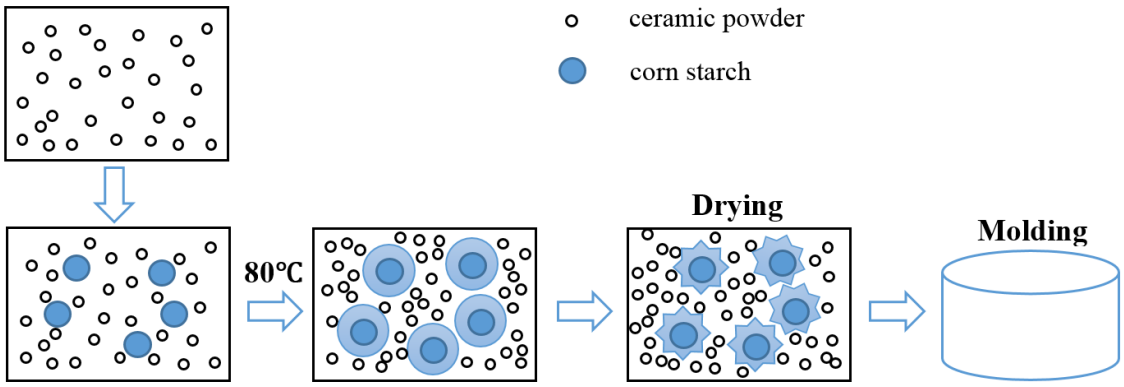

Figure 2.6 Schematic view of ceramic green body formation in this study

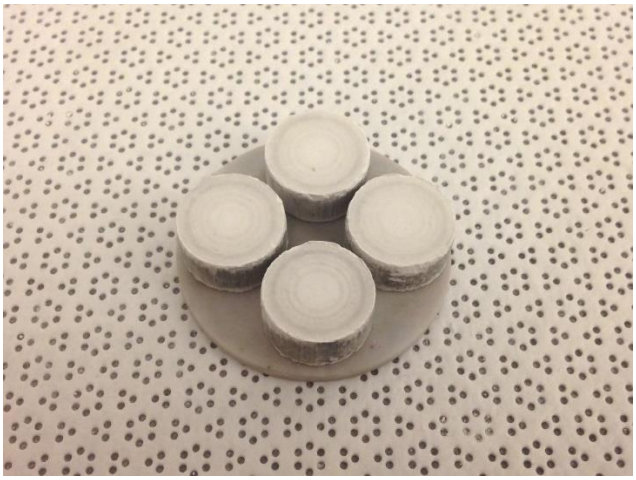

Figure 2.7 Ceramic green body prepared with corn starch

In this study, the PVA and corn starch must be burnt out during the sintering process to develop the desired porosity. According to the thermogravimetric and differential thermal analysis of the compacted ceramics body, the crucial temperature range for burning starch out before ceramic sintering is from 300 to 600 ℃, as shown in Figure 2.8 [28]. Therefore, the samples in this study were heated from room temperature up to 500 ℃ at a

heating rate of 0.5 ℃/min, as well as dwelled at 200 ℃ for 1 hour to remove the water content of samples in order to reduce cracks in samples during the heating process. The samples were held at 500 ℃ for 1 hour to eliminate PVA completely. Then the samples were heated from 500 ℃ to 600 ℃ at a rate of 0.5 ℃/min and assisted by dwelling at 600 ℃ for 2 hours to burn out the corn starch. Thereafter, the heating rate was changed to 5 ℃/min and then the sintering was accomplished at 1500 ℃ for 3 hours. The heating schedule is shown in Figure 2.9. Figure 2.10 shows the block diagram of the specimens' preparation process.

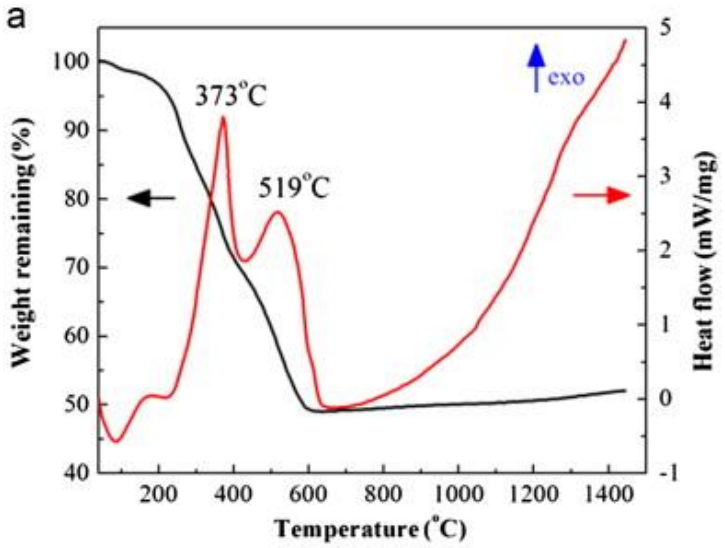

Figure 2.8 TG/DSC analysis for thermal behavior of dried body in air [28]

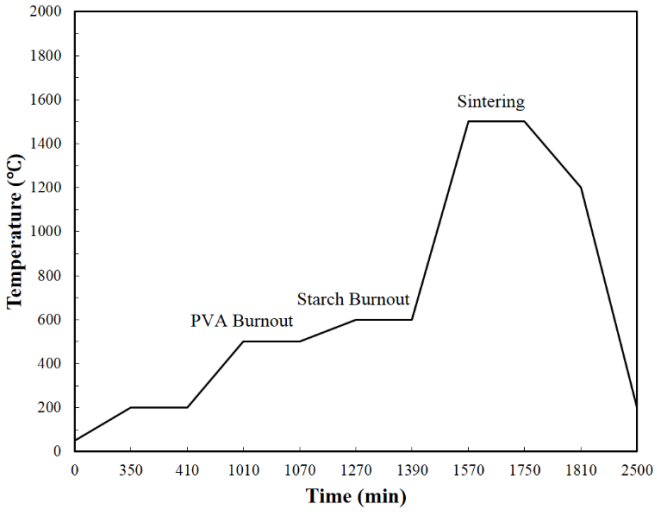

Figure 2.9 Heating schedule for the sintering process

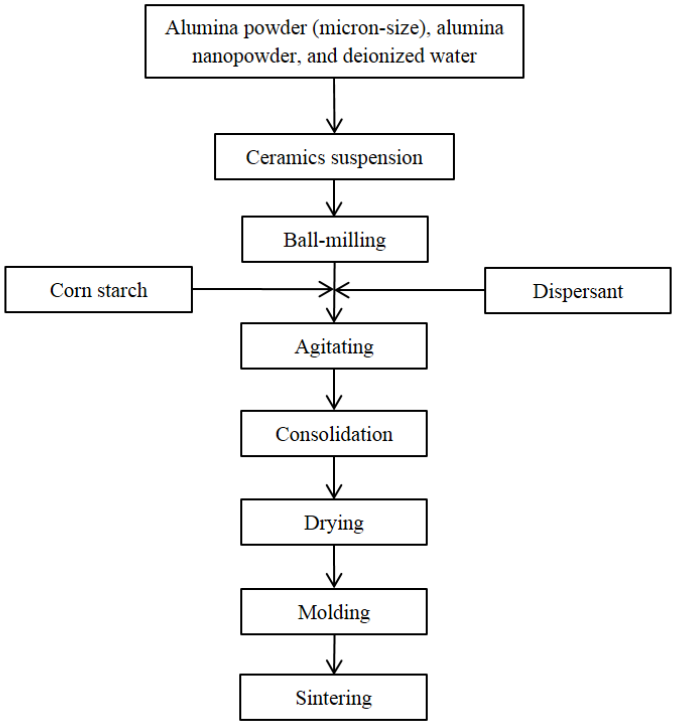

Figure 2.10 Flow chart of preparation process for ceramic specimens

2.2.3 Results and discussion

Figure 2.11 shows the ceramic specimens after the sintering process in this study. The bulk densities of alumina ceramics with different amounts of added corn starch is shown in Figure 2.12. The densities were measured by the Archimedes Technique. This figure shows that the density decreased linearly with increasing starch content. The alumina ceramics with approximate 80% theoretical density (theoretical density of alumina ceramics = 3.95 g/cm^3) was attained with 10% starch content. The density reduced to the minimum value 1.33 g/cm^3 at 50 vol.% starch content. This result indicates that the burnout of corn starch during the sintering process does not influence the sintering of ceramics and the forming of the porous structure. Moreover, the densities of alumina ceramics obtained in this study were greater than that of ceramics prepared by the gel-casting technique [28].

Figure 2.11 Ceramic specimens after sintering process

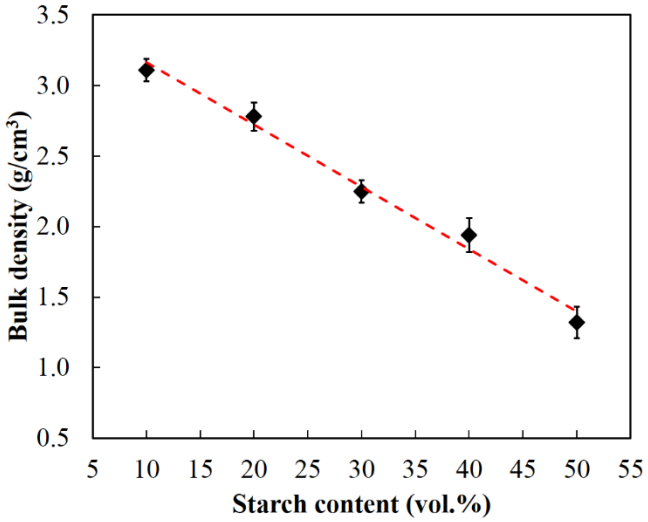

Figure 2.12 Bulk density of sintered samples vs. starch content

Figure 2.13 illustrates the relationship between linear shrinkage of alumina ceramics and starch content. The relationship indicates that the linear shrinkage was not dependent on the amounts of corn starch. As presented in Figure 2.13, linear shrinkages after sintering were from 13.0 to 14.4%. In general, the linear shrinkages presented an upward trend with increasing corn starch content. The shrinkages under 20 vol.% starch content had a similar value and from 30 to 50 vol.% had a similar value but greater than the ones under 20 vol.%. It was believed that the linear shrinkage was only dependent on the large pores formed in the burnout process of starch [19, 22, 25]. As mentioned above, PVA acted as an adhesive agent which might cause the agglomeration of corn starch in this study. If so, the linear shrinkage would change considerably when increasing corn starch content. However, the linear shrinkages were nearly the same in this study. Thus, the linear shrinkage result of this work presented that the PVA did not cause the agglomeration of

corn starch and the burnout process of PVA had no impact on the linear shrinkage when sintering ceramics.

The total porosity obtained in this study as a function of starch content is shown in Figure 2.14. As shown in Figure 2.14, the linearly increasing trend was observed when the starch content increased from 10 vol.% to 50 vol.%. The total porosity of 14.8% was obtained at 10 vol.% starch content while it increases to 55.3% at 50 vol.% starch content. This suggests that the compressive molding after the starch consolidation step did not affect the total porosity.

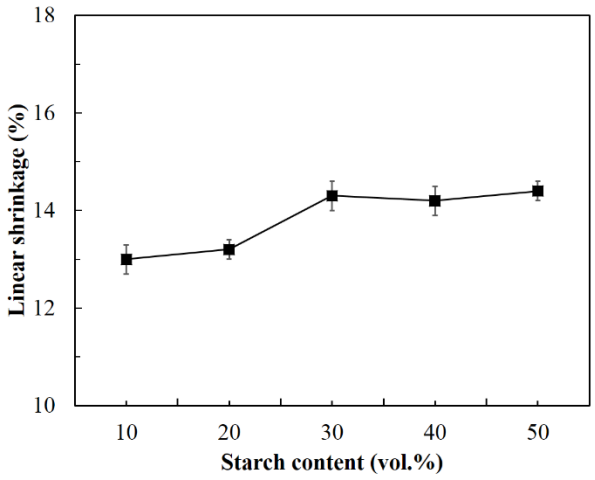

Figure 2.13 Linear shrinkage changes as a function of starch content

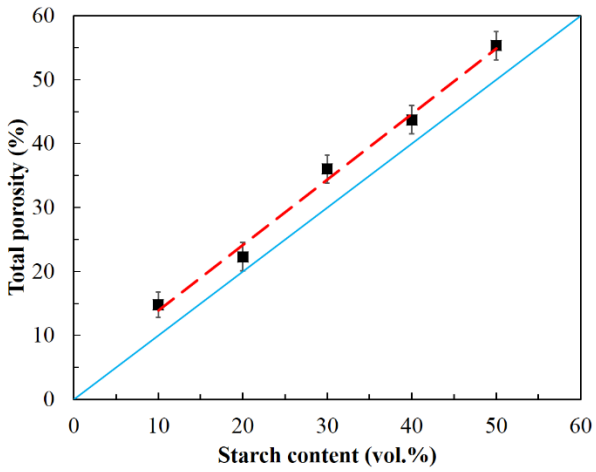

Figure 2.14 Total porosity of sintered alumina ceramics as a function the starch content

Figure 2.14 also makes a comparison between the results achieved in this study and that of the traditional slip casting. In the process of traditional slip casting, no starch swelling step occurs since starch is only used as a pore forming agent. Therefore, the amounts of starch content when preparing the raw materials of ceramics are equal to the total porosity of sintered ceramics (cf. the solid line in Figure 2.14). As another method to produce porous ceramics, the starch consolidation casting can produce the total porosity ranging from 25% to 50%. Total porosities less than 20% are not easy to achieve [22]. For alumina ceramics fabricated in this study, however, the total porosities were typically greater than the amounts of starch added in the preparation process (cf. the dashed line in Figure 2.14). The limits of starch consolidation casting and traditional slip casting were reported in [20, 30-33]. Thus, the relationship found in this study demonstrates that the total porosity of alumina ceramics fabricated using the method combining the starch consolidation and gel-casting process was higher than that of the ceramics made by

traditional slip-casting. The range of total porosity of ceramics in this work was broader than that of the ceramics produced by starch consolidation casting.

Figure 2.15 shows SEM micrographs of typical fracture surfaces of the porous alumina ceramics with different starch contents (0–50 vol.%) after sintering at 1500 ℃ for 3 hours. The microstructure of the alumina ceramics without corn starch is shown in Figure 2.15 (a). As revealed, lower porosity and grain growth can be observed for the samples sintered at this temperature. According to references [19, 32, 33], the densification and the phase transition from gamma to alpha of alumina ceramics had completed typically under this temperature.

As shown in Figure 2.15 (b)–(f), the amorphous materials completely burned and the skeleton was formed through the grains connecting. The porosity and porous structures of the alumina ceramics added starch increased when the amounts of corn starch increased from 10 to 50 vol.%. The reason is that more starch grains connected with each other when more corn starch was added into the ceramics' raw materials, which led to the rise of porosity and porous structures. Moreover, the grains-connecting of corn starch resulted in the increase of channels among pores after sintering. Similar results were also attained by other work using other methods for fabrication of porous alumina ceramics [3, 34, 35]. Comparing the micrographs in Figure 2.15, the alumina samples with 40 vol.% corn starch possessed a more uniform pore size.

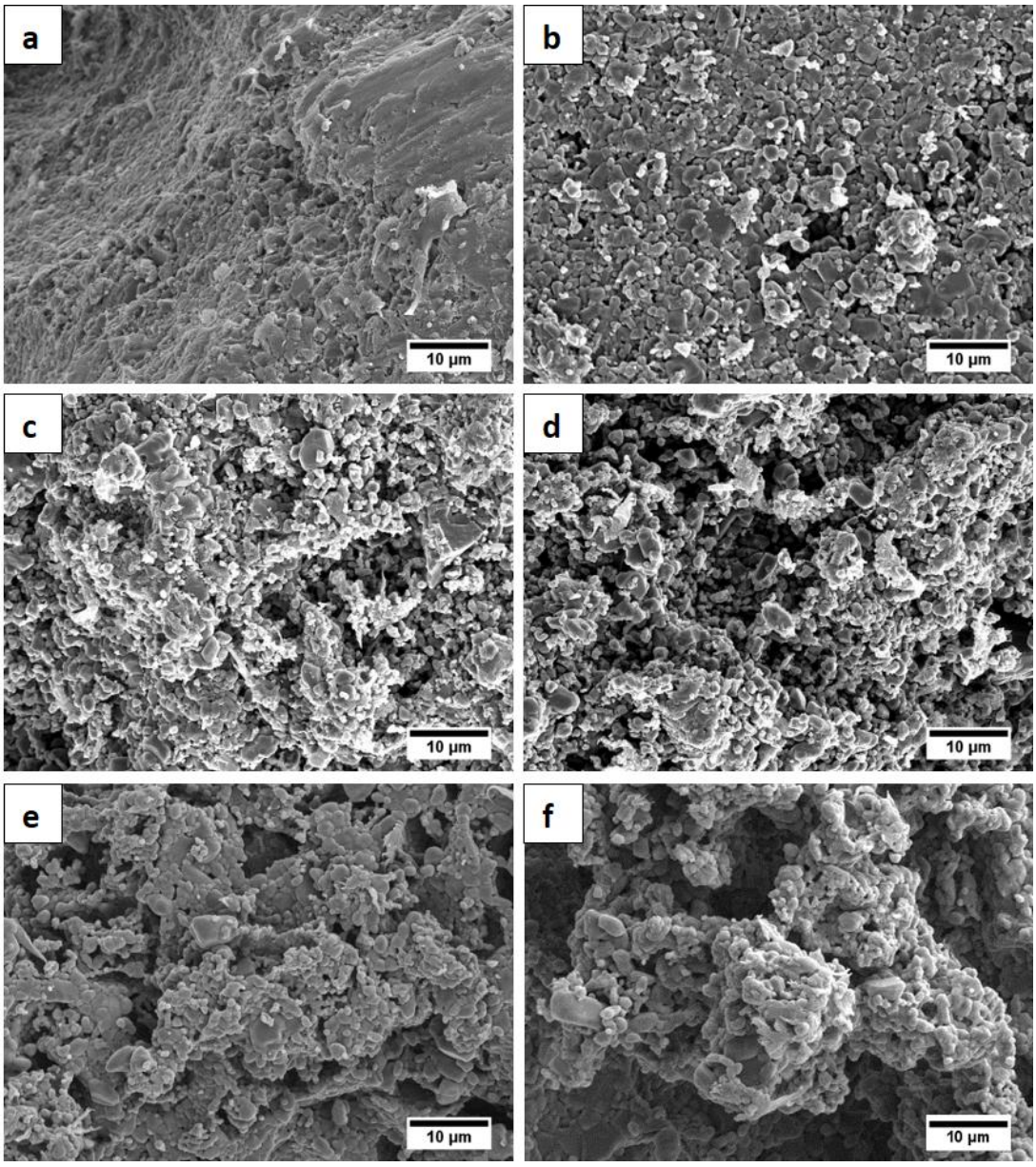

Figure 2.15 SEM micrographs of porous alumina ceramics with different amounts of corn starch (a) 0%, (b)10%, (c) 20%, (d) 30%, (e) 40%, and (f) 50%

The compressive strength of porous alumina ceramics as a function of starch contents is shown in Figure 2.16. The compressive strength decreased significantly when the corn starch contents increased from 10 to 50 vol.% corresponding with a compressive

strength of 5.89–24.16 MPa. The decreasing trend of compressive strength with increasing starch content indicates that size changes of crucial loading area occurred in the samples when sintering with different starch contents. The increasing corn starch content resulted in the higher porosity and more porous structure that can lead to the weak skeletons among pores within the samples.

Generally, a number of expressions can be used to describe the compressive strength-porosity behavior of porous ceramics. One of the simplest methods was firstly proposed by Ryshkewitch and Duckworth [36], and developed to be the *Rice* equation [37]:

$$\sigma = \sigma_0 \exp(-b\varepsilon) \tag{2.6}$$

where σ_0 is the strength of a dense material which is from 30 MPa to 35 MPa for alumina ceramics [28, 37], and σ is the strength of the porous material with a porosity of ε, and b is a parameter depending on the structure and material composition. The value of the parameter b represents the susceptivity of strength on porosity, i.e. the larger b value, the more susceptivity of strength on porosity. The fitting curve in Figure 2.16 can be expressed by

$$\sigma = 33.8 \exp(-0.025\varepsilon) \tag{2.7}$$

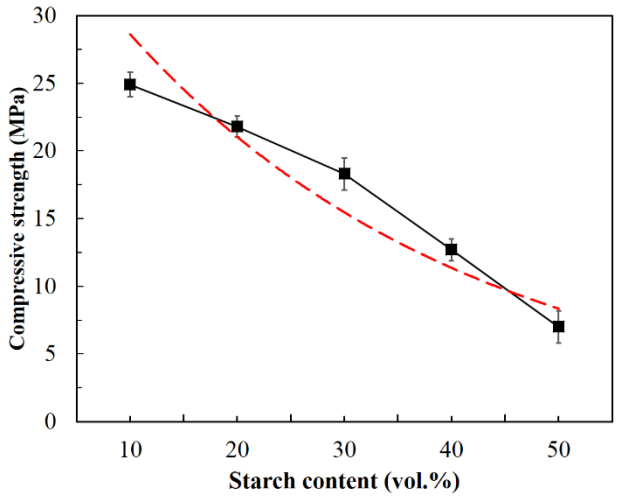

Figure 2.16 Compressive strength of sintered samples vs. starch content

2.2.4 Conclusions

Porous alumina ceramics with different porosity were fabricated by combining the starch consolidation process with the gel-casting process using corn starch as pore-forming agents and also as binders. The bulk density, porosity, and microstructure of the obtained alumina ceramics were studied. It was found that the total porosity range of sintered samples with different amount of starch contents from 10 to 50 vol% is 14.8–55.3% and the total porosity increased with the increase of starch content. A relationship between the total porosity of specimens and corn starch content was obtained. This relationship indicates that the total porosity of alumina ceramics fabricated in this work was higher than that of the ceramics made by traditional slip-casting. The range of total porosity of ceramics in this work was broader than that of the ceramics produced by starch consolidation casting. The relationship between the linear shrinkage of porous alumina ceramics and the starch content also was discussed. The compressive strength of the sintered samples varied within

the range of 5.89–24.16 MPa, corresponding to the starch content of 50–10 vol%. The porous alumina ceramics fabricated in this work with high porosity would be used as preforms for pressure filtration in authors' next research stage and may have the potential for other applications such as hot gases media, catalyst support, and lightweight structural materials.

2.3 Alumina ceramics fabrication with hollow microspheres

In this work, porous alumina ceramics with different porosity were fabricated using hollow microspheres as a pore-forming agent. The relative density, total porosity, and microstructure of the obtained alumina ceramics were studied. The cell morphology of resulting materials has a hierarchical structure with pores of two different sizes. The advantage of using hollow microspheres as a pore-forming agent is that hollow microsphere has lower amounts of gaseous by-products when it is pyrolyzed during sintering process than other microbeads such as PMMA-PEG and is less expensive than other bulk microbeads. The compressive strength of the sintered samples also was measured.

2.3.1 Experimental procedure

As ceramics' raw materials, alumina powder (main size less than 0.5 μm, A16SG, Alcoa Inc., New York City, USA) was chosen as received in this study. Alumina nanopowder (40–80 nm, gamma-phase > 99%, Alfa Aesar Co., Haverhill, USA) was used as a sintering additive. The 5 wt.% polyvinyl alcohol (PVA) solution was added as a binder. Commercially available microspheres (Expancel 920 DE80 d30, particle sizes = 55–85μm,

true density = 30 kg/m3, Akzo Nobel Coating Inc., Amsterdam, Netherlands) was selected as the pore-foaming agent. Expancel microspheres are small spherical plastic particles made of hydrocarbon. The microspheres consist of a polymer shell encapsulating a gas. When heated, the internal pressure of the gas increases and the thermoplastic shell softens, resulting in a dramatic increase in the volume of the microspheres as shown in Figure 2.17 [38]. Product specification for Expancel microspheres is shown in Table 2.2. The commercial Expancel product used in this work is shown in Figure 2.18 and Figure 2.19. No pre-processing to prepare the microspheres in this study.

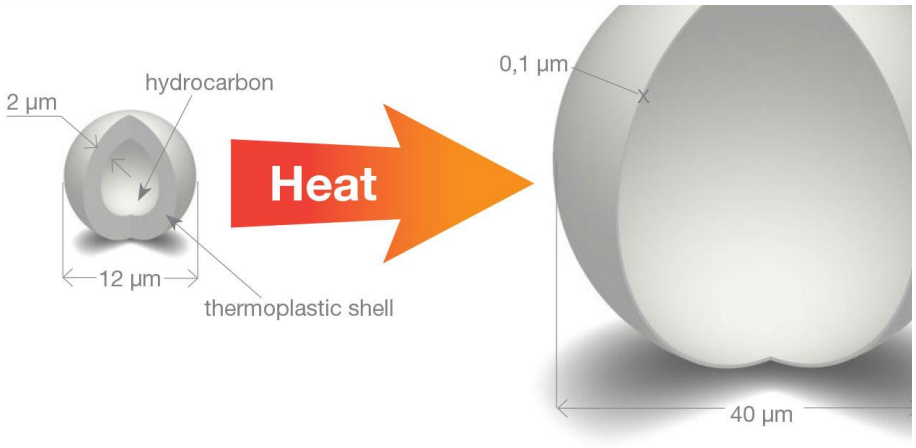

Figure 2.17 Expansion of Expancel microspheres when heated [38]

Table 2.2 Product specification for Expancel Microspheres [38]

Expancel	Particle size (µm)	True density (kg/m^3)	Solvent resistance
551 DE 40 d42	30-50	42±4	3
551 DE 40 d42±2	30-50	42±2	3
461 DE 20 d70	15-25	70±6	4
461 DE 40 d60	20-40	60±5	4
461 DET 40 d25	35-55	25±3	4
461 DET 80 d25	60-90	25±3	4
092 DET 100 d25	80-120	25±3	5
920 DE 40 d30	35-55	30±3	5
920 DET 40 d25	35-55	25±3	5
920 DE 80 d30	55-85	30±3	5

Figure 2.18 Microspheres of Expancel product: 920DE80d30

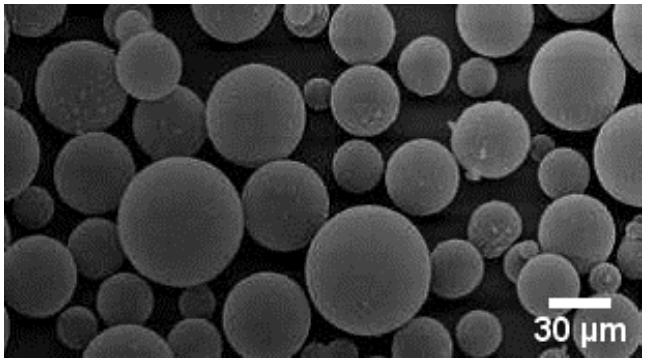

Figure 2.19 SEM image of product 920 DE 80 d30 [38]

The micron scale alumina powder and alumina nanopowder were weighed with the weight ratio of 95%/5%, and then mixed using ball mill with beads (2–3 mm in diameter) for 8 hours. Both jar and milling beads are made of agate while milling medium is deionized water. The 5 wt.% polyvinyl alcohol (PVA) solution was added to the alumina suspension. Amounts of 2.0–4.0% hollow microspheres mixed with the suspension were then measured by the weight fraction of ceramics powders. 0.5 wt.% commercial dispersant for Al_2O_3 (Dolapix CE64, Zschimmer & Schwarz Inc., USA) also added with the hollow

microspheres. The resulting mixtures were agitated using electromagnetic stirrer at room temperature for 24 hours. After that, the suspension was then stirred and dried in an oven at 60 ℃ for a couple of days. The dried powders were compacted into samples of 16 mm-diameter and 5 mm-thickness. The compacted samples were then sintered in an air environment at atmospheric pressure. The sintering process was performed in an electric heating furnace. The block diagram of the preparation process is shown in Figure 2.20.

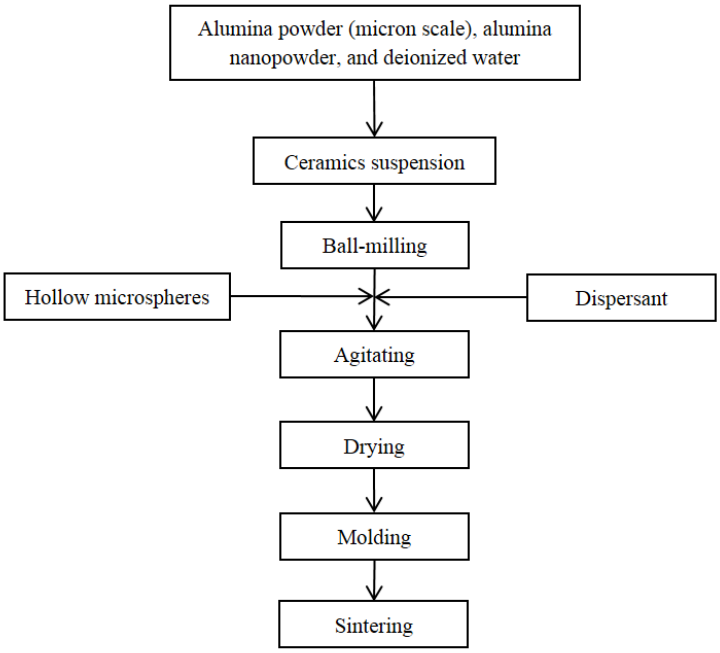

Figure 2.20 Flow chart of preparation process for porous alumina ceramics in this study

In this study, the PVA and hollow microspheres must be burnt out during sintering process in order to get the desired porous ceramics. According to the thermogravimetry analysis and Fourier transform infrared spectroscopy of the compacted ceramics body [39], the crucial temperatures for burning hollow microspheres out before the ceramics sintering is from 300 to 500 ℃. Therefore, the samples in this study were heated from room

temperature up to 300 ℃ at a heating rate of 0.5 ℃/min and stayed at this temperature for 1 hour to eliminate PVA completely. Then the samples were heated from 300 ℃ to 400 ℃ at a rate of 0.5 ℃/min and assisted by dwelling at 400 ℃ for 2 hours to burn out the hollow microspheres. Thereafter, the heating rate was changed to 5 ℃/min and then the sintering was accomplished at 1500 ℃ for 3 hours. The sintering processes aforementioned were performed in a tube furnace (GSL-1700X-80VT-UL, MTI Corp., Richmond, USA). The heating schedule is shown in Figure 2.21.

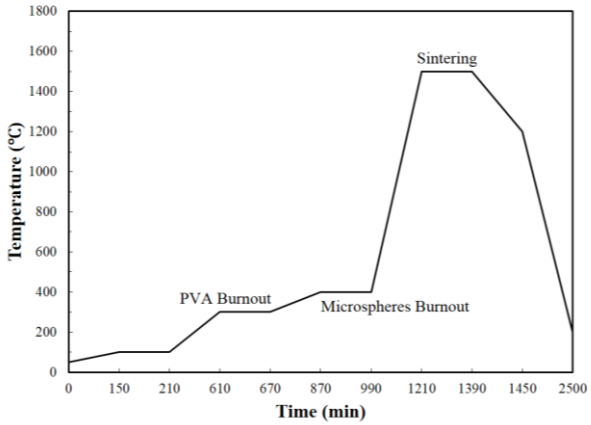

Figure 2.21 Heating schedule for the sintering process

The relative density of sintered ceramics was calculated by the weight-to-volume ratio of the samples. The total porosity of ceramics was determined through the ratio of bulk density to the true density of samples. The grain and cell morphology of obtained ceramics was observed by scanning electron microscopy (SEM, FEI Sirion 200, Hillsboro, USA). The compressive strength was measured at a crosshead speed of 1.0 mm/min. The diameter of the test samples was 13 mm and the thicknesses were from 3.5 mm to 6.5 mm.

2.3.2 Results and discussion

Figure 2.22 shows the specimens using hollow microspheres as the pore-forming agent after sintering process. The relative densities of alumina ceramics added different amounts of hollow microsphere is profiled in Figure 2.23. The bulk densities were measured by Archimedes technique. This figure shows that the density decreases linearly with increasing amount of hollow microsphere. The alumina ceramics with approximate 26% theoretical density (theoretical density of alumina ceramics = 3.95 g/cm^3) was attained when the microsphere content was 2.0 wt.%. The density reduced to the minimum value 0.82 g/cm^3 at 4.0 wt.% microsphere content. This result indicates that the burnout of hollow microspheres during sintering process does not influence the sintering of ceramics and the forming of the porous structure.

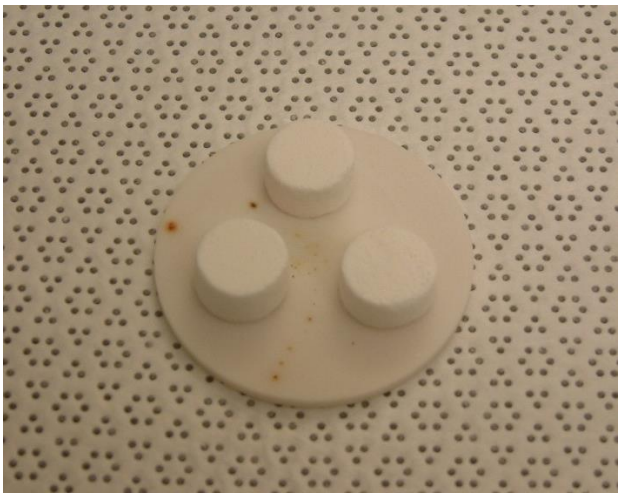

Figure 2.22 Specimens using hollow microspheres as the pore-forming agent after sintering process

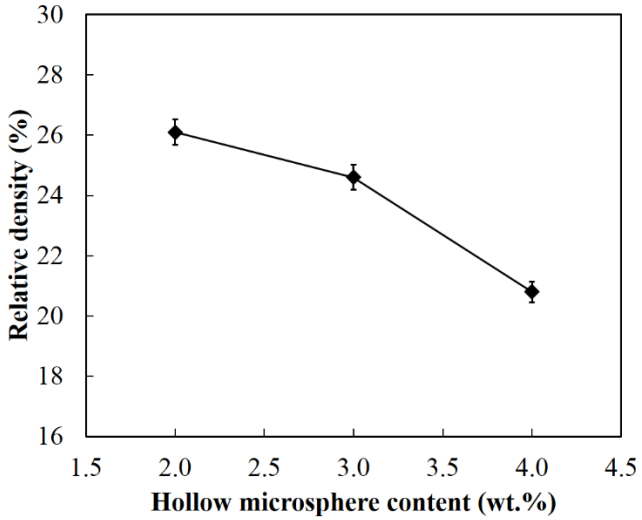

Figure 2.23 Relative density of alumina ceramics varies with microsphere contents

The total porosity obtained in this study as a function of hollow microsphere content is shown in Figure 2.24. As shown in Figure 2.24, the linearly increasing trend was observed when the hollow microsphere content increased from 2.0 wt.% to 4.0 wt.%. The total porosity of 69.3% was obtained at 2.0 wt.% microsphere content while it increased to 75.6% at 4.0 wt.% microsphere content. This result suggests that the microsphere expansion during the sintering process increases the total porosity of sintered ceramics.

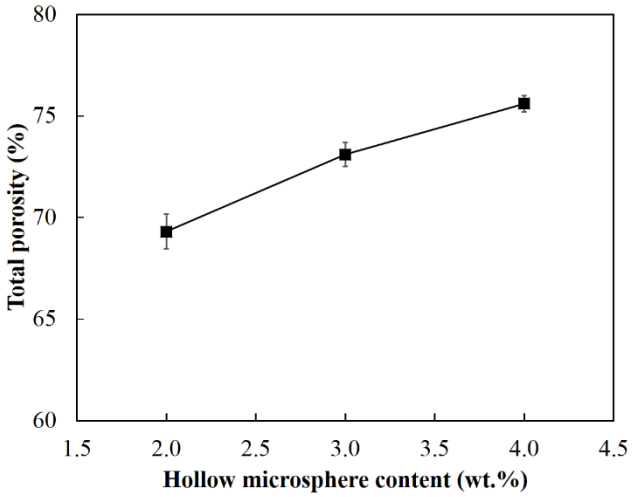

Figure 2.24 Total porosity of sintered alumina ceramics as a function of microsphere content

Figure 2.25 shows that the SEM micrographs of the typical surfaces of the sintered alumina ceramics with different hollow microsphere contents (2.0–4.0 wt.%) after sintering at 1500 ℃ for 3 hours. The pores and grain growth can be observed for the samples sintered at this temperature. As illustrated in Figure 2.25, the cell structure changed from spherical to irregular as the hollow microsphere content was increased in the sintered alumina ceramics. Good morphology and well-distributed cell structure with struts was observed in Figure 2.25 (b) when the content of hollow microsphere was 3.0 wt.%. Such morphology was almost spherical, stating that the shape of hollow microsphere was retained in the sample compacting, in the expansion, and in the pyrolysis of the sintering process. The diameters of the cells were from 20 to 60 μm, and there are no large voids in the ceramics with 3.0 wt.% microsphere content sintered at this temperature. However, the cell structure was collapsed when the microsphere content was up to 4.0 wt.% as shown in Figure 2.25 (c). A lot of small voids can be observed in this case, which illustrates that the shape of

hollow microsphere is destroyed during the ceramic sintering process. From Figure 2.25 (a), although the spherical shape of microsphere was retained to some extent, there was a small number of interconnections between cells when the microsphere content was 2.0 wt.%.

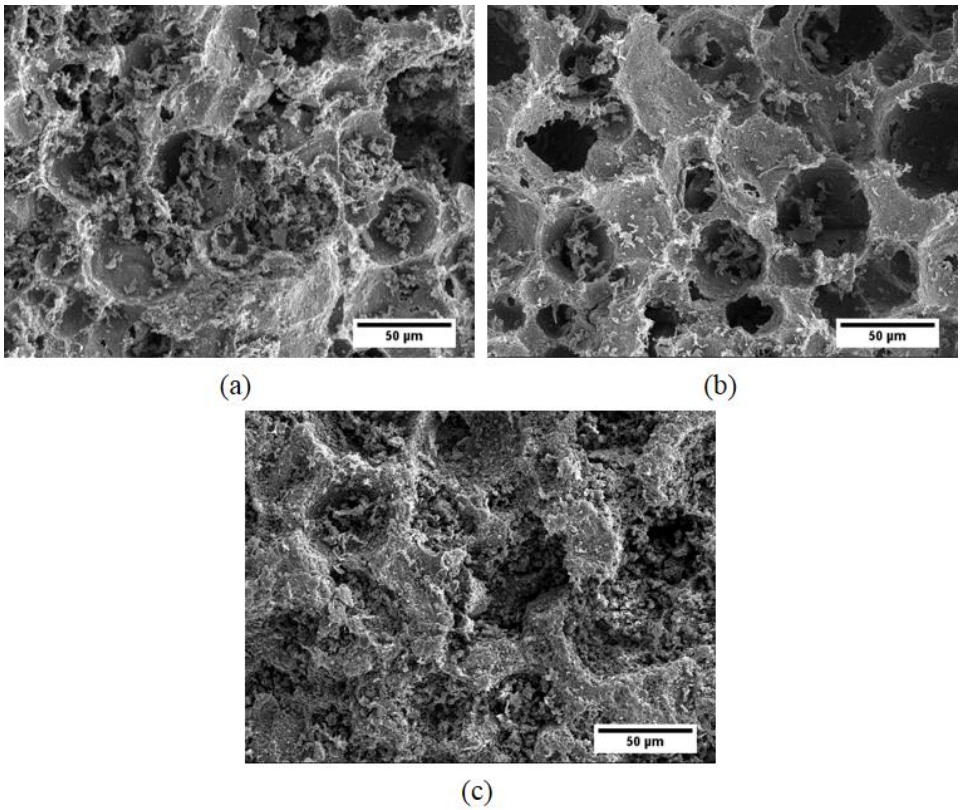

Figure 2.25 SEM micrographs of porous alumina ceramics at 1500 ℃ with different hollow microsphere contents: (a) 2.0 wt.%, (b) 3.0 wt.%, and (c) 4.0 wt.%

The microstructure feature of porous ceramics with 3.0 wt.% hollow microsphere content is shown in Figure 2.26. A hierarchical structure consists of large-sized cells with diameters of 20–60 μm, small-sized pores in cell walls averaging about 10 μm as shown in Figure 2.26 (a). It can be inferred that the large-sized cells and small-sized pores are formed from the elimination of microspheres, bubbles produced by microsphere pyrolysis,

respectively. The large-sized cells mainly attributed to the porosity of ceramics. The small-sized pores acted as cell windows connecting several cells. These cell windows are critically important in the catalyst supports and biomaterials since they sieve mass transfer between contiguous cells. Since the ceramics are fabricated through a direct foaming process which forms the nucleation of gas bubbles within a liquid which then tend to grow and coalesce [4], a large dispersion in pore size is observed. Similar results were also attained by other work by other methods for fabrication of porous alumina ceramics [20, 28, 30, 33]. From Figure 2.26 (c), it can be observed that the alumina samples with 3.0 wt.% hollow microsphere possesses a uniform cells. As shown in Figure 2.25 and Figure 2.26, a variety of structures can be obtained using hollow microsphere as pore-forming agent or so-called structure foam agent for the fabrication of porous ceramics. The microstructure of obtained porous ceramics can actually be designed to be open-celled contain small-sized pores in cell walls, or to be open cells without cell windows, or to contain a lot of pores and voids.

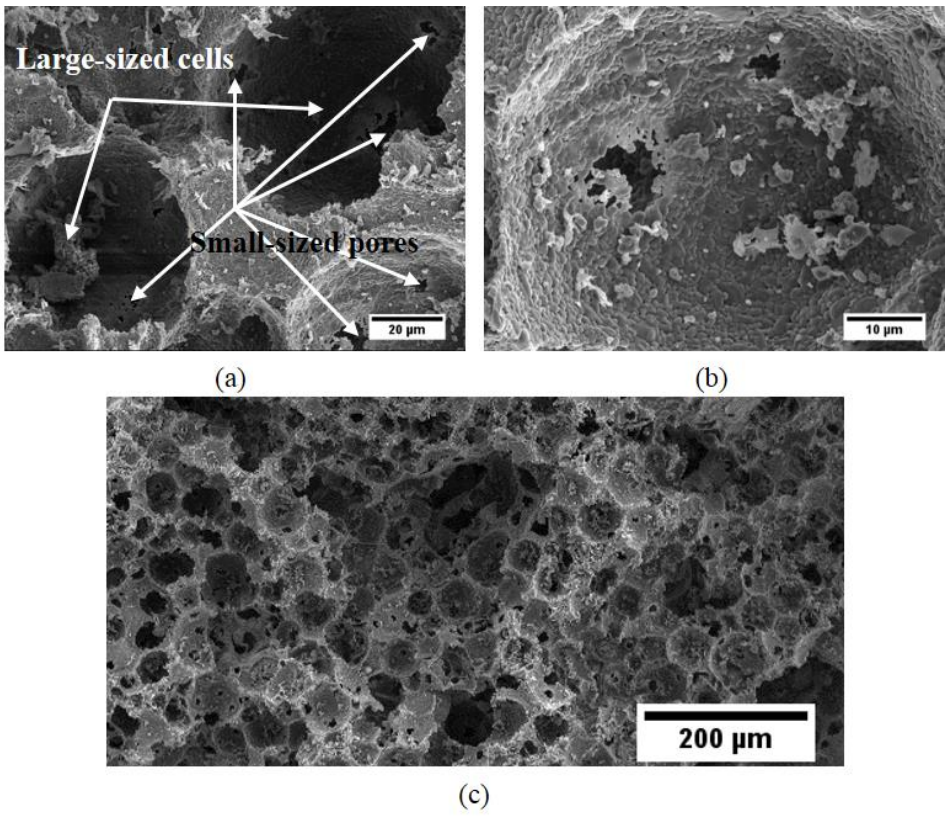

Figure 2.26 Microstructure feature of porous ceramics with 3.0 wt.% microsphere content

The compressive strength of porous alumina ceramics as a function of microsphere contents is shown in Figure 2.27. As can be seen, the compressive strength decreased slightly when the microsphere contents increased from 2.0 to 4.0 wt.% corresponding with a compressive strength of 8.31–11.50 MPa. The decreasing trend of compressive strength with increasing of microsphere content is an indication of the fact that size changes of crucial loading area occur in the samples when sintering with different amounts of pore-forming agent. This tendency has been found in many other porous ceramics [40-42]. The increasing hollow microsphere content resulted in the higher porosity and more porous structure that could lead to the weak struts among pores within the ceramics.

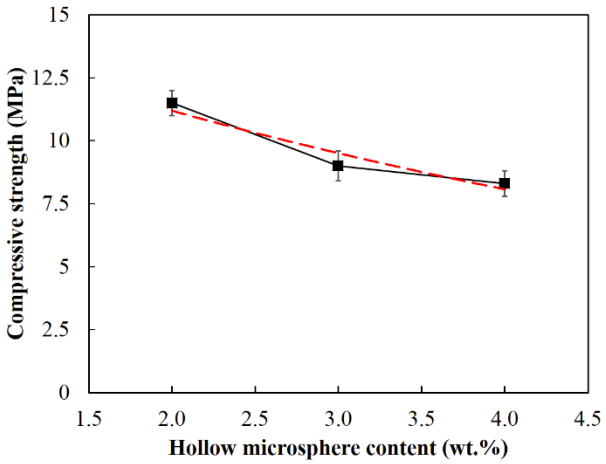

Figure 2.27 Compressive strength of sintered ceramics with different hollow microsphere content

2.3.3 Conclusions

Porous alumina ceramics with two different pore sizes were fabricated using hollow microspheres as a pore-forming agent. The relative density, total porosity, and microstructure of the obtained alumina ceramics were studied. It was found that the total porosity range of sintered samples with different amount of hollow microsphere contents from 2.0 wt.% to 4.0 wt.% was 69.3–75.6% and the total porosity increased with the increase of hollow microsphere contents. The interconnected and spherical cell morphology was obtained with 3.0 wt.% hollow microsphere content. The resulting ceramics consists of a hierarchical structure. The hierarchical structure consists of large-sized cells with diameters of 20–60 μm, small-sized pores in cell walls averaging about 10 μm. Moreover, the compressive strength of the sintered samples varied within the range of 8.31–11.50 MPa, corresponding to hollow microsphere contents of 2.0–4.0 wt.%.

2.4 Conclusions

In this chapter, porous alumina ceramics with different porosity were fabricated by two different methods: one combined the starch consolidation process with the gel-casting process using corn starch as the pore-forming agent and also as the binder. The other one used hollow microspheres as the pore-forming agent. No relative studies using hollow microspheres as the pore-forming agent is reported in the literature so far.

For both of two methods, the bulk density, porosity, and microstructure of the obtained alumina ceramics were studied. It was found that the total porosity range of sintered samples with different amount of starch contents from 10 to 50 vol% is 14.8–55.3% and the total porosity increased with the increase of starch content. The relationship between the total porosity of alumina ceramics was compared with that of the ceramics made by traditional slip-casting. The range of total porosity of ceramics in this work was broader than that of the ceramics produced by starch consolidation casting. The relationship between the linear shrinkage of porous alumina ceramics and the starch content also was discussed. The compressive strength of the sintered samples varied within the range of 5.89–24.16 MPa, corresponding to the starch content of 50–10 vol%. Meanwhile, it was found that the total porosity range of specimens prepared by the second method with the different amount of hollow microsphere contents from 2.0 wt.% to 4.0 wt.% was 69.3–75.6% and the total porosity increased with the increase of hollow microsphere contents. The interconnected and spherical cell morphology was obtained with 3.0 wt.% hollow microsphere content. The resulting ceramics consists of a hierarchical structure. The hierarchical structure consists of large-sized cells with diameters of 20–60 μm, small-sized pores in cell walls averaging about 10 μm. Moreover, the compressive strength of the

sintered samples varied within the range of 8.31–11.50 MPa, corresponding to hollow microsphere contents of 2.0–4.0 wt.%. The porous alumina ceramics fabricated in this work with high porosity would be used as preforms for pressure filtration in authors' next research stage and may have the potential for other applications such as hot gases media, catalyst support, and lightweight structural materials.

REFERENCES

[1] Sepulveda, P., *Gelcasting foams for porous ceramics.* American Ceramic Society Bulletin, 1997. **76**(10): p. 61-65.

[2] Studart, A.R., et al., *Processing Routes to Macroporous Ceramics: A Review.* Journal of the American Ceramic Society, 2006. **89**(6): p. 1771-1789.

[3] Liu, D.-M., *Preparation and characterisation of porous hydroxyapatite bioceramic via a slip-casting route.* Ceramics International, 1998. **24**(6): p. 441-446.

[4] Gibson, L.J. and M.F. Ashby, *Cellular solids: structure and properties*. 1999: Cambridge university press.

[5] Carn, F., et al., *Rational design of macrocellular silica scaffolds obtained by a tunable sol–gel foaming process.* Advanced Materials, 2004. **16**(2): p. 140-144.

[6] Yao, X., S. Tan, and Z. Huang, *Influence of Polymeric Sponge Pre-Treatment on Properties of Reticulated Porous Ceramics.* Guisuanyan Xuebao(Journal of the Chinese Ceramic Society), 2005. **33**(10): p. 1215-1219.

[7] Yao, X., et al., *Effect of recoating slurry viscosity on the properties of reticulated porous silicon carbide ceramics.* Ceramics International, 2006. **32**(2): p. 137-142.

[8] Yao, X., Z. Huang, and S. Tan, *Preparation of silicon carbide reticulated porous ceramics sintered at low temperature with PCS as sintering additive.* J. Inorg. Mater, 2010. **25**(2): p. 168-72.

[9] Karl, S. and A.V. Somers, *Method of making porous ceramic articles*. 1963, Google Patents.

[10] Brezny, R. and D.J. Green, *Fracture Behavior of Open-Cell Ceramics.* Journal of the American Ceramic Society, 1989. **72**(7): p. 1145-1152.

[11] Brockmeyer, J.W., *Ceramic foam filter and aqueous slurry for making same*. 1983, Google Patents.

[12] Hargus, P.M., J.A. Mula, and M.K. Redden, *Process for forming a ceramic foam*. 1989, Google Patents.

[13] Brown, D.D. and D.J. Green, *Investigation of strut crack formation in open cell alumina ceramics.* Journal of the American Ceramic Society, 1994. **77**(6): p. 1467-1472.

[14] Zhu, X., et al., *Improvement in the strut thickness of reticulated porous ceramics.* Journal of the American Ceramic Society, 2001. **84**(7): p. 1654-1656.

[15] Wen, Z.-H., et al., *Preparation of porous ceramics with controllable pore sizes in an easy and low-cost way.* Materials Characterization, 2008. **59**(9): p. 1335-1338.

[16] Rice, R.W., *Ceramic fabrication technology*. Vol. 20. 2002: CRC Press.

[17] Živcová, Z., E. Gregorová, and W. Pabst, *Alumina ceramics prepared with new pore-forming agents.* Processing and Application of Ceramics, 2008. **2**(1): p. 1-8.

[18] Živcová, Z., et al., *Thermal conductivity of porous alumina ceramics prepared using starch as a pore-forming agent.* Journal of the European Ceramic Society, 2009. **29**(3): p. 347-353.

[19] Gregorová, E. and W. Pabst, *Process control and optimized preparation of porous alumina ceramics by starch consolidation casting.* Journal of the European Ceramic Society, 2011. **31**(12): p. 2073-2081.

[20] Lyckfeldt, O. and J. Ferreira, *Processing of porous ceramics by 'starch consolidation'.* Journal of the European Ceramic Society, 1998. **18**(2): p. 131-140.

[21] Bowden, M.E. and M.S. Rippey, *Porous Ceramics Formed Using Starch Consolidation.* Key Engineering Materials, 2002. **206-213**: p. 1957-1960.

[22] Gregorová, E. and W. Pabst, *Porosity and pore size control in starch consolidation casting of oxide ceramics—Achievements and problems.* Journal of the European Ceramic Society, 2007. **27**(2-3): p. 669-672.

[23] Mao, X., S. Wang, and S. Shimai, *Porous ceramics with tri-modal pores prepared by foaming and starch consolidation.* Ceramics International, 2008. **34**(1): p. 107-112.

[24] Živcová, Z., E. Gregorová, and W. Pabst, *Low- and High-temperature Processes and Mechanisms in the Preparation of Porous Ceramics via Starch Consolidation Casting.* Starch - Stärke, 2010. **62**(1): p. 3-10.

[25] Pabst, W., et al., *Preparation and characterization of porous alumina–zirconia composite ceramics.* Journal of the European Ceramic Society, 2011. **31**(14): p. 2721-2731.

[26] Sepulveda, P., et al., *Properties of highly porous hydroxyapatite obtained by the gelcasting of foams.* Journal of the American Ceramic Society, 2000. **83**(12): p. 3021-3024.

[27] Ramay, H.R. and M. Zhang, *Preparation of porous hydroxyapatite scaffolds by combination of the gel-casting and polymer sponge methods.* Biomaterials, 2003. **24**(19): p. 3293-3302.

[28] Li, S., C.-A. Wang, and J. Zhou, *Effect of starch addition on microstructure and properties of highly porous alumina ceramics.* Ceramics International, 2013. **39**(8): p. 8833-8839.

[29] Torquato, S., *Random heterogeneous materials: microstructure and macroscopic properties*. Vol. 16. 2013: Springer Science & Business Media.

[30] Gregorová, E., W. Pabst, and I. Bohačenko, *Characterization of different starch types for their application in ceramic processing.* Journal of the European Ceramic Society, 2006. **26**(8): p. 1301-1309.

[31] Gregorová, E., Z. Živcová, and W. Pabst, *Porosity and pore space characteristics of starch-processed porous ceramics.* Journal of Materials Science, 2006. **41**(18): p. 6119-6122.

[32] Gregorová, E., et al., *Porous alumina ceramics prepared with wheat flour*. Journal of the European Ceramic Society, 2010. **30**(14): p. 2871-2880.

[33] Khattab, R.M., M.M.S. Wahsh, and N.M. Khalil, *Preparation and characterization of porous alumina ceramics through starch consolidation casting technique.* Ceramics International, 2012. **38**(6): p. 4723-4728.

[34] Díaz, A. and S. Hampshire, *Characterisation of porous silicon nitride materials produced with starch.* Journal of the European Ceramic Society, 2004. **24**(2): p. 413-419.

[35] Bhattacharjee, S., L. Besra, and B.P. Singh, *Effect of additives on the microstructure of porous alumina.* Journal of the European Ceramic Society, 2007. **27**(1): p. 47-52.

[36] Ryshkewitch, E., *Compression strength of porous sintered alumina and zirconia.* Journal of the American Ceramic Society, 1953. **36**(2): p. 65-68.

[37] Rice, R., *Comparison of stress concentration versus minimum solid area based mechanical property-porosity relations.* Journal of materials science, 1993. **28**(8): p. 2187-2190.

[38] *Akzo Nobel*. 2016; Available from: https://www.akzonobel.com/expancel/.

[39] Colombo, P., *Macro- and micro-cellular porous ceramics from preceramic polymers.* Composites Science and Technology, 2003. **63**(16): p. 2353-2359.

[40] Zhu, X., D. Jiang, and S. Tan, *Preparation of silicon carbide reticulated porous ceramics.* Materials Science and Engineering: A, 2002. **323**(1): p. 232-238.

[41] Chun, Y.-S. and Y.-W. Kim, *Processing and mechanical properties of porous silica-bonded silicon carbide ceramics.* Metals and Materials International, 2005. **11**(5): p. 351-355.

[42] Eom, J.-H., et al., *Microstructure and properties of porous silicon carbide ceramics fabricated by carbothermal reduction and subsequent sintering process.* Materials Science and Engineering: A, 2007. **464**(1-2): p. 129-134.

CHAPTER 3 MODELING STRUCTURES OF OPEN CELL FOAMS

3.1 Introduction

Foams (ceramic, metal, or polymer), as shown in Figure 3.1 [1, 2], are the materials of high interest in a wide range of application areas. Foams are characterized by polyhedral cells forming a space-filling structure. They are classified as either open cell with a strut-like morphology forming a continuous network, or as closed cell with solid membrane-like faces. Foam structures are frequently observed in nature. Due to the high porosity and large specific strength (strength related to mass) and permeability, they form the most structurally demanding parts of plants and animals [3, 4]. Foams are nowadays commercially used in modern biomedical and technical applications [5-8]. One of the main biomedical interests is the reconstruction of the human body by the implantation of scaffolds [9, 10]. In this case, both mechanical and functional properties of foams (scaffolds) are of key importance. Other important fields of foam applications are engineering applications, such as filtering and catalysis, etc. High porosity polymer foams allow efficient thermal insulating materials to be achieved [11-13]. Thanks to their good resistance to high temperatures and strong chemical corrosion resistance, open cell ceramic foams are used for the filtering of liquid metals in casting processes, combustion supports for porous burners, and as volumetric absorbers in solar thermal and thermochemical reactors [14-20]. They are also commonly used in diesel particulate filter or exhaust gas catalytic converters [21]. The foam structures can also be infiltrated by other materials (mainly metals) in order to produce composites [22, 23]. High porosity open cell metallic foams, usually having a structure of enclosed porous material, have attracted much

attention for designing compact heat exchangers and heat sinks [24, 25]. Metallic foams filled with phase change materials offer a possibility for heat energy storage applications [26, 27]. New manufacturing technologies are available also for open cell metallic foams for structural applications [28, 29].

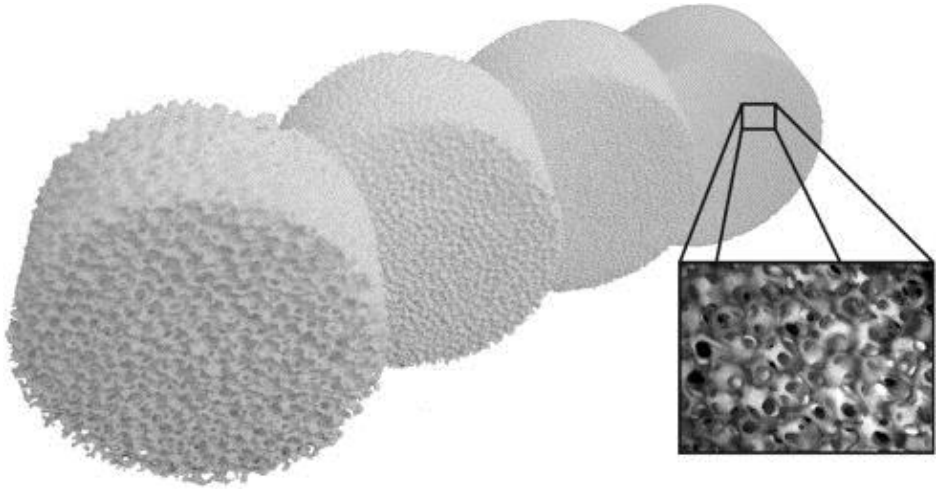

(a)

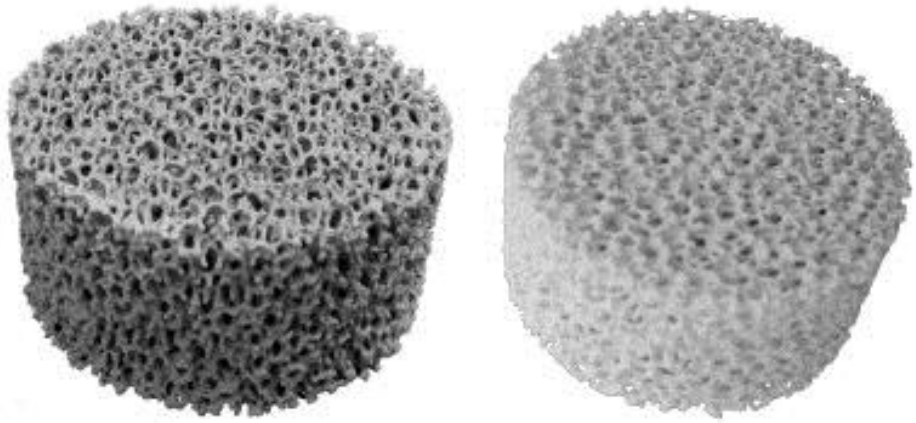

(b)

Figure 3.1 (a) Photo of different foam samples made of Al_2O_3 with 10 ppi (pores per inch), 20 ppi, 30 ppi, 45 ppi, microscopy picture of a 45 ppi sponge (from left to right), and (b) foam samples made of OBSiC (left) and Mullite (right) with 10 ppi [1, 2]

All these applications require materials with specific properties. Some properties (mainly mechanical) are less sensitive to the local geometry of the foam structure [30]. In such a case porosity and average pore size are the only parameters which are required to find structure-property relationships. Other properties, related to flow through the porous media, are more strongly influenced by the local environment of the particular pores and that is why they require a better understanding obtained through explicitly modeling the geometry of the foam structure [31].

There are a number of publications presenting different models of open cell foam structures. In general, there are three approaches to model the foam structures. The first method uses Kelvin cell to obtain the structure. The Kelvin cell (tetrakaidecahedron) has 14 faces (6 quadrilateral and 8 hexagonal) and 24 vertices as shown in Figure 3.2. In 1887, Lord Kelvin proposed that the tetrakaidecahedron was the best shape for packing equal-sized objects together to fill space with minimal surface area. Kelvin thought about this problem in the context of the bubbles which make up a foam. This method entails modeling an idealized periodic cell structure as shown in Figure 3.3. For a long time, Kelvin's foam was considered as an optimal representation of real foam structures. However, this model exhibits unusual behavior regarding mechanical properties that has not been confirmed in real materials [32]. It is likely that the random disorder in real foams is responsible for that [33]. It also has been already proved that Kelvin's structure has certain disadvantages and that it cannot simulate certain mechanical properties of real foams. Due to its lack of randomness, Kelvin's structure is clearly anisotropic which is not true for real foams [32, 33].

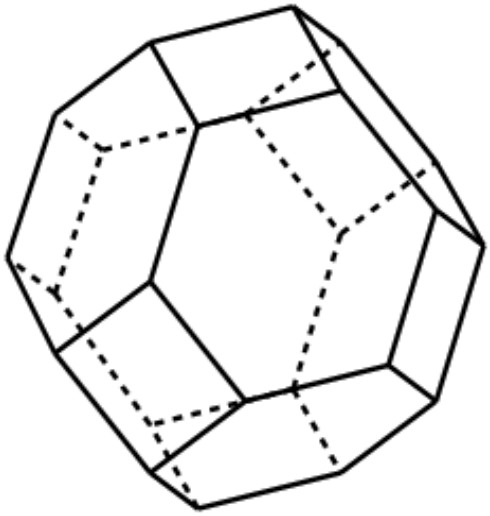

Figure 3.2 Structure of Kelvin cell

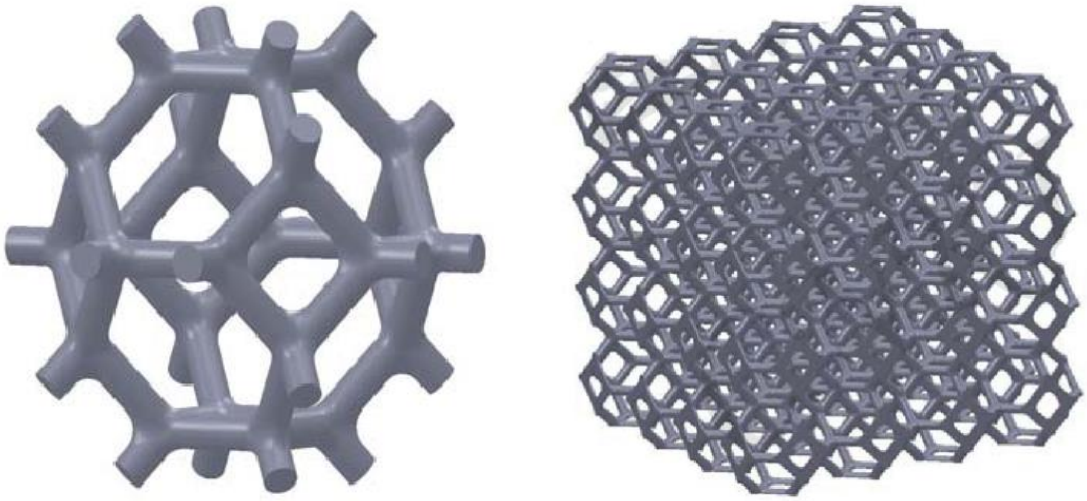

(a) (b)

Figure 3.3 (a) Single Kelvin cell, and (b) Kelvin multi-cells model

Trying to capture the structural random disorder of real foams, many authors use different methods to consider the randomness and imperfection of real foam, which are defined as the second approach modeling the foam structures in this work. Habisreuther et

al. [34] obtained a randomization of the Kelvin structure by relocating the nodes of the ordered Kelvin multi-cells structure, $P_{\mathrm{k,ord}}$, with a vector $\vec{r}_{\mathrm{r}}$ having stochastic direction and stochastic values of the individual components rand($L_{\max}$) between 0 and $L_{\max}$, avoiding any change in network connection (i.e. topology):

$$\overrightarrow{P_{\mathrm{rand}}} = \overrightarrow{P_{\mathrm{ord}}} + \vec{r}_{\mathrm{r}}(L_{\max}) \tag{3.1}$$

$$P_{\mathrm{k,rand}} = P_{\mathrm{k,ord}} + \mathrm{rand}(L_{\max}) \quad k = x, y, z \tag{3.2}$$

$$L_{\max} = C_1(\min(\overline{PP_{\mathrm{N}}}) - d_{\mathrm{s}}) \tag{3.3}$$

$$\overrightarrow{P_{\mathrm{rand}}} = \overrightarrow{P_{\mathrm{ord}}} + \vec{r}_{\mathrm{C}}(C_2 L_{\mathrm{C}}) + \vec{r}_{\mathrm{r}}(L_{\max}) \tag{3.4}$$

In order to avoid possible crossing of the struts, it was necessary to restrict the amount of dislocation of each node to $L_{\max}$ what resulted in narrowing the possible variation range of strut lengths. Therefore, a combined procedure was applied allowing the biggest possible amount of dislocation. In one step a maximal random dislocation $L_{\max}$ of the nodes P was limited to the fraction C_1 of geometrical distance to the neighboring node P_{N} taking into account the strut diameter d_{s}. In another step, the node P was displaced for a random amount of dislocation but in the given direction to the cell center of the ordered structure $\vec{r}_{\mathrm{C}}$. L_{C} represents the distance between the node to be displaced and the cell center. Both of the displacements were sequential conducted, first in the direction to the cell center and afterwards in the random direction. The constants C_1 and C_2 represent the fractions of the maximal displacement being applied in randomizing process. The randomized Kelvin structure is shown in Figure 3.4 [34].

Many other researchers generated the random models by means of the Voronoi tessellation or Poisson-Voronoi tessellation (discussed in Chapter 3.2) using random seed points in space. Within this model, a cell is defined by the space that is closer to a specific

seed point than to any other. The amount of disorder of such a structure depends on the spatial distribution of the seed points. However, it is found that a major disadvantage of Voronoi structures is the usually higher number of struts per node in comparison with real sponge structures and that geometrical parameters of real foams differ from those obtained by Poisson-Voronoi tessellation [34, 35].

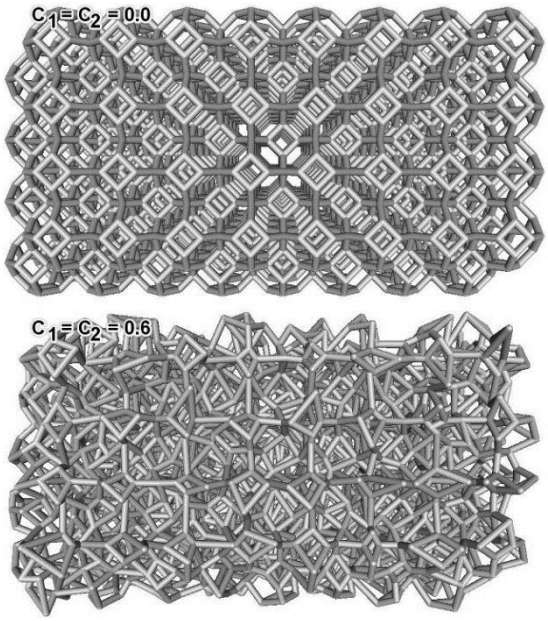

Figure 3.4 Perspective view of the randomized Kelvin structures (8×4×4 cells, round struts). Top: ordered structure $C_1 = C_2 = 0$; bottom: randomized with $C_1 = C_2 = 0.6$ [34]

The third method includes closely resembling of the microstructure of real sponges and it can be accomplished by use of tomographic images or digitized images of the sponge. X-ray micro tomography (μCT) and magnetic resonance imaging (MRI) have recently proved to be a very powerful tool allowing the characterization of the microstructure of materials or the architecture of cellular materials in a non-invasive and non-destructive way. This approach also is called 3D reconstruction technology, which reconstructs three-dimensional model using two-dimensional image slices such as μCT and MRI stacks as

shown in Figure 3.5 [36]. Reconstructed topological image of typical foam structures are shown in Figure 3.6 [37]. However, three-dimensional structures obtained this way are unique for each individual foam sample and may not be necessarily representative. Such high-cost equipment also is not always available and reconstruction process is very complicated and time-consuming.

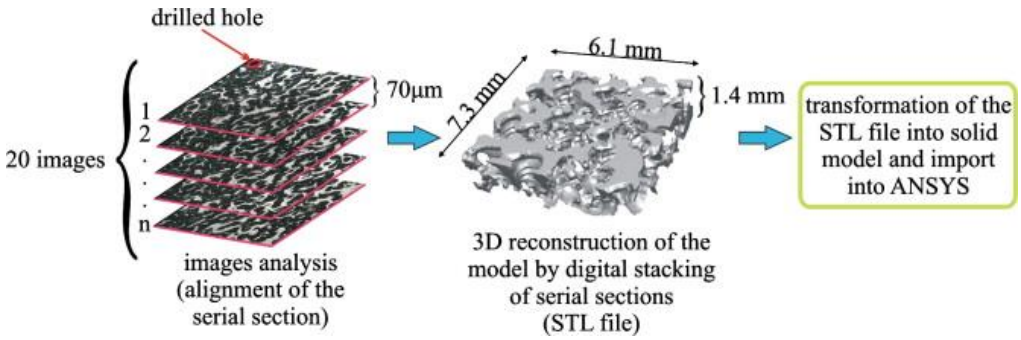

Figure 3.5 Schematic diagram accounting for the image processing to obtain the 3D model [36]

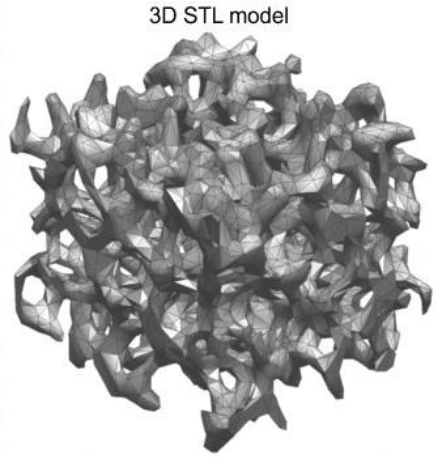

Figure 3.6 A 3D image of the STL file generated from 2D µCT slices for the open cell Ni foam structure [37]

Due to the need for a more general determination of foam properties as well as for the investigation of the effects of changes in structure on foam properties, it is necessary

to generate statistical models that could achieve this function. In this work, we wish to model foam structures that have a roughly uniform cell size, but which are still random and isotropic. A non-periodic, evenly spaced, and isotropic arrangement of seed points is, therefore, necessary. A method for the generation of random foam structures, based on Laguerre-Voronoi tessellations of randomly packed spheres with log-normal volume distribution, is proposed. This model could give the study of the variation coefficient effect on the geometric and topological properties of foams. To evaluate the generated model in this work, a series of parameters are discussed, such as the average number of faces per foam cell, porosity, and specific surface area, etc.

3.2 Methods and modeling

The model generated in this work is referred to as the LV foam model, which is the Laguerre-Voronoi tessellation based on the randomly closed packing of spheres. Voronoi tessellation and Laguerre-Voronoi tessellation are the tools that usually are used to obtain the polycrystalline structures of certain materials or to division spaces in many fields.

3.2.1 Voronoi tessellation

The Voronoi tessellation (VT) is constructed with a set of n separate points, $S = \{p_1, p_2, \cdots, p_n\}$. If the normal Euclidean distance between p_i and any other point q in the space is denoted as $d_V(p_i, q)$, a Voronoi cell (v-cell) corresponding to p_i is defined as

$$v_V(p_i) = \left\{p | p \in R^3,\ d_V(p, p_i) < d_V\left(p, p_j\right), i \neq j\right\} \tag{3.5}$$

i.e., a set of points in three-dimensional space R^3 which are closer to the nucleus point p_i than to any other nucleus points in S. In this sense, $v_V(p_i)$ is the dominant region of p_i.

Each point in S generates its own v-cell; and all v-cells form a VT, which divides three-dimensional space into an array of convex, space-filling and non-overlapping polyhedrons with planar faces as shown in Figure 3.7. The well-known Poisson-Voronoi diagram is a kind of VT with point set S generated through a homogeneous Poisson point process.

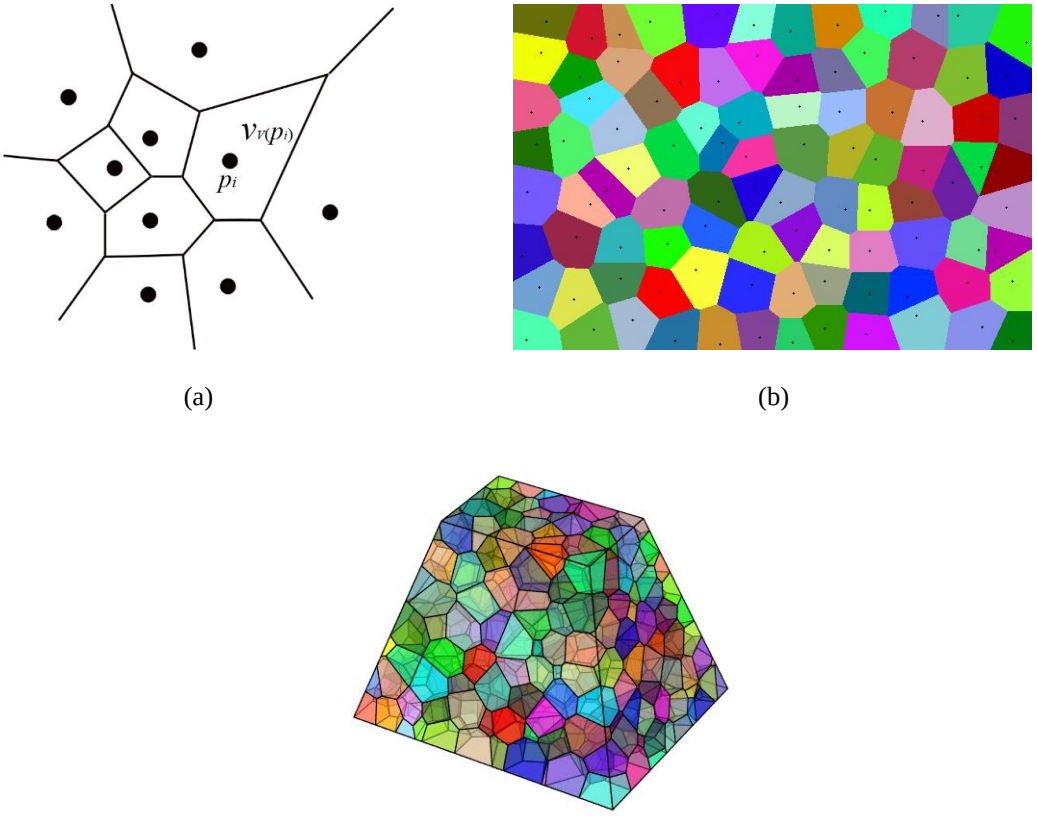

(a) (b)

(c)

Figure 3.7 (a) Illustration of v-cells, (b) a 2D, and (c) a 3D Voronoi tessellation diagram of a set of points

3.2.2 Laguerre-Voronoi tessellation

Laguerre-Voronoi tessellation (LVT), also referred to as power diagram, is a kind of weighted Voronoi tessellation [38]. To point p_i in set S, a weight r_i is assigned, forming a weight set $r = \{r_1, r_2, \cdots, r_n\}$, and the distance between p_i and any point q is measured in Laguerre geometry:

$$d_L(p_i, q) = \{[d_V(p_i, q)]^2 - r_i^2\}^{1/2} \tag{3.6}$$

Similar to VT, a lv-cell corresponding to point p_i is defined as:

$$v_L(p_i) = \{p | p \in R^3,\ d_L(p, p_i) < d_L(p, p_j), i \neq j\} \tag{3.7}$$

and the set of all lv-cells, $V_L(S, r) = \{v_l(p_1, p_2, \cdots, p_n)\}$, is called an LV diagram as shown in Figure 3.8. Here $v_l(p_i)$ is the dominant region of p_i with a weight of r_i. Lv-cells are also space-filling convex polyhedrons without overlapping interconnected in a topological manner in the same way as grains in polycrystalline materials.

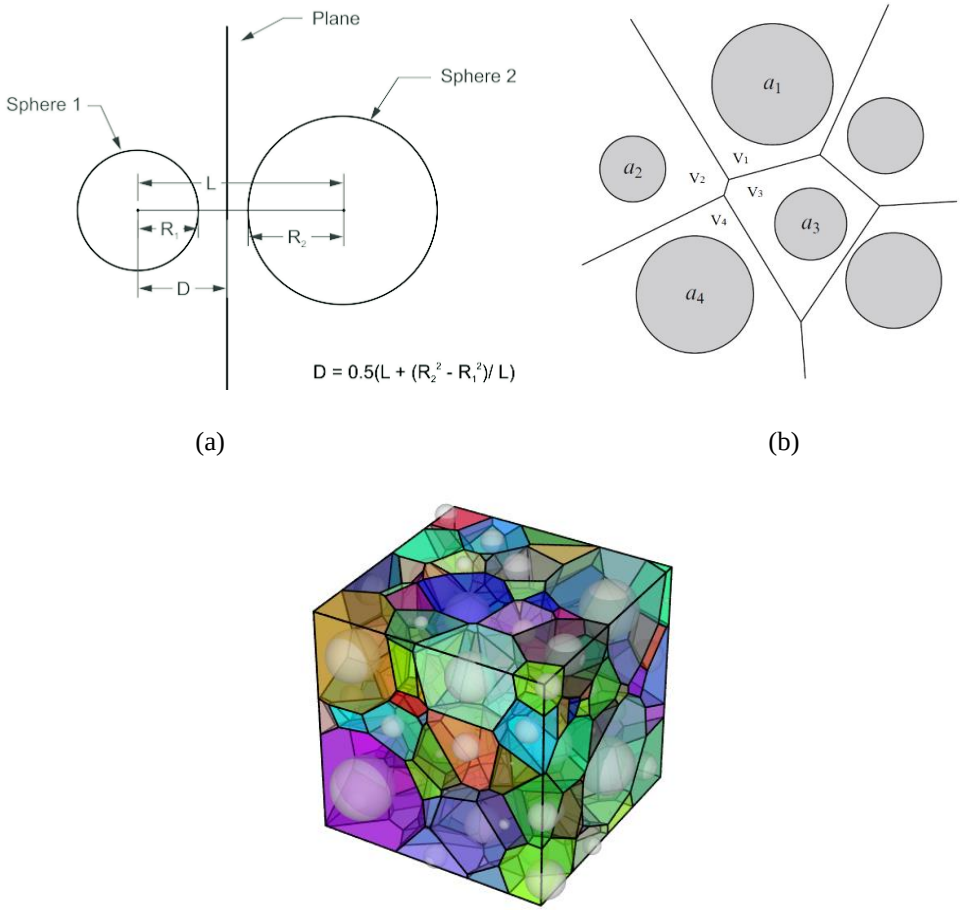

(a) (b)

(c)

Figure 3.8 (a) Schematic illustration of LV tessellation, (b) A 2D, and (c) a 3D Laguerre-Voronoi diagram

3.2.3 Randomly packed spheres

Randomly packed spheres have been extensively studied by both experiments and computer algorithms [39-41]. Among the research methods, computer simulations used to generate randomly packed spheres can be classified into two catalogs: sequential generation method and collective rearrangement algorithms. In this work, the first method is used and a classical molecular dynamics code, LAMMPS (an acronym for Large-scale Atomic/Molecular Massively Parallel Simulator), is employed to generate randomly closed packing of spheres as shown in Figure 3.9 (It is visualized and rendered by OVITO.). LAMMPS has potentials for solid-state materials (metals, semiconductors) and soft matter (biomolecules, polymers) and coarse-grained or mesoscopic systems. It can be used to model atoms or, more generically, as a parallel particle simulator at the atomic, meso, or continuum scale [42]. The LAMMPS code developed in this work is shown in Appendix A.

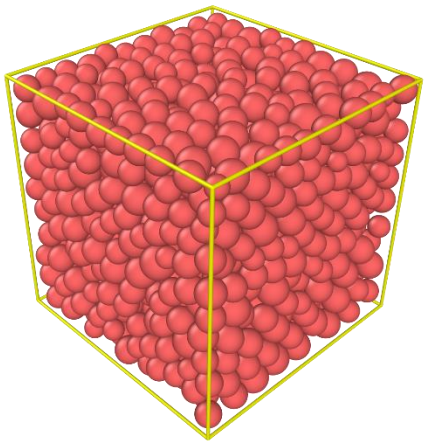

Figure 3.9 A randomly closed packing of spheres generated by LAMMPS

3.2.4 LV tessellation based on randomly packed spheres

The LV diagram is constructed based on randomly packed spheres, which provides point set S consisting of all the centers of spheres and weight set r of the corresponding radii (Figure 3.8 (a)). In the LV diagram, each sphere has its own lv-cell, which, in return, encloses the whole sphere. Neighboring spheres belong to adjacent lv-cells. Tangent plane of two tangent spheres is just the sharing face of the corresponding polyhedrons. Thus, the volume distribution of lv-cells strongly inherits that of the original spheres. Randomly packed spheres serves as a template in the generation of the LV diagram. In order to improve the computational efficiency, LV tessellation firstly is programed with C++ and then is compiled under Linux environment in this work. The output files are created to contain a variety of different statistics about the computed lv-cells, including centroid, volume, and the number of vertices, edges, and faces, etc. Also, the output files of program include the visualization output for a visualization tool, POV-Ray. An LV diagram based on randomly packed spheres is shown in Figure 3.10 (Figure is visualized and rendered by POV-Ray.).

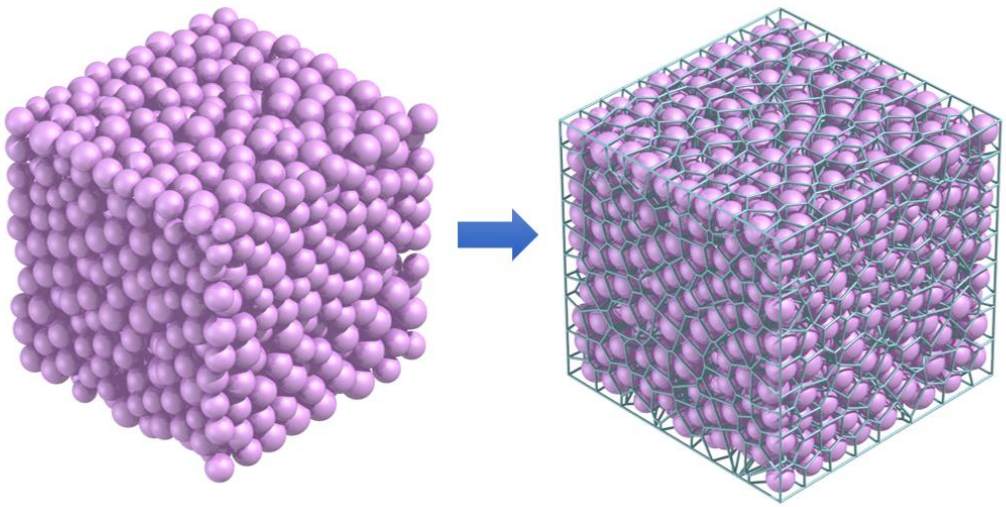

Figure 3.10 An LV diagram based on randomly packed spheres

3.2.5 Foam structure generation

In this work, lv-cells are assumed to represent individual cells of open cell foams. As shown in Figure 3.10, foam structure can be obtained by deleting packed spheres, volumes of lv-cells, and interfaces between any two lv-cells and only keeping the edges of all lv-cells and vertices of all lv-cells. To eliminate possible boundary effect, cells centered within the outer shell of the initial diagram are cut off and not included in the further statistical procedure as shown in Figure 3.11.

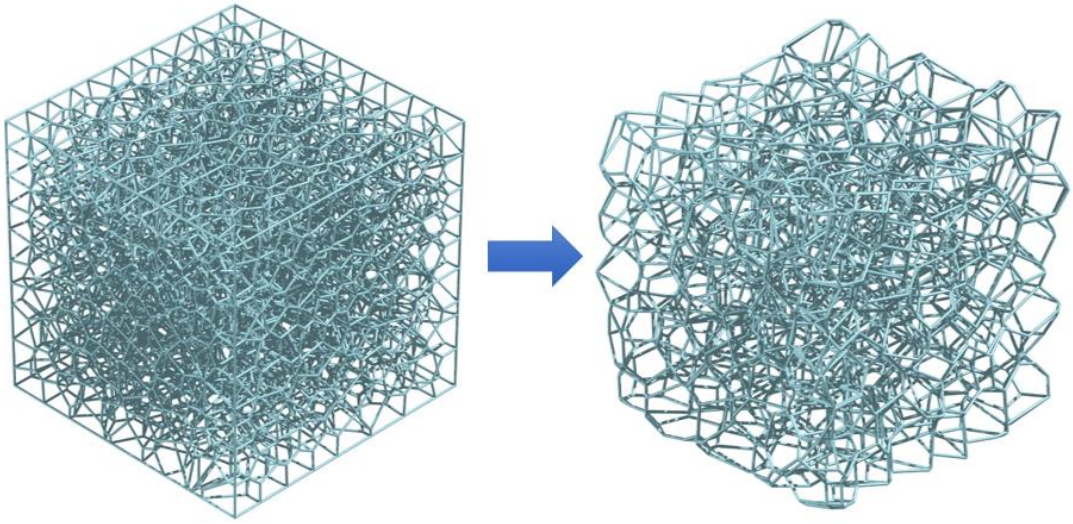

Figure 3.11 Foam structure with cylindrical struts generated by LV tessellation

3.2.6 Modeling procedure

Due to the randomness and imperfection of foams preparation, real foams usually have a coefficient of variation (CV) of pore volumes, ranging from 1.09 to 2.13 and the volume distribution in real foams has been suggested to be log-normal by Rhines et al. [43, 44]. Therefore, the generation of randomly packed spheres with a defined log-normal

distribution of volume in the computations was adopted with the pre-selected average pore volume, $E(V)$ and the coefficient of variation, $CV(V)$.

In conclusion, the procedure for the modeling of foam structures employed in the present study consists of the following six steps:

(1) Generate random closed packing of more than 1,000 spheres within a cubic space. Keep the average pore volume $E(V)$ as a constant, i.e. average pore volume of commercial 10 ppi (pores per inch) alumina foams, and the volume distribution log-normal with $CV(V)$ varying from 0.4 to 3.0 at intervals of 0.2, so 14 types of randomly packed spheres with different $CV(V)$ values are obtained;

(2) Repeat first step for two times. In this way, for each type of randomly packed spheres, three groups of more than 1,000 spheres are generated;

(3) Perform Laguerre-Voronoi tessellation to transform each group into LV diagram;

(4) Delete packed spheres, volumes of lv-cells, and interfaces between any two lv-cells and only keep the edges and vertices of all lv-cells to obtain foam structures;

(5) To eliminate possible boundary effect, cells centered within the outer shell of the initial structure are cut off and not included in the further statistical procedure. As a result, each group of foam structures has about 500 effective foam-cells;

(6) For further analysis, merge the three sets of statistical data of the foam structures tessellated based on randomly packed spheres with the same $CV(V)$ value into one.

The procedure based on the above given six-steps approach is schematically presented in Figure 3.12.

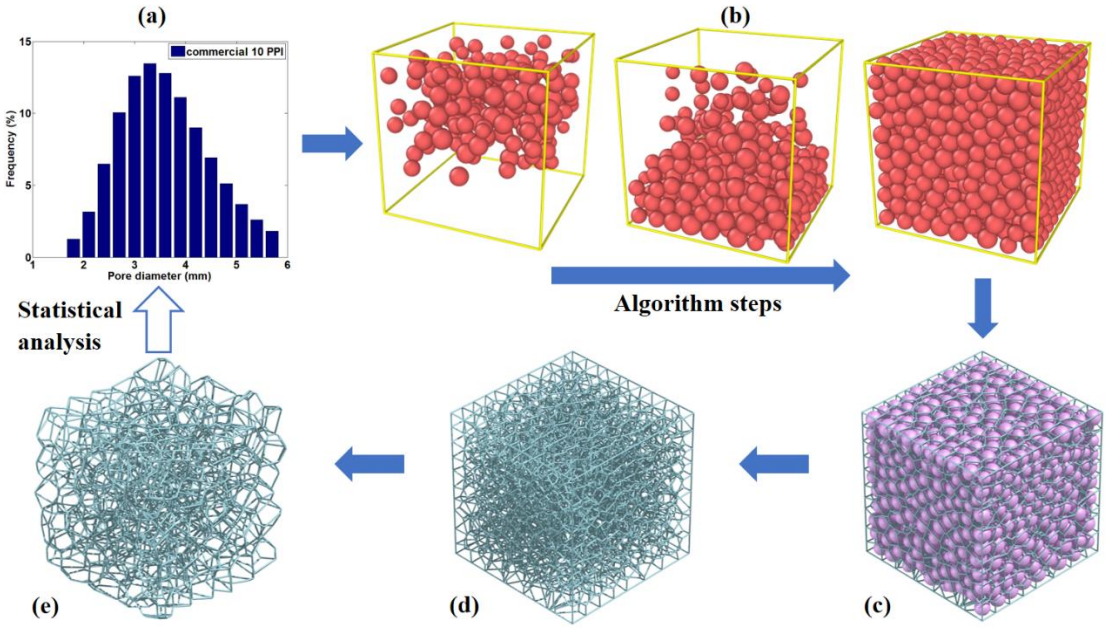

Figure 3.12 Schematic illustration of the procedure for foam structure generation: (a) spheres of pre-selected volume distribution, (b) the algorithm of randomly packed spheres, (c) LV diagram based on randomly packed spheres, (d) lv-cells with cylindrical edges, and (e) foam structure with cylindrical struts

3.3 Results and discussion

3.3.1 Distributions of volume, face and edge number

As the volume distribution in real material has been suggested to be log-normal by Rhines and Patterson [44] and Okazaki and Conrad [43], the log-normal distribution is used

to analyze statistical data of foam structures in present work. Its probability density function is described by the following equation:

$$f(x,\mu|\sigma) = \frac{1}{x\sigma\sqrt{2\pi}}\exp\left(\frac{-(\ln(x)-\mu)^2}{2\sigma^2}\right) \tag{3.8}$$

where μ and σ are two parameters related to expectation $E(x)$ and variance $Var(x)$ by formulas:

$$E(x) = e^{\left(\mu+(\sigma^2/2)\right)} \tag{3.9}$$

$$Var(x) = e^{(2\mu+2\sigma^2)} - e^{(2\mu+\sigma^2)} \tag{3.10}$$

The coefficient of variation, $CV(x)$, is defined as the ratio of the standard deviation $STD(x)$ to the expectation $E(x)$:

$$CV(x) = \frac{STD(x)}{E(x)} \tag{3.11}$$

where $STD(x) = Var(x)^{1/2}$.

In formulas (3.9) and (3.10), $E(x)$ and $Var(x)$ can be given by the unbiased estimators $\bar{V}$ and $\frac{1}{n-1}\sum_{i=1}^{n}(V_i - \bar{V})^2$, where V_i is the volume of the ith foam-cell in certain foam structure and $\bar{V}$ is the average of all the cell volumes in corresponding foam structure. In this work, we assume the volumes distributions in foam structures to be log-normal, whose parameters are calculated using formulas (3.9) and (3.10).

Figure 3.13 shows the relationship between the mean and standard deviation (STD) of foam-cell volumes in the foam structure and $CV(V)$ of spheres volumes in corresponding randomly packed spheres. The mean of foam-cell volumes decreases linearly with increasing $CV(V)$ of spheres while the standard deviation of foam-cell volumes increases when the $CV(V)$ of spheres increases. The standard deviation changes

slightly when the $CV(V)$ of spheres is greater than 1.6. Figure 3.14, Figure 3.15, and Figure 3.16 show the volumes distribution and face number of foam-cells, respectively. Figure 3.14 includes the histogram of foam-cell volumes in the foam structures and fitted log-normal distribution with corresponding parameters. This foam structure is generated based on randomly packed spheres, which have a log-normal volume distribution with $CV(V)$=0.4; Figure 3.15 shows the histogram of face number per foam-cell in the foam structures and fitted log-normal distribution with corresponding parameters. This foam structure also is generated based on randomly packed spheres with a log-normal volume distribution with $CV(V)$=0.4; Figure 3.16 shows the histogram of edge number per cell-face in the foam structures and fitted log-normal distribution with corresponding parameters. This foam structure also is generated based on randomly packed spheres with a log-normal volume distribution with $CV(V)$=0.4.

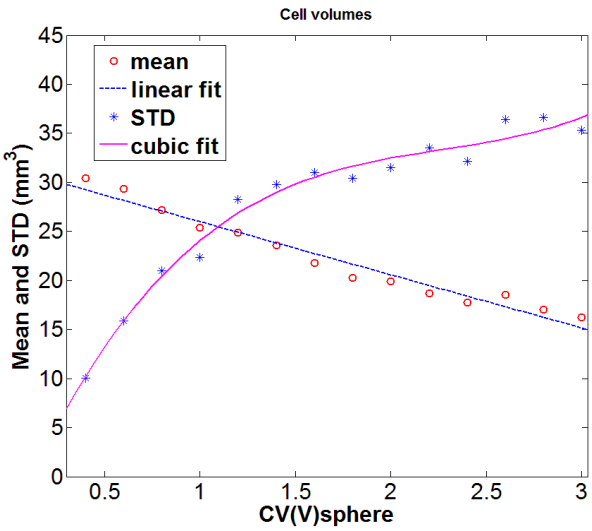

Figure 3.13 Mean and standard deviation (STD) of foam-cell volumes in the foam structure vs. $CV(V)$ of spheres volumes in corresponding randomly packed spheres

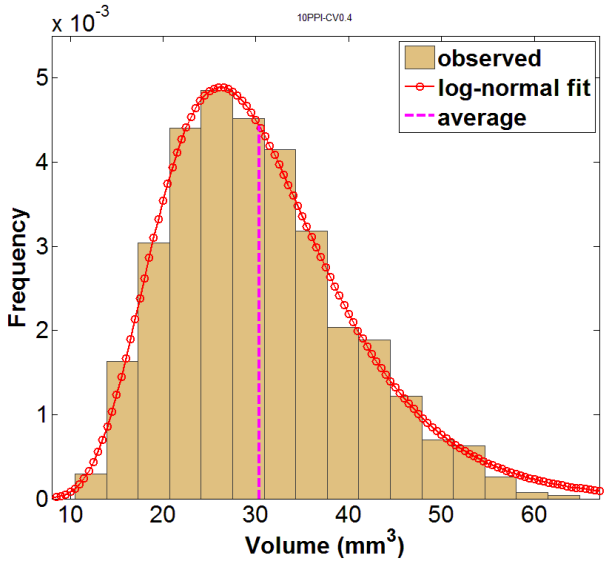

Figure 3.14 Histogram of foam-cell volumes in foam structures (10 ppi) and fitted log-normal distribution with corresponding parameters; this foam structure is generated based on randomly packed spheres, which have a log-normal volume distribution with $CV(V)$=0.4

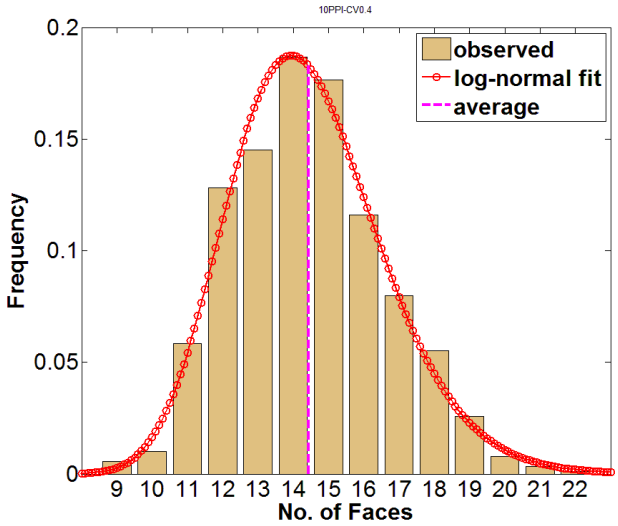

Figure 3.15 Histogram of face number per foam-cell in foam structures (10 ppi) and fitted log-normal distribution with corresponding parameters; this foam structure is generated based on randomly packed spheres, which have a log-normal volume distribution with $CV(V)$=0.4

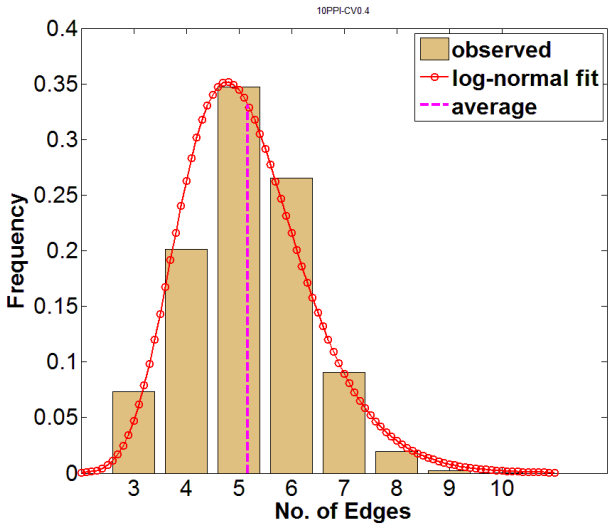

Figure 3.16 Histogram of edge number per cell-face in foam structures (10 ppi) and fitted log-normal distribution with corresponding parameters; this foam structure is generated based on randomly packed spheres, which have a log-normal volume distribution with $CV(V)$=0.4

3.3.2 More analysis for foam structures

For randomly packed spheres with certain $CV(V)_{\text{sphere}}$ value of sphere volumes, corresponding statistics of foam structures, including average number of faces per foam-cell F, average number of edges per face E, and variation coefficient value of foam-cell volumes distribution $CV(V)_{\text{cell}}$, are obtained. Figure 3.17 shows the plot of F vs. CV of sphere volumes in corresponding randomly packed spheres. It is ascertained that real foam ceramics has the average number of faces per cell of 13.7-15.5 [45]. The results in present work are in good agreement with real foams. The relationship between E and $CV(V)_{\text{sphere}}$ is shown in Figure 3.18, and between $CV(V)_{\text{cell}}$ and $CV(V)_{\text{sphere}}$ is drawn in Figure 3.19. Using a quadratic fitting, F vs. $CV(V)_{\text{sphere}}$ and E vs. $CV(V)_{\text{sphere}}$ can be expressed as:

$$F = 0.081\left(CV(V)_{\text{sphere}}\right)^2 - 0.615CV(V)_{\text{sphere}} + 14.669 \tag{3.12}$$

with a norm of residuals of 0.1082,

$$E = 0.0044\left(CV(V)_{\text{sphere}}\right)^2 - 0.0358CV(V)_{\text{sphere}} + 5.1824 \tag{3.13}$$

with a norm of residuals of 0.0062. A cubic fitting is applied to describe the relationship of $CV(V)_{\text{cell}}$ vs. $CV(V)_{\text{sphere}}$:

$$CV(V)_{\text{cell}} = 0.056\left(CV(V)_{\text{sphere}}\right)^3 - 0.395\left(CV(V)_{\text{sphere}}\right)^2 + 1.492CV(V)_{\text{sphere}} - 0.213 \tag{3.14}$$

with a norm of residuals of 0.1375.

These figures show that when $CV(V)_{\text{sphere}}$ increases from 0.40 to 3.0, F decreases from 14.43 to 13.56, E from 5.17 to 5.11, while $CV(V)_{\text{cell}}$ increases from 0.33 to 2.17. Except for a good agreement with real ceramic foams, it is worth mentioning here that, for some natural materials, the average number of faces per cell F, and the average number of edges per face E as shown in Table 3.1. It also can be noted that these results confirm that variation of foam-cells size can be obtained via manipulating the initial randomly packed spheres size distribution (Figure 3.19).

Table 3.1 F and E of some natural materials

	No. of cells	F	E	Reference
Mixed bubbles	150	13.26	5.095	[46]
Uniform bubbles	600	13.702	5.111	[47]
Vegetable cells	450	13.802	5.123	[47]

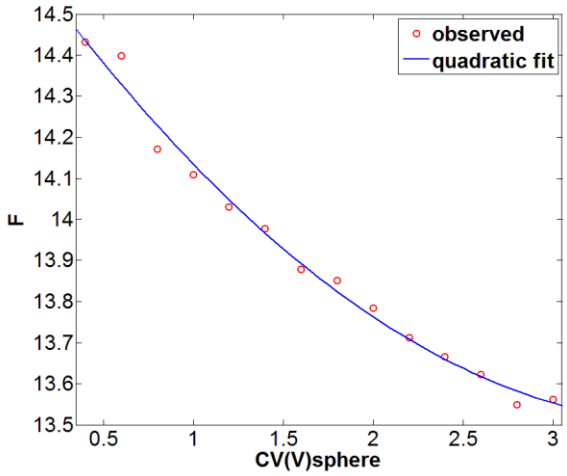

Figure 3.17 Average number of faces per foam-cell in the foam structure vs. CV of sphere volumes in corresponding randomly packed spheres

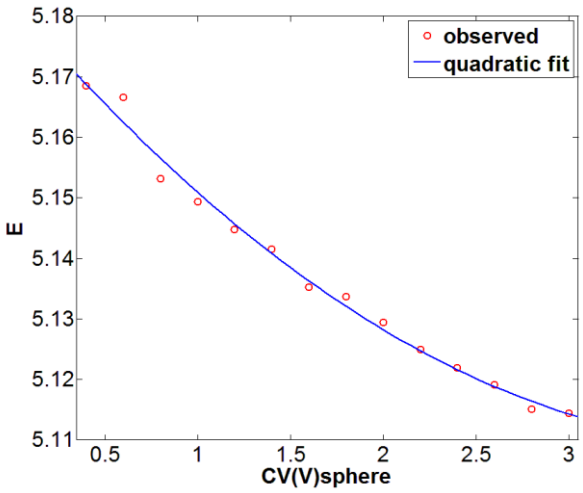

Figure 3.18 Average number of edges per foam-cell in the foam structure vs. CV of sphere volumes in corresponding randomly packed spheres

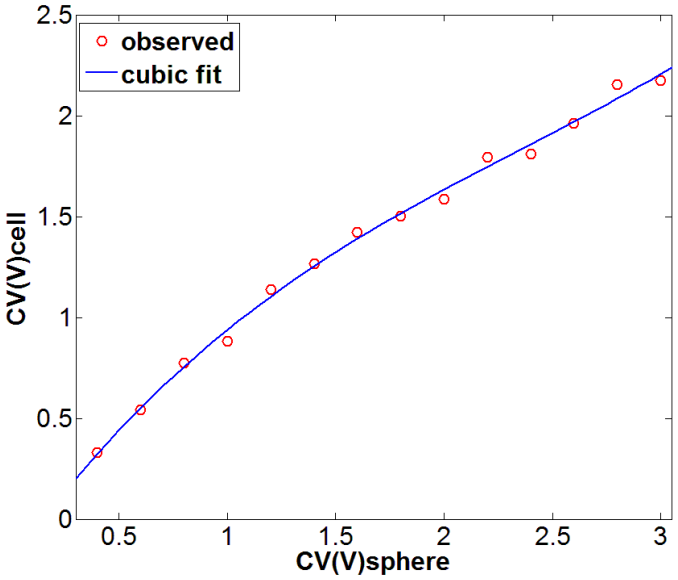

Figure 3.19 CV of foam-cell volume distribution in the foam structure vs. CV of sphere volumes in corresponding randomly packed spheres

3.4 Verification

In this work, the verification of a morphological model that connects macroscopic with mesoscopic features of foams (especially ceramic foams in this work) is based on a work by Gibson and Ashby [48, 49]. On the basis of morphological analysis of numerous natural foams, they found that the average number of struts per cell window is about 5. A structure built by packed polyhedron with pentagonal faces would represent closely the foam morphology. However, a package of regular pentagonal dodecahedra does not fill the entire space. Alternatively, a dense package of Kelvin cell (Figure 3.20) will be considered. The Kelvin cell can be described as a truncated octahedron, exhibiting six square and eight hexagonal faces. The average number of struts per face is 5.14, which is close to the corresponding value for a pentagonal dodecahedron. Another important geometrical

feature of foam structures is that of the shape of the strut. Most of the models assume cylindrical struts with a constant diameter along the cell edges (or edges of cells). In some models overlapping of the struts at vertices is accepted without evaluation of the related error. The struts of real foams in this work are simplified by using cylinders of a constant diameter.

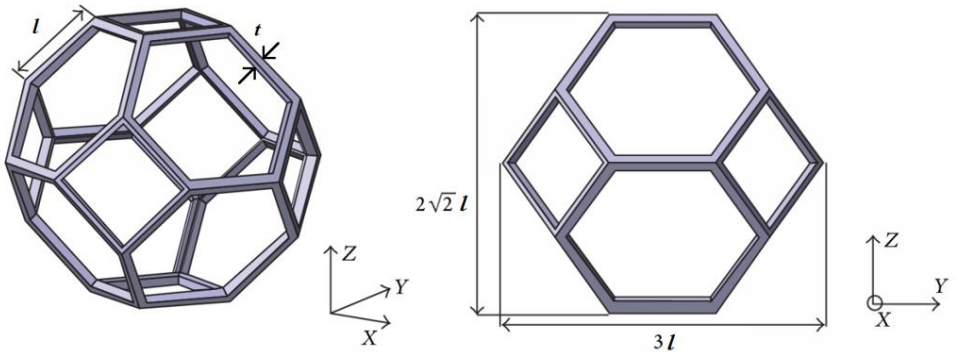

Figure 3.20 Geometry parameters of single Kelvin cell

Gibson and Ashby derived the following equation for the relative density and porosity of a package of Kelvin cell as a function of the strut dimensions:

$$\varepsilon = 1 - \frac{\rho}{\rho_s} = 1 - \varphi = 1 - 1.06\left(\frac{t}{l}\right)^2 \tag{3.15}$$

where ε is porosity of foam structures; ρ is the density of foam structures, ρ_s is the density of solid skeleton and $\rho/\rho_s = \varphi$ is called relative density; l represents the length and t the edge width of the struts (see Figure 3.20, t can be replaced by d_s the diameter of the struts when considering ceramic foams). The length of the struts l is difficult to assess. More convenient would be an equation containing the cell diameter d_{cell} as an input parameter. In the Kelvin cell, the cell diameter d_{cell} is defined as the distance between two square faces that are parallel to each other, which can be calculated as follows:

$$d_{cell} = 2\sqrt{2}l \tag{3.16}$$

which follows that

$$\varepsilon = 1 - 1.06\left(\frac{d_s}{d_{cell}/2\sqrt{2}}\right)^2 = 1 - 8.48\left(\frac{d_s}{d_{cell}}\right)^2 \tag{3.17}$$

The exposed geometric surface areas of all struts in a Kelvin cell can be calculated. The cell volume is

$$V_{cell} = 11.31l^3 \tag{3.18}$$

The unit cell consists of 36 struts. Each of them belongs to three cells, which yields an average of 12 struts/cell. The surface area of a strut (with a cylindrical shape) amounts to $\pi l d_s$. This results in a surface area of $12\pi l d_s$ per cell or, expressed in area per unit volume as a function of d_s and d_{cell}:

$$S_V = \frac{12\pi l d_s}{V_{cell}} = \frac{12\pi l d_s}{11.31l^3} = \frac{12\pi d_s}{11.31\left(d_{cell}/2\sqrt{2}\right)^2} = \frac{26.66}{d_s}\left(\frac{d_s}{d_{cell}}\right)^2 \tag{3.19}$$

Combining Equations (3.16) and (3.19) gives the following relationship, in which the geometric surface area is described as a function of the porosity or relative density and the strut diameter:

$$S_V = \frac{4}{d_s}(1 - \varepsilon) \tag{3.20}$$

or

$$S_V = \frac{4}{d_s}\frac{\rho}{\rho_s} \tag{3.21}$$

For a dense randomly packed spheres in this work, d_{cell} in the Equations (3.17) and (3.19) can be replaced with the average diameter of packed spheres $E(d)$:

$$d_{cell} = E(d) + 2d_s \tag{3.22}$$

$$\varepsilon = 1 - 8.48\left(\frac{d_s}{E(d) + 2d_s}\right)^2 \tag{3.23}$$

$$S_V = \frac{26.66}{d_s}\left(\frac{d_s}{E(d) + 2d_s}\right)^2 \tag{3.24}$$

Therefore, the foam structures with different properties, including variation coefficient of foam-cell volumes $CV(V)$, porosity ε, relative density ρ/ρ_s, and specific surface area S_V, can be generated by controlling the average diameter $E(d)$ and variation coefficient $CV(d)$ of packed spheres, and the strut diameter d_s.

Figure 3.21 shows the porosities of foam structures generated by changing the ratio of strut diameter d_s to the average diameter $E(d)$ of randomly packed spheres under $CV(V)$=1.5. The theoretical curve is drawn using Equation (3.23). The results obtained from the model in current work is in a good agreement with the theoretical result. Using a quadratic expression to fit the relation between porosity vs. $d_s/E(d)$ follows that

$$\varepsilon = -6.477(d_s/E(d))^2 - 0.068(d_s/E(d)) + 1.003 \tag{3.25}$$

with a norm of residuals of 0.0406.

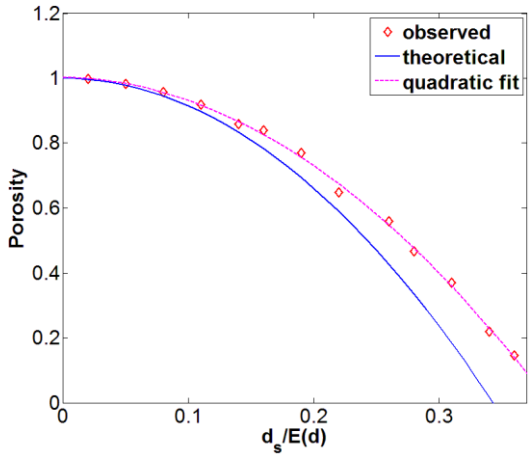

Figure 3.21 Porosity vs. the ratio of strut diameter d_s to the average diameter $E(d)$ of randomly packed spheres under $CV(V)$=1.5

Given different strut diameter d_s, the Equation (3.24) is plot in Figure 3.22. As presented, using current model different foam structures with different specific surface area can be obtained via changing strut diameter d_s and the ratio of d_s to the average diameter of randomly packed spheres $E(d)$. Figure 3.23 shows the observed specific surface areas of foam structures generated in current work. The simulated results are consistent with the theoretical values.

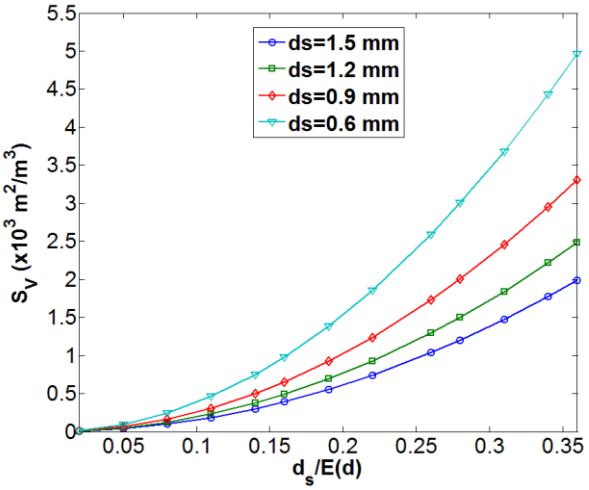

Figure 3.22 Specific surface area S_V vs. $d_s/E(d)$ under different strut diameter d_s

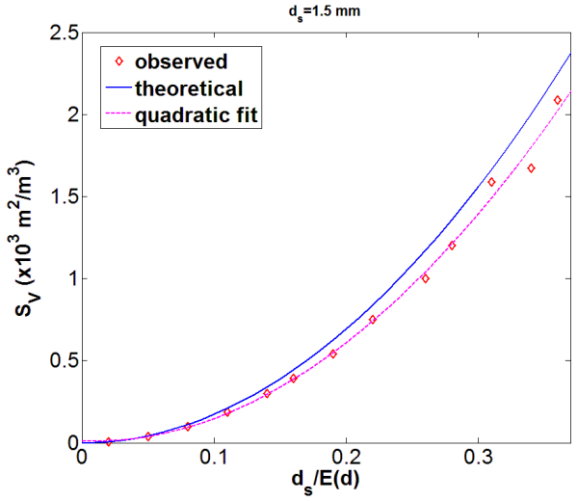

Figure 3.23 Specific surface area S_V vs. $d_s/E(d)$ under d_s=1.5 mm

For each structure with different $CV(d)$ the strut diameter d_s was altered to see its impact on the properties of the modeled foam. In total 36 structures were examined with the porosity and specific surface area calculated using Equation (3.23) and (3.24). The results of these calculations are drawn in Figure 3.24 and Figure 3.25. It can be noted that $CV(d)$ influences ε and S_V more strongly when the ratio of the strut diameter to pore size, $d_s/E(d)$, is higher.

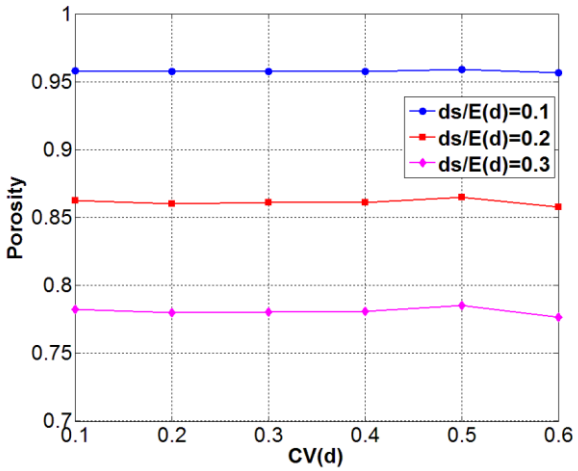

Figure 3.24 Porosity ε for simulated foam structures calculated using Equation (3.23)

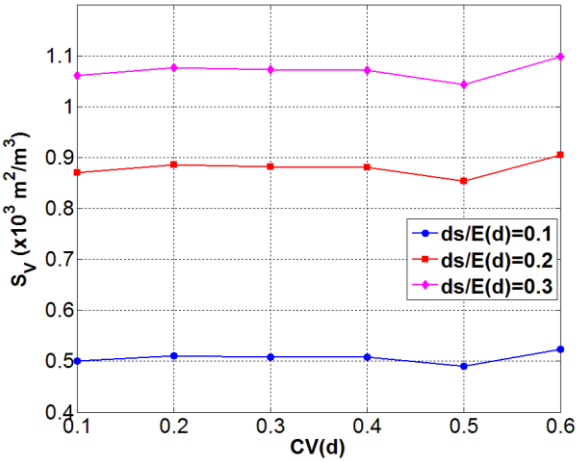

Figure 3.25 Specific surface area for simulated foam structures calculated using Equation (3.24)

The model proposed in this work was also assessed using commercial alumina foams with different pores per inch (ppi). The characteristics of the foam structures used for assessment were obtained in the literature. The experiments were firstly characterized by 3D X-ray tomography on representative samples. Subsequently, methods of image analysis were applied to measure structural parameters. The values of these parameters are listed in Table 3.2 [35].

Table 3.2 Structural parameters of the foams obtained by 3D X-ray tomography [35]

Parameter	Foam (ppi)				
	10	20	30	40	50
Porosity, ε (%)	74	69	70	70	75
Specific surface area, $S_V(\mathrm{m}^2/\mathrm{m}^3)$	1053	1476	1738	2081	2449
Average pore diameter, $E(d)$(mm)	3.53	2.44	2.08	1.64	1.17
Variation coefficient of pore diameter, $CV(d)$	0.28	0.26	0.28	0.3	0.33
Average strut diameter, $E(d_s)$(mm)	1.35	1.17	0.90	0.86	0.58

The porosity and specific surface area of foam structures are calculated using our model and compared with the parameters obtained from other models available in the literature as shown in Figure 3.26 and Figure 3.27. The real foams used for verification had similar porosity, which varied from 69% to 75%. The simulated results in this work are in a good agreement with that of real foams. The results from the literature presented in Figure 3.26 yielded a strong scatter of the estimates with the porosity differing up to 20%.

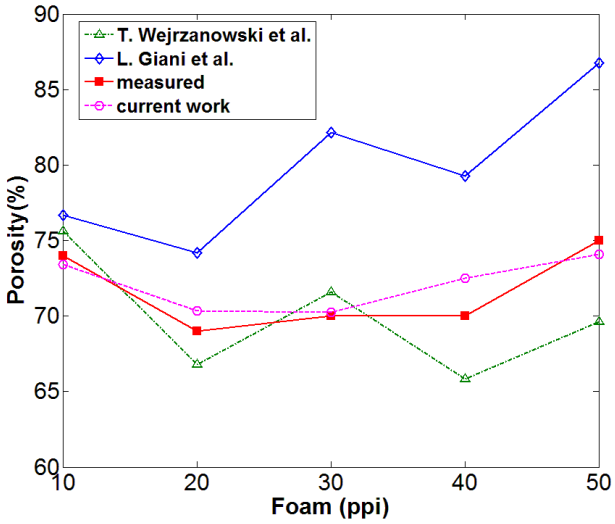

Figure 3.26 Porosity of foam structures in current work vs. the results in the literature

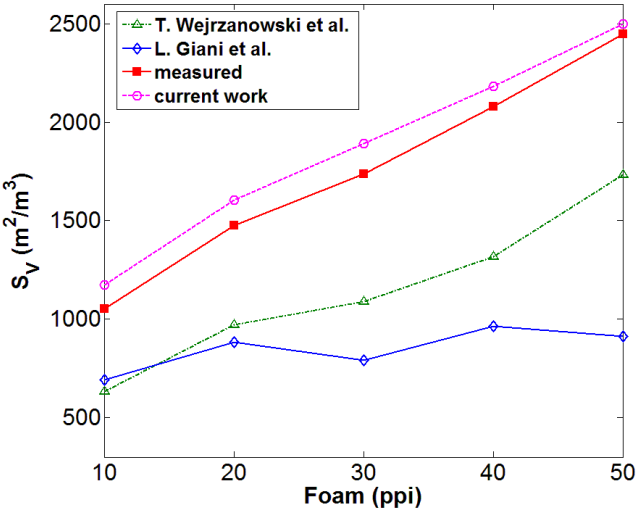

Figure 3.27 Specific surface area of foam structures in current work vs. the results in the literature

Figure 3.28 shows the cell parameters of real foams modeled in current work. As shown, the average numbers of vertices, edges, and faces are in close proximity to that of Kelvin cell.

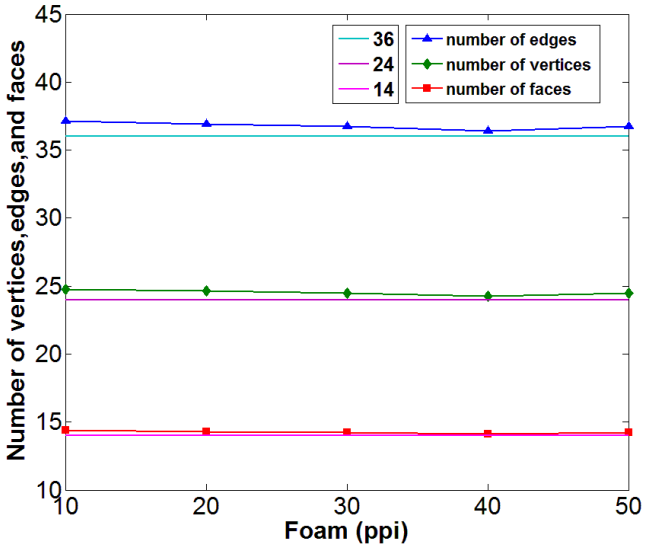

Figure 3.28 Cell parameters of real foams modeled in current work

3.5 Conclusions

An original geometrical model based on randomly packed spheres is proposed using Laguerre-Voronoi tessellations, referred to as LVT structure, to simulate geometrical and topological characteristics in the microstructure of open cell foams. The model permits the study of the coefficient of variation effect on the pore size in real foams. The distribution of foam-cell volumes in foam structures generated in this work is strongly influenced by the log-normal distribution of sphere volumes in corresponding randomly packed spheres. The statistical data of foam structures, including volume, face, and edge number distributions, F, E and $CV(V)_{\text{cell}}$, are very close to those of real materials. The results also show that higher diversity in the sphere size results in the reduction of the average number of faces per foam-cell. It is found that this parameter varies from 13.56 to 14.43 for different sphere size variation coefficients. Compared to structures generated by Poisson-Voronoi tessellations whose the number of faces per cell is about 15.5, the

Laguerre-Voronoi approach gives results which are much closer to the real foams. Further analysis has shown that the porosity of foam structures, ε, decreases with the ratio of strut diameter to the average diameter of randomly packed spheres, $d_s/E(d)$, while the specific surface area of foams, S_V, increases with $d_s/E(d)$.

Another issue undertaken here is the model verification using commercial foams. The struts of real foams, which typically exhibit thickness distribution, are simplified in the model by using cylinders of a constant diameter. This simplification is very common in the literature. The results show that the proposed model provides more accurate results compared with other models available in the literature. The proposed model gives a better inside into understanding interrelationships between statistical geometry parameters and the properties of isotropic foam structures. It enables for calculation structural parameters difficult to measure experimentally, which might have a significant impact on foams properties.

REFERENCES

[1] Dietrich, B., M. Kind, and H. Martin, *Axial two-phase thermal conductivity of ceramic sponges – Experimental results and correlation.* International Journal of Heat and Mass Transfer, 2011. **54**(11-12): p. 2276-2282.

[2] Dietrich, B., *Heat transfer coefficients for solid ceramic sponges – Experimental results and correlation.* International Journal of Heat and Mass Transfer, 2013. **61**: p. 627-637.

[3] Dhara, S., et al., *Nature inspired novel processing routes for ceramic foams.* Advances in applied ceramics, 2005. **104**(1): p. 9-21.

[4] Jian-zhong, Z., W. Jiu-Gen, and M. Jia-Ju, *Porous structures of natural materials and bionic design.* Journal of Zhejiang University Science A, 2005. **6**(10): p. 1095-1099.

[5] Yaszemski, M.J., et al., *Evolution of bone transplantation: molecular, cellular and tissue strategies to engineer human bone.* Biomaterials, 1996. **17**(2): p. 175-185.

[6] Sikavitsas, V.I., J.S. Temenoff, and A.G. Mikos, *Biomaterials and bone mechanotransduction.* Biomaterials, 2001. **22**(19): p. 2581-2593.

[7] Borah, B., et al., *Three-dimensional microimaging (MRμI and μCT), finite element modeling, and rapid prototyping provide unique insights into bone architecture in osteoporosis.* The anatomical record, 2001. **265**(2): p. 101-110.

[8] Ren, L., et al., *Novel approach to fabricate porous gelatin–siloxane hybrids for bone tissue engineering.* Biomaterials, 2002. **23**(24): p. 4765-4773.

[9] Schieker, M., et al., *Biomaterials as scaffold for bone tissue engineering.* European journal of trauma, 2006. **32**(2): p. 114-124.

[10] Swieszkowski, W., et al., *Repair and regeneration of osteochondral defects in the articular joints.* Biomolecular engineering, 2007. **24**(5): p. 489-495.

[11] Placido, E., M. Arduini-Schuster, and J. Kuhn, *Thermal properties predictive model for insulating foams.* Infrared Physics & Technology, 2005. **46**(3): p. 219-231.

[12] Coquard, R. and D. Baillis, *Modeling of heat transfer in low-density EPS foams.* Journal of heat transfer, 2006. **128**(6): p. 538-549.

[13] Kaemmerlen, A., et al., *Radiative properties of extruded polystyrene foams: Predictive model and experimental results.* Journal of Quantitative Spectroscopy and Radiative Transfer, 2010. **111**(6): p. 865-877.

[14] Kaplan, M. and M.J. Hall, *The combustion of liquid fuels within a porous media radiant burner.* Experimental Thermal and Fluid Science, 1995. **11**(1): p. 13-20.

[15] Fend, T., et al., *Porous materials as open volumetric solar receivers: Experimental determination of thermophysical and heat transfer properties.* Energy, 2004. **29**(5-6): p. 823-833.

[16] Zhou, M., et al., *Deep filtration of molten aluminum using ceramic foam filters and ceramic particles with active coatings.* Metallurgical and Materials Transactions A, 2003. **34**(5): p. 1183-1191.

[17] Antsiferov, V.N., *Foam ceramic filters for molten metals: reality and prospects.* Powder Metallurgy and Metal Ceramics, 2003. **42**(9-10): p. 474-476.

[18] Mital, R., J. Gore, and R. Viskanta, *A study of the structure of submerged reaction zone in porous ceramic radiant burners.* Combustion and flame, 1997. **111**(3): p. 175-184.

[19] Randrianalisoa, J., Y. Bréchet, and D. Baillis, *Materials selection for optimal design of a porous radiant burner for environmentally driven requirements.* Advanced Engineering Materials, 2009. **11**(12): p. 1049-1056.

[20] Furler, P., et al., *Solar thermochemical CO2 splitting utilizing a reticulated porous ceria redox system.* Energy & Fuels, 2012. **26**(11): p. 7051-7059.

[21] Fino, D., et al., *Innovative means for the catalytic regeneration of particulate traps for diesel exhaust cleaning.* Chemical Engineering Science, 2003. **58**(3): p. 951-958.

[22] Peng, H., Z. Fan, and J. Evans, *Bi-continuous metal matrix composites.* Materials Science and Engineering: A, 2001. **303**(1): p. 37-45.

[23] Cheng, H. and F. Han, *Compressive behavior and energy absorbing characteristic of open cell aluminum foam filled with silicate rubber.* Scripta materialia, 2003. **49**(6): p. 583-586.

[24] Boomsma, K., D. Poulikakos, and F. Zwick, *Metal foams as compact high performance heat exchangers.* Mechanics of materials, 2003. **35**(12): p. 1161-1176.

[25] Wang, Q., et al., *A review on application of carbonaceous materials and carbon matrix composites for heat exchangers and heat sinks.* International Journal of Refrigeration, 2012. **35**(1): p. 7-26.

[26] Khateeb, S.A., et al., *Thermal management of Li-ion battery with phase change material for electric scooters: experimental validation.* Journal of Power Sources, 2005. **142**(1): p. 345-353.

[27] Hong, S.-T. and D.R. Herling, *Open-cell aluminum foams filled with phase change materials as compact heat sinks.* Scripta Materialia, 2006. **55**(10): p. 887-890.

[28] Yu, S., et al., *Compressive property and energy absorption characteristic of open-cell ZA22 foams.* Materials & Design, 2009. **30**(1): p. 87-90.

[29] Pang, Q., et al., *Synthesis and mechanical properties of open-cell Ni–Fe–Cr foams.* Materials Science and Engineering: A, 2012. **534**: p. 699-706.

[30] Lu, G., G.M. Lu, and Z. Xiao, *Mechanical properties of porous materials.* Journal of Porous Materials, 1999. **6**(4): p. 359-368.

[31] Edouard, D., et al., *Pressure drop modeling on SOLID foam: State-of-the art correlation.* Chemical Engineering Journal, 2008. **144**(2): p. 299-311.

[32] Zhu, H.X., N.J. Mills, and J.F. Knott, *Analysis of the high strain compression of open-cell foams.* Journal of the Mechanics and Physics of Solids, 1997. **45**(11-12): p. 1875-1904.

[33] Roberts, A.P. and E.J. Garboczi, *Elastic moduli of model random three-dimensional closed-cell cellular solids.* Acta materialia, 2001. **49**(2): p. 189-197.

[34] Habisreuther, P., N. Djordjevic, and N. Zarzalis, *Statistical distribution of residence time and tortuosity of flow through open-cell foams.* Chemical Engineering Science, 2009. **64**(23): p. 4943-4954.

[35] Wejrzanowski, T., et al., *Structure of foams modeled by Laguerre–Voronoi tessellations.* Computational Materials Science, 2013. **67**: p. 216-221.

[36] Michailidis, N., et al., *An image-based reconstruction of the 3D geometry of an Al open-cell foam and FEM modeling of the material response.* Mechanics of Materials, 2010. **42**(2): p. 142-147.

[37] Michailidis, N., et al., *Experimental and FEM analysis of the material response of porous metals imposed to mechanical loading.* Colloids and Surfaces A: Physicochemical and Engineering Aspects, 2011. **382**(1-3): p. 124-131.

[38] Fan, Z., et al., *Simulation of polycrystalline structure with Voronoi diagram in Laguerre geometry based on random closed packing of spheres.* Computational Materials Science, 2004. **29**(3): p. 301-308.

[39] Scott, G.D., *Packing of spheres: packing of equal spheres.* Nature, 1960. **188**(4754): p. 908-909.

[40] Scott, G. and D. Kilgour, *The density of random close packing of spheres.* Journal of Physics D: Applied Physics, 1969. **2**(6): p. 863.

[41] He, D. and N. Ekere, *Computer simulation of powder compaction of spherical particles.* Journal of materials science letters, 1998. **17**(20): p. 1723-1725.

[42] *LAMMPS Molecular Dynamics Simulator*. 2016; Available from: http://lammps.sandia.gov/.

[43] Okazaki, K. and H. Conrad, *Grain size distribution in recrystallized alpha-titanium.* Transactions of the Japan Institute of Metals, 1972. **13**(3): p. 198-204.

[44] Rhines, F. and B. Patterson, *Effect of the degree of prior cold work on the grain volume distribution and the rate of grain growth of recrystallized aluminum.* Metallurgical Transactions A, 1982. **13**(6): p. 985-993.

[45] Roberts, A.P. and E.J. Garboczi, *Elastic properties of model random three-dimensional open-cell solids.* Journal of the Mechanics and Physics of Solids, 2002. **50**(1): p. 33-55.

[46] Matzke, E.B. and J. Nestler, *Volume-shape relationships in variant foams. A further study of the role of surface forces in three-dimensional cell shape determination.* American Journal of Botany, 1946: p. 130-144.

[47] Matzke, E.B., *The three-dimensional shape of bubbles in foam-an analysis of the rôle of surface forces in three-dimensional cell shape determination.* American Journal of Botany, 1946: p. 58-80.

[48] Gibson, L.J. and M.F. Ashby. *The mechanics of three-dimensional cellular materials*. in *Proceedings of the Royal Society of London A: Mathematical, Physical and Engineering Sciences*. 1982. The Royal Society.

[49] Gibson, L.J. and M.F. Ashby, *Cellular solids: structure and properties*. 1999: Cambridge university press.

CHAPTER 4 COMPUTATIONAL MODELING OF THE ELASTIC PROPERTY OF THREE DIMENSIONAL OPEN CELL FOAMS

4.1 Introduction

Engineered cellular solids (foams) have been developed for a range of applications [1], as discussed in Chapter 3 of this work, for example, filtration, insulation, and light-weight structure components, etc., and their natural counterparts (e.g., bone and sponge) have a cellular structure that optimizes performance in a particular setting. Commercially available foams can either have closed cell or open cell microstructures, depending on the foaming technology used in the manufacturing processing. The useful properties of open cell solids depend on the material from which they are fabricated, their relative density, and their internal geometrical microstructure. Their macroscopic properties are dictated by the solid materials used to produce the foams, and more importantly by the geometrical aspects of the microstructures of the foams, such as the microscopic topology. It is essential to examine the relation between the physical properties of open cell solids to their relative density and complex microstructure, in order to understand how such properties can be optimized for a given application and to facilitate more application of foams [2-7].

Since the microstructures of foams are normally of order mm in size and can be easily identified, it is desirable to establish the relationship between the microstructure and the macroscopic mechanical properties of foams. Numerous micromechanics models have been developed (see, for example, Gibson and Ashby [8]; Banhart [9]). Many studies have focused on how local cell features, such as strut shape, affect the properties of periodic arrays of cells. Some of the theoretical results for such models are generalizable to real

materials, but some are not. On the other hand, the effect of randomness and imperfections (e.g., isotropy), and the interaction between cells on a cells-scale have been examined as most real open cell solids are not periodic.

In general, the models in the literature can be categorized into two approaches. In the first approach of modeling, idealized models with the repetitive unit cell are proposed to provide the homogenized behavior of foams, including two dimensional foam/honeycomb models [8, 10-15] and three dimensional bubble models, cubic, tetrahedral, and tetrakaidecahedral (Kelvin cell) models [8, 16-21]. Based on the developed idealized models with repetitive unit cell, the mechanical properties of foams (e.g., Young's modulus, bulk modulus, Poisson ratio, and multi-axial failure surface, etc.) are evaluated. Idealized models with repetitive unit cell have been proven to be useful in understanding some important features of real foams, however, there exist several drawbacks. It is found that they usually over-predict the bulk modulus and hydrostatic yield strength of real foams. To overcome this drawback, various morphological defects (e.g., non-uniform and wavy cell edges) have to be included [10, 12, 22, 23]. Furthermore, for the sake of computational efficiency, many models employ periodic boundary conditions in which a representative volume element is repeated to represent the entire foam structure. Another problem in idealized models with the repetitive unit cell is that they, in theory, are only applicable to foams with regular and periodic cells while real foams always have an irregular microstructure and almost are isotropic [24-31].

The second approach of micromechanics modeling, i.e., so-called "super-cell models", has thus been developed in order to give a better representation of the morphological structure of real foams, which usually contains a number of irregular cells

and imperfections. Among super-cell models, Voronoi models in conjunction with the finite element method are most widely used. Gibson and her co-workers developed two dimensional Voronoi models [32-39]. They found that the elastic and plastic uni-axial responses of two dimensional Voronoi foams to external loading, on average, is not far away from that of periodic regular honeycombs. They also found that removing a few percent of cell edges would lead to a sharp decrease in stiffness and strength under a uni-axial loading. Comprehensive analysis of the effects of various morphological defects upon the macroscopic mechanical properties of foams is presented by Chen et al. [12]. By introducing imperfections into the microstructure of foams, Chen et al. predicted an elliptical yield surface for elastoplastic foams under a multi-axial loading. Finite element analysis of three dimensional Voronoi models is much more computationally challenging. So far, most available studies on three dimensional Voronoi foams have been limited to investigating their elastic properties [12, 18, 22, 40-44] . Zhu et al. found that, at very small values of relative density ρ (e.g., $\rho = 0.01$), the predicted Young's modulus of three dimensional random Voronoi foams is 50% greater than that of Kelvin foams while the bulk modulus of Voronoi foams is about 20% less than that of Kelvin foams [24]. Despite of this discrepancy, the computed uni-axial stress-strain curves of three dimensional elastic random Voronoi foams, for the compressive engineering strain up to 50%, is quantitatively similar to that of Kelvin foams. The predicted plateau stress of random Voronoi foams, however, is significantly lower than that of perfect Kelvin foams under hydrostatic compression [19, 44].

The irregularity of cell shapes, cell size variations, fractured cell wall imperfections are some types of disparity and randomness effects that are considered in investigating the

mechanical properties in the literature [22, 45, 46]. Zhu et al. used random Voronoi foam models by applying finite element method to study the effects of cell irregularity [24]. Li et al. analyzed the effect of only one type of imperfection is analyzed at a time as presented in the literature [47]. Since several imperfections commonly exist simultaneously in foam structures, these sources of scattering from ideal repeated structures must be modeled at the same time to have reliable mechanical models [8]. Due to this necessity, one of the recent studies on the elastic properties of open cell foams takes into account two types of imperfections which are an irregularity of cell shapes and cell wall imperfections in the same foam model [47, 48].

In other studies recently developed to examine mechanical properties of cellular solids, complex heterogeneity of the three dimensional porous materials is captured by the automated serial-sectioning techniques [49-52]. In those techniques, a number of sectional images are taken via a light microscopy montage from the cellular structure injected with an epoxy resin. Then, three dimensional foam models are generated by distinguishing foam regions from epoxy regions which are in different colors and comparing successive sectional images in a computational environment. Imperfections and uniqueness for each individual foam sample are highly incorporated into the three dimensional models in [49]. However, the number of sections or thickness of layers determines the accuracy of the model, which increases the manual work and modeling time.

In this work, an alternative three dimensional random Laguerre-Voronoi foam model is developed to investigate the elastic properties of open cell ceramic foams. At the first stage, three dimensional model of ceramic foams having pre-selected cell size distribution with random coordinates and orientations is created via a finite element

analysis (FEA) software package: ANSYS. Randomness and imperfections are included in the modeling via a LAMMPS program written for calculation of cell locations and sizes with the assumption of spherical cell geometry. At the second stage, different groups of finite element models are then generated using the developed Laguerre-Voronoi foam model. Each of these foam specimens contains different numbers of lv-cells. The cell morphology of the random foam models is not included in this chapter since it has been analyzed in Chapter 3. A size sensitivity study is first performed to determine the appropriate number of cells to be included in each foam specimen and the suitable number of specimens to be used in statistical analysis. This is followed by a finite element analysis to calculate the effective Young's modulus, shear modulus, and Poisson ratio of the foams. Finally, the results obtained in this work are compared with some results in the literature. It is shown that presented approach yields more accurate mechanical models for open cell ceramic foams than that of other models in the literature. A few conclusions on the models and the obtained results are summarized in the final part.

4.2 Modeling

As discussed in Chapter 3, foam models are obtained by the Laguerre-Voronoi tessellation method applied to a set of spheres with specified size distribution, randomly packed in a cube. The foam struts are generated by placing cylinders with defined radius along the lv-cell edges.

The procedure for the modeling of foam structures employed in the present study consists of the following four steps:

(1) Generation of spheres with a pre-selected size distribution (in the computations log-normal distribution of volume is adopted with certain average value $E(V)$, and variation coefficient $CV(V)$);

(2) Randomly packing of the spheres;

(3) Performing the Laguerre-Voronoi tessellation;

(4) Generation of struts.

The procedure based on the above given four-steps approach is schematically presented in Figure 4.1.

Steps (1) and (2) are computed in an open source software package, LAMMPS, which is normally used for molecular dynamics simulations. LAMMPS runs by reading in scripts and executing the commands. The basic idea of step (2) is to randomly "pour" spheres into the top of the simulation cell and then let them fall to the bottom under gravitational forces. A quadratic potential is applied for the pairwise interactions between any two different spheres, so they're technically real solid balls. This allows one to use a straightforward molecular dynamics simulation with gravity turned on to do the packing. A visualization software, OVITO is used to visualize the steps (1) and (2). After sphere packing, the Laguerre–Voronoi tessellation are performed to obtain porous structures. In the Laguerre–Voronoi tessellation method the lv-cell faces are generated using the intersecting planes located in the proportional distance between two neighboring spheres surfaces. In the step (4) the cylinders with constant diameter are created along the cell edges. Additionally, spheres that have diameters equal to those of the cylinders are placed in the cell vertices to assure dimensional conformity along the edges. Steps (3) and (4) are performed using a script written in the APDL language for the package ANSYS.

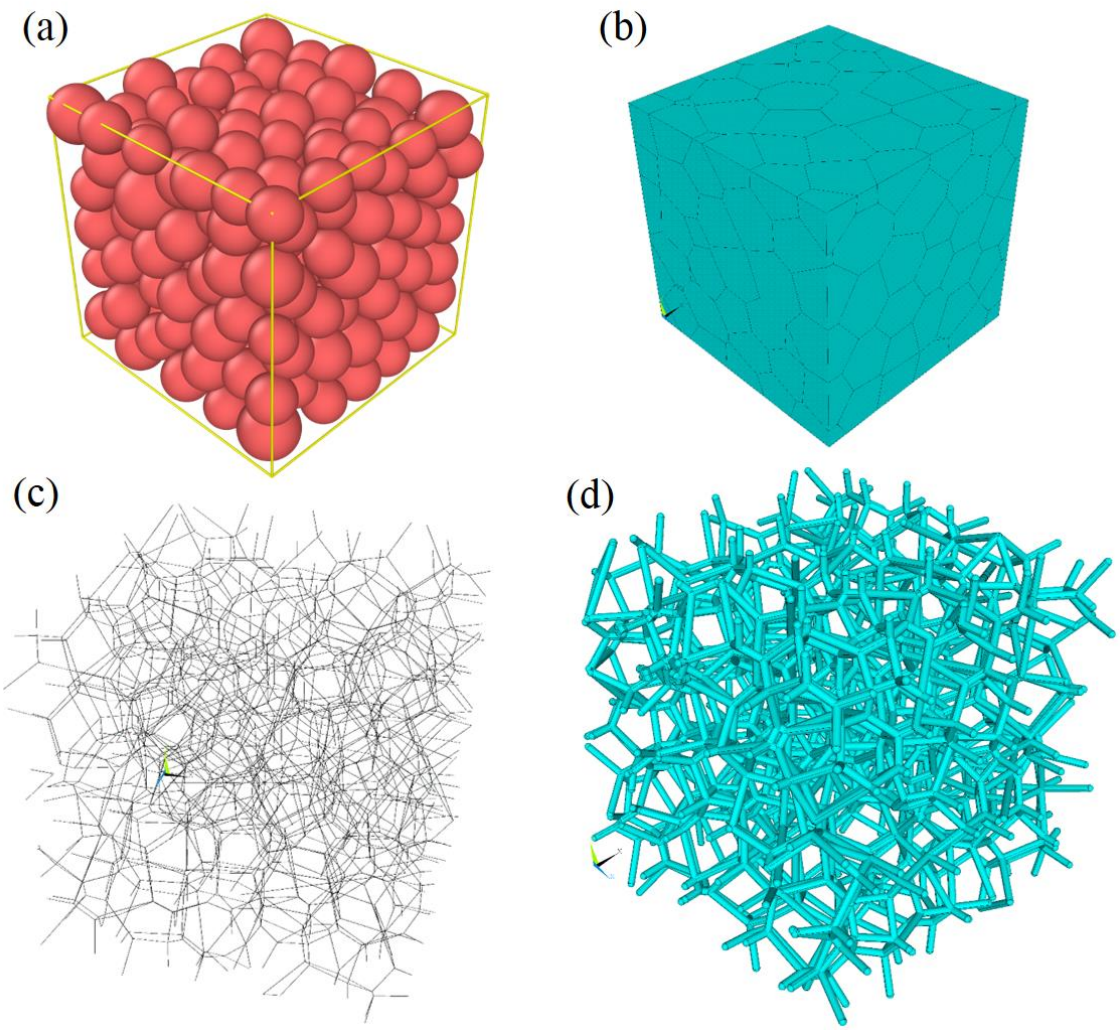

Figure 4.1 Schematic illustration of Laguerre-Voronoi tessellations developed for generating foam structures: (a) randomly packed spheres with the pre-selected volume distribution, (b) cellular structure obtained using Laguerre-Voronoi tessellations, (c) lv-cell edges of the cellular structure, and (d) foam structure with cylindrical struts

According to the structure parameters of real ceramic foams, as shown in Table 3.2, a set of eighteen type of structures (see Table 4.1) with a coefficient of pore volume variation $CV(d)$ ranging from 0.25 to 0.28 is generated. For each type of structure, totally two same structures are developed to obtain the mean value of each parameter. Variation

coefficient of pore volume $CV(V)$ is set using a selected range of sphere diameters in the first step of Laguerre-Voronoi tessellation procedure described above. The $CV(V)$ values of pore volume for each structure are calculated as $CV(V)$ for lv-cells (Figure 4.1 (b)). Each structure is limited by a bounding box of cubic shape and consisted of at least 125 cells. This is expected to be sufficiently high number of cells to study their effect on the properties of the structures in question, which will be discussed in Chapter 4.4. Strut diameters values were varied from 0.3 to 1.3 mm, which resulted in porosity ranging from 60.0 to 94.7%. The strut diameter 1.3 mm was used to generate structures representative for 10 ppi commercial ceramic foams.

Table 4.1 Structure parameters for models generated using Laguerre-Voronoi tessellation procedure

Structure (ppi)	Mean pore diameter (mm)	$CV(d)$	Mean strut diameter (mm)	Porosity (%)	Specific surface area ($\times 10^3$ m^2/m^3)
10	3.53	0.25	1.2	72.7	909.6
			1.1	75.9	893.1
			1.0	78.4	871.7
			0.8	84.0	810.4
			0.6	89.4	714.9
			0.4	94.7	568.7
20	2.44	0.26	0.8	67.0	1306.5
			0.6	76.9	1207.1
			0.55	79.5	1169.9
			0.5	82.1	1126.3
			0.4	86.6	1015.7
			0.3	92.3	791.0
30	2.08	0.28	0.8	60.0	1574.7
			0.6	71.6	1486.7
			0.55	74.2	1449.8
			0.5	77.7	1404.9
			0.4	83.6	1285.5
			0.3	89.4	1113.4

Figure 4.2 shows the foam structures generated for commercial 10 ppi ceramic foams with different porosities: (c) 75% and (d) 95%. Figure 4.3 and Figure 4.4 show the

foam structures for commercial 20 ppi and 30 ppi ceramic foams with porosity from 72% to 92%.

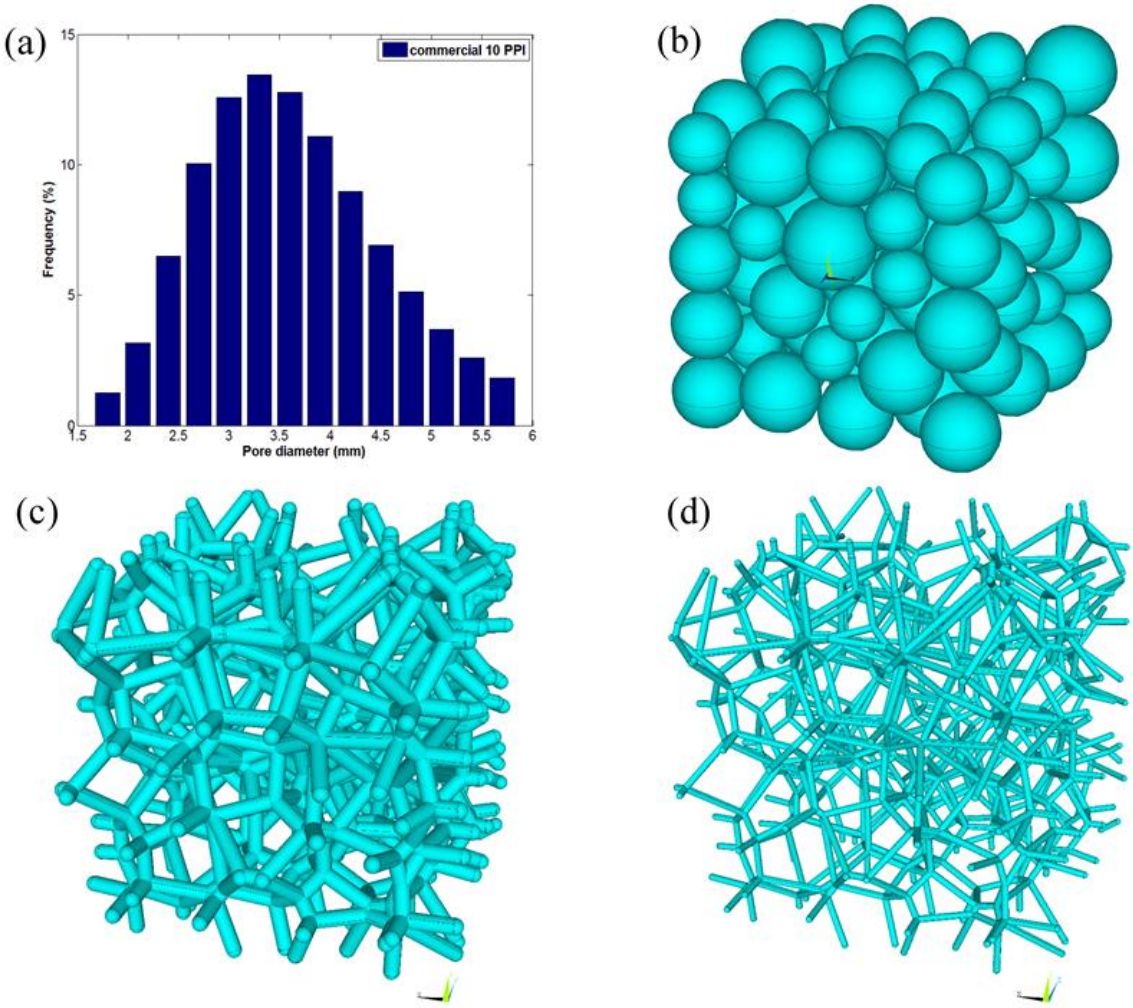

Figure 4.2 Foam structures generated for commercial 10 ppi ceramic foams: (a) the pore size distribution obtained by X-ray tomography, (b) randomly packed spheres, (c) foam structure with porosity 75%, and (d) foam structure with porosity 95%

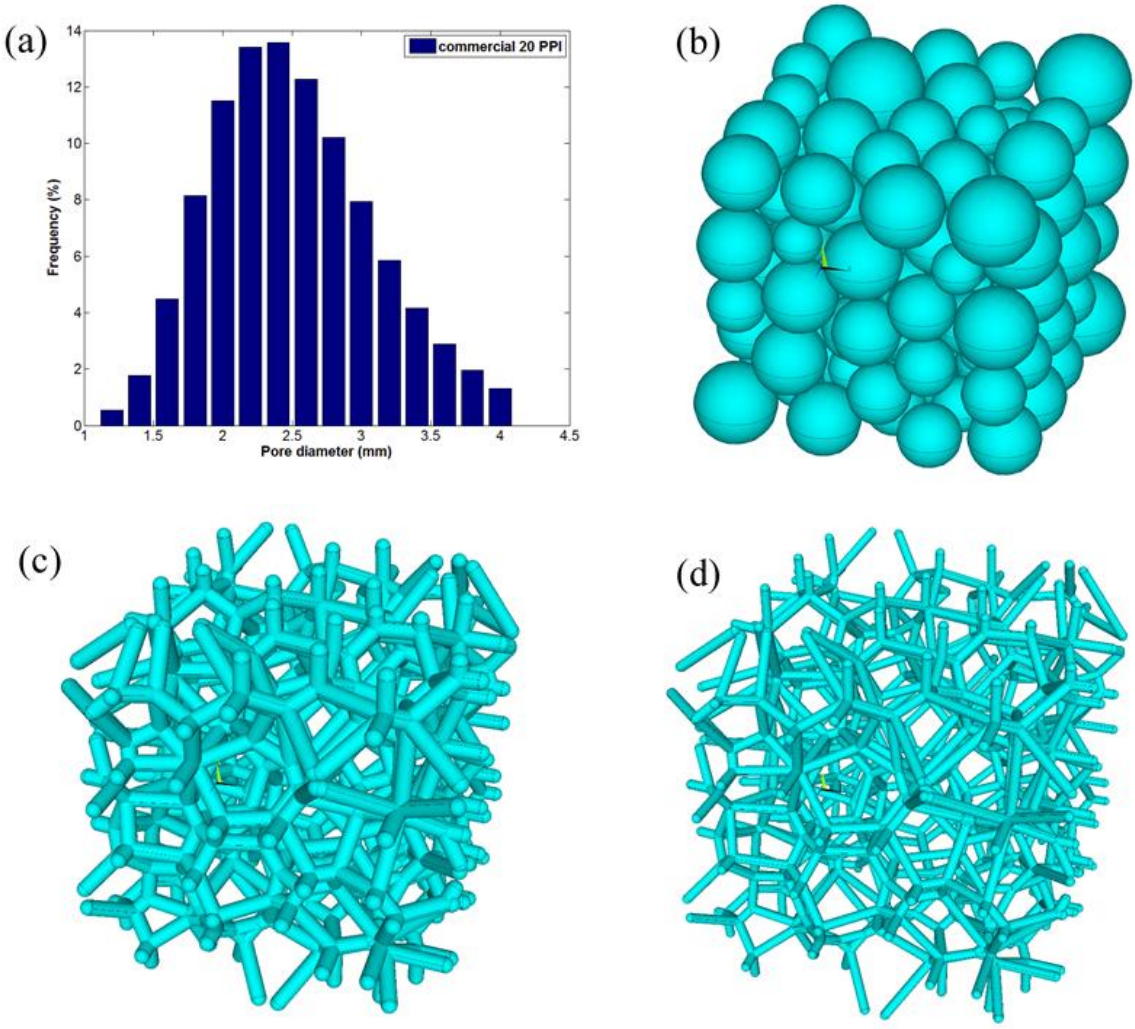

Figure 4.3 Foam structures generated for commercial 20 ppi ceramic foams: (a) the pore size distribution obtained by X-ray tomography, (b) randomly packed spheres, (c) foam structure with porosity 72%, and (d) foam structure with porosity 90%

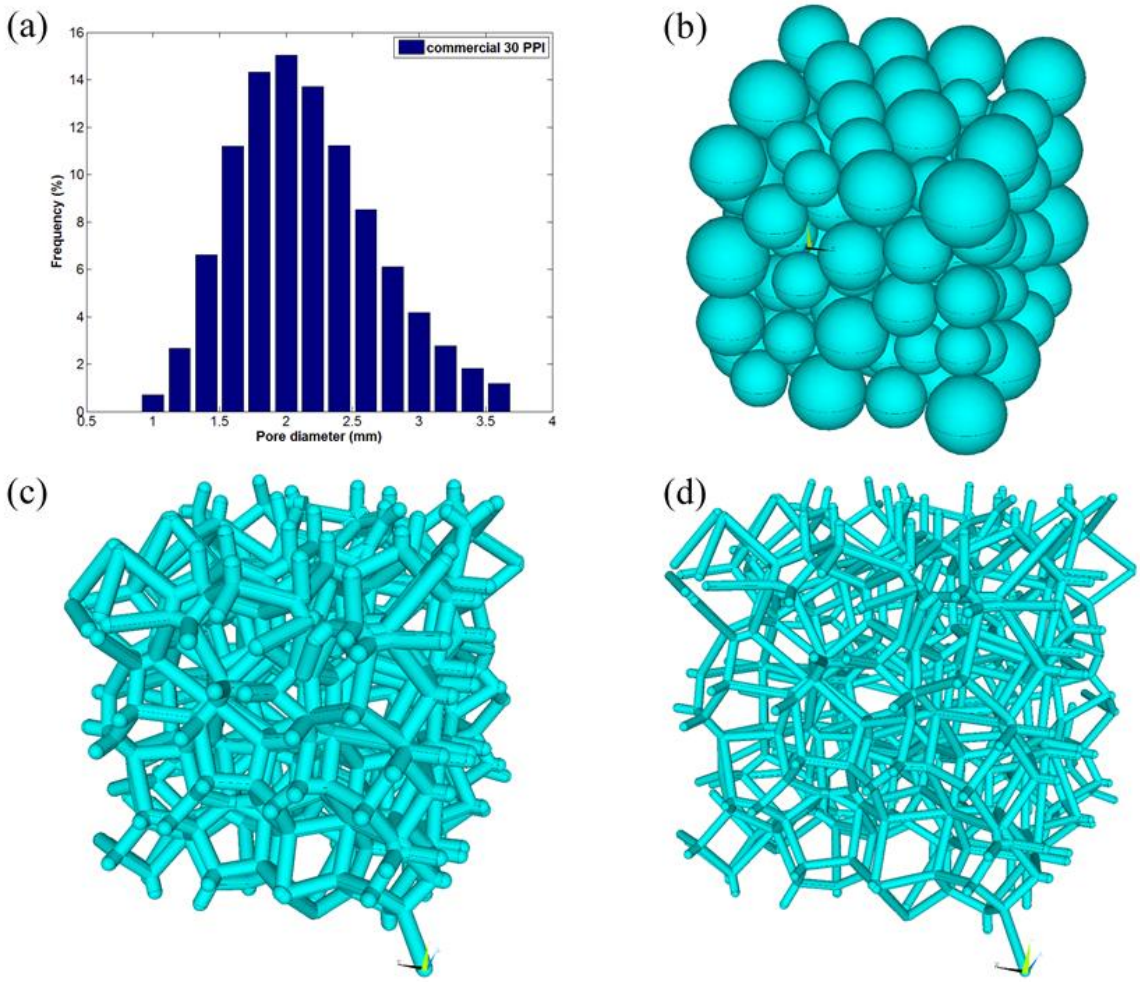

Figure 4.4 Foam structures generated for commercial 30 ppi ceramic foams: (a) the pore size distribution obtained by X-ray tomography, (b) randomly packed spheres, (c) foam structure with porosity 75%, and (d) foam structure with porosity 92%

4.3 Finite element analysis

A finite element study is performed to obtain the elastic properties of foams with cell shape and variation coefficient using the commercial finite element analysis software ANSYS 16.0 (Ansys, Inc., Canonsburg, PA, USA). Alumina ceramic foams are considered here. The Young's modulus E_s and Poisson's ratio ν_s of the alumina strut material are,

respectively, taken to be 370 GPa and 0.22 [53]. Each cell strut of the foams is modeled by a few to a number of Timoshenko beam elements (i.e., element type Beam189 in ANSYS which is a three-node beam element), the number of which depends on the slenderness ratio of the cell strut. The Timoshenko beam elements are appropriate for both slender and stout beams, which involves bending, stretching, twisting and shearing deformation mechanisms. Previous studies have proved that using such a beam element to model each strut is sufficient for convergence [40, 46-48]. It is noted that exceptionally short struts do exist in foam structures having highly irregular cell shapes. Typical beam elements cannot represent these short struts well. However, the effect incurred from using inappropriate element types could be negligible since short struts only account for a small fraction (a few percent) of the total number of struts [54].

In current work, uni-axial compressive tests on foam structures along three orthogonal directions, x_1, x_2 and x_3, are considered in three separate analyses to obtain the effective Young's moduli and Poisson's ratios of the foam relative to the three directions. In x_1x_2 plane, the performed analyses refer to Figure 4.5. For instance, displacement constraints may be imposed at the bottom nodes of the specimen in the x_2 direction and at the nodes on the left side of the specimen in the x_1 direction, if strains are applied on the top and/or right sides of the specimen, as shown in Figure 4.5. The cases in x_2x_3 and x_3x_1 planes are the same as that of x_1x_2 plane. The analysis settings of ceramic foam models in ANSYS are shown in Figure 4.6. In each analysis, a small compressive strain (e.g., -0.001) is applied in the loading direction such that no local buckling of struts would take place. The effective Young's modulus, E_1, and Poisson's ratios, ν_{12} and ν_{13}, of the foam along the x_1 direction are given by

$$E_1 = \frac{-F_1}{\delta_1 L_2 L_3} \tag{4.1}$$

$$\nu_{12} = -\frac{u_2^1}{\delta_1 L_2}, \nu_{12} = -\frac{u_3^1}{\delta_1 L_3} \tag{4.2a,b}$$

where δ_1 is the applied compressive strain, here which is -0.001, and F_1 is the total reaction force along x_1 direction on the defined boundary, which is to be obtained from the finite element analysis, and $u_j^i, i,j \in \{1,2,3\}$, is the lateral displacement (extension) in the x_j direction perpendicular to the loading direction x_i. The effective Young's moduli and Poisson's ratios along the x_2 and x_3 directions, E_2, E_3, ν_{21}, ν_{23}, ν_{31} and ν_{32}, can be similarly determined as described in equation

$$E_2 = \frac{-F_2}{\delta_2 L_1 L_3} \tag{4.3}$$

$$\nu_{21} = -\frac{u_1^2}{\delta_2 L_1}, \nu_{23} = -\frac{u_3^2}{\delta_2 L_3} \tag{4.4a,b}$$

$$E_3 = \frac{-F_3}{\delta_2 L_1 L_2} \tag{4.5}$$

$$\nu_{31} = -\frac{u_1^3}{\delta_3 L_1}, \nu_{32} = -\frac{u_2^3}{\delta_3 L_2} \tag{4.6a,b}$$

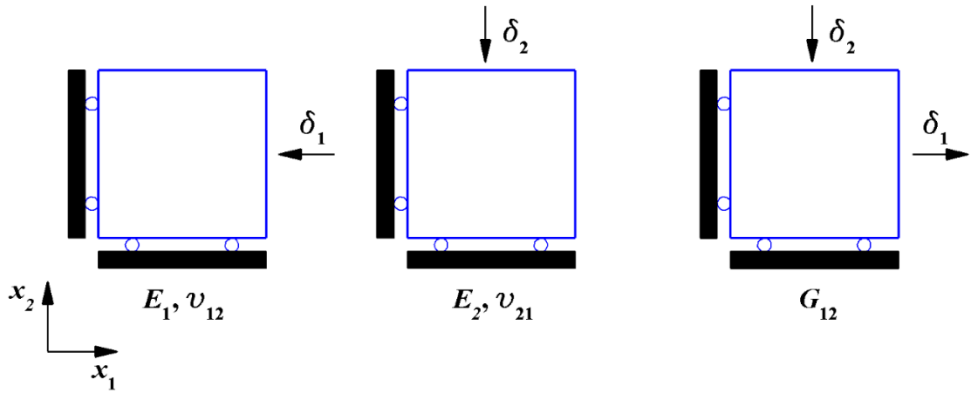

Figure 4.5 Performed analyses for determining the elastic properties

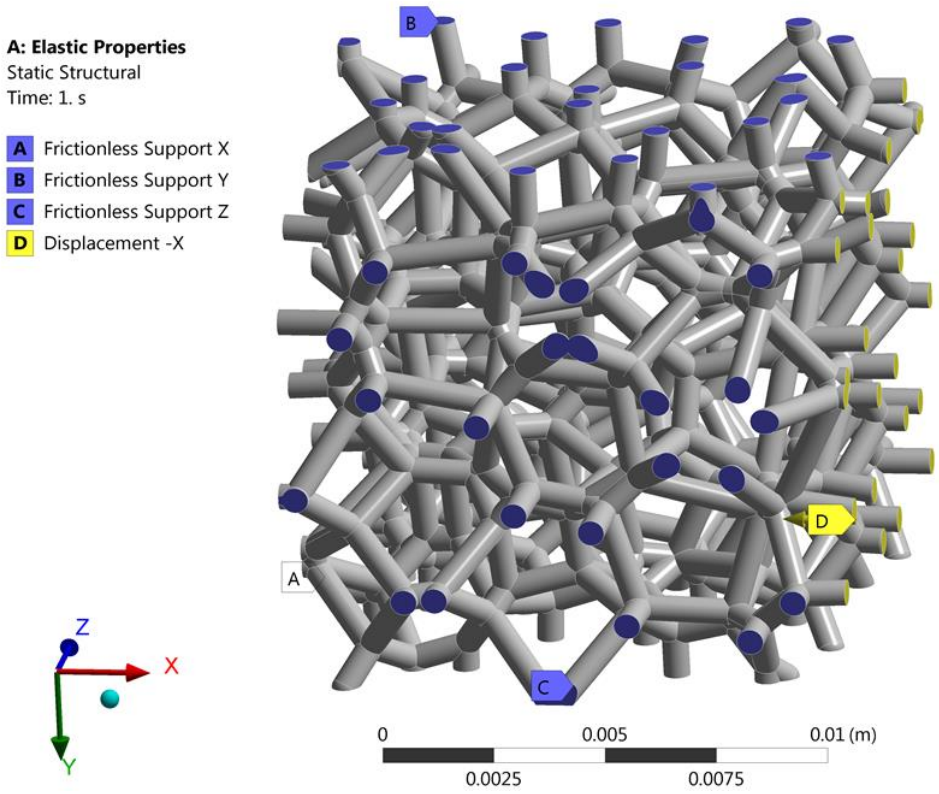

Figure 4.6 Boundary conditions of ceramic foam models in ANSYS

To obtain the effective shear modulus G_{12}, a bi-axial loading test is performed. A small tensile strain $\delta_1 = 0.001$ in the x_1 direction and a small compressive strain $\delta_1 = -0.001$ in the x_2 direction are applied simultaneously (see Figure 4.5). Then, the effective shear modulus G_{12}, defined by $G_{12} = \tau_{12}/\gamma_{12}$, is given by

$$G_{12} = \frac{F_1/L_2 - F_2/L_1}{2L_3(\delta_1 - \delta_2)} \tag{4.7}$$

where F_1 and F_2 are obtained from the finite element analysis. The other two shear moduli, G_{23} and G_{31}, can be similarly determined by

$$G_{23} = \frac{F_2/L_3 - F_3/L_2}{2L_1(\delta_2 - \delta_3)} \tag{4.8}$$

$$G_{31} = \frac{F_3/L_1 - F_1/L_3}{2L_2(\delta_3 - \delta_1)} \tag{4.9}$$

In modeling uni-axial or bi-axial loading tests, displacement boundary conditions are typically used in the literature [23, 32, 39, 54]. However, displacement boundary conditions that only restrain normal displacements might underestimate foams' elastic properties (e.g., Li et al., [47, 48]). Since the specimens are cut out of an infinite structure that can be regarded as periodic, spatially periodic boundary conditions should be applied to ensure that the predicted properties of the specimens are representative of those of the foam material [43, 47, 48, 55]. The specimens obtained by the procedure described in Chapter 4.2 are periodic, i.e., each node on one face (e.g., h^+) has a matched node on the opposite face of the specimen (e.g., h^-), as shown in Figure 4.7. For a uni-axially deformed specimens subjected to prescribed strain δ_i, the periodic boundary conditions may be represented by

$$u_i^{k^+} - u_i^{k^-} = \delta_i\left(x_i^{k^+} - x_i^{k^-}\right), \omega_i^{k^+} - \omega_i^{k^-} = 0, i \in \{1, 2, 3\} \tag{4.10a,b}$$

where $x_i^{k^+}$ and $x_i^{k^-}$ are the positions of the matched nodes k^+ and k^- on the specimens boundary faces with outward unit normal vectors e_i and $-e_i$, respectively; $u_i^{k^+}$ and $u_i^{k^-}$ are the normal displacement components of k^+ and k^- respectively; $\omega_i^{k^+}$ and $\omega_i^{k^+}$ are the rotations of matched notes k^+ and k^-, respectively. In addition, it should be noted that the periodic boundary conditions defined by Equation (4.10) work well only for foams undergoing small deformations, which is the case here with the applied compressive strain taken to be $\delta_i = -0.001$ in using Equations (4.1)–(4.9) [46-48]. However, non-periodic

localized deformations might occur (e.g., Gong et al., [17, 21, 56]) when foams are subjected to a large compressive strain and periodic boundary conditions cannot be adequately applied any more.

The periodic boundary conditions given in Equation (4.10) can be implemented in ANSYS and by introducing four reference nodes N0, N1, N2, and N3, which define three two-node AXIAL connector elements E01, E02, and E03 as shown in Figure 4.7. The three connector elements intersect at reference node N0 and are located along the e_1, e_2 and e_3 directions, respectively. Nodes N1, N2 and N3 are allowed to move axially only along their associated connector elements. The degrees of freedom of the matched nodes may be coupled with those of the reference nodes by

$$u_i^{k^+} - u_i^{k^-} - \frac{x_i^{k^+} - x_i^{k^-}}{X_i^{K^+} - X_i^{K^-}}\left(U_i^{K^+} - U_i^{K^-}\right) = 0, \qquad \omega_i^{k^+} - \omega_i^{k^-} - \left(\Omega_i^{K^+} - \Omega_i^{K^-}\right) = 0, i \in \{1,2,3\} \tag{4.11a,b}$$

where X_i, U_i, and Ω_i are the positions, displacements and rotations of the reference nodes, respectively; the superscript K^+ stands for reference nodes N1, N2, and N3, and the superscript K^- denotes reference node N0. For uni-axial compression along direction $-e_1$, for example, node N0 is fixed and a displacement corresponding to $\delta_1 = -0.001$ is applied at node N1.

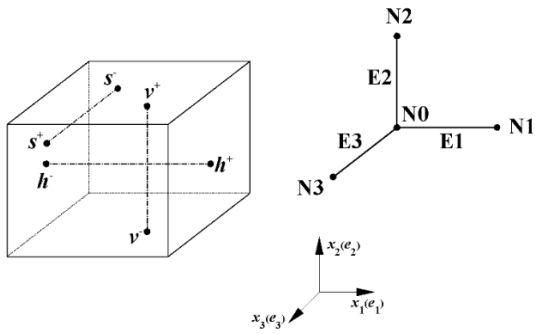

Figure 4.7 Matched nodes for implementing spatially periodic boundary conditions

In the meshing of foam models partition option of the ANSYS software is used to divide the volume of foam models into simple parts to mesh entire body easily. Because of the complicated 3-D topology, tetrahedron elements are used for foam models. Finite element models of ceramic foams have a large number of elements with large degrees of freedom. For example, the 125-cells model having 90% porosity consists of approximate 1,200,000 quadratic 10-noded tetrahedron elements, around 2,000,000 nodes, and approximate ten million degrees of freedom. These approximate numbers of finite elements and degrees of freedom increase as the porosity value decreases. Moreover, for convergence tests of finite element analyses, the number of elements is increased in the analyses. Examples of meshes generated on foam structures are shown in Figure 4.8.

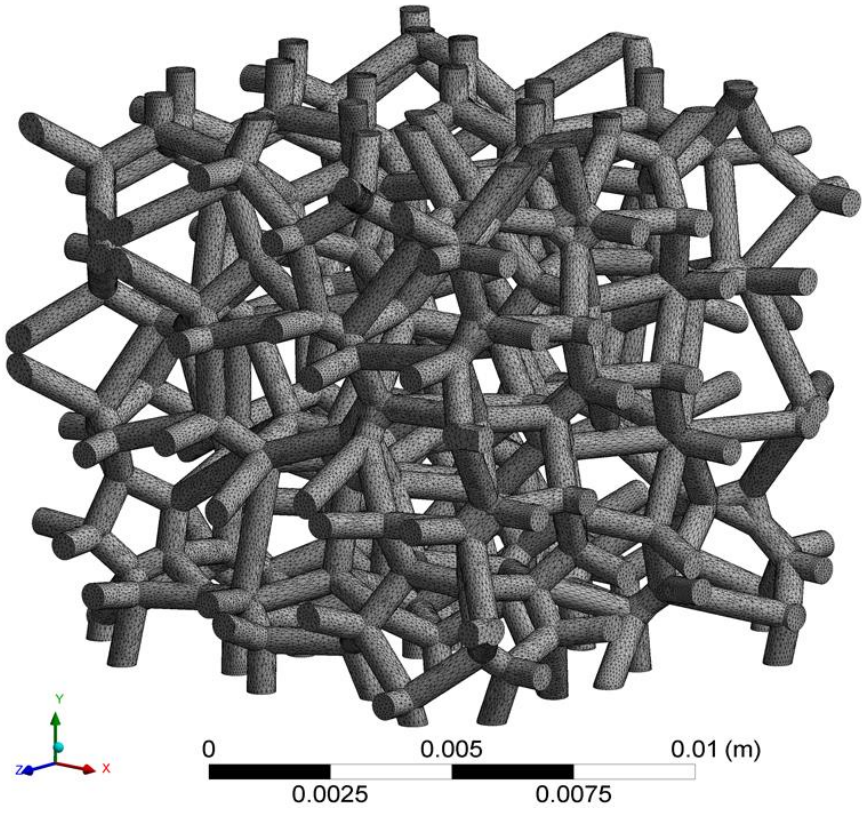

(a)

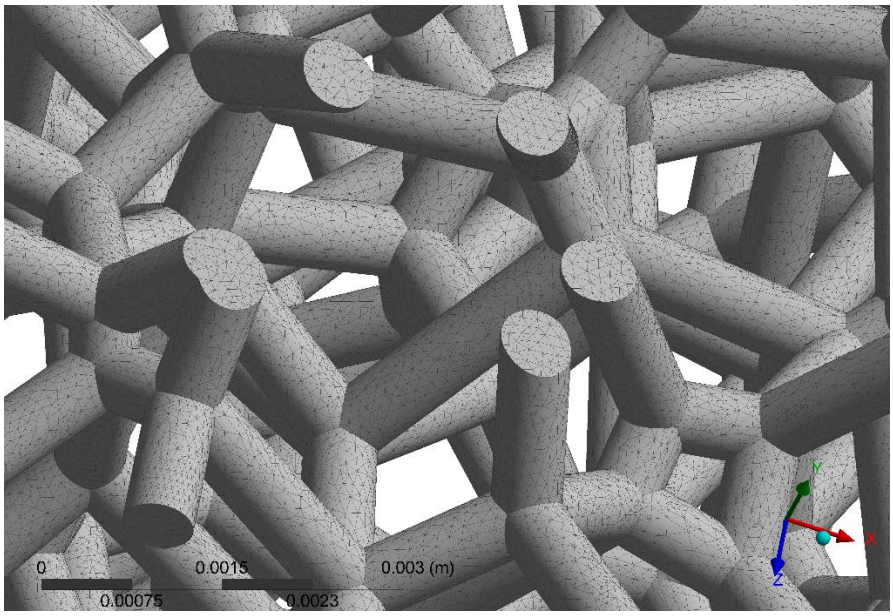

(b)

Figure 4.8 Examples of meshed foam models for finite element analysis

In conclusion, an algorithm is developed and implemented using APDL language (ANSYS software) which includes commands allowing to generate meshed geometry file, define boundary conditions, set solution parameters, calculate results, post-process obtained data and save them into the output file. Based on Chapter 4.2 and 4.3, the procedure of modeling foam structures and subsequent finite element analysis for the investigation of foam structures' elastic properties are depicted in Figure 4.9.

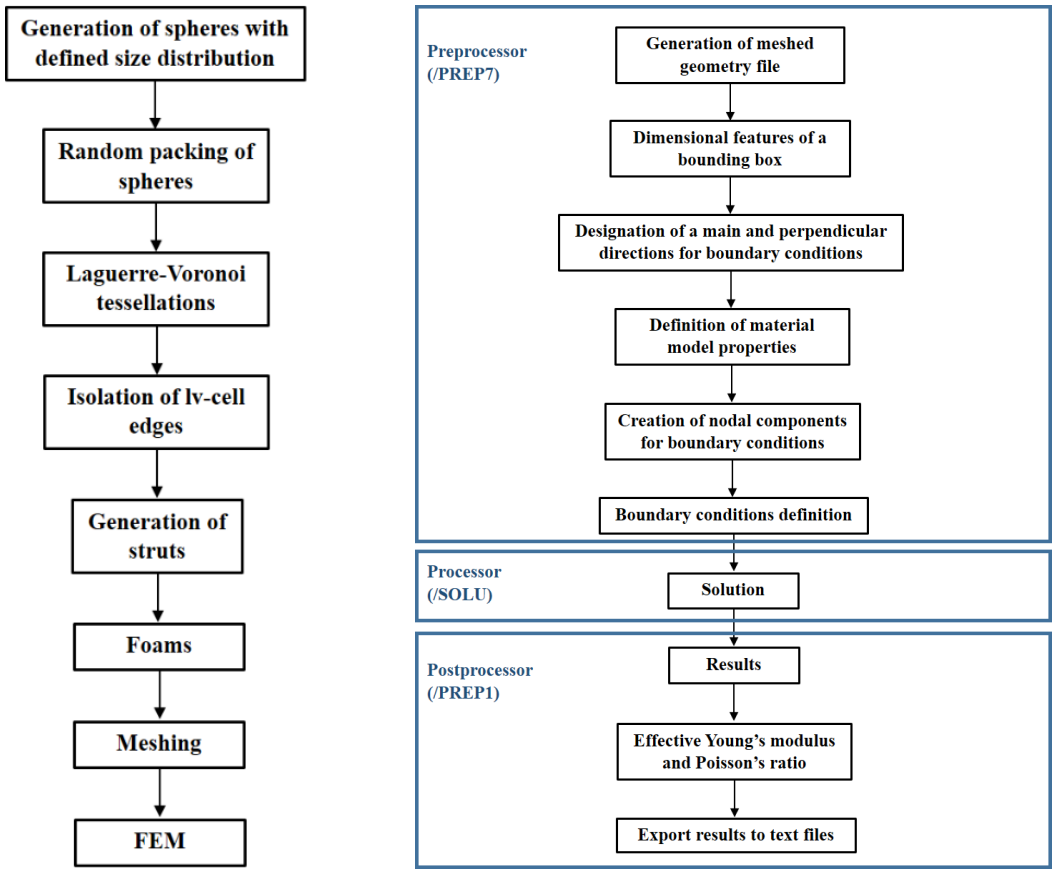

(a) (b)

Figure 4.9 (a) Schematic illustration of procedures for modeling foam structures, and (b) finite element analysis algorithm for investigating elastic properties of foam structures

4.4 Results and discussion

4.4.1 Sensitivity of model size

Before proceeding to model three dimensional foams, an important issue that needs to be considered is to determine the appropriate number of cells to be involved in one model. Since the foam models in this work have random structure, numerical results based on a foam model with only very few cells show too much scatter to draw definitive conclusions on the macroscopic properties. On the other hand, if a foam model consists of

too many cells the computational cost would be too high and be very time-consuming. Therefore, it is necessary to have a trade-off between the number of cells involved in the foam models and repeatable results.

Based on a finite element analysis of random materials using representative volume elements of various sizes, Kanit et al. found that for a given precision the effective elastic properties of the materials can be obtained through using either a large representative volume elements accompanied by a small number of models or a small representative volume elements accompanied by a large number of models [57]. This indicates that the number of models and cells needs to be carefully chosen for accurate predictions. For this part, five different scales of foam models are considered: C-2, C-3, C-4, C-5, and C-6 corresponding to foam specimens with 2 x 2 x 2, 3 x 3 x 3, 4 x 4 x 4, 5 x 5 x 5, and 6 x 6 x 6 cells, respectively. In each model, ten random foam specimens with a porosity of approximate 90% based on five different kinds of commercial alumina ceramic foams: 10 ppi, 20 ppi, 30 ppi, 40 ppi, and 50 ppi, are generated to obtain the mean value and standard deviation of effective elastic properties. The foam specimens are loaded by the uni-axial compression. The corresponding elastic constants such as Young's modulus, Poisson's ratio, and shear modulus can be derived from the initial slopes of the computed stress-strain curves. The obtained numerical results of E_1, E_2, E_3, ν_{12}, ν_{23}, ν_{31}, G_{12}, G_{23}, and G_{31} are drawn in Figure 4.10–Figure 4.12.

From Figure 4.10–Figure 4.12 it can be seen that as the number of cells increases, the mean values of the effective Young's moduli and the effective shear moduli decrease slightly while that of the effective Poisson's ratios remain almost the same. The standard deviations (error bars in Figure 4.10–Figure 4.12) of all properties decrease significantly

with the increase of the number of cells from 8 to 125. When the number of cells is equal to 125, the standard deviation is no more than 5% of the mean value for all properties. Further increases in the number of cells do not result in obvious changes in the values of standard deviation, although small fluctuations (reflecting the random nature of the foam structures) are observed. Therefore, 125-cells is selected as the number of cells to be included in each specimen for further analyses.

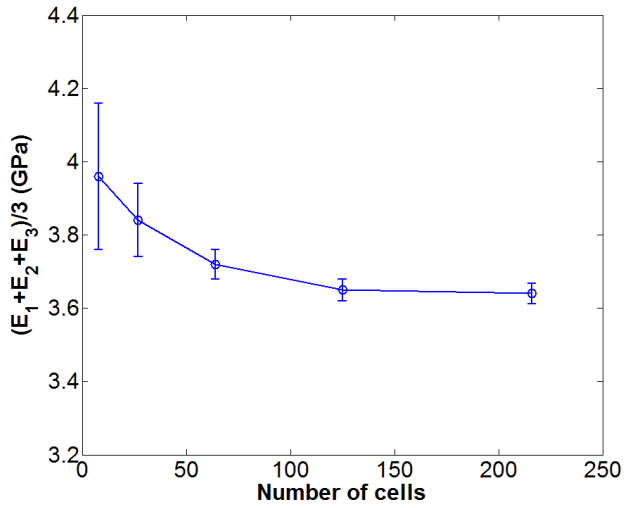

Figure 4.10 Young's modulus vs. the number of cells

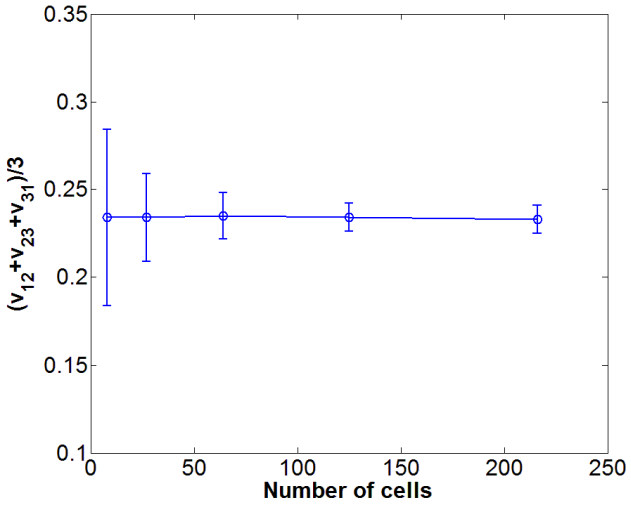

Figure 4.11 Poisson's ratio vs. the number of cells

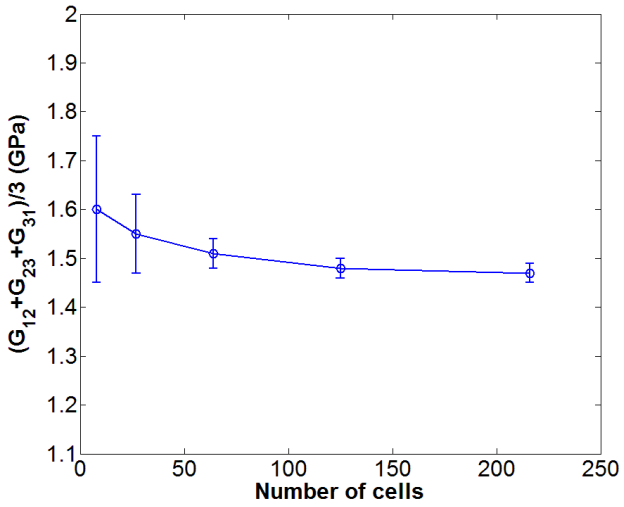

Figure 4.12 Shear modulus vs. the number of cells

4.4.2 Effects of porosity (or relative density)

With the aim of obtaining the definitive mechanical responses of foam models under defined testing in this work, a set of distinct cross-sections in the direction of loading are analyzed as shown in Figure 4.13. Figure 4.14 shows the numerical results of alumina foam models under uni-axial compression loading.

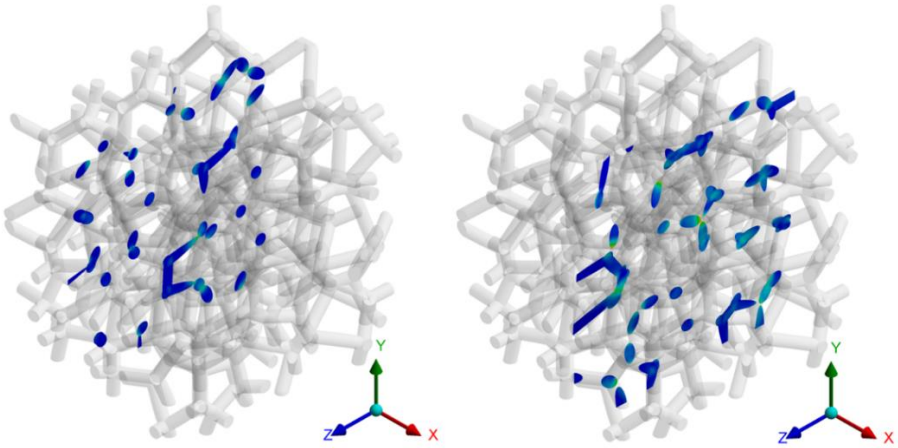

Figure 4.13 Two of distinct cross-sections in the direction of loading: cross-section 4 (left) and 8 (right)

Figure 4.15 shows the numerical results of alumina foam models under bi-axial loading. The overall results of alumina foam model under uni-axial and bi-axial loading are shown in Figure 4.16 and Figure 4.17.

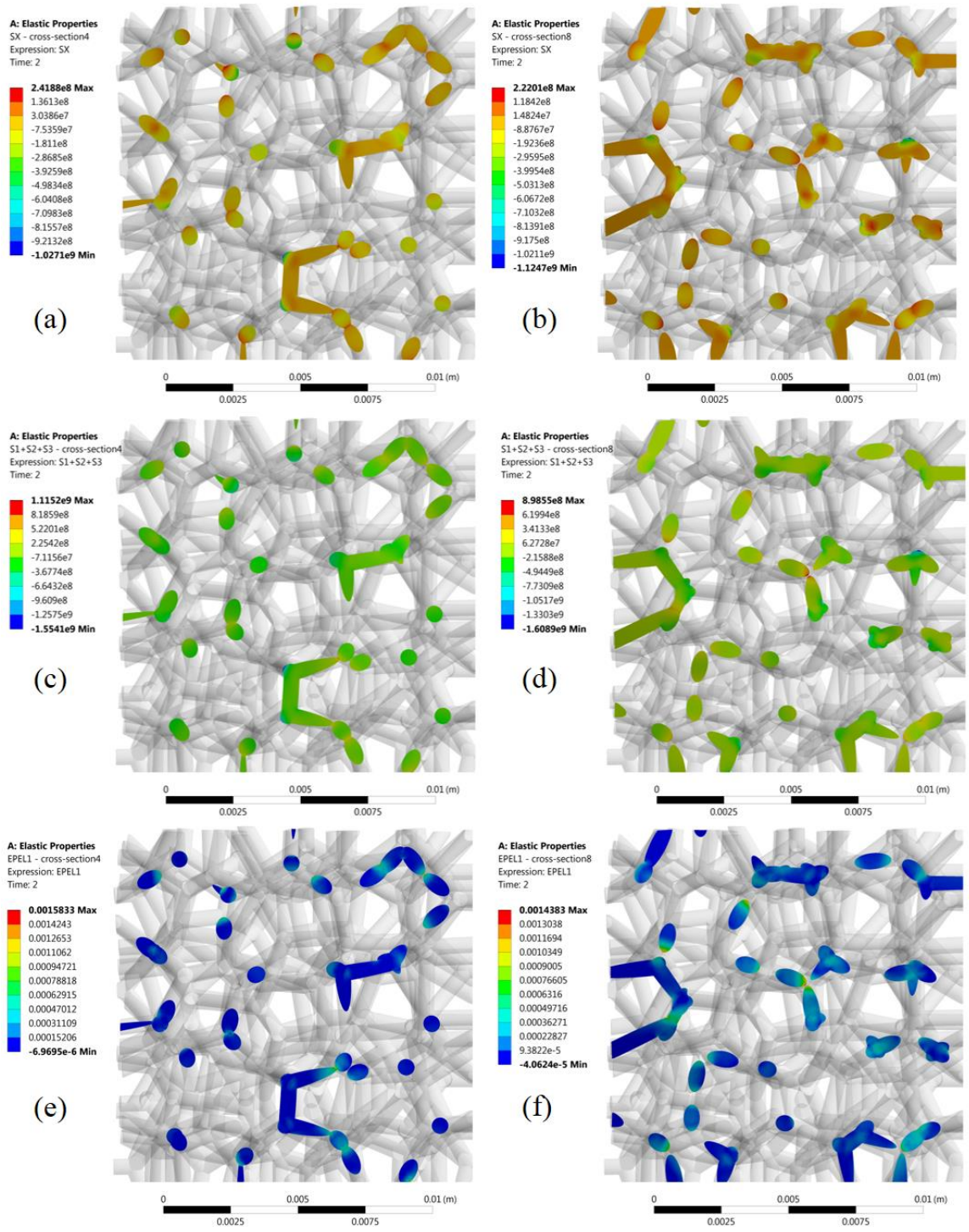

Figure 4.14 Finite element analysis results: (a), (c), and (e) are, respectively, normal stress, total stress, and strain of cross-section 4; (b), (d), and (e) are, respectively, normal stress, total stress, and strain of cross-section 8 under uni-axial loading in x direction

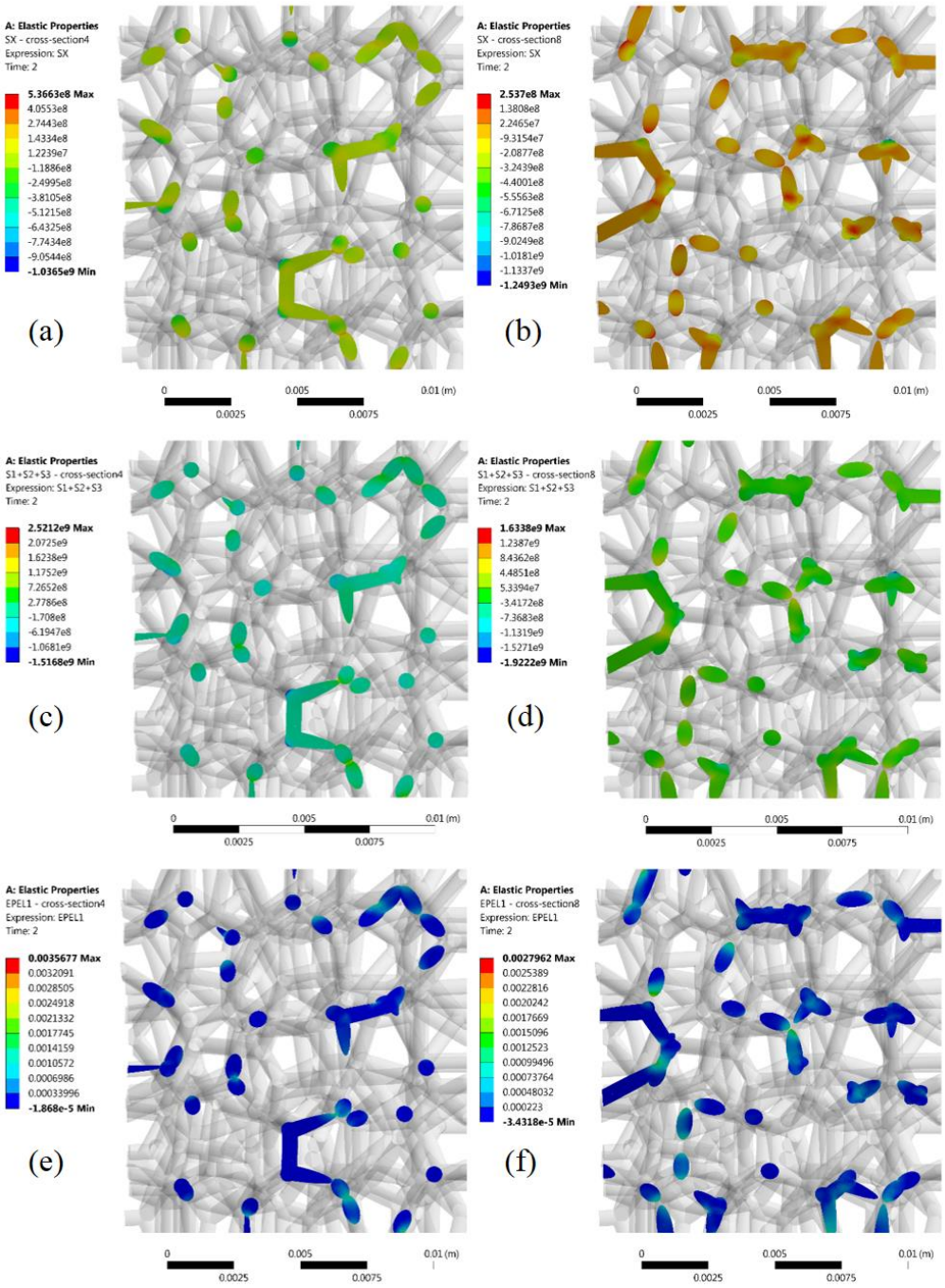

Figure 4.15 Finite element analysis results: (a), (c), and (e) are, respectively normal stress, total stress, and strain of cross-section 4; (b), (d), and (e) are, respectively, normal stress, total stress, and strain of cross-section 8 under bi-axial loading in x and y directions

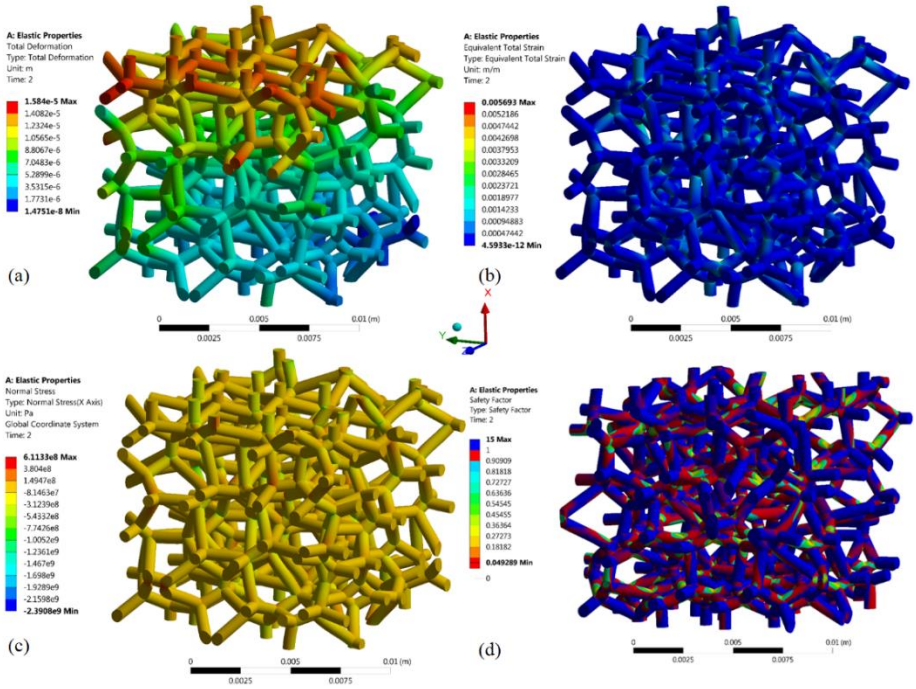

Figure 4.16 Total numerical results of alumina foam models under uni-axial loading: (a) total deformation, (b) equivalent total strain, (c) normal stress, and (d) safety factor

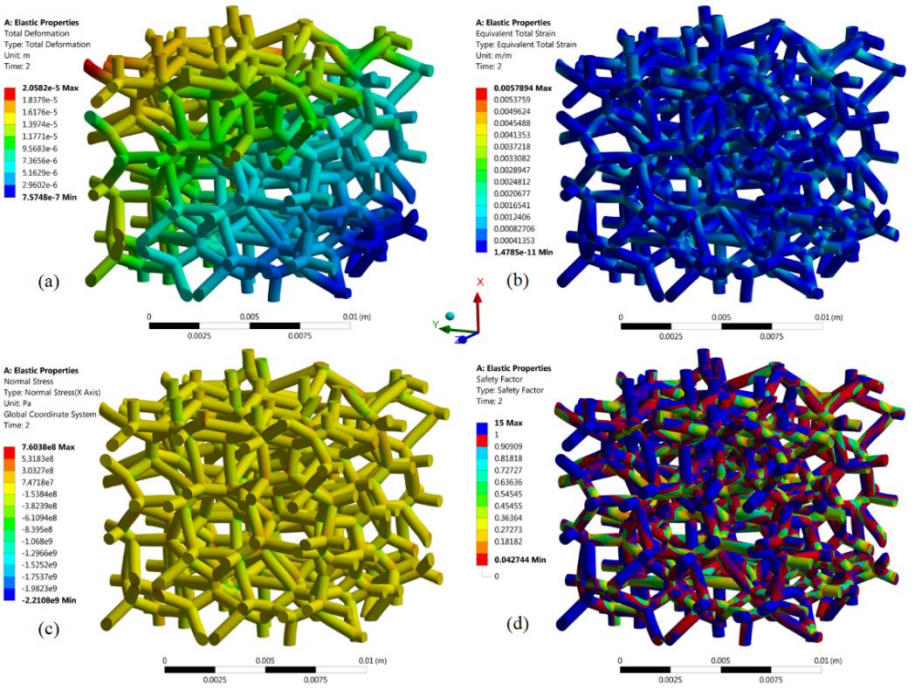

Figure 4.17 Total numerical results of alumina foam models under bi-axial loading: (a) total deformation, (b) equivalent total strain, (c) normal stress, and (d) safety factor

Some of the open cell foam models in the literature are used to compare with the finite element analysis's results. Gibson and Ashby found that Young's modulus and bulk modulus of open cell foams are proportional to the square of relative density and relative density, respectively, using a cubic foam model. Their results indicate that the respective deformation mechanisms of open cell foams under uni-axial and hydrostatic loading are foam struts stretching and bending [8]. This conclusion has been confirmed by others using perfect Kelvin foam model [18-20, 58]. In addition, Zhu et al. have calculated the dependence of elastic constants (i.e., Young's modulus, Poisson's ratio and bulk modulus) of open cell Voronoi foams upon the relative density and showed that the deformation mechanism of Voronoi foams is similar to that of perfect Kelvin foams in the small relative density regime [24]. The effects of the porosity (or relative density) of foam models on its elastic properties of is also considered in this work. Note that in this work the foam models of the same morphological structure but different porosities or relative densities are obtained by varying the radius of the constituent struts of the foam models.

First of these is Warren and Kraynik's theoretical tetrahedral unit cell model developed for linear elastic properties of three dimensional open cell foams [10]. According to this approach, effective compressive elastic constants for uniform struts in a tetrahedral structure are given as:

$$E = \frac{E_s \varphi^2 (11 + 4\varphi)}{(10 + 31 + 4\varphi^2)} \tag{4.12}$$

$$\nu = \frac{(1 - \varphi)(5 + 4\varphi)}{(10 + 31\varphi + 4\varphi^2)} \tag{4.13}$$

where E_s is Young's modulus of solid material that alumina foam is made and φ is the relative density, which is equal to $1 - \varepsilon$, ε is porosity of foams. Relative density is defined

as the volume fraction of the solid material of the foam to total volume of the bulk geometry, $\varphi = \rho/\rho_s$ (see Chapter 3.4). As stated previously the foam material, namely core material, is assumed to be isotropic with Young's modulus E_s and Poisson's ratio ν_s are taken as 370 GPa and 0.22, respectively [53].

Second model for open cell foam obtained by Zhu et al. yields closed form solutions for the elastic constants of Kelvin foams as follows [20]:

$$E = \frac{1.009 E_s \varphi^2}{1 + 1.514\varphi} \tag{4.14}$$

$$\nu = 0.5 \frac{1 - 1.514\varphi}{1 + 1.514\varphi} \tag{4.15}$$

$$G = \frac{0.32 E_s \varphi^2}{1 + 0.96\varphi} \tag{4.16}$$

Another approach taken as a comparison criterion is three dimensional Voronoi models without imperfections developed by Gan et al. [40]. In that study, three dimensional random Voronoi cells are used to obtain mechanical properties of linearly elastic open cell foams where curve fitting to FEM results yields:

$$E = \frac{E_s \varphi^2}{1 + 6\varphi} \tag{4.17}$$

$$\nu = \nu_s + (0.5 - \nu_s) \frac{1 - \varphi}{1 + 14\varphi} \tag{4.18}$$

where ν_s is Poisson's ratio of solid material that alumina foam is made.

The last study used for comparison is Roberts and Garboczi's study, which adopts random Voronoi tessellation technique for the elastic properties of open cell foams [43]. Open cell tessellation model of Roberts and Garboczi is fitted by the formula $E = E_s C(1 - \varepsilon)^n$ which is derived by Gibson and Ashby [8]; the parameters C and n are found

as 0.930 and 2.04, respectively, for the high porosity foams, i.e., $0.9 < \varepsilon < 0.96$. Because constant Poisson's ratio assumption is made through Roberts and Garboczi's study, here this work only use Young's modulus formula which is shown below:

$$E = 0.93E_s\varphi^{2.04} \tag{4.19}$$

The finite element calculated Young's modulus E, Poisson's ratio ν, and shear modulus G for foam models having different porosity values, and the comparison with other researchers' results are drawn in Figure 4.18–Figure 4.20.

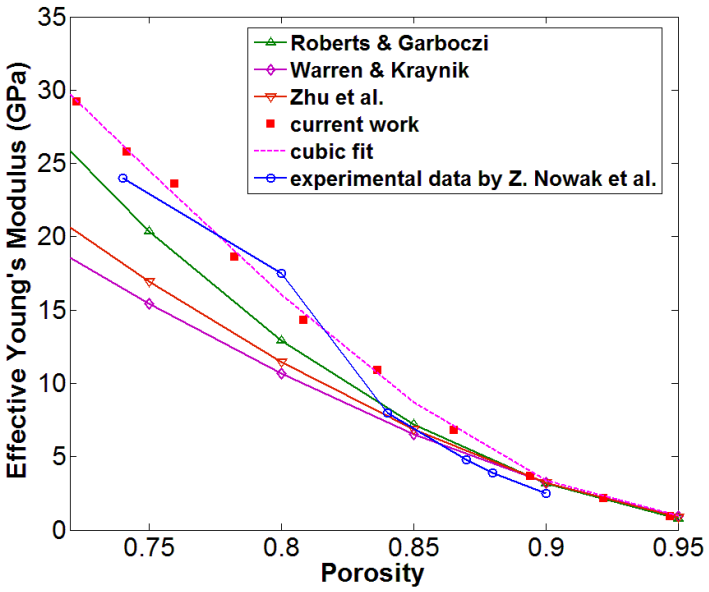

Figure 4.18 Effective Young's modulus variation with porosity

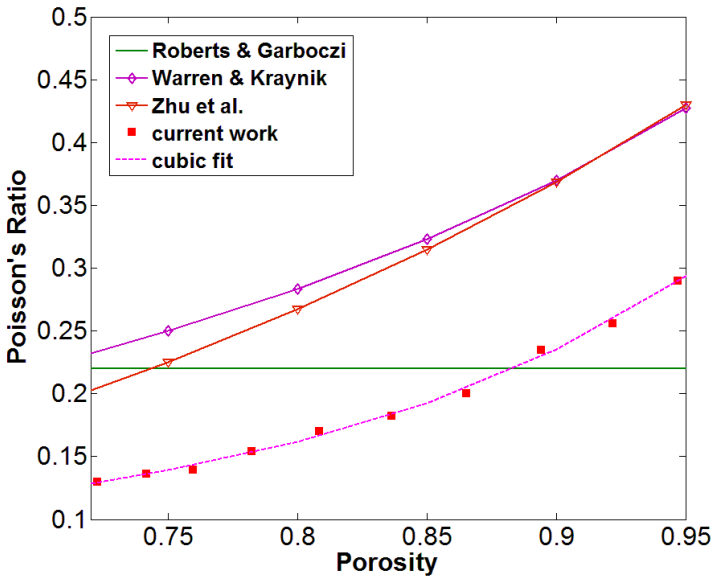

Figure 4.19 Poisson's ratio variation with porosity

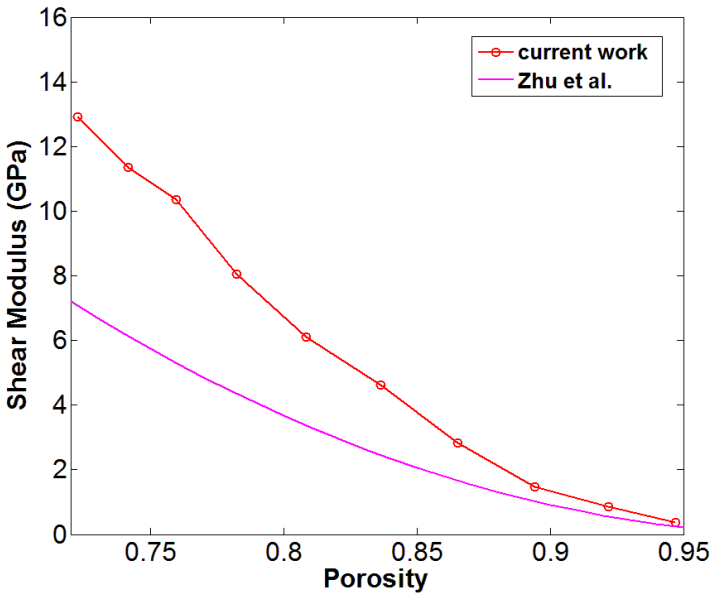

Figure 4.20 Shear modulus variation with porosity

Curve fitting the numerical results yields:

$$E = E_s[3.32(1-\varphi)^3 - 7.37(1-\varphi)^2 + 4.98(1-\varphi) - 0.92] \quad (4.20)$$

$$\nu = \nu_s[20.68(1-\varphi)^3 - 42.09(1-\varphi)^2 + 30(1-\varphi) - 6.91] \quad (4.21)$$

Equations ((4.12)–(4.21) are included in Figure 4.18–Figure 4.20 for the purpose of comparison. It is seen from Figure 4.18 that, in the range of high porosity ($90\% < \varepsilon < 95\%$), results ((4.20) and ((4.21) for alumina foam models developed in current work are close to those of Kelvin foams ((4.12)–((4.19): the discrepancy is normally less than 1%. In addition, Zhu et al. also reported slightly different results for Voronoi foams. Even at very high value of ε (i.e., ε > 96%), they found that the predicted Young's modulus of Voronoi foams is 50% greater than that of Kelvin foams while the bulk modulus of Voronoi foams is about 20% less than that of Kelvin foams. The underlying reason for the difference between the results of Voronoi foams and those of Kelvin foams cannot be readily identified. Also, the results of Laguerre-Voronoi foams in this work is closer to those of Voronoi foams by Robarts and Garboczi than Kelvin cells. Such phenomenon is not hard to understand since Laguerre-Voronoi foams and Voronoi foams, as discussed in Chapter 3, have similar generation algorithm and thus similar foam structure. As seen in Figure 4.18, the results of current work generally are also in a good agreement with the experimental data by Z. Nowak et al., who studied the elastic responses of alumina foams with porosity of 74–90% under compression loadings [53]. For smaller values of ε, however, it can be seen from Figure 4.18 that the Young's modulus of foam models in this work (Equation (4.20)) deviates significantly from that of perfect Kelvin foams (Equation ((4.14)). This could be due to the fact that the current numerical analysis is based on Timoshenko beam theory and can be applied to stout beams, corresponding to foams with moderate or even small values of porosity, whilst the closed form solutions ((4.14)–((4.15)

are based on Euler-Bernoulli beam theory and are thus only suitable for foams with large ε. Furthermore, it should be noted that the struts of real open cell foams with lower porosity (say less than 80%) cannot be simply modeled as uniform beams any more: plateau border effect will predominant in such foams [10, 12]. This might be the major reason that the results for lower porosity in the literature deviates significantly from each other.

From Figure 4.19, it is noted that the Poisson's ratio of this work has a similar trend as another tow theoretical models: tetrahedral cell model by Warren and Kraynik and Kelvin cell model by Zhu et al. However, the amplitude of variation of this work is smaller than those of two theoretical models. Moreover, the Poisson's ratio results of this work are close to the constant assumption of Roberts and Garboczi, i.e., assuming Poisson's ratio as a constant is acceptable. The results of current work can be regarded as a verification for the constant assumption of Poisson's ratio in open cell foams study. As for shear modulus, from Figure 4.20 it is seen that results of the current model are in a good agreement with that of Kelvin cell model by Zhu et al. when porosity is greater than 90%. The shear modulus predictions of these two models have a big difference at low porosity (say <85%).

4.5 Conclusions

The main benefit of this study is that three-dimensional random Laguerre-Voronoi models are developed in ANSYS. The proposed method can generate accurate foam models having randomly distributed parameter values. At the first stage, three dimensional model of ceramic foams having pre-selected cell size distribution with random coordinates and orientations is created via the software package ANSYS. At the second stage, different groups of finite element models are then generated using the developed Laguerre-Voronoi

foam model. The size sensitivity study presents that each of foam specimens at least contains 125 lv-cells.

The developed foam models are used to simulate the macroscopic elastic properties of open cell foams under uni-axial and bi-axial loading and are compared with the existing open cell foam models in the literature. In the high porosity regime, it is found that the elastic properties predicted by random Laguerre-Voronoi foam models are almost the same as those by perfect Kelvin foam models while in the low porosity regime the results of present work deviate significantly from those of other models in the literature. However, the results of current work generally are in a better agreement with experimental data than other models. Thus, the Laguerre-Voronoi foam models generated in this work are quite close to real foam topology and yields more accurate results than other open cell foam models.

REFERENCE

[1] Gibson, L.J. and M.F. Ashby. *The mechanics of three-dimensional cellular materials*. in *Proceedings of the Royal Society of London A: Mathematical, Physical and Engineering Sciences*. 1982. The Royal Society.

[2] Gibson, L.J. and M.F. Ashby, *Cellular solids: structure and properties*. 1999: Cambridge university press.

[3] Stone, R.M., *Strength and stiffness of cellular foamed materials.* 1997.

[4] Nieh, T., K. Higashi, and J. Wadsworth, *Effect of cell morphology on the compressive properties of open-cell aluminum foams.* Materials Science and Engineering: A, 2000. **283**(1): p. 105-110.

[5] Twigg, M.V. and J.T. Richardson, *Theory and Applications of Ceramic Foam Catalysts.* Chemical Engineering Research and Design, 2002. **80**(2): p. 183-189.

[6] Ashby, M.F., et al., *Metal foams: a design guide: Butterworth-Heinemann, Oxford, UK, ISBN 0-7506-7219-6, Published 2000, Hardback, 251 pp., $75.00*. 2002, Elsevier.

[7] Ashby, M.F., et al., *Metal Foams: A Design Guide: A Design Guide*. 2000: Elsevier.

[8] Gibson, L.J., M. Ashby, and C. Solids, *Structure and properties.* Cellular Solids, 1997: p. 307-308.

[9] Banhart, J., *Manufacture, characterisation and application of cellular metals and metal foams.* Progress in materials science, 2001. **46**(6): p. 559-632.

[10] Warren, W. and A. Kraynik, *The linear elastic properties of open-cell foams.* Journal of Applied Mechanics, 1988. **55**(2): p. 341-346.

[11] Triantafyllidis, N. and M. Schraad, *Onset of failure in aluminum honeycombs under general in-plane loading.* Journal of the Mechanics and Physics of Solids, 1998. **46**(6): p. 1089-1124.

[12] Chen, C., T. Lu, and N. Fleck, *Effect of imperfections on the yielding of two-dimensional foams.* Journal of the Mechanics and Physics of Solids, 1999. **47**(11): p. 2235-2272.

[13] Papka, S. and S. Kyriakides, *In-plane biaxial crushing of honeycombs—: Part II: Analysis.* International Journal of Solids and Structures, 1999. **36**(29): p. 4397-4423.

[14] Papka, S. and S. Kyriakides, *Biaxial crushing of honeycombs:—Part 1: Experiments.* International Journal of Solids and Structures, 1999. **36**(29): p. 4367-4396.

[15] Gu, S., T. Lu, and A. Evans, *On the design of two-dimensional cellular metals for combined heat dissipation and structural load capacity.* International Journal of Heat and Mass Transfer, 2001. **44**(11): p. 2163-2175.

[16] Warren, W. and A. Kraynik, *The nonlinear elastic behavior of open-cell foams.* Journal of Applied Mechanics, 1991. **58**(2): p. 376-381.

[17] Gong, L. and S. Kyriakides, *Compressive response of open cell foams Part II: Initiation and evolution of crushing.* International Journal of Solids and Structures, 2005. **42**(5): p. 1381-1399.

[18] Warren, W. and A. Kraynik, *Linear elastic behavior of a low-density Kelvin foam with open cells.* Journal of Applied Mechanics, 1997. **64**(4): p. 787-794.

[19] Warren, W., M. Neilsen, and A. Kraynik, *Torsional rigidity of a plateau border.* Mechanics Research Communications, 1997. **24**(6): p. 667-672.

[20] Zhu, H., N. Mills, and J. Knott, *Analysis of the high strain compression of open-cell foams.* Journal of the Mechanics and Physics of Solids, 1997. **45**(11): p. 1875-1904.

[21] Gong, L., S. Kyriakides, and W.Y. Jang, *Compressive response of open-cell foams. Part I: Morphology and elastic properties.* International Journal of Solids and Structures, 2005. **42**(5-6): p. 1355-1379.

[22] Grenestedt, J.L. and K. Tanaka, *Influence of cell shape variations on elastic stiffness of closed cell cellular solids.* Scripta Materialia, 1998. **40**(1): p. 71-77.

[23] Simone, A. and L. Gibson, *Effects of solid distribution on the stiffness and strength of metallic foams.* Acta Materialia, 1998. **46**(6): p. 2139-2150.

[24] Zhu, H., J. Hobdell, and A. Windle, *Effects of cell irregularity on the elastic properties of open-cell foams.* Acta materialia, 2000. **48**(20): p. 4893-4900.

[25] Li, K., X.L. Gao, and A.K. Roy, *Micromechanics model for three-dimensional open-cell foams using a tetrakaidecahedral unit cell and Castigliano's second theorem.* Composites Science and Technology, 2003. **63**(12): p. 1769-1781.

[26] Sihn, S. and A.K. Roy, *Modeling and prediction of bulk properties of open-cell carbon foam.* Journal of the Mechanics and Physics of Solids, 2004. **52**(1): p. 167-191.

[27] Kırca, M., et al., *Computational modeling of micro-cellular carbon foams.* Finite Elements in Analysis and Design, 2007. **44**(1-2): p. 45-52.

[28] Jang, W.-Y., A.M. Kraynik, and S. Kyriakides, *On the microstructure of open-cell foams and its effect on elastic properties.* International Journal of Solids and Structures, 2008. **45**(7-8): p. 1845-1875.

[29] Alkhader, M. and M. Vural, *Mechanical response of cellular solids: Role of cellular topology and microstructural irregularity.* International Journal of Engineering Science, 2008. **46**(10): p. 1035-1051.

[30] Guessasma, S., et al., *Relating cellular structure of open solid food foams to their Young's modulus: Finite element calculation.* International Journal of Solids and Structures, 2008. **45**(10): p. 2881-2896.

[31] Guessasma, S., *Young's modulus of 2D cellular structures under periodic boundary conditions and subject to structural effects.* Computational Materials Science, 2008. **44**(2): p. 552-565.

[32] Silva, M.J., W.C. Hayes, and L.J. Gibson, *The effects of non-periodic microstructure on the elastic properties of two-dimensional cellular solids.* International Journal of Mechanical Sciences, 1995. **37**(11): p. 1161-1177.

[33] Redenbach, C., *Microstructure models for cellular materials.* Computational Materials Science, 2009. **44**(4): p. 1397-1407.

[34] Thiyagasundaram, P., B.V. Sankar, and N.K. Arakere, *Elastic Properties of Open-Cell Foams with Tetrakaidecahedral Cells Using Finite Element Analysis.* AIAA Journal, 2010. **48**(4): p. 818-828.

[35] Michailidis, N., et al., *Experimental and FEM analysis of the material response of porous metals imposed to mechanical loading.* Colloids and Surfaces A: Physicochemical and Engineering Aspects, 2011. **382**(1): p. 124-131.

[36] Schladitz, K., et al., *Model Based Estimation of Geometric Characteristics of Open Foams.* Methodology and Computing in Applied Probability, 2011. **14**(4): p. 1011-1032.

[37] D'Angelo, C., A. Ortona, and P. Colombo, *Influence of the loading direction on the mechanical behavior of ceramic foams and lattices under compression.* Acta Materialia, 2013. **61**(14): p. 5525-5534.

[38] Wejrzanowski, T., et al., *Modeling structures of cellular materials for application at various length-scales.* Computer Methods in Materials Science, 2013. **13**(4): p. 493--500.

[39] Silva, M. and L. Gibson, *Modeling the mechanical behavior of vertebral trabecular bone: effects of age-related changes in microstructure.* Bone, 1997. **21**(2): p. 191-199.

[40] Gan, Y.X., C. Chen, and Y.P. Shen, *Three-dimensional modeling of the mechanical property of linearly elastic open cell foams.* International Journal of Solids and Structures, 2005. **42**(26): p. 6628-6642.

[41] Shulmeister, V., et al., *A numerical study of large deformations of low-density elastomeric open-cell foams.* Mechanics of Materials, 1998. **30**(2): p. 125-140.

[42] Roberts, A.P. and E.J. Garboczi, *Elastic moduli of model random three-dimensional closed-cell cellular solids.* Acta materialia, 2001. **49**(2): p. 189-197.

[43] Roberts, A.P. and E.J. Garboczi, *Elastic properties of model random three-dimensional open-cell solids.* Journal of the Mechanics and Physics of Solids, 2002. **50**(1): p. 33-55.

[44] Zhu, H. and A. Windle, *Effects of cell irregularity on the high strain compression of open-cell foams.* Acta Materialia, 2002. **50**(5): p. 1041-1052.

[45] Grenestedt, J.L. and F. Bassinet, *Influence of cell wall thickness variations on elastic stiffness of closed-cell cellular solids.* International Journal of Mechanical Sciences, 2000. **42**(7): p. 1327-1338.

[46] Li, J.-q., et al., *Preparation and dielectric properties of porous silicon nitride ceramics.* Transactions of Nonferrous Metals Society of China, 2006. **16**: p. s487-s489.

[47] Li, K., X.L. Gao, and G. Subhash, *Effects of cell shape and cell wall thickness variations on the elastic properties of two-dimensional cellular solids.* International Journal of Solids and Structures, 2005. **42**(5-6): p. 1777-1795.

[48] Li, K., X.L. Gao, and A.K. Roy, *Micromechanical modeling of three-dimensional open-cell foams using the matrix method for spatial frames.* Composites Part B: Engineering, 2005. **36**(3): p. 249-262.

[49] Maruyama, B., et al., *A new technique for obtaining three-dimensional structures in pitch-based carbon foams.* Scripta materialia, 2006. **54**(9): p. 1709-1713.

[50] *<Effects of cell irregularity on the elastic properties of open-cell foams.pdf>*.

[51] Zhou, J., et al., *Design of Mechanical Properties of Open-Cell Porous Materials Based on μCT Study of Commercial Foams.* MATEC Web of Conferences, 2015. **30**: p. 03005.

[52] Zhou, J., et al., *Micro-Computed Tomography and Finite Element Method Study of Open-Cell Porous Materials.* MATEC Web of Conferences, 2015. **30**: p. 03006.

[53] Nowak, Z., et al., *Mechanical Properties Of The Ceramic Open-Cell Foams Of Variable Cell Sizes.* Archives of Metallurgy and Materials, 2015. **60**(3).

[54] Van der Burg, M., et al., *On the linear elastic properties of regular and random open-cell foam models.* Journal of Cellular Plastics, 1997. **33**(1): p. 31-54.

[55] Laroussi, M., K. Sab, and A. Alaoui, *Foam mechanics: nonlinear response of an elastic 3D-periodic microstructure.* International Journal of Solids and Structures, 2002. **39**(13): p. 3599-3623.

[56] Gong, L., S. Kyriakides, and W.-Y. Jang, *Compressive response of open-cell foams. Part I: Morphology and elastic properties.* International Journal of Solids and Structures, 2005. **42**(5): p. 1355-1379.

[57] Kanit, T., et al., *Determination of the size of the representative volume element for random composites: statistical and numerical approach.* International Journal of solids and structures, 2003. **40**(13): p. 3647-3679.

[58] Zhu, H.X., J.F. Knott, and N.J. Mills, *Analysis of the elastic properties of open-cell foams with tetrakaidecahedral cells.* Journal of the Mechanics and Physics of Solids, 1997. **45**(3): p. 319-343.

CHAPTER 5 NUMERICAL INVESTIGATION OF PRESSURE DROP AND HEAT TRANSFER THROUGH OPEN CELL FOAMS

5.1 Introduction

The use of porous structures with high external surface area and continuous three-dimensional cellular structure, as discussed Chapter 3 and Chapter 4, represents an important breakthrough in many industrial applications, especially in catalytic systems. The main advantage of using these porous structures is the high contact area (specific surface area) between the fluid and solid phase and also the low pressure drop along the catalyst bed. One eminent example in chemical engineering is packed beds, which are frequently utilized in catalytic converters and thermal energy storage device [1-4]. However, due to the low porosity (in the range of 30%–60%), packed beds induce a high pressure drop at high flow rates which is detrimental for the operating system, especially when the high space velocity is required for maintaining acceptable selectivity. In addition, the conduction through the packed bed is not perfect since the particles in a packed bed were not well connected with each other but by local contact points; therefore, the effective thermal conductivity of such system is generally low and some heterogeneous temperature zones could be formed inside the catalyst bed [5-8]. It is then of interest to find new support materials which could remediate these drawbacks.

The industrial importance of materials with open cell structures in the form of ceramic or metallic foams, in order to overcome the shortcomings of the conventional packed beds, e.g., spheres and pellets, has grown in recent years. These materials exhibit specific properties such as high specific surface area, high porosity (60%–95%), low

density, favorable mechanical, thermal and corrosion resistance. Thus, they are well suited to serve as compact heat exchangers, reaction catalyst support, flow stabilizers or filters. High porosities enable a considerable reduction of the pressure drop along the catalyst bed even at high flow rates; also, the solid ligaments (or struts) in open cell foams allow the continuous connection of the different catalyst domains which increase the effective thermal conductivity of the entire system without thermal breaking points as occurred in packed beds.

Open cell foams can be manufactured with different geometries and shapes, allowing, for example, the adjustment of axial or radial flow patterns in the reactor. The pore structure of a typical commercial product of foam, as shown in Figure 3.1, evidences a high degree of interconnectivity through the entire matrix of the foam. The small thickness of the struts or wall constituting the foam or monolith can allow the significant reduction of the diffusional phenomena reducing secondary reactions and by-products. In commercial products and industrial applications, open cell foams (ceramic or metallic), in general, are primarily characterized by following parameters: the volumetric porosity denoted by ε, which is defined as the ratio of total void volume to cumulative volume occupied by the solid matrix and void volume; ligament thickness t (which is replaced with the struts diameter d_s in this dissertation) and length l; and the number of pores per linear inch (ppi), as shown in Figure 5.1.

In order to take advantage of these remarkable properties of open cell foams, new reactor or column designs with open cell foams as internals are inevitable [8-12]. In this context, an accurate knowledge or prediction of the pressure drop and heat transfer

properties is essential for a successful design and operation of high performance industrial systems.

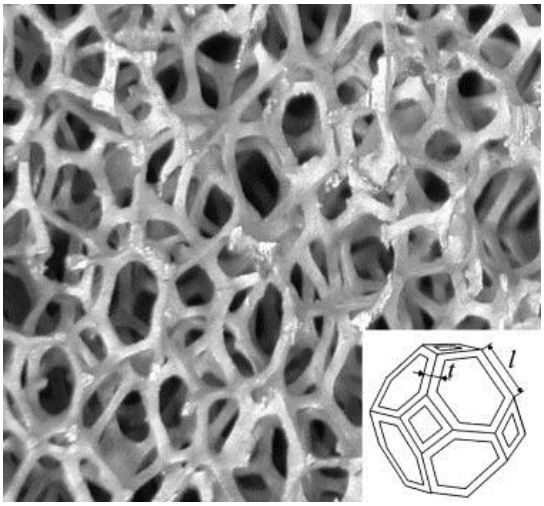

Figure 5.1 Photo of a 10 ppi aluminum foam and Kelvin cell representation of a single cell [13]

During the past decade, therefore, considerable research has been conducted on open-cell foams which has led to a greater understanding of their structure–property relationships and to the development of important correlations. Such correlations are necessary to predict the relevant data which in turn are required for designing the chemical engineering equipment such as, e.g., heat exchangers, reactor, and column with open-cell foams as internals.

Bhattacharya et al. [14] investigated the pressure drop of different aluminum foams, which were inserted in a wind tunnel. The measurements were conducted by using air as the coolant. The 15 tested Aluminum foams presented 5–40 ppi and a porosity that varied between 90.6% and 97%. The experimental results show that the permeability increases with pore diameter and porosity of the medium, while the inertial coefficient depends only on porosity. Moreover, analytical models in agreement with experimental data are

proposed to predict permeability and inertial coefficient. Kim et al. [15] experimentally studied the pressure drops with respect to air flowing in forced convection through six aluminum foams, with 10–40 ppi and porosity from 89% to 96%. A simple correlation to calculate pressure drop is also presented. Paek et al. [16] measured the air flow through metal foams with cell size between 0.65 and 2.50 mm and different porosity from 89% to 96%. They found that at constant porosity the permeability increases as the cell size increases.

Dukhan et al. [17, 18] reported experimental pressure drops for air flowing across nine compressed and uncompressed samples of open-cell aluminum foams with porosity which varies from 68% to 92% and pore density from 10 to 40 ppi. At a constant porosity, the pressure gradient increases as the pores density increases while at constant a pores density, it increases with decreasing porosity. Permeability and inertial coefficient were correlated to the surface area per unit volume and porosity. Crosnier et al. [19] presented the pressure drop with air flowing in 20 and 40 ppi aluminum foam and 20 ppi stainless steel foam using air, with porosities greater than 90%. They stated that the smaller the pore diameter the smaller the permeability and the larger the pressure drop. Permeability and inertial coefficient were functions of the pore size, the surface area, the porosity and the solid structure of the foam. Khayargoli et al. [20] studied the airflow in nickel and nickel–chromium foams, permeability increased and inertial coefficient decreased with increasing the pore size. Topin et al. [21] investigated several foam samples with 10, 40, 60, 100 ppi of copper and nickel with single phase flow of air and water and experimentally determined the permeability and inertial coefficient. Permeability increases with pore diameter while inertial coefficient decreases when pore size and fiber thickness increase. Tadrist et al. [22]

measured the permeability and inertial coefficient of three aluminum foams (10, 20, and 40 ppi). Liu et al. [23] obtained the pressure drop during air flow through seven aluminum foam samples with porosity ranging from 87% to 96% and the pore density from 5 to 40 ppi. They observed that with the similar porosity, the decreasing of pore size increases the pressure drop and also proposed an empirical correlation based on the pressure drops measured by the same authors on aluminum samples and the measurements relative to ceramic foam materials by Richardson et al. [24].

Hwang et al. [25] presented the pressure drops, permeability and inertia coefficient for air flowing in 10 ppi aluminum foams with porosity 70%, 80%, 95%, while Kim et al. [26] measured pressure drop relative to air flowing through FeCrAlY foams, with cell size between 1 and 3 mm and relative density between 4.6% and 12.5%. The experimental data show that higher pressure drops per unit of cell were obtained for foams having smaller porosity and smaller pore diameters. Poulikakos et al. [27, 28] measured the hydraulic performance of compressed and uncompressed aluminum foams using water flowing with maximum frontal velocity of 1.4 m/s. Holding the porosity constant and decreasing the pore size in the uncompressed metal foams, the permeability decreased and the inertial coefficient increased. They also suggested a new numerical approach to model porous media as idealized units of eight cells.

A wide review of available correlations for computing pressure drop during single phase flow in metal foams is presented by Edouard et al. [29] and Mahjoob et al. [30]. In the literature [29], the authors presented that among all correlations those by Lacroix et al. [31], and Du Plessis et al. [32] are more suitable to estimate the pressure drop within foam structures since they do not involve any fitting of the data. Fourie and Du Plessis [33] and

Bhattacharya et al. [14] proposed other equations which do not require experimental coefficients, while correlations based on experimental data relative to air and water flowing in ceramic foams are stated by Richardson et al. [24], Garrido et al. [34], Moreira et al. [35]. For Du Plessis et al. [32] the permeability and the inertia coefficient are complex functions of porosity and pore size. Bhattacharya et al. [14] modified the model of Du Plessis et al. to take into account the variation of the shape of fiber cross section with porosity and to incorporate a correction for the tortuosity of the metal foam samples. Lacroix et al. [31] reported a model which is based on a cubic lattice approach of the foam structure and it is validated by experimental data of air (velocity < 4 m/s) through SiC and Al_2O_3 foams. Other Authors, such as Paek et al. [16], Beavers and Sparrow [36], Hamaguchi et al. [37] and Vafai and Tien [38], developed four different correlations for the prediction of the pressure drops by using the experimental value of the permeability.

Meanwhile, several different research groups have studied both experimentally and analytically the heat transfer characteristics of open cell foams. Lin et al. [39] proposed a simple analytical model to evaluate the utility of metal foams as compact heat exchangers. A cubic unit cell model consisting of slender cylinders as edges was developed to obtain the most important trends of heat transfer due to forced convection, and conduction through cell ligaments of the cellular foam. Calmidi et al. [40, 41] investigated the heat transfer behavior of different aluminum foams that were inserted in a wind tunnel. The measurements were conducted by heating the base of the foam and using air as the coolant. The seven tested aluminum foams presented 5–40 ppi and a porosity that varied between 89% and 97%. They found that the experimental Nusselt number based on the length of the heated section increases with the Reynolds number. Also at a constant number of pores

density, the Nusselt number seems to be higher at high porosity. Hsieh et al. [42] carried out an experimental study to analyze the heat transfer characteristics of several heat sinks made of aluminum metal foams with different porosities (87%–96%) and ppi (10–40). Hsieh et al. experimentally investigated the effect of porosity in heat transfer. In fact, they measured the heat transfer performance of four samples with 20 ppi and different porosities. The Nusselt number based on the length of the test section decreases with the decrease in porosity. At a constant porosity, they found that the heat transfer performance is better at higher ppi number. Kim et al. [43] experimentally studied the heat transfer in forced convection of air across aluminum foams. The authors tested three foams, which presented 10 ppi, 20 ppi, and 40 ppi with a constant porosity of 92%. The authors found that at constant Reynolds number, the heat transfer performance is improved by changing the pores density from 10 to 40 ppi. Moreover, Boomsma et al. [28] tested several different metal foam heat exchangers during liquid flow and they compared the results with the performance of several commercially available units. The porous heat exchangers presented thermal resistances lower than the commercially available heat sinks while requiring the same pumping power. Finally, Boomsma and Poulikakos [27] investigated the effective thermal conductivity of a three-dimensionally structured metal foam saturated with liquid.

Most of the research in the literature on heat transfer through open cell foams has been focused on single phase flow. Similarly, a majority of the literature views foam structures as an alternative extended surface (i.e., fins) using air as the coolant. Examples of experimental studies on forced convection of air through metal foams include those by Younis and Viskanta [44], Hwang et al. [25], Hsieh et al. [42], Duckhan and Chen [45],

Garrido et al. [46, 47], Mancin et al. [6, 7, 9], and Zhao [11]. Among these work, Mancin et al. [9] published the heat transfer measurements performed for forced convection of air through multiple copper foam samples. The samples investigated consisted of ppi values in the range 5–40, and porosity values in the range 90.5%–93.4%. The effect of different structural parameters of open cell foams on the global heat transfer coefficient, normalized mean wall temperature, pressure gradient, permeability, inertia coefficient, and drag coefficient were discussed. Zhao [11] provided a review of several thermal transport mechanisms in open cell foams including conduction, forced convection, natural convection, thermal radiation, as well as pool boiling and flow boiling heat transfer. Very few researchers had focused on detailed heat transfer analysis at the pore scale, either by numerical or experimental approaches.

However, the recent literature shows that the state-of-the-art correlations for predicting the heat transfer and pressure drop properties of open cell foams lack general applicability and therefore need improvement. After reviewing the literature, it is believed that one of the main sources of deviation for most correlations is the use of empirical coefficients. Since these coefficients are usually determined for a limited set of data, they are not suitable for extrapolation to a wider range of porosity, pores density, and/or working fluids, thus causing a considerable deviation from measured pressure drop data.

Hence, further research is definitely needed in this area in order to come up with correlations featuring enhanced applicability. In this regard, the focus of the present work is to address the problem of pressure drop prediction in open cell foams, thereby achieving a higher level of accuracy and reliability. This work presents a universal correlation for pressure drops of open cell foams based on theoretical grounds and the tortuosity of foams

is taken into account for the pressure drop. Then a numerical study of pressure drops for different open cell ceramic foams of pore densities between 10 ppi and 50 ppi, of porosities from 70% to 95%. Permeability and friction factor of foams are also evaluated and the computed interstitial heat transfer coefficients are investigated. Furthermore, the presented pressure drop correlation provides a simple method for determining hydraulic diameters for open cell foams with unknown geometric parameters (strut, window and pore diameter, etc.) based on pressure drop simulations. A correlation is derived the hydraulic diameter from the number of pores per inch (ppi). Final, this work states that it is possible to perform computational design for open cell foams with defined flow properties using the Laguerre-Voronoi model developed in Chapter 3 and Chapter 4 of this work.

5.2 Theoretical background

Ergun et al. studied the fluid flow through randomly packed beds and proposed the definition of friction factor to calculate the pressure drop of packed beds [48, 49]. According to [48, 49], there have been two main approaches for developing friction factor expressions for packed columns. In one method the packed bed is visualized as a bundle of tangled tubes of weird cross section; the theory is then developed by applying the results for single straight tubes to the collection of crooked tubes. In the second method the packed bed is regarded as a collection of submerged objects, and the pressure drop is obtained by summing up the resistances of the submerged particles. The tube bundle theories have been somewhat more successful, and this work discusses them here. Figure 5.2 depicts a packed bed column.

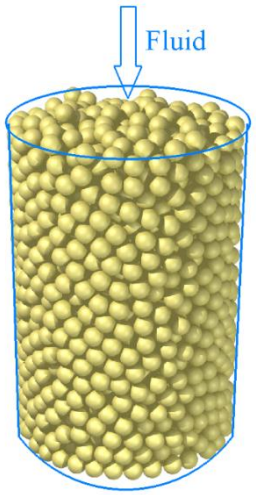

Figure 5.2 A cylindrical tube packed with spheres

A number of materials could be used for the packing in beds: spheres, cylinders, and so forth. It is assumed throughout the following discussion that the packing is statistically uniform, so that "channeling" is ignored (in actual situations, channeling frequently occurs, and then the development given here does not consider the channeling). It is further assumed that the diameter of the packing particles is small in comparison to the diameter of the bed in which the packing is contained and that the bed diameter is uniform.

Byron Bird et al. defined the friction factor for the packed bed by the following equation [50]:

$$f = \frac{1}{4}\left(\frac{D_p}{L}\right)\left(\frac{P_0 - P_L}{\frac{1}{2}\rho v_0^2}\right) \tag{5.1}$$

where L is the length of the packed bed, D_p is the mean particle diameter, $P_0 - P_L$ is the pressure drop, and v_0 is the superficial velocity, which is equal to the volume flow rate divided by the void cross section of the bed, $v_0 = w/\rho S$.

The pressure drop between two ends of a representative tube in the tube bundle model is given by the following equation [50]:

$$P_0 - P_L = \frac{1}{2}\rho\langle v\rangle^2 \left(\frac{L}{R_h}\right) f_{tube} \tag{5.2}$$

where the friction factor for a single tube, f_{tube}, is a function of the Reynolds number $Re_h = 4R_h\langle v\rangle\,\rho/\mu$, and $\langle v\rangle$ is the average velocity in the tube [50]. Substituting this pressure difference into Equation (5.1) yields

$$f = \frac{1}{4}\frac{D_p}{R_h}\frac{\langle v\rangle^2}{v_0^2} f_{tube} = \frac{1}{4\varepsilon}\frac{D_p}{R_h} f_{tube} \tag{5.3}$$

In the second equation, the void fraction, ε, is the fraction of space in the bed not occupied by the packing. Then $v_0 = \langle v\rangle\varepsilon$, which results from the definition of the superficial velocity mentioned above [50].

The hydraulic radius can be expressed in terms of the void fraction ε and the wetted surface s per unit volume of bed as follows:

$$R_h = \left(\frac{\text{cross section available for flow}}{\text{wetted perimeter}}\right) = \left(\frac{\text{volume available for flow}}{\text{total wetted surface}}\right)$$

$$= \left(\frac{\text{volume of voids}}{\text{volume of bed}}\right) \Big/ \left(\frac{\text{wetted surface}}{\text{volume of bed}}\right)$$

$$R_h = \frac{\varepsilon}{s} \tag{5.4}$$

The quantity s is related to the specific surface S_V (total particle surface per volume of particles) by

$$S_V = \frac{s}{1-\varepsilon} \tag{5.5}$$

The quantity is also used to define the mean particle diameter D_p as follows:

$$D_p = \frac{6}{S_V} \tag{5.6}$$

This definition is selected since, for spheres of uniform diameter, D_p is exactly the diameter of a sphere. From the Equations (5.4), (5.5), and (5.6), it is obvious that the hydraulic radius is $R_h = D_p\varepsilon/6(1-\varepsilon)$ [50]. Substituting it into Equation (5.3) yields

$$f = \frac{3}{2}\left(\frac{1-\varepsilon}{\varepsilon}\right) f_{tube} \tag{5.7}$$

This results can be applied to laminar and turbulent flows by finding out appropriate expressions for f_{tube}.

(a) For laminar flow, $f_{tube} = 16/Re_h$ [50]. This is exact for circular tubes only. To consider the non-cylindrical surfaces and tortuous fluid paths encountered in typical packed bed operations, it has been found that replacing 16 by 100/3 allows the tube bundle model to describe the packed bed data. When this modified expression for the tube friction factor is substituted, Equation (5.7) becomes

$$f = \frac{(1-\varepsilon)^2}{\varepsilon^3}\frac{75}{\left(D_p G_0/\mu\right)} \tag{5.8}$$

in which $G_0 = \rho v_0$ is the mass flux through the system, and μ is the dynamic viscosity of fluid. Substituting Equation (5.8) into Equation (5.1) obtains

$$\frac{P_0 - P_L}{L} = 150\left(\frac{\mu v_0}{D_p^2}\right)\frac{(1-\varepsilon)^2}{\varepsilon^3} \tag{5.9}$$

which is the Blake-Kozeny equation [50]. Equations (5.8) and (5.9) are generally good for $(D_p G_0/\mu\,(1-\varepsilon)) < 10$ and for porosities less than $\varepsilon = 0.5$.

(b) For highly turbulent flow a treatment similar to the above expression can be given. This case can be analyzed with the expression for the friction factor definition for flow in a circular tube. For highly turbulent flow in tubes with any appreciable roughness,

however, the friction factor is a function of the roughness only and is not dependent on the Reynolds number. If it is assumed that the tubes in all packed beds have similar roughness characteristics, then the value of f_{tube}, may be taken to be the same constant for all systems. Taking f_{tube} = 7/12 proves to be an acceptable choice [50]. When this is substituted into Equation (5.7), f is given by

$$f = \frac{7}{8}\frac{1-\varepsilon}{\varepsilon^3} \tag{5.10}$$

Substituting Equation (5.10) into Equation (5.1) gets

$$\frac{P_0 - P_L}{L} = \frac{7}{4}\left(\frac{\rho v_0^2}{D_p}\right)\frac{1-\varepsilon}{\varepsilon^3} \tag{5.11}$$

which is the Burke-Plummer equation, valid for $(D_p G_0/\mu\,(1-\varepsilon)) > 1000$ [50]. Note that the dependence on the porosity is different from that for laminar flow.

(c) For the transition region, a superpose of the pressure drop equations for (a) and (b) above is applied to obtain

$$\frac{P_0 - P_L}{L} = 150\left(\frac{\mu v_0}{D_p^2}\right)\frac{(1-\varepsilon)^2}{\varepsilon^3} + \frac{7}{4}\left(\frac{\rho v_0^2}{D_p}\right)\frac{1-\varepsilon}{\varepsilon^3} \tag{5.12}$$

For very small v_0, this simplifies to the Blake-Kozeny equation, and for very large v_0, to the Burke-Plummer equation. Such empirical superposition of asymptotes often leads to satisfactory results [50]. Equation (5.12) can be rewritten to dimensionless forms [50]:

$$\frac{(P_0 - P_L)\rho}{G_0^2}\frac{D_p}{L}\left(\frac{\varepsilon^3}{1-\varepsilon}\right) = 150\frac{1-\varepsilon}{D_p G_0/\mu} + \frac{7}{4} \tag{5.13}$$

This is so-called Ergun equation, which is shown in Figure 5.3 along with the Blake-Kozeny and Burke-Plummer equations and experimental data. It has been applied with success to gas flow through packed beds by using the average density of the gas at the

arithmetic average of pressures [50]. Here G_0 is constant through the bed, whereas v_0 changes through the bed for compressible fluids. For large pressure drops, however, it seems more appropriate to apply Equation (5.12) locally by expressing the pressure gradient in differential form [50].

The Ergun equation is but one of many that have been proposed for describing packed bed. In the literature, many authors have adopted Ergun-type equation for deriving correlations for pressure drop prediction in foam structures. Foam-like structures are viewed as an inverse of bed-like structures where solid particles are substituted by pores. They usually replace particle diameter, D_p, with the equivalent hydraulic diameter, d_h. An extensive review of pressure drop correlations for foams was provided by Edouard et al. [29]. All presented formulae are based on the Darcy-Forchheimer relation. The Darcy-Forchheimer equation (5.14) have been broadly applied to evaluate the permeability and pressure drop of both packed beds and open cell foams.

$$\frac{\Delta P}{L} = \frac{\mu}{k_1} v + \frac{\rho}{k_2} v^2 \tag{5.14}$$

in which $\Delta P/L$ is the average pressure gradient, μ, ρ and v are the dynamic viscosity, density and velocity of the fluid, and the coefficients k_1 and k_2 are called viscous and inertial permeabilities, respectively. These permeabilities should be functions of beds' or foams' geometry.

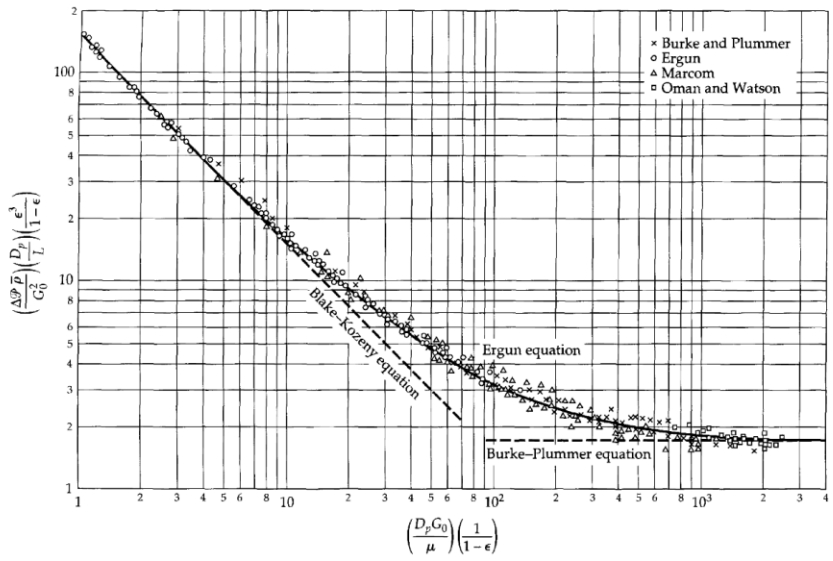

Figure 5.3 The Ergun equation for flow in packed beds, and the two related asymptotes, the Blake-Kozeny equation and the Burke-Plummer equation [50]

The Darcy-Forchheimer equation is a general relation pressure drop in porous media. Although obtained empirically by Forchheimer, it can be shown that in emerges form a proper averaging of the Navier-Stokes equations and it can actually be applied to various kinds of porous structures like packed beds of spheres, rings, or virtually any other structures.

Additionally, varying numerical constants preceding the geometry dependent coefficients are often used. This kind of general correlation was proposed by Gibson and Ashby [51]:

$$\frac{\Delta P}{L} = \alpha \frac{(1-\varepsilon)^2}{\varepsilon^3 S_V^2} \mu U + \beta \frac{(1-\varepsilon)}{\varepsilon^3 S_V} \rho U^2 \tag{5.15}$$

where the characteristic dimension is the reciprocal of the specific surface area, S_V. This formula was used by Richardson et al. [24], where a series of high porosity ($\varepsilon > 90\%$)

alumina foams of ppi number in range from 10 to 65 were investigated. They verified a few specific relations between S_V and the mean pore diameter, d, and selected the one presented by Kozeny [52] for packed beds of particles. The pore diameter was found from the image analysis of slices of the foam structures. The coefficient α and β were fitted to the experimental data and became functions of porosity and mean pore diameter.

5.3 Analytical pressure drop for open cell foams

From the discussion in the last section, it is noted that in the open literature there are many pressure drop correlations for open cell foams, however, none of them exhibits a general applicability. Edouard et al. [29] reviewed state-of-art correlations for pressure drop prediction in foam structures. They reported that the standard deviation between experimental data and theoretical values of the pressure drop can be as high as 100%. Garrido et al. [46] evaluated pressure drop correlations from the literature by comparing the predictions with their own experimental data. It was concluded that the prediction of all of the correlations from the literature was not satisfactory. In order to develop a general pressure drop correlation for open cell foams completely based on theoretical analysis that allows for the prediction of pressure drop only based on easily measurable geometric foam properties and which thus possesses an improved adaptability and applicability, this work begins with the basic Hagen-Poiseuille equation. Consider an empty tube of length L and inner diameter D, as shown in Figure 5.4. The pressure drop for laminar fluid flow through this tube can be given according to the Hagen–Poiseuille equation [3, 53]:

$$\frac{\Delta P}{L} = 32 \frac{\mu}{d_h^2} v \tag{5.16}$$

in which d_h is the equivalent hydraulic diameter (4 × cross-sectional area available for flow/wetted perimeter).

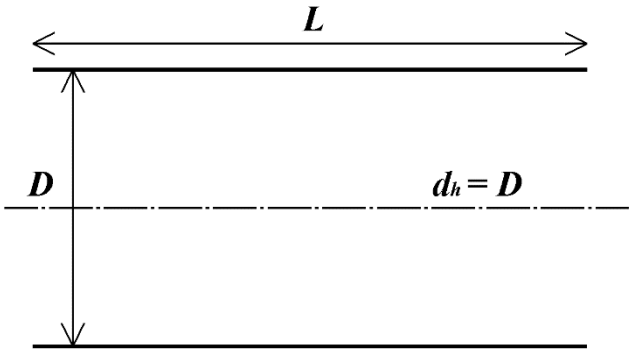

Figure 5.4 An empty tube of length *L* and diameter *D*

As mentioned in the last section, a considerable amount of work has been done in correlating data for porous media. It is found that for fluid flow at low velocities, viscous forces account for the pressure drop within the accuracy of measurement, whereas for higher velocities, kinetic effects become more important and the pressure drop appears to vary with some power of the velocity, the exponent ranging between 1 and 2 [48]. At high velocities, however, kinetic effects do not alone account for the pressure drop without the aid of factors which in turn are functions of flow rate [48].

The transition from the dominance of viscous to kinetic effects, for most packed systems, is smooth, indicating that there should be a continuous function relating pressure drop to flow rate. A general relationship may be developed using the Kozeny assumption that the porous media is viewed as a bundle of tangled tubes of weird cross-sections, as shown in Figure 5.5, such that the total specific surface area, open porosity, and hence the hydraulic diameter are equal to that of the open cell foam. Therefore, for higher flow

velocities, a term for kinetic energy losses which proposed by Brillouin [48] for capillary flow might be added to the above equation to get

$$\frac{\Delta P}{L} = 32\frac{\mu}{d_h^2}v + \frac{1}{2}\frac{\rho}{d_h}v^2 \tag{5.17}$$

This equation, like many others that relate pressure drop to polynomials of the fluid flow rate, differs from them in that the coefficients have definite theoretical significance.

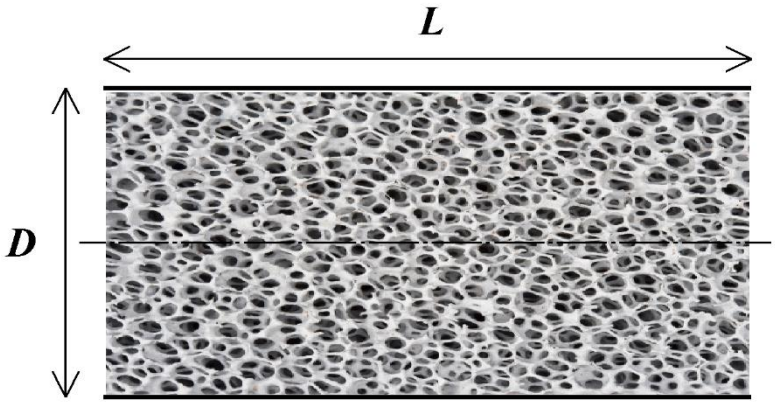

(a)

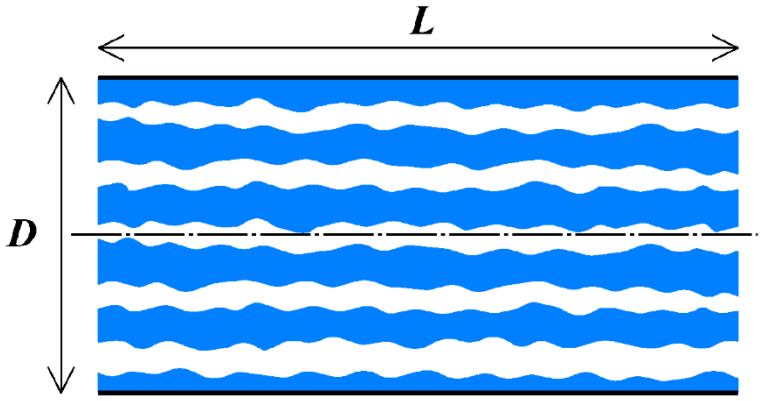

(b)

Figure 5.5 (a) An open cell foam packed in a tube of length *L* and diameter *D* and (b) a schematic of a tube bundle model for the packed foam in (a)

For an open cell foam packed in a tube, the flow path is complicated and sinuous and the streamlines frequently diverge and converge. The kinetic losses, which occur only once for the capillary, vary with a frequency that is statistically related to the sinuousness of the flow path. For these reasons, a correction factor must be applied to Equation (5.17). This factor may be designated as τ, which is called tortuosity [3]. Equation (5.17) becomes

$$\frac{\Delta P}{L} = 32\tau \frac{\mu}{d_h^2} v + \frac{1}{2}\tau \frac{\rho}{d_h} v^2 \tag{5.18}$$

or

$$\frac{\Delta P}{\tau L} = 32 \frac{\mu}{d_h^2} v + \frac{1}{2} \frac{\rho}{d_h} v^2 \tag{5.19}$$

The first term in Equation (5.18) is called the viscous term, and the second is identified as the inertial term. The hydraulic diameter of the open cell foam is obtained by:

$$d_h = 4 \cdot \frac{\text{cross section available for flow}}{\text{wetted perimeter}} = 4 \cdot \frac{A_f}{U} \cdot \frac{L}{L} = 4 \cdot \frac{V_f}{S} \cdot \frac{V}{V} = \frac{4\varepsilon}{S_V} \tag{5.20}$$

where A_f is cross section available for flow, U is the wetted perimeter; V_f is volume available for flow; S is total wetted surface; V is the volume of the open cell foam; ε is the porosity of the open cell foam; and S_V is the specific surface area of the open cell foam.

In the open cell foam packed in a tube, as discussed above, the fluid has to flow through a complicated and tortuous path covering a longer distance L_t compared to the straight path L. Moreover, the velocity is not the same as that of the straight tube but higher, designated as v'. Taking these facts into consideration, Equation (5.19) can be translated for open cell foam as follows:

$$\frac{\Delta P}{L_t} = 32 \frac{\mu}{d_h^2} v' + \frac{1}{2} \frac{\rho}{d_h} v'^2 \tag{5.21}$$

The tortuous distance L_t depends on the tortuosity of the flow which in turn should depend on the structural or geometrical properties of the open cell foam packed in the tube and can be calculated as follow [3]:

$$L_t = \tau L \tag{5.22}$$

in which L is the straight path length of the tube and L_t the tortuous length: $L_t = L +$ additional path length due to the tortuosity.

Based on the work of Carman [54], the velocity of a fluid through a porous medium of open porosity ε and tortuosity τ can be expressed by

$$v' = \frac{v}{\varepsilon}\tau \tag{5.23}$$

Taking the definitions of velocity and tortuosity above, Equation (5.21) can be rewritten as follows:

$$\frac{\Delta P}{L} = 32\tau^2 \frac{\mu}{\varepsilon d_h^2} v + \frac{1}{2}\tau^3 \frac{\rho}{\varepsilon^2 d_h} v^2 \tag{5.24}$$

Equation (5.24) could depict the pressure drop for fluid flow cross the porous media packed in a tube, for example, an open cell foam and is independent of any empirical coefficients.

The concept of tortuosity for porous media was first proposed by Kozeny [52], who pointed out that for the fluid flow in a porous medium of length L, the actual path L_t covered by a fluid element is greater than L, which is due to the tortuosity of the flow path (see Equation (5.22)). Sobieski et al. [55] stated that, when a fluid flows cross a porous medium of length L, there are numerous (and not only one) possible channels. Each of these channels features a path length of L_i, thus giving a (microscopic) tortuosity of L_i/L. This would result in multiple (microscopic) tortuosities, and the overall tortuosity L_t/L

would then be the average value of all microscopic tortuosities. This overall tortuosity is difficult to determine directly under most situations. However, one can consider an imaginary channel which has the same fluid conducting property as the sum of all microscopic channels. In the following contents, a similar method is utilized to derive a correlation for the overall tortuosity of open cell foams.

According to the basic definition of tortuosity (5.22) can be rewritten as follows:

$$\tau = \frac{L_t}{L} = \frac{L + \text{additional length}}{L} \tag{5.25}$$

Now consider the tube shown in Figure 5.4. The properties of the tube with respect to the internal diameter could be calculated by the following formulae as shown in Table 5.1. Accordingly, the tortuosity of the empty tube is $\tau_{\text{empty}} = L/L = 1$.

Table 5.1 Formulae for tube's geometric properties

Property	Formula
Surface area, S	πDL
Volume, V	$\pi D^2 L/4$
Specific surface area, S_V	$4/D$
Dimensionless specific surface area, DS_V	4

For open cell foams of open porosity ε packed in a tube as shown in Figure 5.5(a), the overall tortuosity τ can be obtained by

$$\tau = \frac{L + L'}{L} = 1 + \frac{L'}{L} \tag{5.26}$$

in which L' is the additional length of the flow path due to the tortuosity of the open cell foam. By transforming Equation (5.26) one could get the following equation:

$$\tau = 1 + \frac{\pi DL'/V}{\pi DL/V} = 1 + \frac{\pi DL'/V}{4/D} = 1 + \frac{D(\pi DL'/V)}{4} \tag{5.27}$$

Here, the additional path length L' is confined in the effective free volume of the open cell foam (with a porosity of ε) which in turn is placed into the tube with a total internal volume of V. Therefore, in Equation (5.27), in order to consider the effective free volume, V is replaced by $V\varepsilon$. Furthermore, the effective pore size will be reduced from the tube's internal diameter to some average pore size of open cell foams. According to Inayat et al. [56, 57], the predominant size for tortuosity and hence pressure drop of open cell foams is not average pore size d, or average strut diameter d_s, but the average window size d_w, as shown in Figure 5.6, since a window is an opening into the cell and serves as a medium for cell-to-cell communication. The average window size d_w is determined by converting the average area of the square and hexagonal windows to an equivalent circle, as explained in Figure 5.6. In order to determine the areas, the dimensions of the square and hexagonal windows (accessible from top, bottom, and sides of the foam samples) could be measured with a vernier caliper. Also, magnified digital images of the foam samples could be analyzed by the software *DatInf measure*. In some researches [31, 58, 59], d_w is obtained by Equation (5.28) if only the cell diameter is known. This equation also is used by some foam manufacturers to give customers the approximate window diameter for their products.

$$d_w = \frac{d}{2.3} \tag{5.28}$$

Then Equation (5.27) can then be written as follows:

$$\tau = 1 + \frac{d_w(\pi d_w L'/V)}{4\varepsilon} \tag{5.29}$$

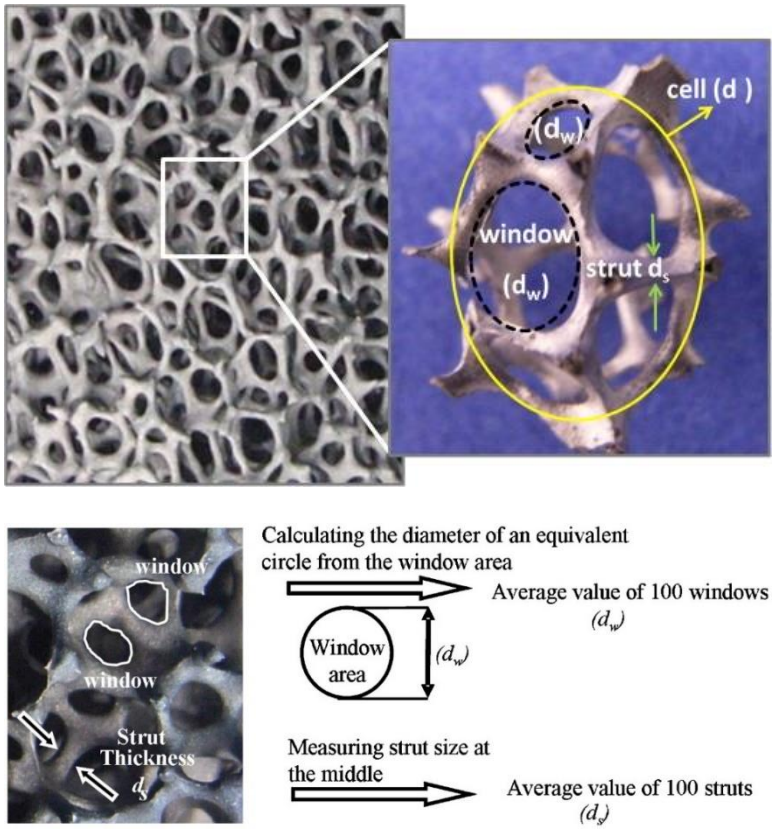

Figure 5.6 Calculation of the average window size of open cell foams [3, 60]

Assume L' is the length of an imaginary tube whose surface area $\pi d_w L'$ is equal to the surface area of the open cell foam, then $d_w(\pi d_w L'/V)$ should be equal to the dimensionless specific surface area of the open cell foam. Hence, Equation can be written as:

$$\tau = 1 + \frac{\text{dimensionless}(S_V)}{4\varepsilon} \tag{5.30}$$

This equation could give the overall tortuosity of an open cell foam packed in a tube. The overall tortuosity depends on the open porosity and specific surface area of the open cell foam. Note that the tortuosity given in Equation (5.30) represents the tortuosity of the fluid path inside the open cell foam. For the calculation of the tortuosity, an imaginary tube with

the same fluid flow capacity as that of the open cell foam has been assumed and its specific surface area is equal to that of the open cell foam. Therefore, the additional path L' for the fluid flow resulted from the porous structure is dependent on the struts of the open cell foams and calculated by the inverse dimensionless hydraulic diameter which is second term in Equation (5.30).

S_V can be determined by applying mathematical correlations using easily measurable structural parameters of open cell foams, for instance, open porosity, strut diameter, and window diameter, etc. In the open literature, there are many correlations available to calculate the specific surface area. Most of them, however, do not have the accurate estimates as compared to the experimental data.

As for the Kelvin cell discussed in this work, the specific surface area can be directly obtained via Equation (3.20): $S_V = 4(1-\varepsilon)/d_s$. Inayat et al. [60] proposed a theoretical correlation for calculating the strut diameter with the window diameter and open porosity of open cell foams, as shown in Equation (5.31). This work gives a close agreement to the experimental data from the open literature. The conclusions stated by Inayat et al. [60] also were confirmed by other researchers [61, 62].

$$d_s = \frac{0.6164 d_w (1-\varepsilon)^{0.5}}{1 - 0.971(1-\varepsilon)^{0.5}} \tag{5.31}$$

Substituting Equation (5.31) into Equation (3.20) yields

$$S_V = 6.489 \frac{1 - 0.971(1-\varepsilon)^{0.5}}{d_w (1-\varepsilon)^{0.5}} (1-\varepsilon) \tag{5.32}$$

Here d_w is the window diameter of the open cell foam mentioned above. The dimensionless S_V , i.e. $d_w(S_V)$ obtained from Equation (5.32) is substituted into Equation (5.30) to get the following equation:

$$\tau = 1 + 1.622\frac{1 - 0.971(1-\varepsilon)^{0.5}}{(1-\varepsilon)^{0.5}}\frac{(1-\varepsilon)}{\varepsilon} \tag{5.33}$$

Some other authors also presented mathematical expressions to predict the tortuosity of porous structures. Most of them are derived from the cubic unit cell model and defined as

$$\tau = \frac{L_t}{L} \equiv \frac{\text{void volume}}{\text{minimum free area perpendicular to the flow direction}} \tag{5.34}$$

Obviously, this definition does not consider the effect of the internal specific surface area of the tube in which the open cell foam is packed. Furthermore, as discussed in Chapter 4 of this work, the cubic unit cell model may not be suitable for open cell foams since this model overestimates the specific surface area and the pressure drop [29]. Also, it is not easy to define and determine so-called minimum free area perpendicular to the fluid flow direction for open cell foams. Thus, it is not recommended using the cubic unit cell model to calculate the pressure drop in open cell foams. In order to compare the result of this work with other results in the open literature, the overall tortuosity curves are plotted in Figure 5.7.

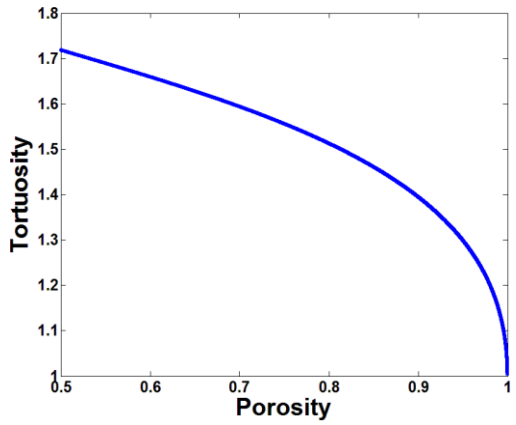

Figure 5.7 Tortuosity vs. open porosity

Equation (5.24) can be rewritten as

$$\frac{\Delta P}{L} = C_1 \frac{\mu}{\varepsilon d_h^2} v + C_2 \frac{\rho}{\varepsilon^2 d_h} v^2 \tag{5.35}$$

so that the coefficients of viscous C_1 and inertia C_2 terms with respect to hydraulic diameter are given as

$$C_1 = 32\tau^2 \tag{5.36}$$

$$C_2 = \frac{1}{2}\tau^3 \tag{5.37}$$

Although the form of Equation (5.35) is similar to that of correlations reported in the open literature, the important difference is that C_1 and C_2 are not empirical values. They are derived on the theoretical grounds of fluid flow in a tube and are functions of structural properties of the open cell foam. From Equation (5.35), it also can be noted that for very small velocity v, it could be simplified to only have the viscous term, $C_1 \frac{\mu}{\varepsilon d_h^2} v$, and for very large v, it could be simplified to the inertial term, $C_2 \frac{\rho}{\varepsilon^2 d_h} v^2$. Leva et al. reported that in packed tubes, when the flow velocity is low, the viscous forces are predominant, and the pressure drop is proportional to $(1-\varepsilon)^2/\varepsilon^3$; whereas, at higher flow velocities, the inertial forces are dominant and the corresponding dependence on $(1-\varepsilon)/\varepsilon^3$ [48]. Equation (5.35) has a similar form to the pressure drop correlation for packed tubes, but not exactly expected from that of packed tubes. Furthermore, it can be observed that Equation (5.35) has a universal form which is independent on the material and geometrical factors of foams, but dependent on the properties of fluids. Therefore, Equation (5.35) could be applied to all kinds of open cell foams similar to those investigated in this work.

The dimensionless forms for the velocity and pressure drop of the open cell foam are Reynolds number, Re, and Hagen number, Hg, respectively. The Reynolds number and Hagen number are introduced as given in Equations (5.38) and (5.39).

$$Re = \frac{d_h v}{\varepsilon \nu} \tag{5.38}$$

$$Hg = \frac{\Delta P}{L} \frac{d_h^3}{\rho \nu^2} \tag{5.39}$$

Here ν is kinematic viscosity, $\nu = \mu/\rho$. Then the dimensionless form of Equation (5.35) becomes

$$Hg = C_1 Re + C_2 Re^2 \tag{5.40}$$

From the process of derivation above, the developed correlation Equation (5.35) or (5.40) has a universal form independent of structural properties and materials of open cell foams. Therefore, this correlation possesses the adaptability and applicability for different working fluids for a wide range of Reynolds numbers and for a wide range of pore sizes, porosities, and materials of open-cell foams. For comparison purposes, different methods of calculating the coefficients of viscous and inertia terms for open cell foams from the literature are shown in Figure 5.8.

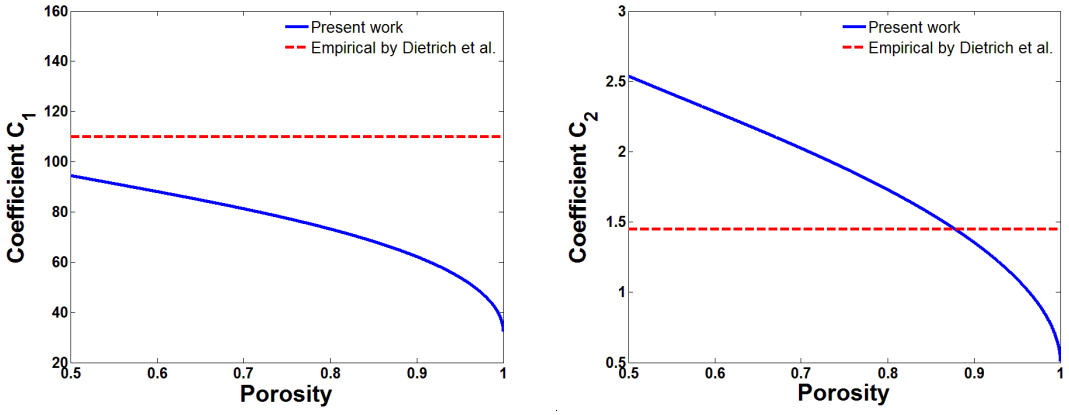

(a) (b)

Figure 5.8 A comparison of coefficients of (a) viscous and (b) inertial terms

5.4 Numerical model

In order to verify the correlation proposed in the last chapter, fluid flow simulations are performed using Finite Volume Method in this work. The procedure of modeling three dimensional open cell foam structures is developed in Chapter 4.2 and Chapter 4.3. Foam structures are created using Laguerre-Voronoi tessellation (LVT). LVT is applied to spheres with specified size distribution, which are packed in the cuboid volume. The foam struts are created by cylinders with defined constant diameter generated along cell edges, as shown in Figure 5.9. The structure presented in Figure 5.9 can be successfully applied to the calculation of flow and thermal properties of open cell foams. In this chapter, the study is performed over structures of pores density (10, 20, 30, 40, and 50 ppi), porosity (70, 75, 80, 85, 90, 95%), and flow velocity (0.5, 1–10, 12, 14, 16, 18, 20 m/s). They are systematically varied for a total of 480 simulations. The resulting Reynolds number based on the hydraulic diameter is included in the range 50–10000.

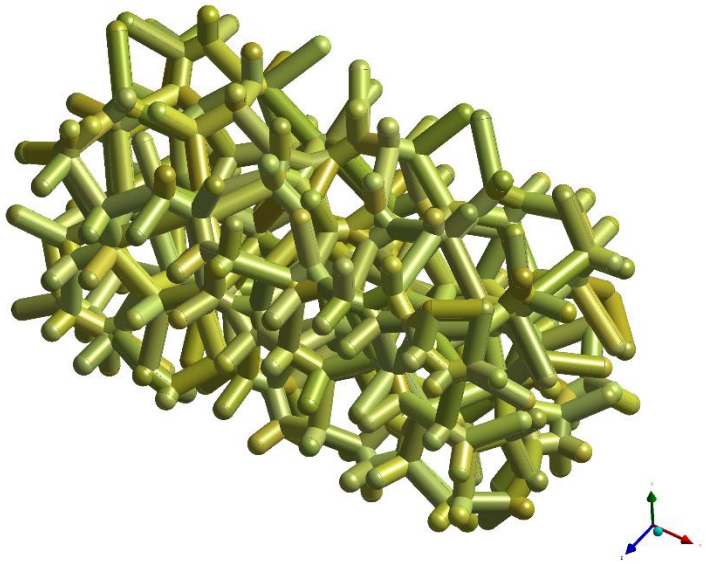

Figure 5.9 An open cell foam structure generated by LVT for flow simulations

To study flow and thermal phenomena through open cell foams, the volume constructed from struts must be subtracted from the box. The results of the subtracted operation can then be meshed and simulated as a fluid field. Subtracted operation can be performed in software DesignModeler. The generated foam structures are then imported into another meshing tool in order to build the discretized computational domains for ANSYS Fluent. The meshing procedure is proved to be very challenging because of the complexity of the foam structures, which needs an unstructured grid generation algorithm. A high level of refinement is necessary to capture the intricate features of the structure and to ensure a good resolution of the flow boundary layer next to the foam struts.

Meshing a complex volume would place a significant demand on memory during meshing operation. The meshes thus produced would need huge computational resources for numerical analysis of fluid flow and heat transfer. Therefore, in this work only smaller

regions are considered for meshing operation. Furthermore, the length of the open cell foams in the flow direction has effects on simulations since a not fully developed flow may produce incorrect results. To ensure a fully developed flow conditions in the numerical simulations, the foam must have an adequate number of pores in the flow direction. Diani et al. [1] reported a sensitivity analysis to determine the number of pores that is necessary for obtaining the fully developed flow. The reported simulations were analyzed on the 40 ppi sample with fluid domains having different number of pores along the flow direction but the same boundary conditions and fluid properties. The difference in the pressure gradient was determined on computational domains consisting of 5, 10, and 20 pores in the flow direction. It was observed that the differences in the pressure gradient between the 5 pores and the 10 pores sized domains was -15.7%, whereas between the 10 pores and 20 pores sized domains, the difference was only -3.2%. Thus, a domain size of approximately 10 pores in the flow direction is considered sufficient for attaining fully developed fluid flows.

At a constant mesh element size, and considering computational domains with 10 pores along the flow direction, the number of mesh elements directly depends on the number of pores density of the open cell foam; the number of mesh elements increases when pores density increases since the pore size decreases, and vice versa. The total mesh count ranges from $6.0 - 15 \times 10^6$ cells. Mesh independence is attained when an average mesh length scale of $0.01d$ (d is pore diameter) is employed. The computational domain is defined as a square duct consisting of an undisturbed inlet and outlet region and an intermediate section containing the foam structure. The computational domain in this work is meshed in ICEM CFD. Figure 5.10 shows an example of meshing in ICEM CFD.

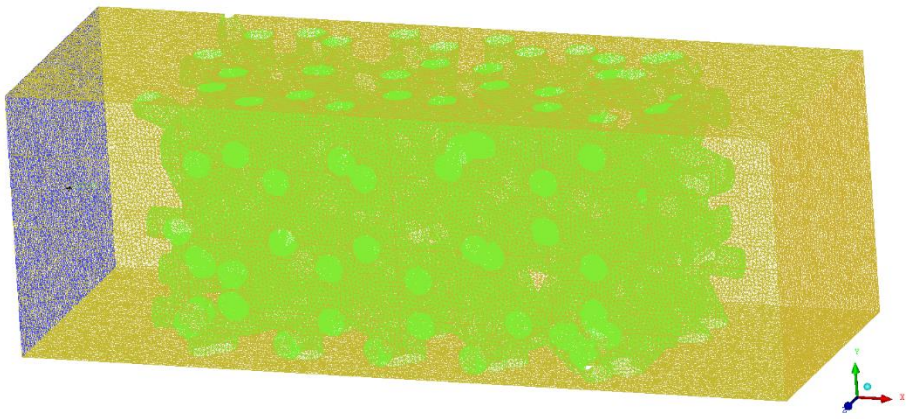

Figure 5.10 An example of meshing in ICEM CFD

Diani et al. [63] studied the pressure drop for the flow of air through the copper foams by solving the continuity and momentum equations directly on the pore-scale control volume. In this work, the analysis is extended to solve for heat transfer. The equation for conservation of mass in a control volume is defined as

$$\frac{\partial \rho}{\partial t} + \nabla(\rho \vec{v}) = S_m \tag{5.41}$$

in which ρ is the fluid density and $\vec{v}$ is the velocity vector and S_m is a source term which accounts for added mass to the continuous phase from dispersed second phase or/and any other user-defined sources. Equation (5.41) is the general form of the mass conservation equation and is valid for both incompressible and compressible fluids.

The conversation of momentum in a static reference frame is given by

$$\frac{\partial \rho \vec{v}}{\partial t} + \nabla(\rho \vec{v} \vec{v}) = -\nabla p + \nabla(\vec{\sigma}) + \rho \vec{g} + \vec{F} \tag{5.42}$$

in which p is the static pressure, $\vec{\sigma}$ is the stress tensor, $\rho \vec{g}$ and $\vec{F}$ are the gravitational and body force and external body forces terms, respectively. The stress tensor is defined as

$$\vec{\sigma} = \mu\left[(\nabla\vec{v} + \nabla(\vec{v})^T) - \frac{2}{3}\nabla\vec{v}I\right] \tag{5.43}$$

in which μ is the fluid dynamic viscosity, I is the unit tensor and the second term on the right hand side accounts for the effect of volume dilation.

The governing equation for heat transfer is given by

$$\frac{\partial}{\partial x_i}\left(\rho v_i c_p T\right) = \frac{\partial}{\partial x_i}\left(\lambda\frac{\partial T}{\partial x_i}\right) \tag{5.44}$$

where v_i represents velocity in the i-direction, c_p is specific heat, λ is fluid thermal conductivity, and T is fluid temperature. These governing equations are based on the three dimensional steady-state Reynolds Average Navier-Stokes equations. They are solved using the finite volume commercial software ANSYS Fluent, using a first-order upwind difference scheme for flow and energy calculations. The SIMPLE scheme is utilized for pressure-velocity coupling, and the flow domain is deemed converged when the absolute values of all residuals fall below 1.0×10^{-6} for the flow calculations, and below 1.0×10^{-8} for the energy calculations.

As depicted in Figure 5.11, the following boundary conditions are employed:

(1) velocity-inlet boundary condition with a specified temperature 300 K at the inlet of the fluid domain (y-z plane at x minimum);

(2) pressure-outlet boundary condition with a gauge pressure $p = 0$ at the outlet of the fluid domain (y-z plane at x maximum);

(3) symmetric boundary conditions on the lateral sides of the domain (x-y plane at z maximum, x-y plane at z minimum, x-z plane at y maximum, and x-z plane at y minimum); and

(4) the foam surface is assumed to be perfectly smooth with a no-slip boundary condition and constant heat flux 10 $\mathrm{kW/m^2}$ at the interface between the solid and fluid domain.

A constant heat flux boundary condition represents an ideal condition in which the foam finned surface efficiency is equal to 1. The air is used as the fluid in the simulation, which is assumed to be a Newtonian fluid having a constant density and viscosity. The density and viscosity of the air are 1.225 $\mathrm{kg/m^3}$ and 1.7894×10^{-5} $\mathrm{Pa \cdot s}$, respectively. The next section states the details of results obtained, as well as a comparison with the proposed correlation and experimental data.

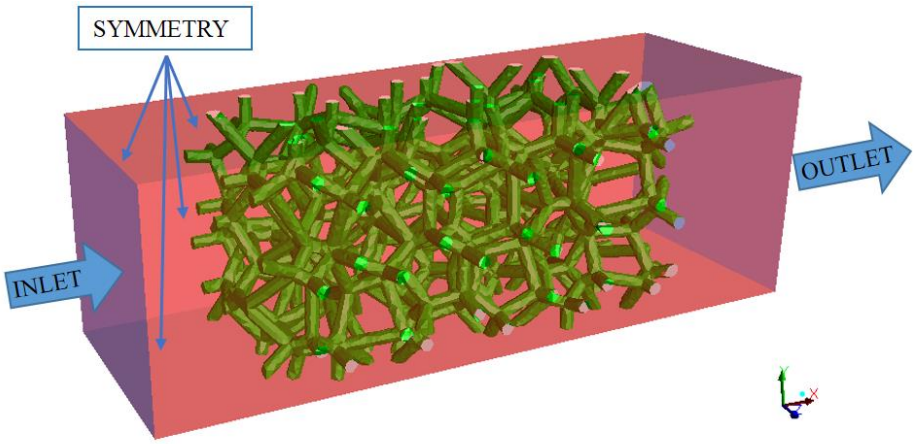

Figure 5.11 Boundary conditions employed in this work

5.5 Results and discussion

The visualization of the velocity field, temperature field, and pressure field inside foam structures investigated in this work are shown in Figure 5.12–Figure 5.15. Figure 5.12 shows the velocity field contours and temperature field contours for the cases of an inlet velocity of 2.0 m/s and imposed heat flux of 10 $\mathrm{kW/m^2}$ for 10 ppi foam with six

different porosities: 70%, 75%, 80%, 85%, 90%, and 95%. Velocity contours and temperature contours are shown in Figure 5.13 for the cases of different velocities from 2 m/s to 20 m/s and imposed heat flux of 10 kW/m^2 in a cross section for 10 ppi-80% foams. The struts of metal foams act as obstacles to the flow, homogenizing the fluid flow and temperature field. The fluid is well mixed through foams because of the tortuous nature of the three dimensional foam structures. There are many local hot spot temperatures presenting in the regions downstream of struts, which correspond to stagnant zones with low air velocities; however, even though the maximum air temperature can rise up to a higher value, the mean air temperature can keep a lower one due to the mixing induced by such enhanced surfaces, as can be seen in Figure 5.12 and Figure 5.13.

Details of the flow field of an inlet velocity of 2 m/s for foams with the same porosity 80% and five different pore densities of 10 ppi, 20 ppi, 30 ppi, 40 ppi, and 50 ppi are given in Figure 5.14. From the velocity contours of Figure 5.14, it can be seen that at every strut flow fluid is separated and accelerated through the pores apertures, where high velocity streaks show the flow passing through the narrowest passages. The overall pressure change has an apparent linear behavior, however, the complex structure of pores causes a complex pressure distribution inside the foam and stagnation areas are observed in front of the struts. Figure 5.15 shows the details of the velocity contours inside the 30 ppi-80% foam at three different cross sections.

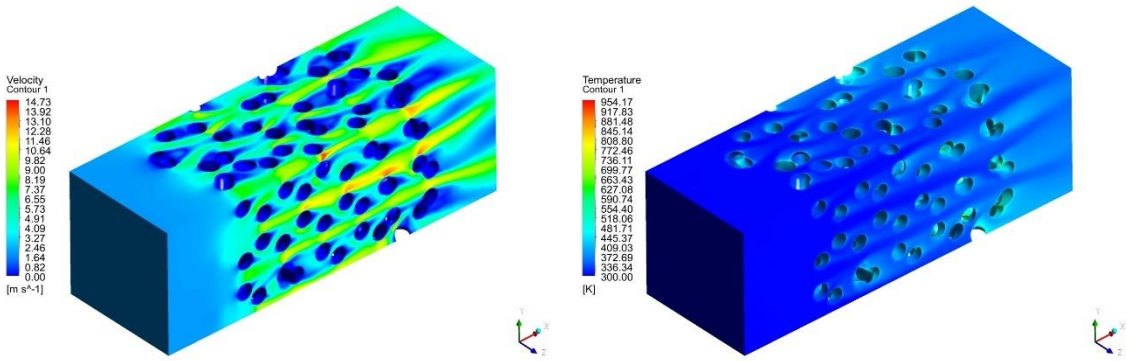
Velocity
Contour 1
14.73
13.92
13.10
12.28
11.46
10.64
9.82
9.00
8.19
7.37
6.55
5.73
4.91
4.09
3.27
2.46
1.64
0.82
0.00
[m s^-1]
Temperature
Contour 1
954.17
917.83
881.48
845.14
808.80
772.46
736.11
699.77
663.43
627.08
590.74
554.40
518.06
481.71
445.37
409.03
372.69
336.34
300.00
[K]

(a)

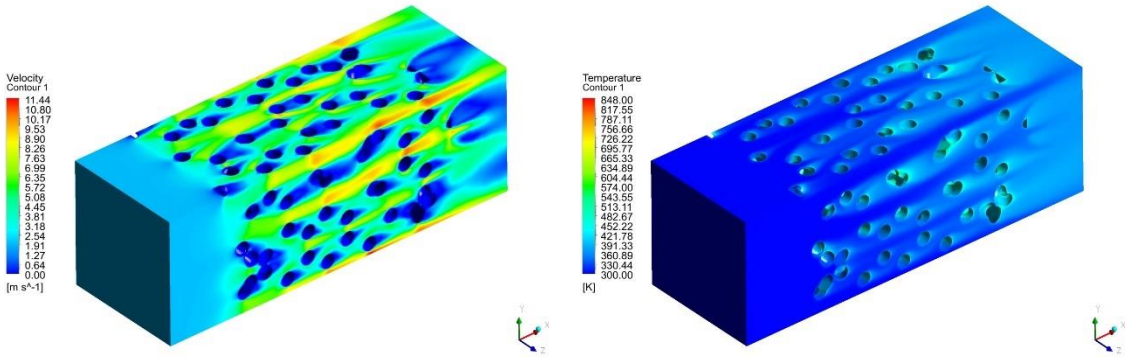
Velocity
Contour 1
11.44
10.80
10.17
9.53
8.90
8.26
7.63
6.99
6.35
5.72
5.08
4.45
3.81
3.18
2.54
1.91
1.27
0.64
0.00
[m s^-1]
Temperature
Contour 1
848.00
817.55
787.11
756.66
726.22
695.77
665.33
634.89
604.44
574.00
543.55
513.11
482.67
452.22
421.78
391.33
360.89
330.44
300.00
[K]

(b)

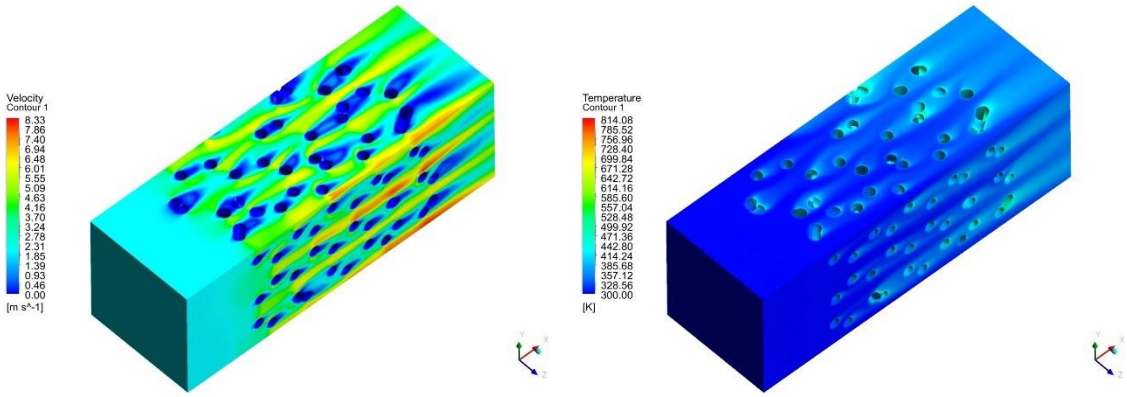
Velocity
Contour 1
8.33
7.86
7.40
6.94
6.48
6.01
5.55
5.09
4.63
4.16
3.70
3.24
2.78
2.31
1.85
1.39
0.93
0.46
0.00
[m s^-1]
Temperature
Contour 1
814.08
785.52
756.96
728.40
699.84
671.28
642.72
614.16
585.60
557.04
528.48
499.92
471.36
442.80
414.24
385.68
357.12
328.56
300.00
[K]

(c)

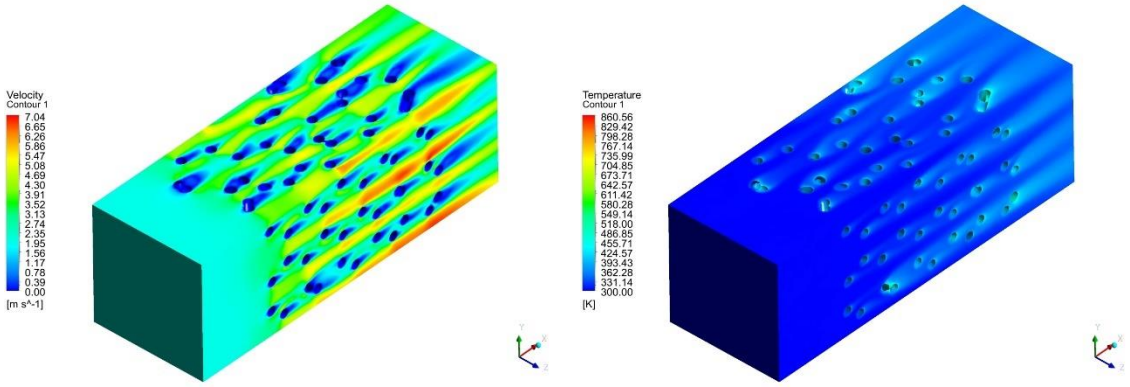

(d)

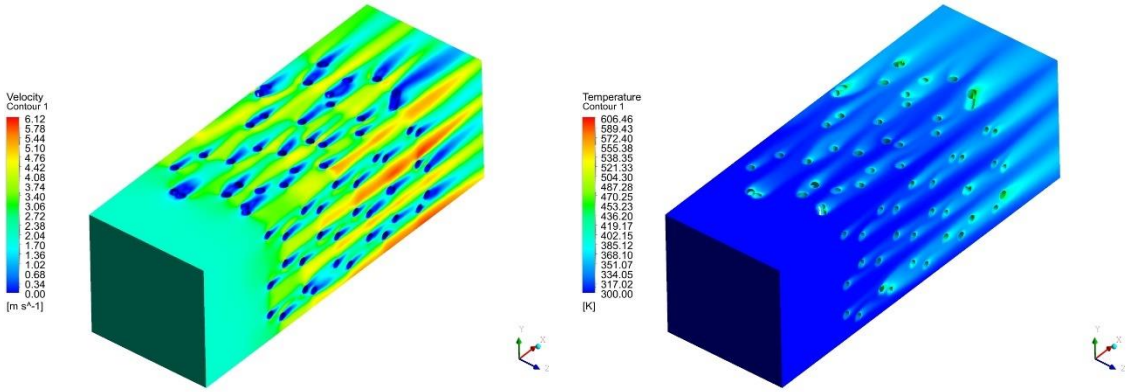

(e)

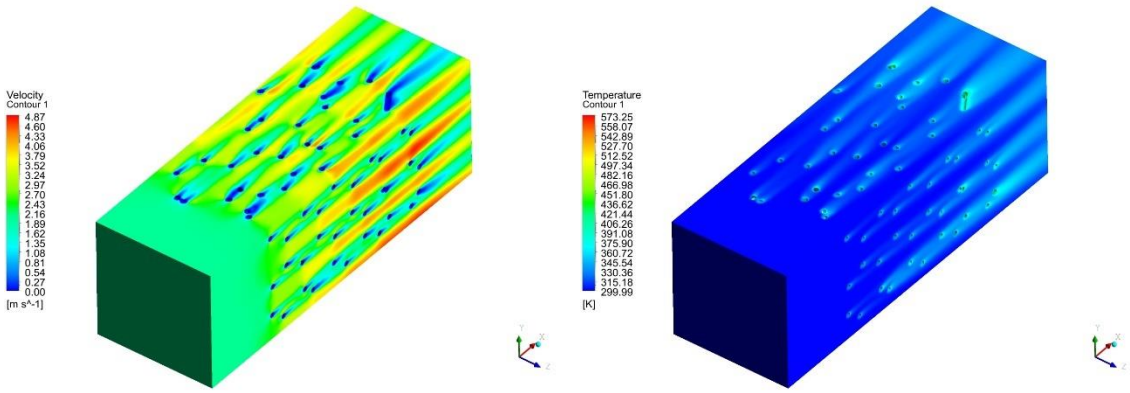

(f)

Figure 5.12 Velocity field contours (left), and temperature field contours (right) shown for the cases of an inlet velocity of 2.0 m/s and imposed heat flux of 10 kW/m^2 for 10 ppi foam with six different porosities: (a) 70%, (b) 75%, (c) 80%, (d) 85%, (e) 90%, and (f) 95%

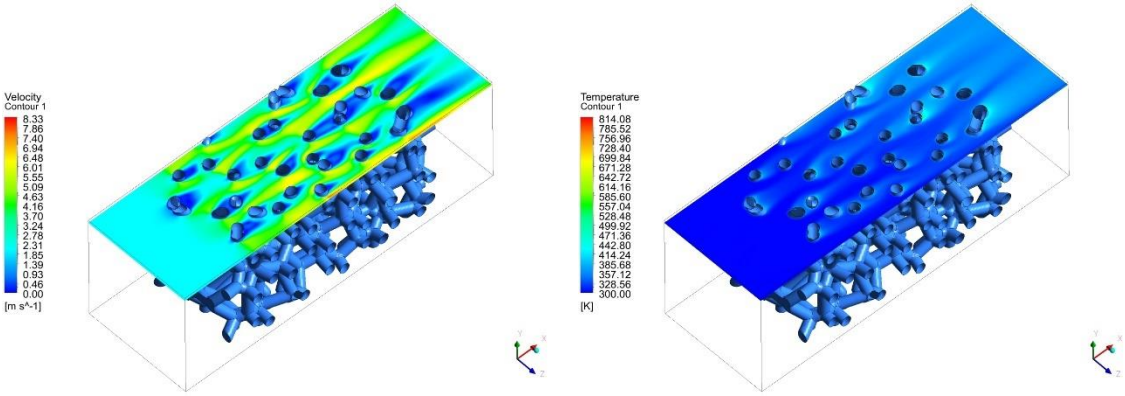
Velocity
Contour 1
8.33
7.86
7.40
6.94
6.48
6.01
5.55
5.09
4.63
4.16
3.70
3.24
2.78
2.31
1.85
1.39
0.93
0.46
0.00
[m s^-1]
Temperature
Contour 1
814.08
785.52
756.96
728.40
699.84
671.28
642.72
614.16
585.60
557.04
528.48
499.92
471.36
442.80
414.24
385.68
357.12
328.56
300.00
[K]

(a)

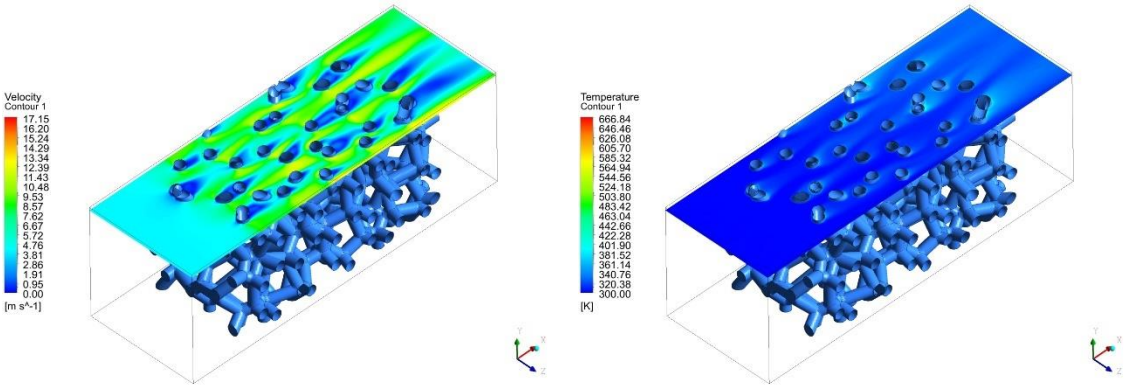
Velocity
Contour 1
17.15
16.20
15.24
14.29
13.34
12.39
11.43
10.48
9.53
8.57
7.62
6.67
5.72
4.76
3.81
2.86
1.91
0.95
0.00
[m s^-1]
Temperature
Contour 1
666.84
646.46
626.08
605.70
585.32
564.94
544.56
524.18
503.80
483.42
463.04
442.66
422.28
401.90
381.52
361.14
340.76
320.38
300.00
[K]

(b)

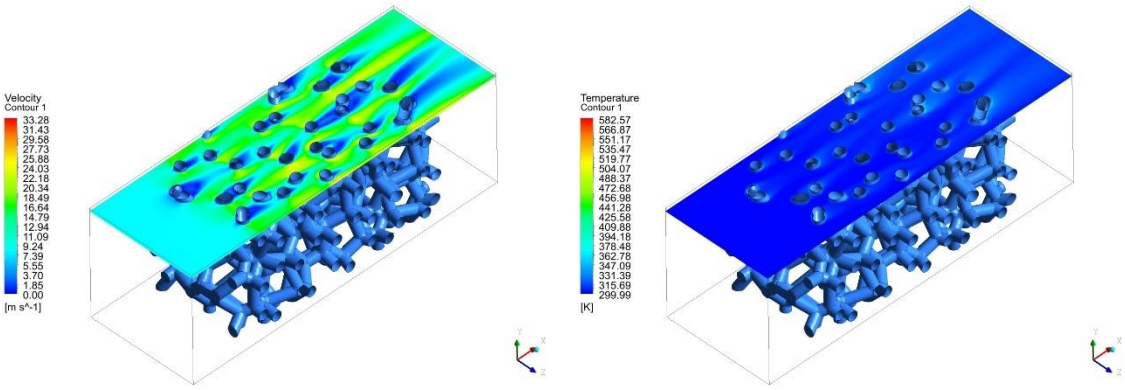
Velocity
Contour 1
33.28
31.43
29.58
27.73
25.88
24.03
22.18
20.34
18.49
16.64
14.79
12.94
11.09
9.24
7.39
5.55
3.70
1.85
0.00
[m s^-1]
Temperature
Contour 1
582.57
566.87
551.17
535.47
519.77
504.07
488.37
472.68
456.98
441.28
425.58
409.88
394.18
378.48
362.78
347.09
331.39
315.69
299.99
[K]

(c)

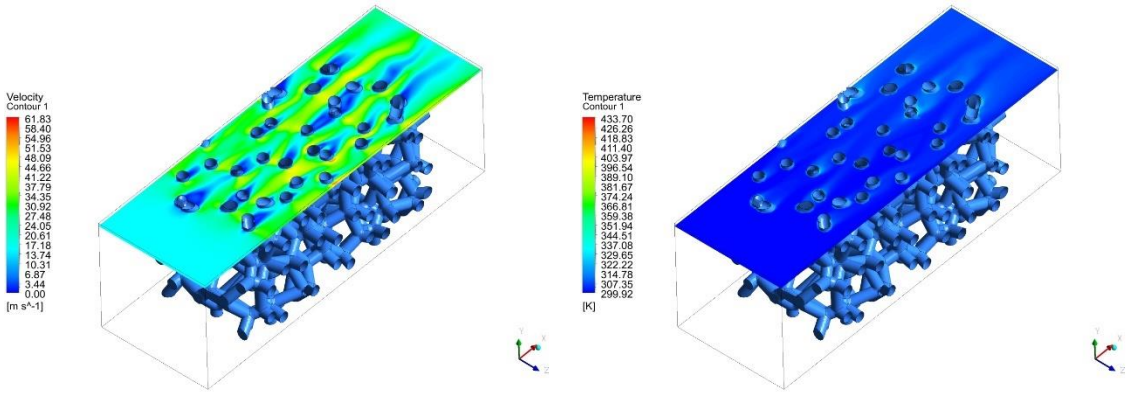

(d)

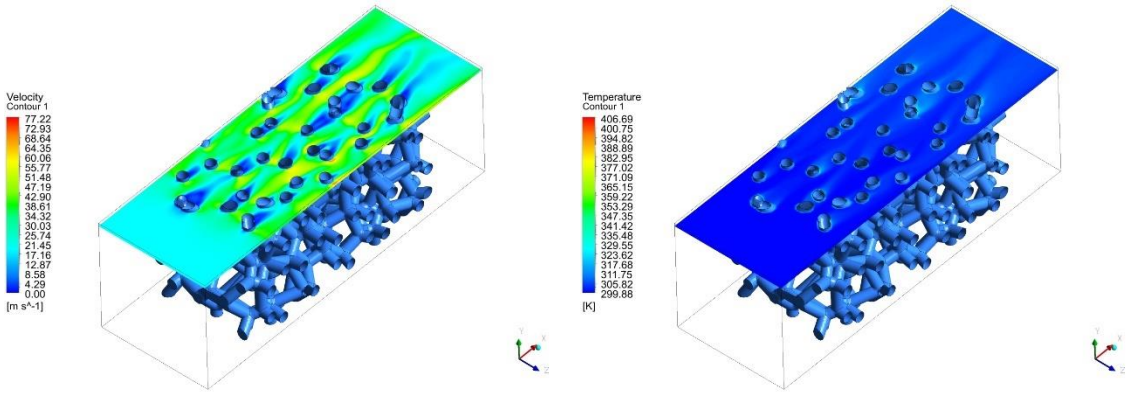

(e)

Figure 5.13 Velocity field contours (left), and temperature field contours (right) shown for the cases of different velocities: (a) 2 m/s, (b) 4 m/s, (c) 8 m/s, (d) 16 m/s, and (e) 20 m/s and imposed heat flux of 10 kW/m^2, in a cross section for 10 ppi-80% foams

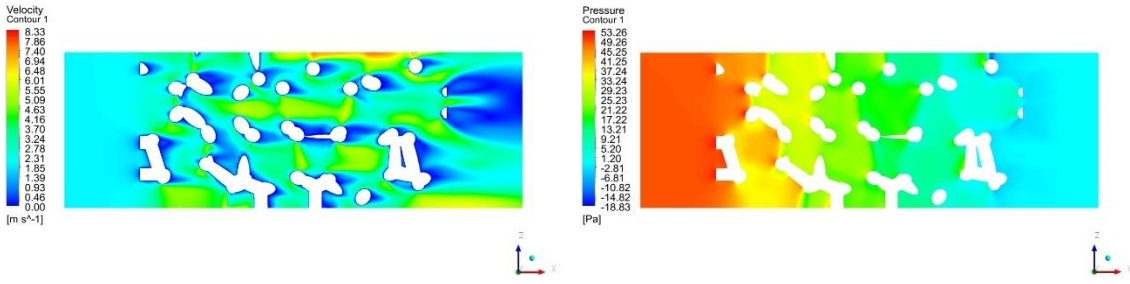

(a)

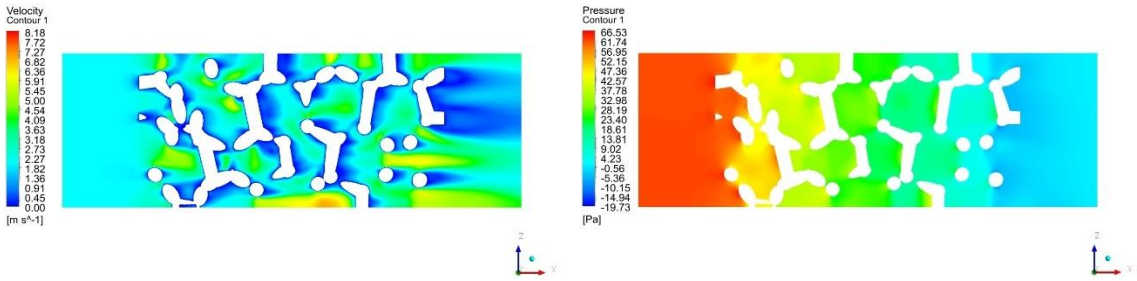

(b)

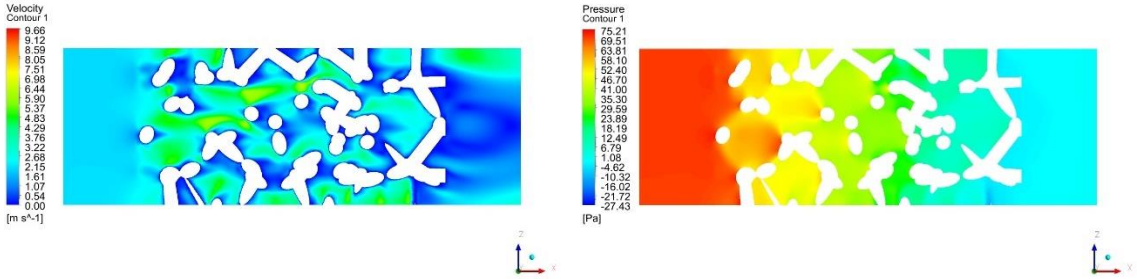

(c)

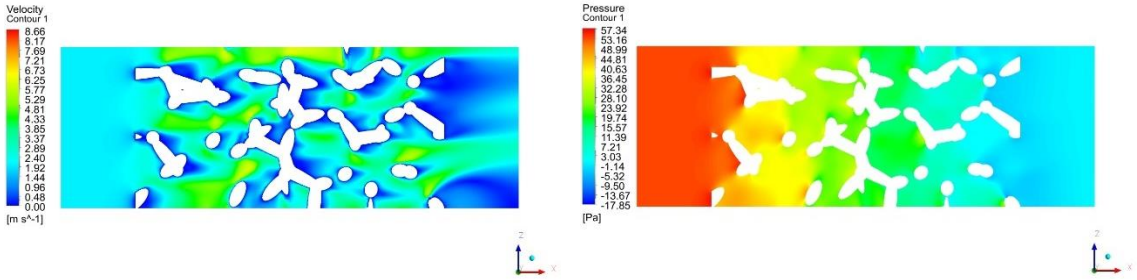

(d)

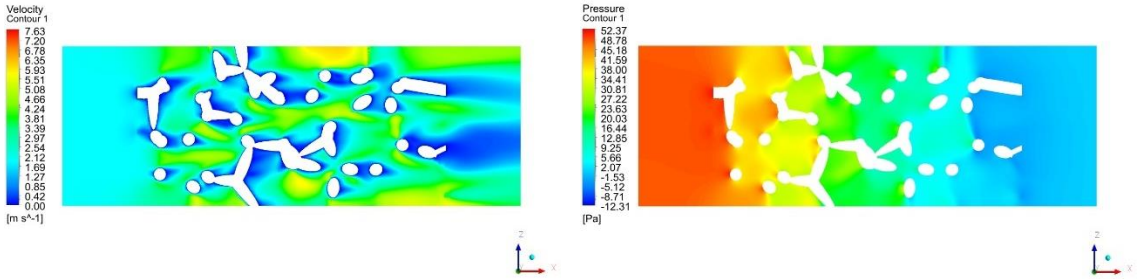

(e)

Figure 5.14 Details of the flow field of an inlet velocity of 2 m/s for foams with the same porosity 80% and five different pore densities: (a) 10 ppi, (b) 20 ppi, (c) 30 ppi, (d) 40 ppi, and (e) 50 ppi. Left: cut plane of the velocity magnitude field; right: cut plane of the pressure field

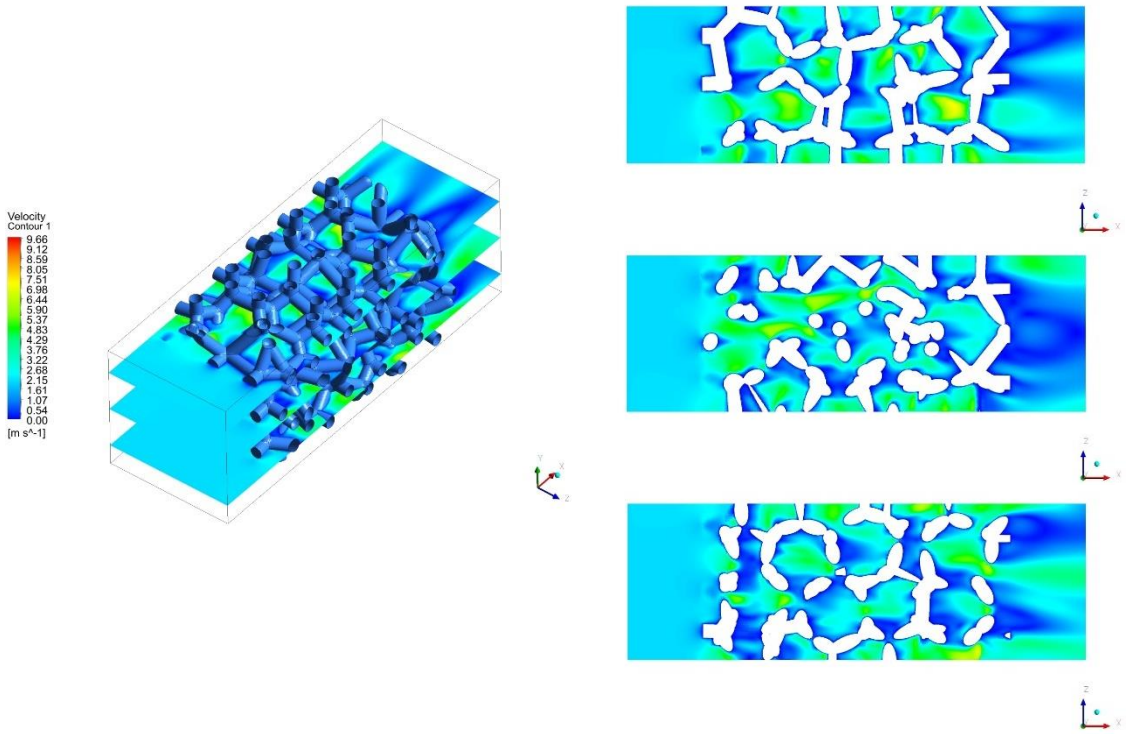

Figure 5.15 Details of the velocity contours inside the 30 ppi-80% foam at three different cross sections

5.5.1 Pressure drop of foams with different porosity

Five different open cell foams with porosity from 70% to 95% are simulated and compared (see Table 5.2–Table 5.6). The pore density varies from 10 ppi to 50 ppi. The results of the simulations of flows across designed foams are also compared with the theoretical prediction developed in Chapter 5.3 under the same ppi number and different porosities, as shown in Figure 5.16. It can be observed that the expected result of increasing pressure drop with decreasing porosity is obtained. Decreasing porosity means an increase in solid materials in the same sample volume, which results in an increase in flow friction. Furthermore, it can be noted that, in general, the pressure drops obtained from numerical simulations are consistent with that of the theoretical model. There is a good agreement when the flow velocity is low. According to Equation (5.38), the definition of Reynolds

number in this work, the Reynolds number would be less than 2000–3000 when the velocity smaller than 6–10 m/s. The fluid flow falling into such regime is called laminar flow, otherwise it is called turbulent flow.

Table 5.2 Structural parameters and porosity of the simulated 10 ppi foam structure

Pore density	Average pore diameter d (mm)	Strut diameter d_s (mm)	Porosity (%)
10 ppi	3.53	1.30	70
		1.12	75
		0.90	80
		0.76	85
		0.60	90
		0.40	95

Table 5.3 Structural parameters and porosity of the simulated 20 ppi foam structure

Pore density	Average pore diameter d (mm)	Strut diameter d_s (mm)	Porosity (%)
20 ppi	2.44	0.90	70
		0.76	75
		0.64	80
		0.54	85
		0.40	90
		0.28	95

Table 5.4 Structural parameters and porosity of the simulated 30 ppi foam structure

Pore density	Average pore diameter d (mm)	Strut diameter d_s (mm)	Porosity (%)
30 ppi	2.08	0.76	70
		0.66	75
		0.56	80
		0.46	85
		0.34	90
		0.24	95

Table 5.5 Structural parameters and porosity of the simulated 40 ppi foam structure

Pore density	Average pore diameter d (mm)	Strut diameter d_s (mm)	Porosity (%)
40 ppi	1.64	0.62	70
		0.52	75
		0.44	80
		0.36	85
		0.28	90
		0.20	95

Table 5.6 Structural parameters and porosity of the simulated 50 ppi foam structure

Pore density	Average pore diameter d (mm)	Strut diameter d_s (mm)	Porosity (%)
50 ppi	1.17	0.44	70
		0.38	75
		0.32	80
		0.26	85
		0.20	90
		0.13	95

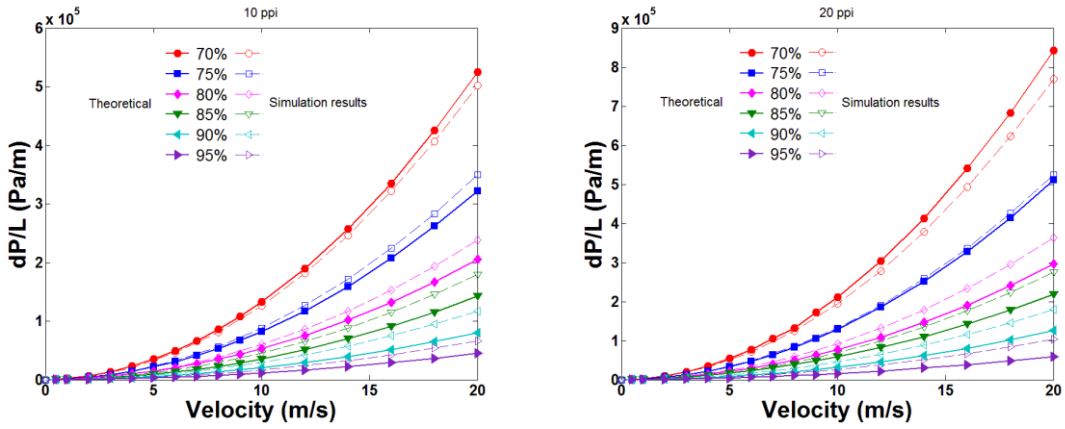

(a) (b)

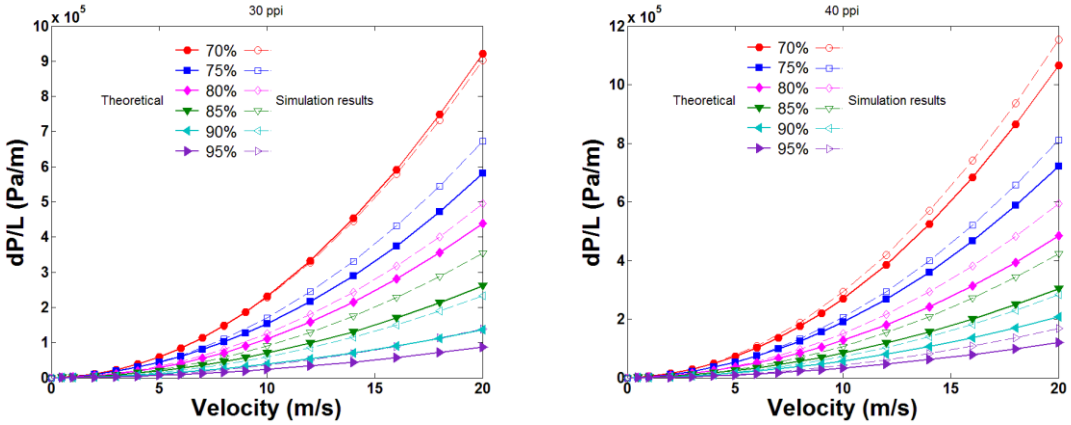

(c)

(d)

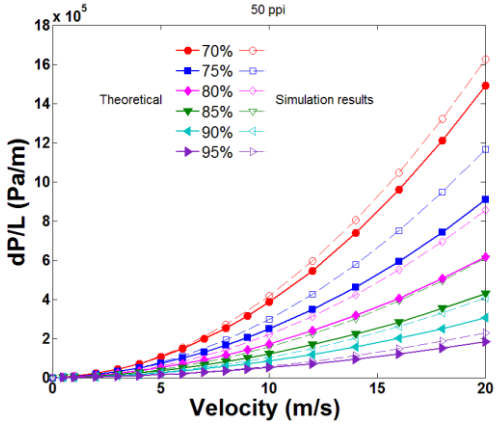

(e)

Figure 5.16 Comparison of pressure drop from simulations and the theoretical prediction for (a) 10 ppi, (b) 20 ppi, (c) 30 ppi, (d) 40 ppi, and (e) 50 ppi

Figure 5.17 shows the comparison of simulation results and theoretical model in the laminar regime. In the laminar regime, the theoretical model proposed in Chapter 5.3 can predict the pressure drop more accurate than that of turbulent flow. The following discussion gives a possible explanation of this phenomenon. In fluid dynamics, turbulence is a flow regime characterized by chaotic changes in pressure and flow velocity where inertial forces dominate viscous forces. The difference between laminar flow and turbulent

flow is shown in Figure 5.18. Laminar flows are parallel with no disruption, e.g., no mass transfer, between layers. However, the fluid in turbulent flow undergoes irregular fluctuations or mixing. There are transfers of mass and momentum between different layers or positions. The velocity of the fluid at a point is continuously changed in magnitude and direction, which results in swirling and eddying as the bulk of the fluid moves in a specific direction. Moreover, unsteady vortices, in turbulent flow, appear on many scales and interact with each other. Drag due to boundary layer skin friction increases. The structure and location of boundary layer separation often change. It is obvious that turbulent flow is far more complicated than laminar flow. Figure 5.18 (b) shows a flow visualization of a turbulent jet.

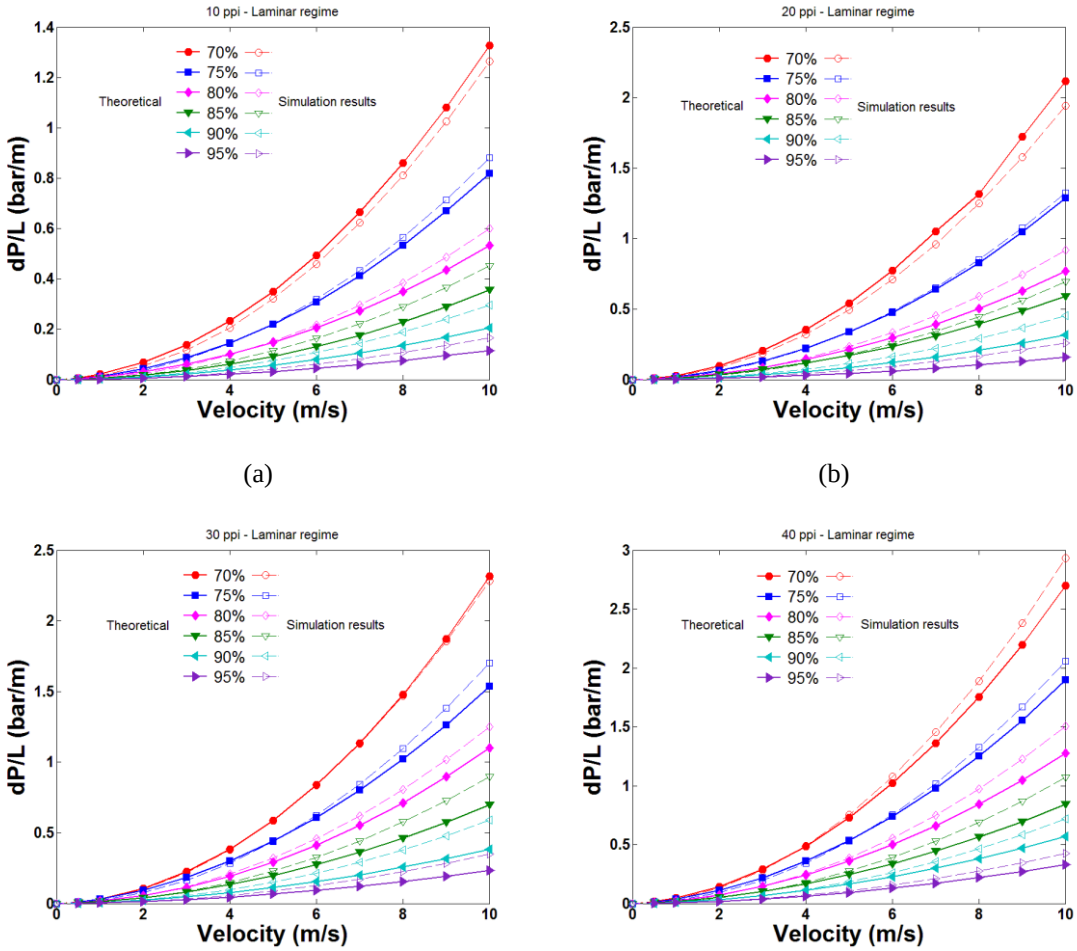

(a) (b)

(c) (d)

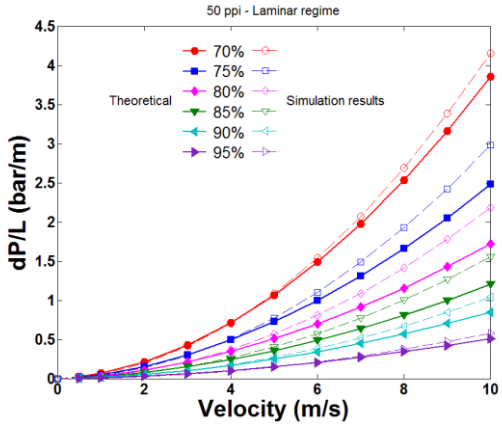

(e)

Figure 5.17 Comparison of pressure drop from simulations and the theoretical prediction in the laminar regime for (a) 10 ppi, (b) 20 ppi, (c) 30 ppi, (d) 40 ppi, and (e) 50 ppi

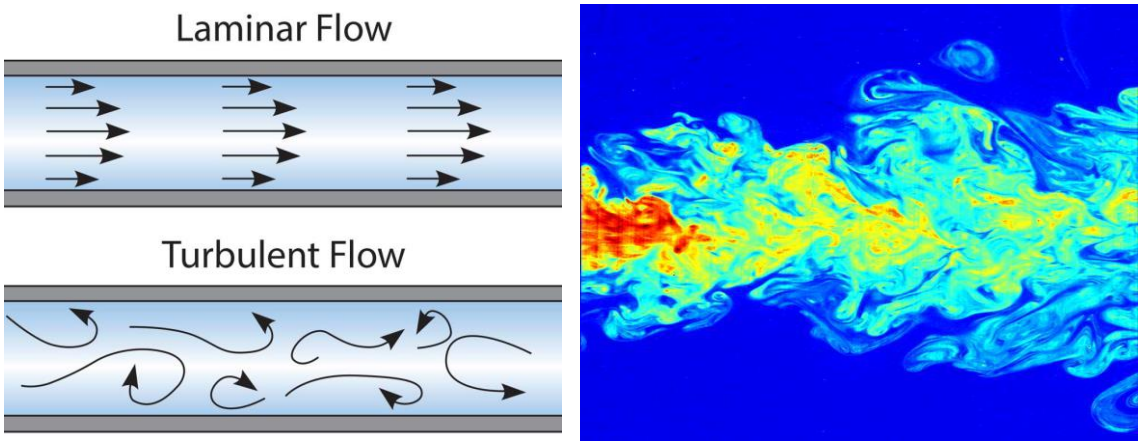

(a) (b)

Figure 5.18 (a) A schematic illustration of laminar flow and turbulent flow, and (b) flow visualization of a turbulent jet [64]

In present simulations, the fluid needs to flow around many cylinders, which are the struts of the open cell foams. The crossflow of tubes or cylinders shows many flow regimes, that are dependent on the Reynolds number. By increasing the flow velocity, as

shown in Figure 5.19, a number of different flow situations can be created, each situation being identified by a specific Reynolds number range. For all cases it is assumed that the undisturbed flow is laminar. For very low values of Reynolds number (e.g., $Re < 1$) the flow remains attached to the cylinder through all periphery (the first case from left in Figure 5.19). For $1 < Re < 30$ the flow remains symmetrical in shape but flow separation occurs downstream of the cylinder as shown in second case from left in Figure 5.19 giving origin to stationary vortices. For values of Reynolds number $40 < Re < 4000$ alternating vortices of symmetrical intensity are shed downstream of the cylinder forming the so called "von Kármán vortex trail" (third case from left in Figure 5.19). For Reynolds number values above the last range the flow downstream of the cylinder became turbulent as shown in fourth and fifth cases in Figure 5.19. In this work, however, the flow is far more complicated than the flow around one cylinder mentioned above, as shown in velocity fields in Figure 5.12–Figure 5.15, since the fluid has to flow around a number of cylinders most of which are not perpendicular to the flow direction. Hence, the flow fields in present work are more complex than that of the laminar flow and even that of the turbulent flow. Figure 5.20 and Figure 5.21 show that the velocity vector fields obtained from present simulations. The flow fields in present work are rather complicated either at low velocity 0.5 m/s or high velocity 20 m/s, and can be viewed as a turbulent mode. It is observed that the velocity direction of a point in flow field, especially at high velocities, is not necessarily parallel with the flow direction, but could have an angle from the flow direction and even could be perpendicular to it, as shown in Figure 5.20 (d), and Figure 5.21 (b) and (d). As for the velocity direction of any point in laminar flow, however, it is about parallel with the flow direction.

For the theoretical model developed in Chapter 5.3, the open cell foams are viewed as a bundle of tangled tubes of weird cross-sections, as shown in Figure 5.5 (b). The viscous term and inertial term in Equation (5.18) are derived from the laminar flow situation in tubes with the introduction of tortuosity into the flow inside foams. To verify the rationality of assumptions during the derivation process, the streamlines inside part of investigated foams are given in Figure 5.22. Since the integration of the streamline stops if it hits one of the foam struts, it can be clearly seen that the majority of streamlines gets trapped on the foam. Obviously, in reality, the streamlines would not simply disappear if they hit one of the struts, in fact, several other phenomena would be expected to take place such as fluid splashing and backflow, all of which are outside the scope of this work. From Figure 5.22, it is approved that the tortuosity can be applied to the flow inside foams and Equation (5.18) has its physical meaning in this work. It should be noted that Equation (5.18) does not consider the transfer of mass and momentum between different layers in fluid flow in open cell foams. When the fluid velocity is low, e.g., in the laminar-like regime in this work, velocity < 6 m/s, there is no much mass transfer between different layers, and thus the theoretical model can obtain a good prediction of pressure drop for open cell foams.

In order to compare the theoretical predictions and simulation results more efficiently and clearly, Figure 5.17 is replotted to Figure 5.23. The pressure drops for 10 ppi foams globally match the numerical results with an average relative and absolute deviation of 11.33% and 17.26%, respectively, demonstrating the accuracy of the theoretical model developed. Relative deviation e_r, absolute deviation e_{abs}, and standard deviation STD between the numerical and theoretical results for each type of foams are summarized in Table 5.7–Table 5.11.

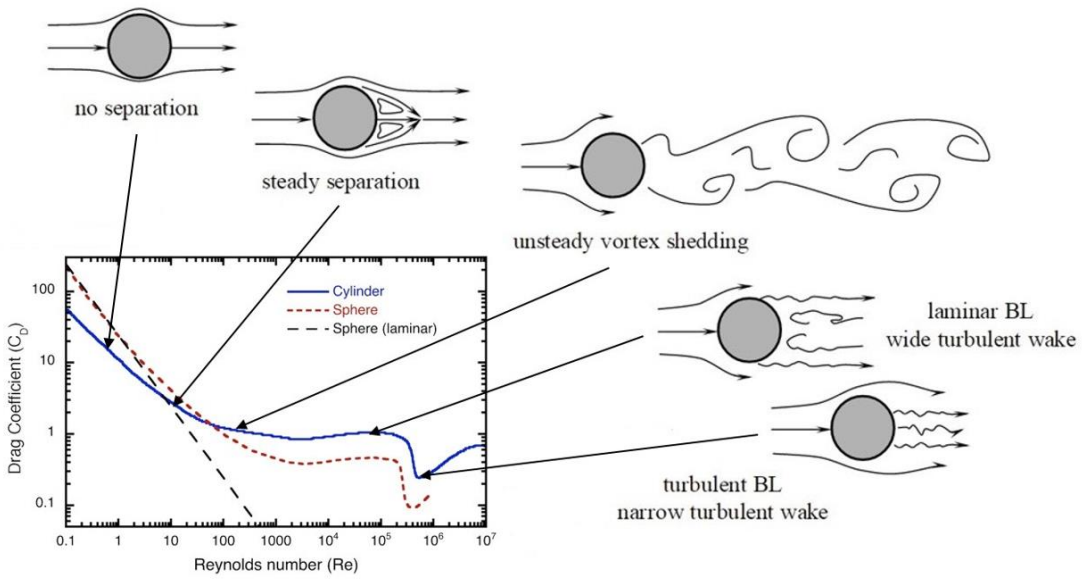

Figure 5.19 Different types of flow around a cylinder as a function of the Reynolds number

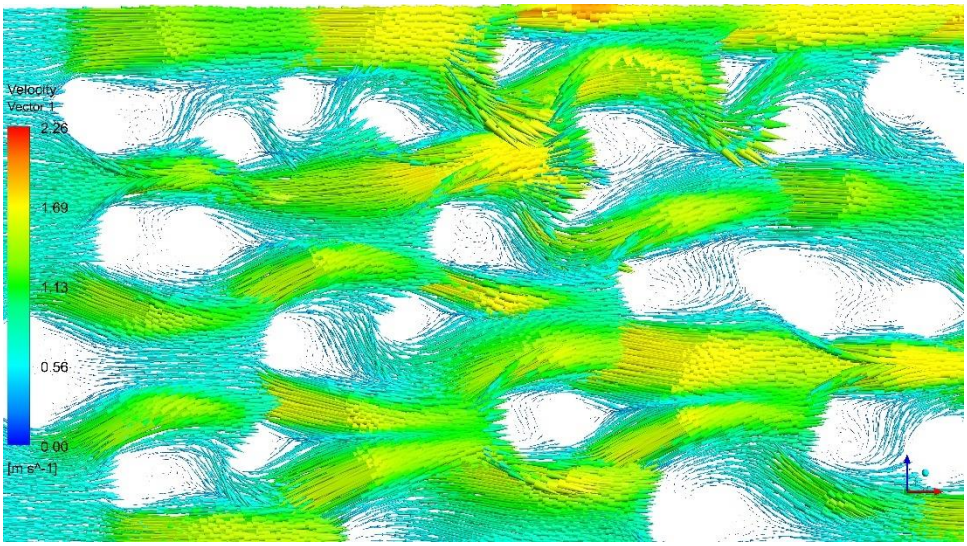

(a)

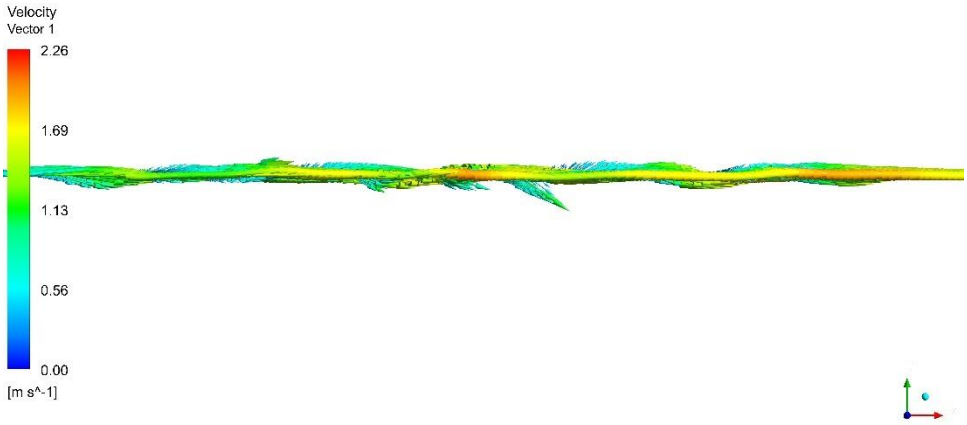
Velocity
Vector 1
2.26
1.69
1.13
0.56
0.00
[m s^-1]

(b)

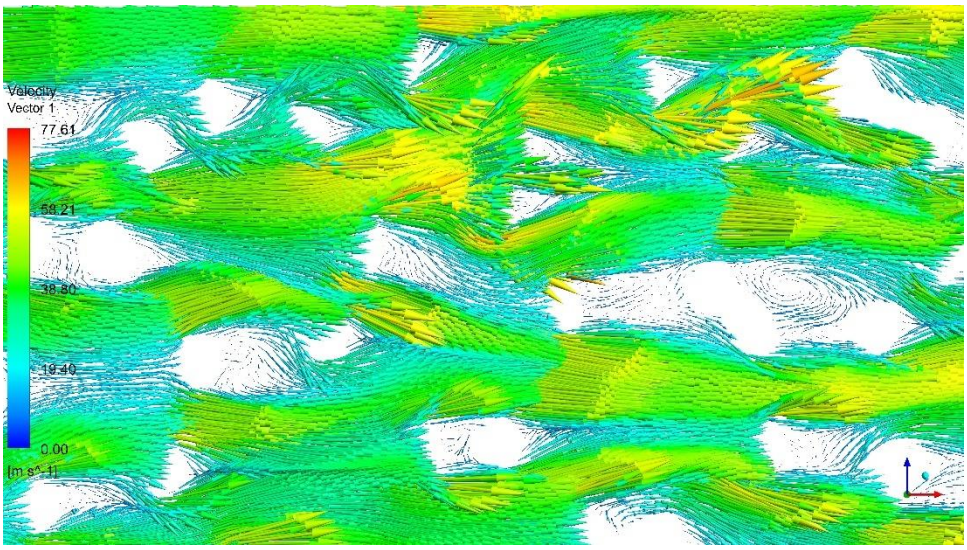
Velocity
Vector 1
77.61
58.21
38.80
19.40
0.00
[m s^-1]

(c)

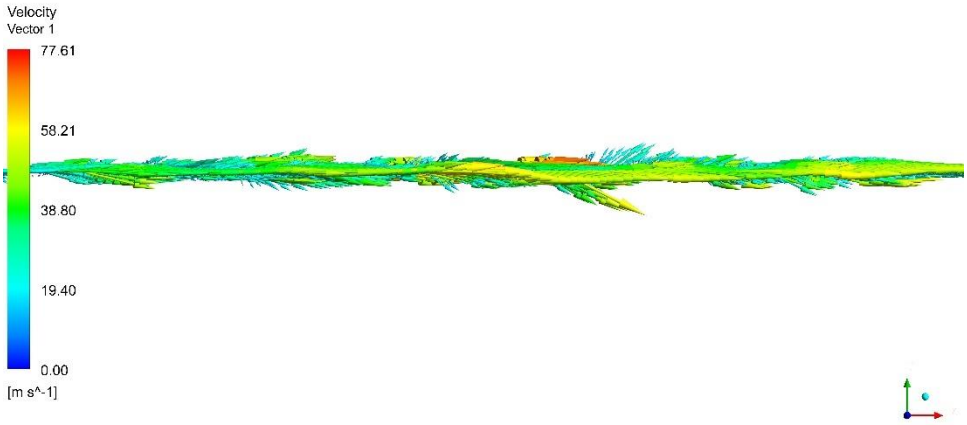

(d)

Figure 5.20 Cut plan of velocity vector fields at y=10 mm for the 10 ppi-80% foam for the case of an inlet velocity of (a) and (b) 0.5 m/s, (c) and (d) 20 m/s

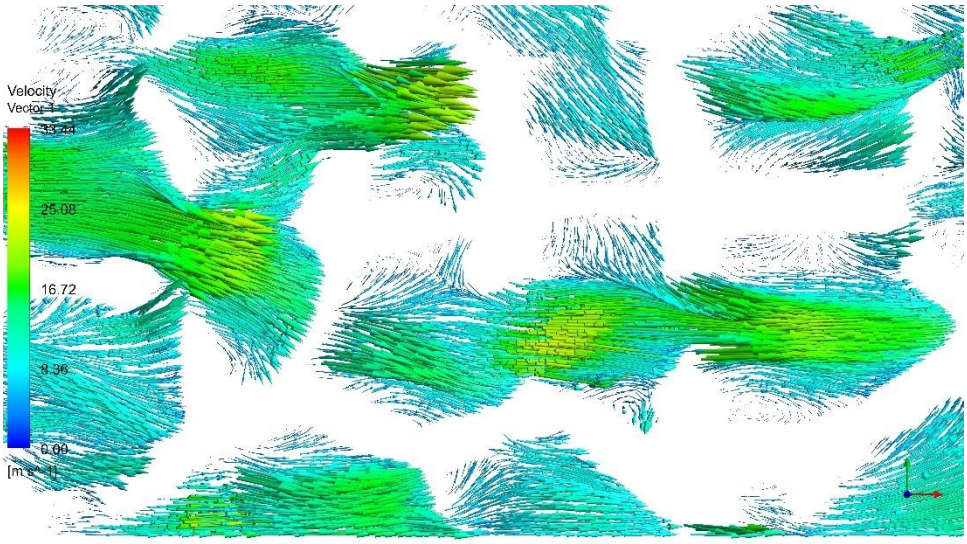

(a)

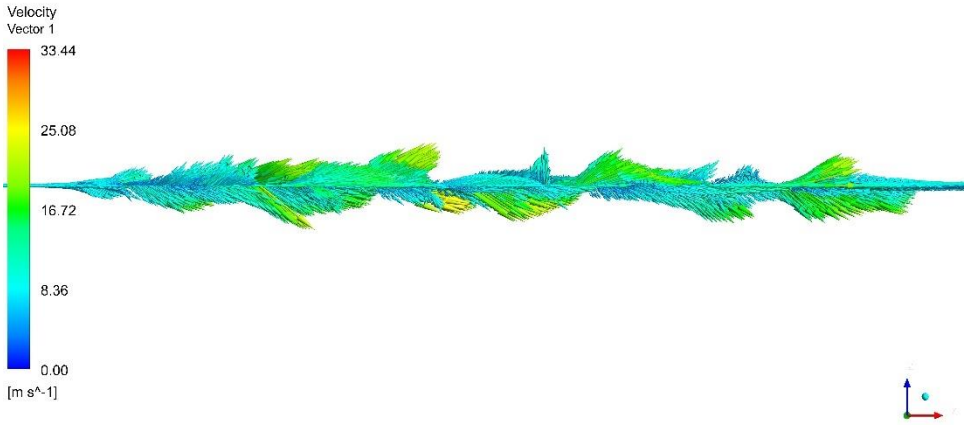
Velocity
Vector 1
33.44
25.08
16.72
8.36
0.00
[m s^-1]

(b)

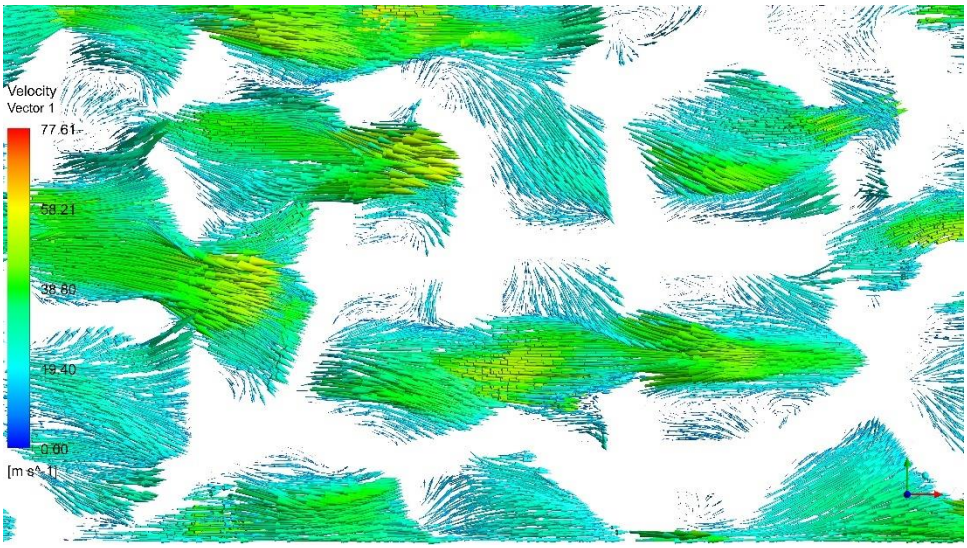
Velocity
Vector 1
77.61
58.21
38.80
19.40
0.00
[m s^-1]

(c)

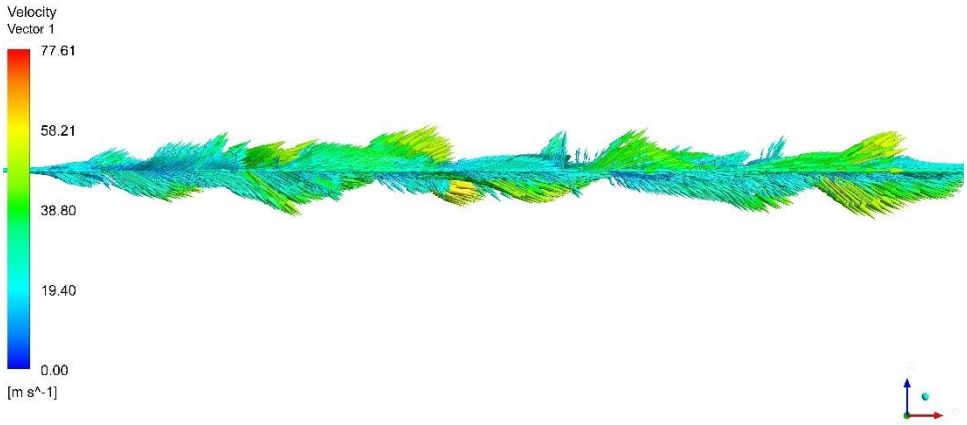

(d)

Figure 5.21 Cut plan of velocity vector fields at z=5 mm for the 10 ppi-80% foam for the case of an inlet velocity of (a) and (b) 8.0 m/s, (c) and (d) 20 m/s

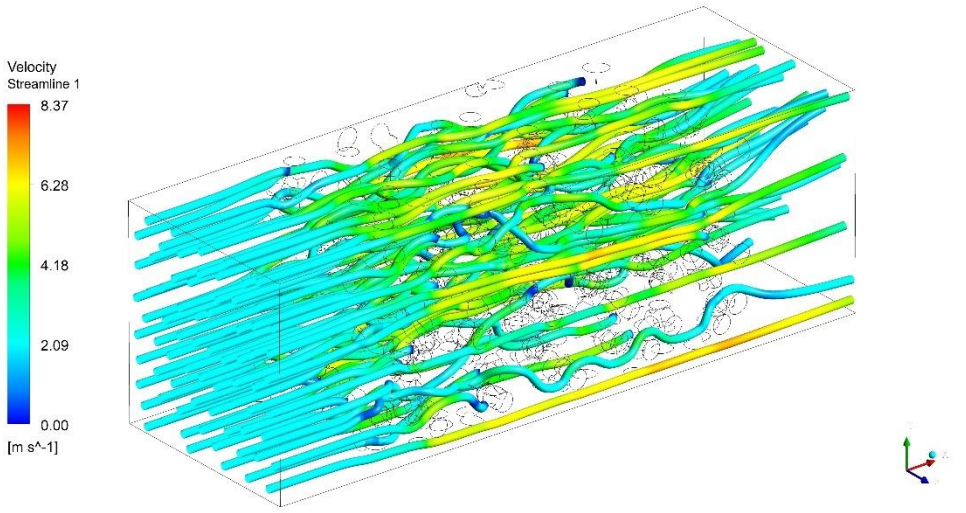

(a)

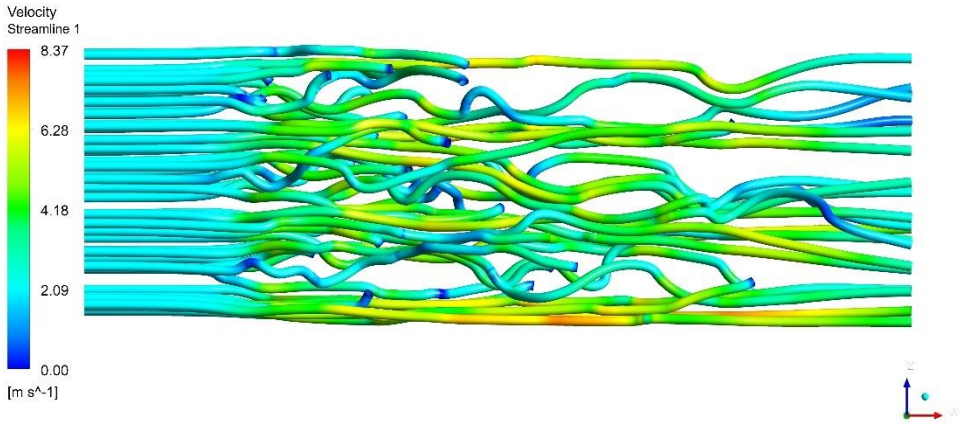
Velocity
Streamline 1
8.37
6.28
4.18
2.09
0.00
[m s^-1]

(b)

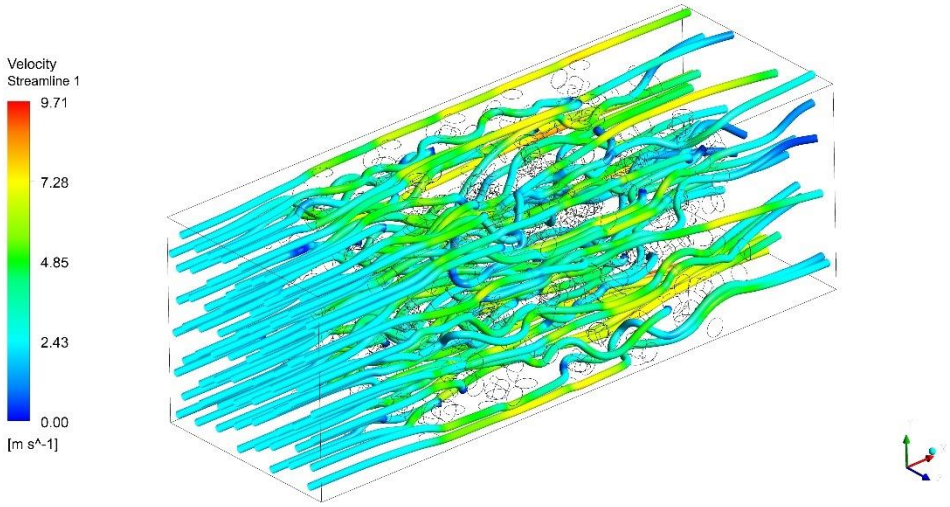
Velocity
Streamline 1
9.71
7.28
4.85
2.43
0.00
[m s^-1]

(c)

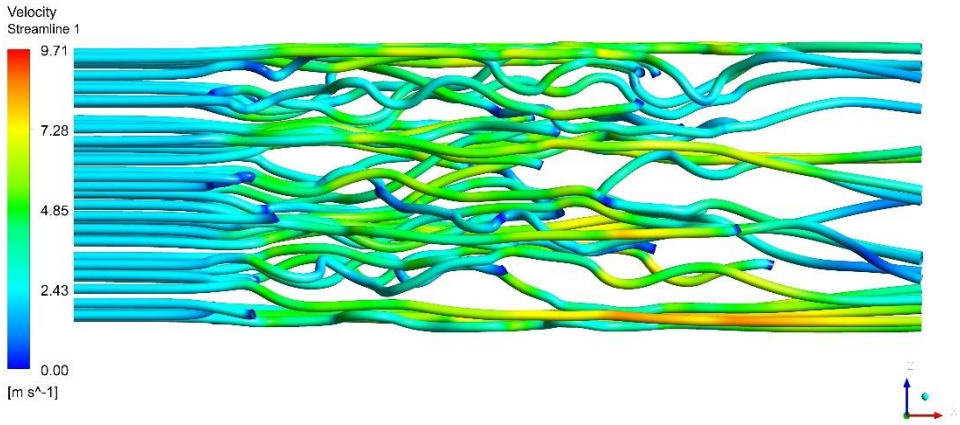
Velocity
Streamline 1
9.71
7.28
4.85
2.43
0.00
[m s^-1]

(d)

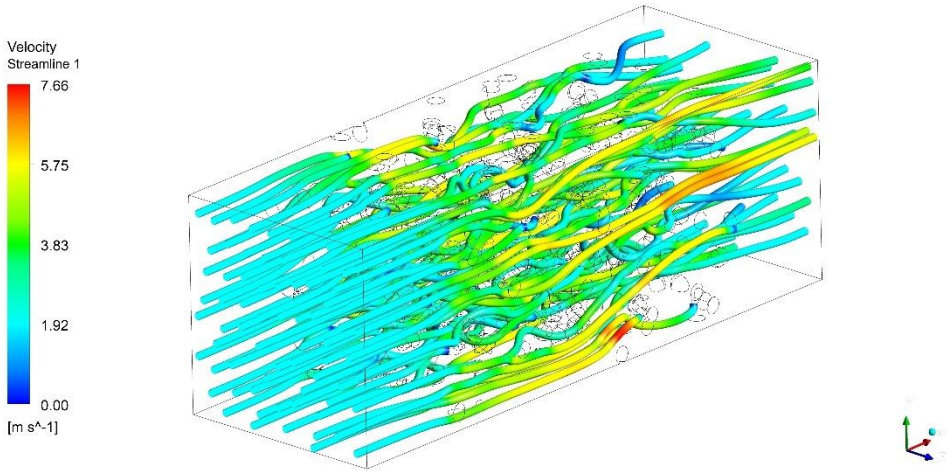
Velocity
Streamline 1
7.66
5.75
3.83
1.92
0.00
[m s^-1]

(e)

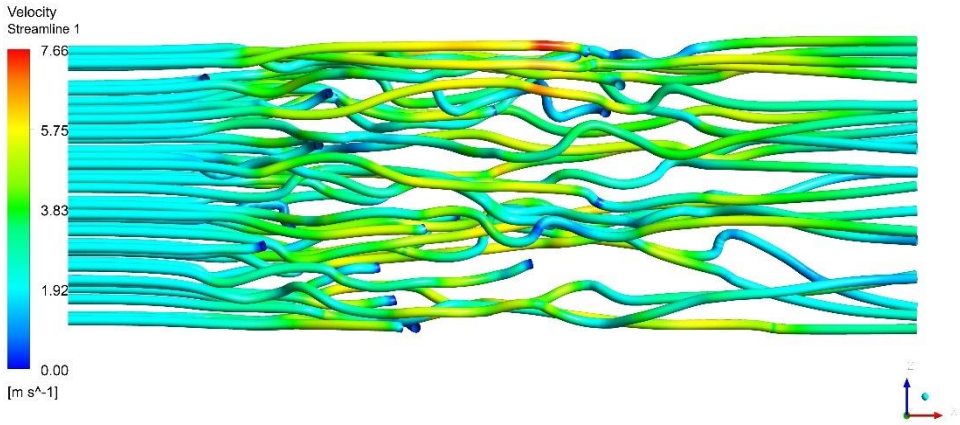

(f)

Figure 5.22 Streamlines on (a) 10 ppi-80% foam, (b) at y=10 mm plane of (a), (c) 30 ppi-80% foam, (d) at y=6 mm plane of (d), (e) 50 ppi-80% foam, and (f) at y= 4 mm plane of (e) for velocity 2.0 m/s colored by velocity

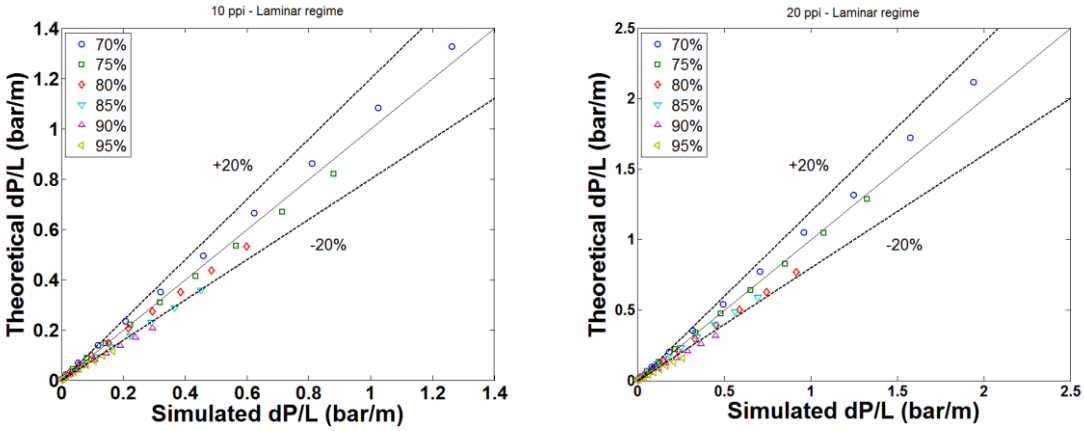

(a) (b)

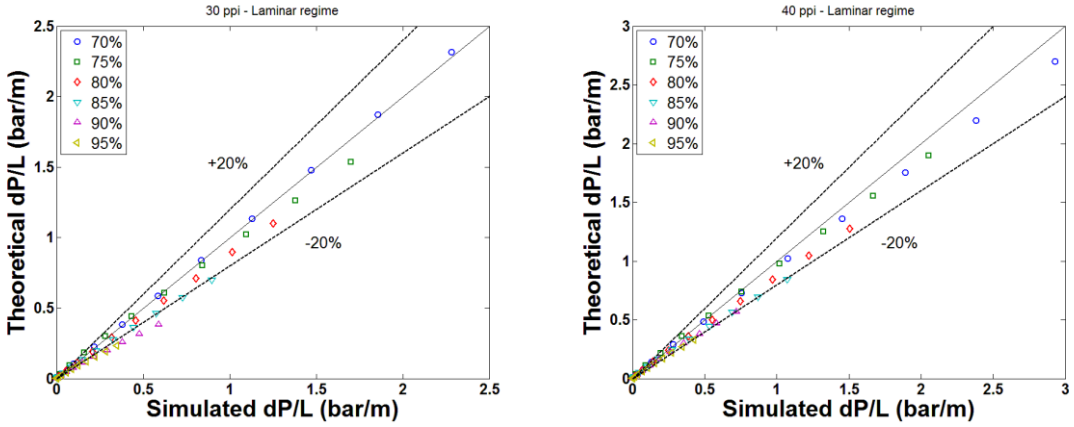

(c)

(d)

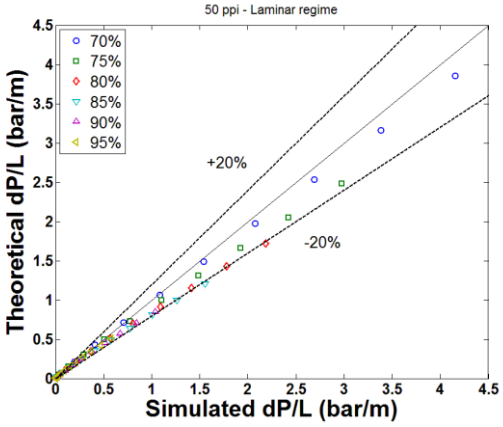

(e)

Figure 5.23 Comparison between numerical simulation results and theoretical predictions for pressure drops: (a) 10 ppi, (b) 20 ppi, (c) 30 ppi, (d) 40 ppi, and (e) 50 ppi

Table 5.7 Difference between numerically simulated and theoretical predictions of dP/L for 10 ppi foam

Parameter	Foam	Porosity (%)	e_r (%)	e_{abs} (%)	STD (%)
dP/L	10 ppi	70	-14.36	9.42	12.31
		75	-4.98	11.51	14.84
		80	-4.59	14.37	18.13
		85	16.63	10.84	14.43
		90	23.31	16.37	20.94
		95	51.99	41.06	76.28

Table 5.8 Difference between numerically simulated and theoretical predictions of dP/L for 20 ppi foam

Parameter	Foam	Porosity (%)	e_r (%)	e_{abs} (%)	STD (%)
dP/L	20 ppi	70	-11.55	4.53	6.11
		75	-4.54	7.86	10.33
		80	3.56	13.34	16.84
		85	-2.88	15.39	19.17
		90	26.76	13.22	17.18
		95	38.52	21.20	27.03

Table 5.9 Difference between numerically simulated and theoretical predictions of dP/L for 30 ppi foam

Parameter	Foam	Porosity (%)	e_r (%)	e_{abs} (%)	STD (%)
dP/L	30 ppi	70	-4.44	4.98	6.63
		75	-6.85	13.70	17.05
		80	4.70	8.56	11.09
		85	9.27	15.13	18.94
		90	25.89	20.80	25.89
		95	25.66	18.69	23.75

Table 5.10 Difference between numerically simulated and theoretical predictions of dP/L for 40 ppi foam

Parameter	Foam	Porosity (%)	e_r (%)	e_{abs} (%)	STD (%)
dP/L	40 ppi	70	-0.99	8.90	11.31
		75	-5.86	11.54	14.44
		80	2.82	12.17	15.27
		85	6.26	15.51	19.28
		90	5.66	15.30	19.15
		95	8.16	16.63	21.03

Table 5.11 Difference between numerically simulated and theoretical predictions of dP/L for 50 ppi foam

Parameter	Foam	Porosity (%)	e_r (%)	e_{abs} (%)	STD (%)
dP/L	50 ppi	70	-1.63	7.67	9.51
		75	2.67	12.72	15.56
		80	6.88	14.42	17.71
		85	8.06	14.98	18.50
		90	2.84	14.57	18.17
		95	-7.73	15.78	19.76

5.5.2 Pressure drop of foams with different pore density

In Figure 5.24, the samples simulated present the same porosity but with different pore densities in each figure. It can be observed that an increase in the pore density implies an increase of the pressure drop. That is, the flow resistance increases for increasing ppi number at a constant porosity. Indeed, the channel through which fluid has to flow becomes smaller and the fluid frictions get stronger, inducing higher pressure drops. Figure 5.24 also states that open cell foams with the same porosity and different pore density present different pressure drop properties. This indicates that not only the porosity is important for the pressure drop description in open cell foams but also the pore density. The flow resistance is affected by the pore density, and thus the pressure drop, influenced by the flow resistance (refer to the contents of Chapter 5.2 and Chapter 5.3), is dependent on the pore density.

In order to compare with the data in the open literature, only data from foams with features similar to those of current foam structures are taken into account. Dietrich et al. measured the pressure drop of open cell foams with porosity 80% [65]. The authors observed four kinds of foams with different pore densities: 10, 20, 30, and 45 ppi. Figure 5.25 shows the results of Dietrich's experiments and the comparison with the results of present work. Figure 5.26 depicts the experimental set-up used in Dietrich's pressure drop investigation. As shown in Figure 5.25, the simulated results, e.g., 10, 20, and 30 ppi, are consistent with the experimental data from Dietrich's work with small differences. The predicted values by present model, as discussed in Chapter 5.5.1, are less than the experimental results. An error of -20% might be considered to predict pressure drops of open cell foams when using the correlation developed in this work.

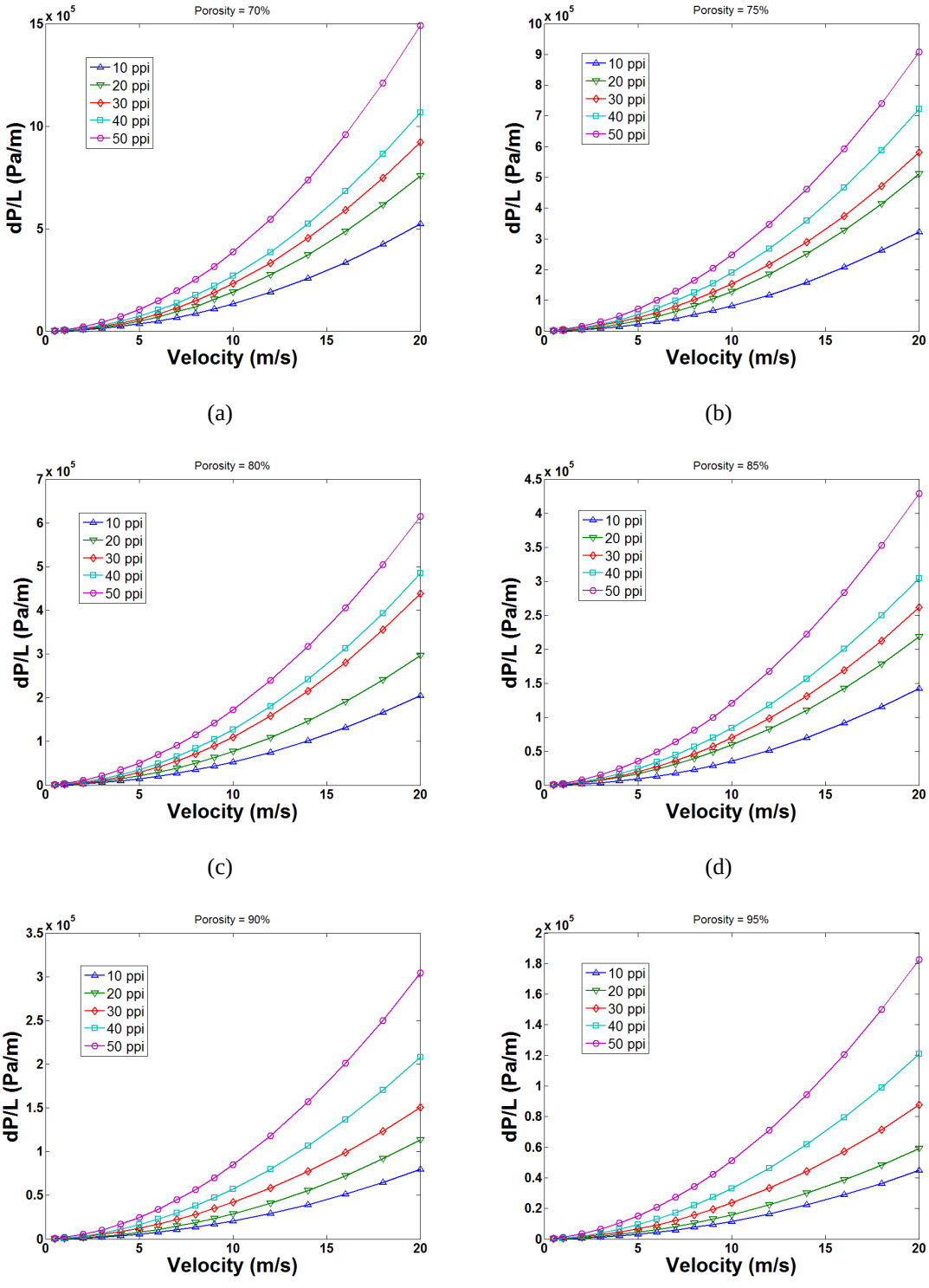

Figure 5.24 Pressure drop versus air velocity for different pore densities under same porosity: (a) 70%, (b) 75%, (c) 80%, (d) 85%, (e) 90%, and (f) 95%

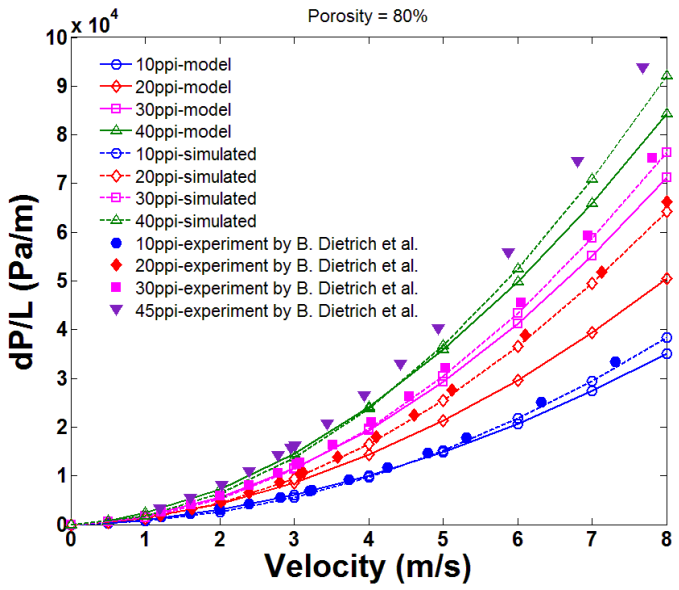

Figure 5.25 Comparison of experimental data by Dietrich et al. with simulated and theoretical results from this work

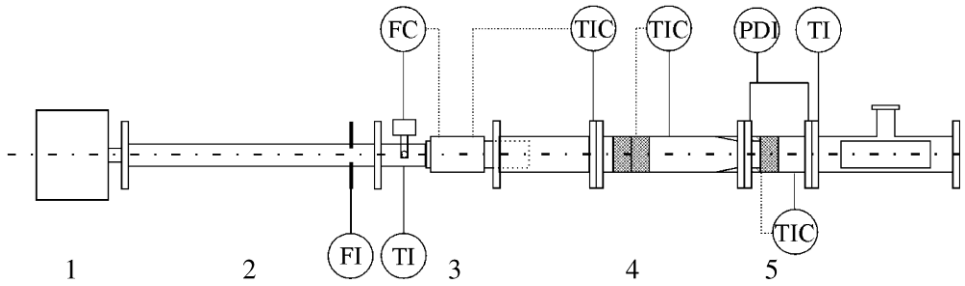

Figure 5.26 Experimental set-up of Dietrich's measurement: 1-blower, 2-orifice measuring section, 3-heater, 4-flow straighter, and 5-foam test section for pressure drop measuring [65]

Figure 5.27 and Figure 5.28 show the data obtained from 20 ppi foams with three different porosities and from ε=85% foams with three different pore densities, respectively. Garrido et al. [46] analyzed 10, 20, 30, and 45 ppi foams with porosities between 75% and 85% and 40 ppi metal foams. The apparatus in Garrido's analysis is shown in Figure 5.29. The theoretical model developed in this work is in good agreement with the experimental

data, especially for 20 ppi-80% and 20 ppi-85% foams, whereas the simulated results are consistent with the experimental data at porosity 85%. In addition, Figure 5.27 and Figure 5.28 also give a model predicting the pressure drop, which is proposed by Lacroix et al. [31]. As mentioned in Chapter 5.2, it is well known that the Ergun equation (refer to Equation (5.13)) describes the pressure drop data of sphere-packed beds highly satisfactorily. It is expected that Equation (5.13) is also a suitable approach for determining the pressure drop of open cell foams. Lacroix et al. used the unchanged Ergun equation (Equation (5.13)), substituting the particle diameter (d_p) by the strut diameter (d_s) derived from cubic lattice model. The substitution is based on the comparison of open cell foams and particles of packing beds with the same porosity and the same specific surface area per unit volume, leading to $d_p = \frac{3}{2} d_s$. Thus, the modified Ergun equation proposed by Lacroix et al. is a combination of two different geometric models, the hydraulic diameter model, from which the Ergun equation is dependent on the particle diameter and porosity, and the cubic lattice model. Mancin et al. tested the pressure drops presenting 5, 10, 20 and 40 ppi, porosity around 92%–93%, and 0.02 m of foam core height using Al6001 aluminum foams. The relevant geometrical characteristics of those commercial foams are listed in Table 5.12. The comparison between part of pressure drop data of this work and Mancin's results is shown in Figure 5.30. Figure 5.31 shows the experimental set-up of Mancin's research. From Figure 5.30, it can be noted that the simulated data are in good agreement with Mancin's experiments. Lacroix's model also is plotted in Figure 5.30.

Lacroix et al. stated in the conclusion: "Although no physical reason can be invoked in principle to explain the extension of the Ergun equation, the model is in good agreement with experimental data derived from a large number of parameters" [31]. However, the

modified Ergun equation is not able to predict pressure drop in a general way. As shown in Figure 5.27, Figure 5.28, and Figure 5.30, the data obtained from experiments are not well described by the modified Ergun equation. For substitution of the particle diameter in the Ergun equation, the experimental strut diameters are utilized. Unfortunately, the experimental strut diameters do not account for the solid deposited in the intersections, predicting a too high geometric specific surface area and a higher pressure drop of the open cell foams. The same conclusion is obtained from the dependence of pressure drop on pore diameter, which is as well strongly overrated by the modified Ergun equation when compared with the data and model of this work.

Since none of the predictions by the literature are totally satisfying and the published pressure drop results of foams vary considerably, it is not surprising that different authors use different approaches for representing their pressure drops. Another reason is presumably because irregularities in the morphology differ dependent on the foam manufacturer and the raw material used. For the reasons explained in this chapter, the simulated results could be used to represent the pressure drops of the foam structures developed in this work and commercial foams which have the similar geometric factors to those of this work. The error of the model given by this work sometimes can be up to around $\pm$20%, thus the correlation of this work should be used only for a first estimation of the pressure drop in open cell foams.

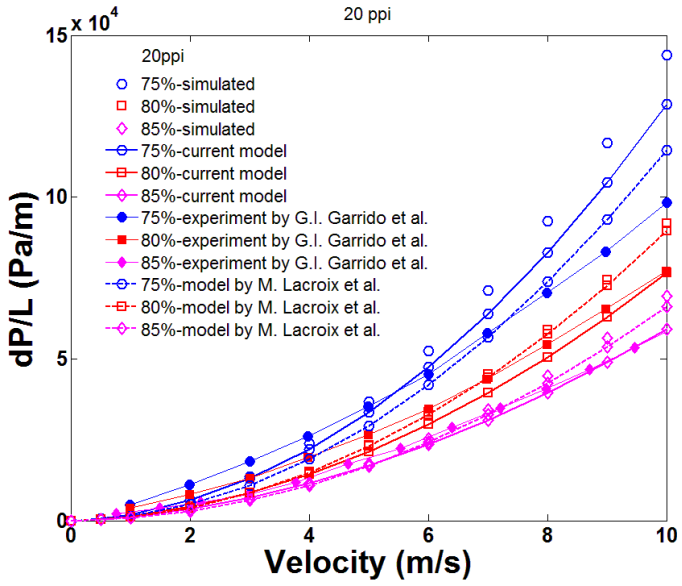

Figure 5.27 Comparison between pressure drop results of this work with literature data; different markers represent different porosities: circles-75%, squares-80%, and diamonds-85%

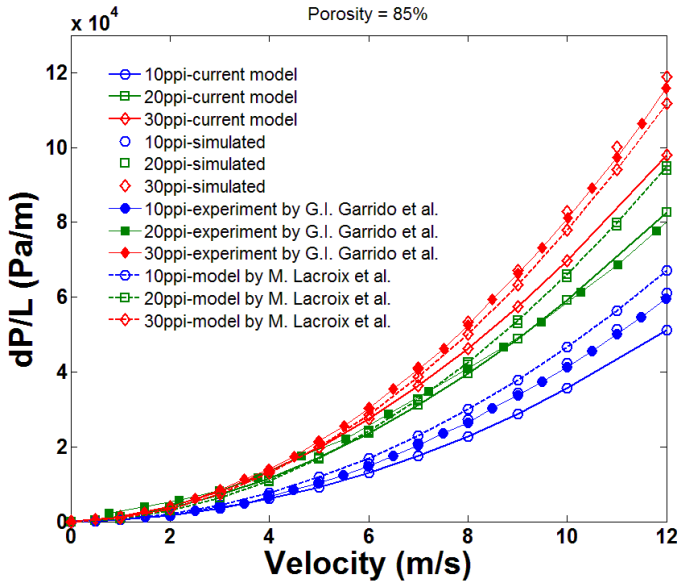

Figure 5.28 Comparison between pressure drop results of this work with literature data; different markers represent different pore densities: circles-10 ppi, squares-20 ppi, and diamonds-30 ppi

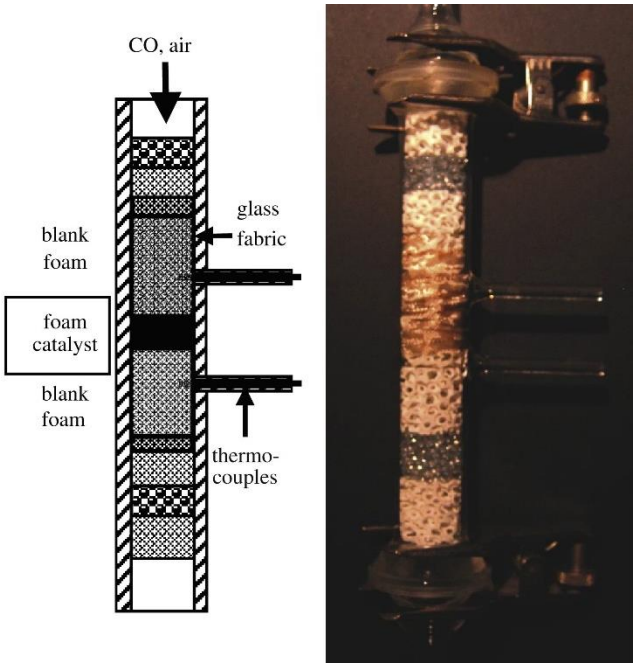

Figure 5.29 Apparatus used to measure pressure drops of foams in Garrido's work [46]

Table 5.12 Relevant geometrical characteristics of the tested Al6001 aluminum foams [7]

Parameter	10 ppi-90.3%	10 ppi-93.4%	10 ppi-95.6%	20 ppi-93.2%	40 ppi-93.0%
ppi	10	10	10	20	40
Porosity, ε (%)	90.3	93.4	95.6	93.2	93.0
Relative density (%)	9.7	6.6	4.4	6.8	7.0
Height (m)	0.04	0.04	0.04	0.04	0.04
Area per unit of volume, S_V (m^2m^{-3})	839	692	537	1156	1679
Fiber thickness, (mm)	0.529	0.45	0.445	0.367	0.324
Fiber length (mm)	1.87	1.785	1.351	1.218	1.072

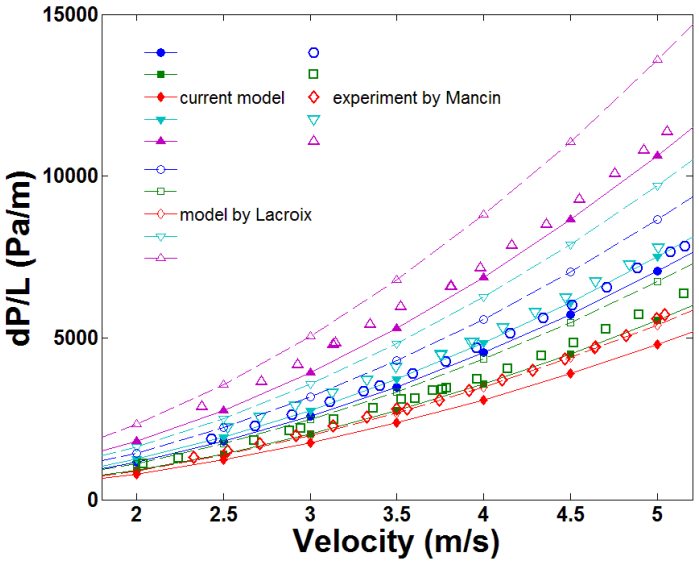

Figure 5.30 Comparison between pressure drop results of this work with literature data; different markers represent different foams: circles (10 ppi-90.3%), squares (10 ppi-93.4%), diamonds (10 ppi-95.6%), inverse triangles (20 ppi-93.2%), and triangles (40 ppi-93.0%)

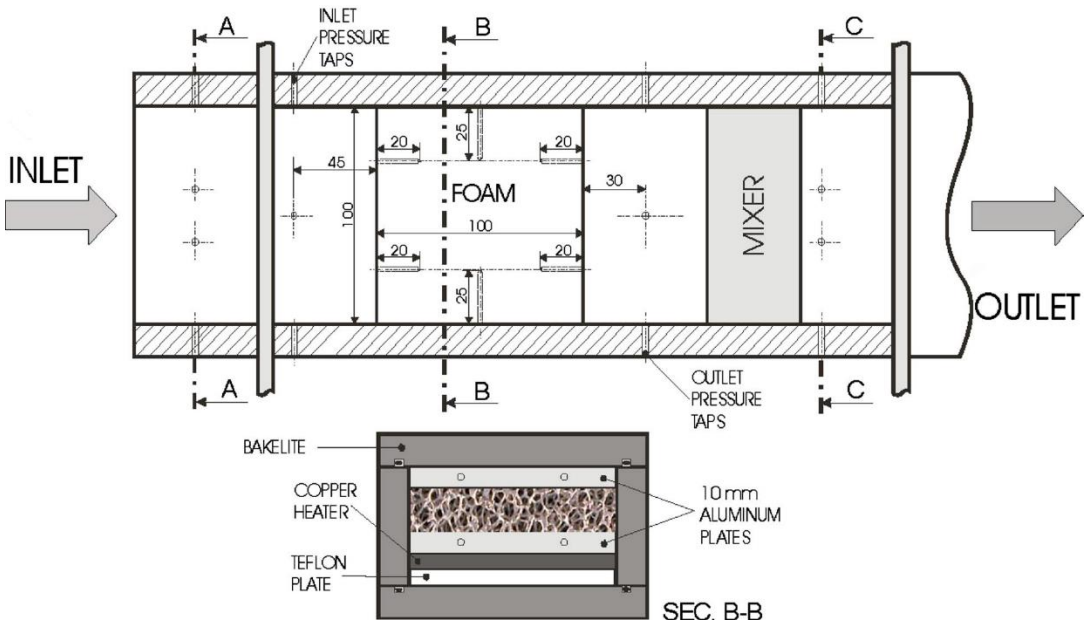

Figure 5.31 Experimental set-up in Mancin's work [7]

Equation (5.38)–Equation (5.40) give the dimensionless form of the pressure drop for open cell foams. The dimensionless forms for the foams with different pore density but the same porosity should be the same. Figure 5.32 shows the simulation results in dimensionless form for Reynolds number versus Hagen number. It is found that the simulation data with the same porosity correlate to a single line, which is given by

$$\log Hg = c' \log Re + c'' \tag{5.45}$$

The values of the coefficients c' and c'' are listed in Table 5.13.

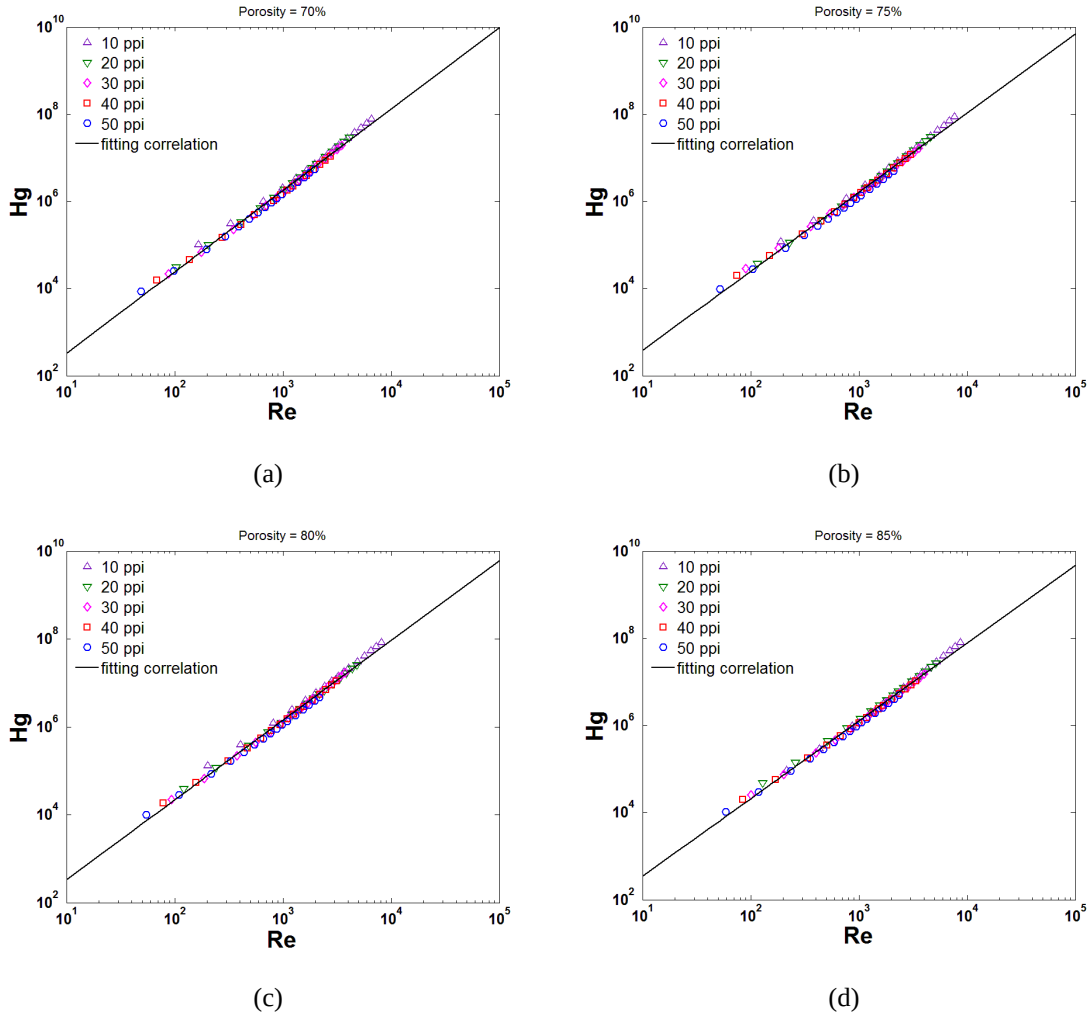

(a) (b)

(c) (d)

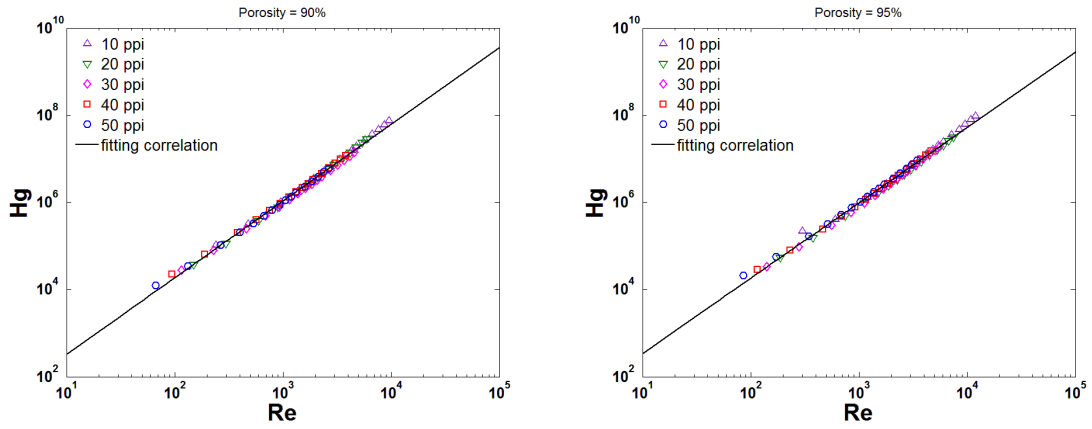

(e) (f)

Figure 5.32 Dimensionless air velocity (Reynolds number) versus dimensionless pressure drop (Hagen number) for the foams with different porosities: (a) 70%, (b) 75%, (c) 80%, (d) 85%, (e) 90%, and (f) 95%

Table 5.13 Values of coefficients c' and c'' of Equation (5.45) for foams with same porosity

Porosity	70%	75%	80%	85%	90%	95%
Coefficient c' of Equation (5.45)	1.8653	1.8131	1.8108	1.7820	1.7578	1.7261
Coefficient c'' of Equation (5.45)	0.6539	0.7699	0.7179	0.7542	0.7546	0.8086

5.5.3 Evaluation of the permeability

Permeability, an important flow parameter which governs the pressure drop in a porous medium, is calculated here for all of the foam structures investigated in this work. The results are reported for the inlet velocity v from 0.5 m/s to 20 m/s. For this computation, as described previously, a velocity inlet boundary condition is employed at the inlet while a pressure outlet boundary condition is used at the flow outlet. All other boundaries transverse to the main flow direction are made symmetric and a no-slip boundary condition is employed for the metal foam wall. The resulting pressure drop is then used to estimate the permeability K employing Darcy's law [66]:

$$-\frac{\partial P}{\partial x_i} = \frac{\mu}{K} v_m + \frac{\rho C_E}{\sqrt{K}} v_m^2 \tag{5.46}$$

$$v_m = \frac{A_p}{A_t} v \tag{5.47}$$

in which A_p is the average pore area, A_t the total cross-sectional area in a flow direction x_i (x, y or z), and C_E the Ergun's coefficient. v_m is the modified inlet velocity, based on the total cross-sectional area of the foam structure. $\sqrt{K}$ is called the flow penetration length. The pressure gradient is calculated considering only the fully developed region (identified as a region with a linear pressure gradient). Table 5.14–Table 5.18 show the permeability and Ergun's coefficient values for flow of air which is working fluid in simulations of present work. It may be noted here that the smallest sample size is ~10 mm in the flow direction, which is sufficient to obtain fully developed flow for the range of Reynolds numbers studied in this work. Table 5.19 reports some of values published in the open literature. It is worth pointing out that, for a fixed pore density or porosity, the experimental and numerical values of K published in the literature show a wide dispersion.

Table 5.14 Permeability and Ergun's coefficient predictions for 10 ppi foams

Foams	Porosity, ε (%)	Permeability, K ($\times 10^{-7}\mathrm{m}^2$)	Ergun's coefficient, C_E
10 ppi	70	0.429	0.446
	75	0.439	0.240
	80	0.348	0.117
	85	0.351	0.075
	90	1.137	0.065
	95	2.095	0.045

Table 5.15 Permeability and Ergun's coefficient predictions for 20 ppi foams

Foams	Porosity, ε (%)	Permeability, K ($\times 10^{-7}\mathrm{m}^2$)	Ergun's coefficient, C_E
20 ppi	70	1.489	1.351
	75	0.576	0.441
	80	0.269	0.149
	85	0.160	0.071
	90	2.429	0.154
	95	0.759	0.034

Table 5.16 Permeability and Ergun's coefficient predictions for 30 ppi foams

Foams	Porosity, ε (%)	Permeability, K ($\times 10^{-7}\mathrm{m}^2$)	Ergun's coefficient, C_E
30 ppi	70	1.569	1.517
	75	0.078	0.174
	80	1.019	0.442
	85	0.171	0.089
	90	0.193	0.042
	95	0.480	0.040

Table 5.17 Permeability and Ergun's coefficient predictions for 40 ppi foams

Foams	Porosity, ε (%)	Permeability, K ($\times 10^{-7}\mathrm{m}^2$)	Ergun's coefficient, C_E
40 ppi	70	0.156	0.545
	75	0.072	0.209
	80	0.105	0.149
	85	0.092	0.074
	90	0.154	0.059
	95	0.304	0.043

Table 5.18 Permeability and Ergun's coefficient predictions for 50 ppi foams

Foams	Porosity, ε (%)	Permeability, K ($\times 10^{-7}\mathrm{m}^2$)	Ergun's coefficient, C_E
50 ppi	70	0.047	0.409
	75	0.031	0.165
	80	0.038	0.107
	85	0.057	0.080
	90	0.092	0.065
	95	0.149	0.044

Table 5.19 Summary of some permeability values published in the literature

ppi	Porosity (%)	K ($\times 10^{-7}$ m^2)	Reference
10	91.3	1.731	[67], num.*
	92.0	1.040	[43], exp.**
	92.6	4.290	[7], exp.
	94.9	1.490	[14], exp.
20	91.3	1.606	[67], num.
	92.0	0.760	[43], exp.
	92.3	1.100	[14], exp.
	93.5	2.420	[23], exp.
30	90.0	1.644	[68], exp.
	93.0	0.630	[69], exp.

*Numerical data; **Experimental data.

5.5.4 Friction factor and heat transfer coefficient

Calculating the pressure drop of packed beds is derived from the definition of the friction factor f [49, 70]:

$$\frac{\Delta P}{L} = f \cdot \rho \cdot \frac{v^2}{\varepsilon^2} \cdot \frac{1}{d_h} \tag{5.48}$$

According to Ergun's work [48, 49], the friction factor f can be expressed by

$$f = A \cdot \frac{1}{Re} + B \tag{5.49}$$

Substituting Equation (5.49) into Equation (5.48) with $Re = \rho d_h v/\mu$ yields

$$\frac{\Delta P}{L} = A \frac{\mu}{\varepsilon d_h^2} v + B \frac{\rho}{\varepsilon^2 d_h} v^2 \tag{5.50}$$

Comparing Equation (5.50) with Equation (5.35) one can obtain

$$A = C_1, B = C_2 \tag{5.51}$$

Thus, Equation (5.49) can be written as

$$f = C_1 \cdot \frac{1}{Re} + C_2 \tag{5.52}$$

Then substituting Equation (5.36) and Equation (5.37) into Equation(5.52) yields

$$f = 32\frac{\tau^2}{Re} + \frac{1}{2}\tau^3 \tag{5.53}$$

Here tortuosity τ is given by Equation (5.33). It can be seen that the friction factor of open cell foams is a function of the Reynolds number of flow and tortuosity, and thus of Reynolds number of flow and the porosity of foams. Ergun et al., Inayat et al., and Dietrich et al. also reported similar results about the friction factor of open cell foams. However, only in this work the friction factor is presented by the tortuosity of foams.

The friction factor data for the foam structures designed in this work are shown in Figure 5.33. It may be inferred from Figure 5.33 that friction factor scales as $1/Re$ at lower Reynolds numbers, while at higher Reynolds numbers, the non-linear term C_2 begins to dominate because of the inertial effects. This deviation from linear to non-linear behavior is observed for $Re \sim > 100$. This dependence has also been investigated by the work of Paek et al. [16] and Vafai et al. [38] for low velocities. At higher Reynolds numbers, inertial effects become dominant and pressure drop is no longer a linear function of velocity. More specifically, when Re is equal to 0.1, viscosity accounts for around 99% of the pressure drop, while for Re is equal to 3000, kinetic effects account for 97% of the pressure drop.

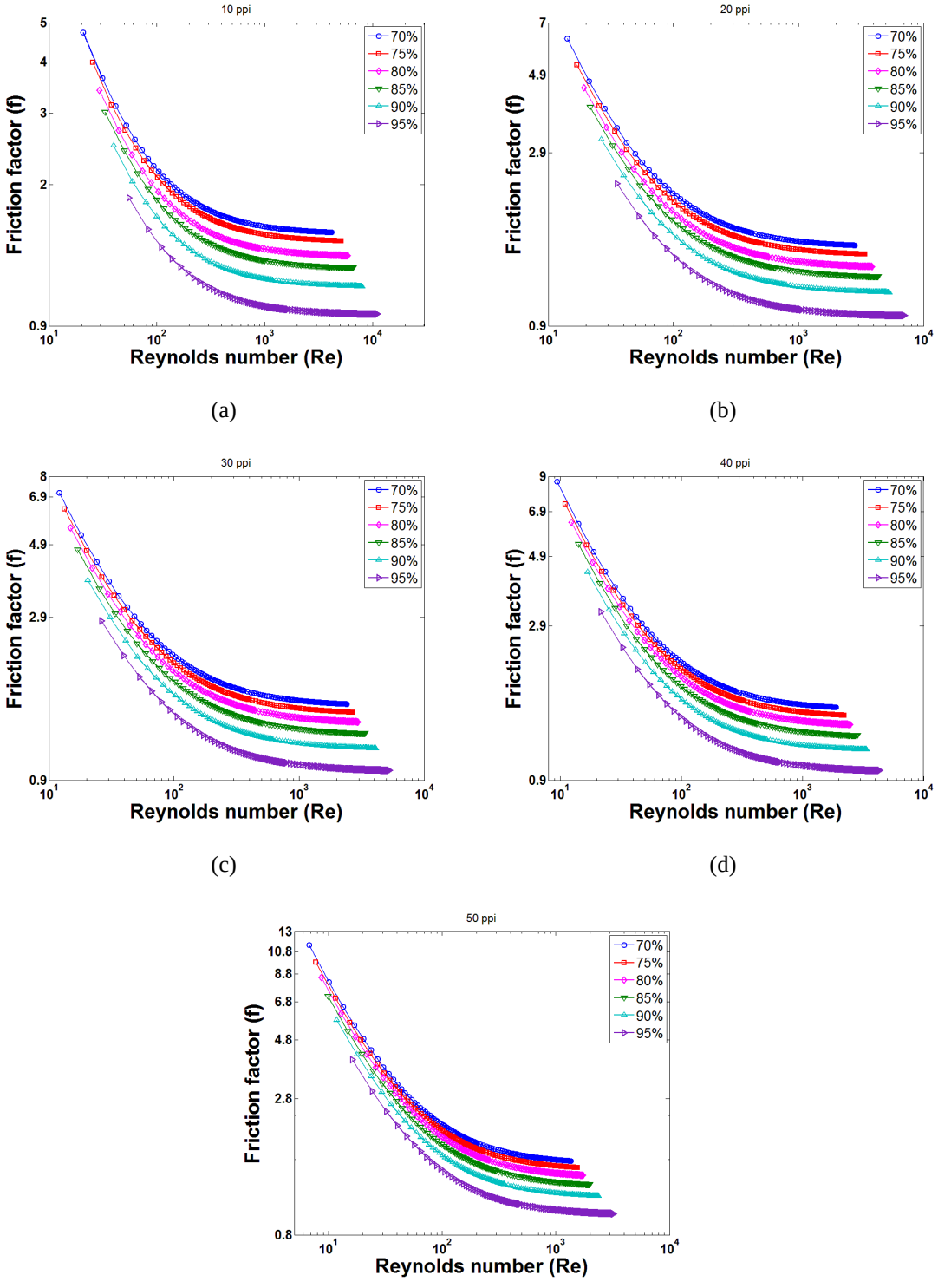

Figure 5.33 Friction factor as a function of Reynolds number for foams of different pore densities and porosities: (a)10 ppi, (b) 20 ppi, (c) 30 ppi, (d) 40 ppi, and (e) 50 ppi

Beginning with the converged flow field, heat transfer coefficients are computed by imposing a constant heat flux, q'' at the interface separating the solid and fluid regions, that is, solving the energy equation in the fluid region using the converged flow solution. Thus, it is possible to calculate the average interfacial heat transfer coefficient h, which is defined as

$$h = \frac{q''}{\bar{T}_{wall} - \bar{T}_{air}} \tag{5.54}$$

which is an average value representative of the entire fluid domain. In this equation, and are the mean value of temperature for the wall and air, respectively. This numerical heat transfer coefficient is an average heat transfer coefficient since the heat flux is imposed uniformly on the entire surface. The heat transfer coefficients for the 10 ppi, 20 ppi, 30 ppi, 40 ppi, and 50 ppi foam structures are shown in Figure 5.34. The pore density effects on the heat transfer behavior at constant porosity 95% are highlighted in Figure 5.35 where the heat transfer coefficient is plotted against the air velocity.

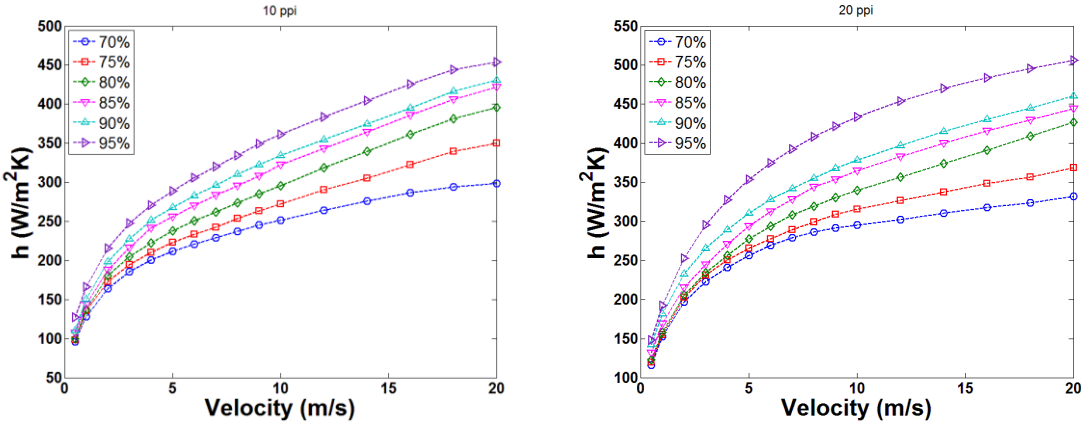

(a) (b)

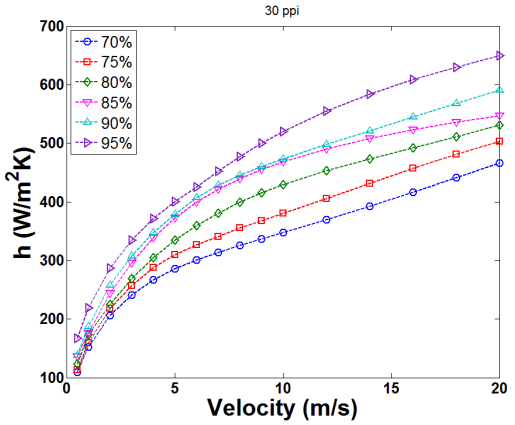

(c)

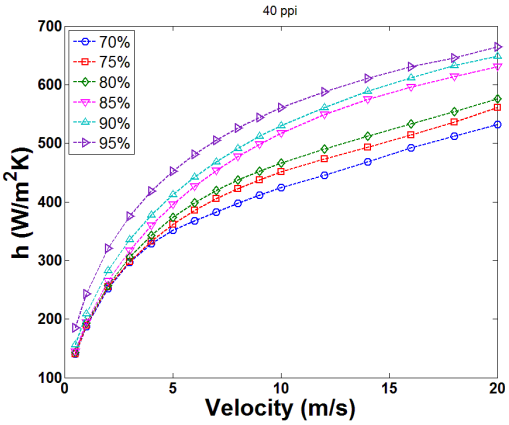

(d)

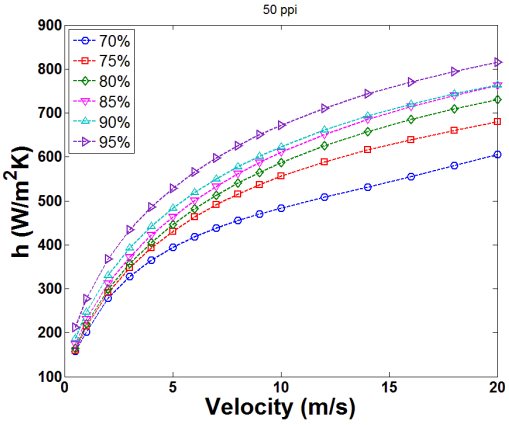

(e)

Figure 5.34 Heat transfer coefficient as a function of velocity with air as the interstitial fluid: (a) 10 ppi, (b) 20 ppi, (c) 30 ppi, (d) 40 ppi, and (e) 50 ppi

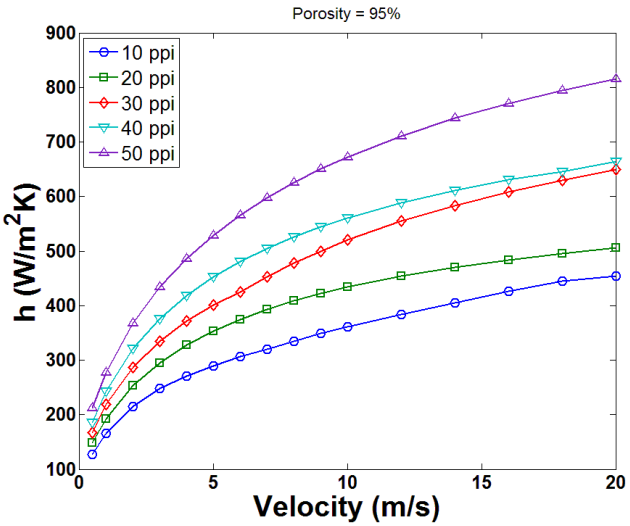

Figure 5.35 Pore density effects at constant porosity 95% on the heat transfer coefficient plotted against air velocity

As shown in Figure 5.34, the heat transfer coefficient increases with the air velocity and the heat transfer coefficient increases when the porosity increases at constant pore density. All foam structures exhibit similar behavior, especially for low velocities. This is expected since at lower range of velocities, heat transfer is predominated by conduction and little convection, it is similar for the foams as they have the same pore density. At higher velocities, it is seen that the convection effects become dominant and deviations are observed between the foams. Similar results also are found by Diani et al. [1] and Mancin et al. [7, 9]. The data can be interpolated by the simple equation:

$$h = b \cdot v^{d} \tag{5.55}$$

Table 5.20 and Table 5.24 report the values of the coefficients b and d of Equation (5.55). The authors would like to underline that the values of the exponent d for five different foams are very close. This means that the investigated foams show almost the

same dependence on the air velocity. From Figure 5.35. it can be seen that at constant porosity the heat transfer coefficient increases when increasing the pore density.

Table 5.20 Values of the coefficients b and d of Equation (5.55) for 10 ppi foams

10 ppi	70%	75%	80%	85%	90%	95%
Coefficient b of Equation (5.55)	132.9	132.5	133.4	143.1	151.9	168.1
Coefficient d of Equation (5.55)	0.2771	0.32	0.3568	0.3569	0.3461	0.3337

Table 5.21 Values of the coefficients b and d of Equation (5.55) for 20 ppi foams

20 ppi	70%	75%	80%	85%	90%	95%
Coefficient b of Equation (5.55)	166.8	167	163.5	174.6	188.4	210
Coefficient d of Equation (5.55)	0.2417	0.2709	0.3184	0.3158	0.3009	0.3063

Table 5.22 Values of the coefficients b and d of Equation (5.55) for 30 ppi foams

30 ppi	70%	75%	80%	85%	90%	95%
Coefficient b of Equation (5.55)	156.9	166.5	182.5	205.7	207.4	224.4
Coefficient d of Equation (5.55)	0.355	0.366	0.3633	0.3435	0.3545	0.3599

Table 5.23 Values of the coefficients b and d of Equation (5.55) for 40 ppi foams

40 ppi	70%	75%	80%	85%	90%	95%
Coefficient b of Equation (5.55)	201	203.7	208.3	212.5	226.4	264.1
Coefficient d of Equation (5.55)	0.3257	0.3404	0.3445	0.3752	0.3614	0.3185

Table 5.24 Values of the coefficients b and d of Equation (5.55) for 50 ppi foams

50 ppi	70%	75%	80%	85%	90%	95%
Coefficient b of Equation (5.55)	222.7	234.1	236.8	246.3	265.7	298
Coefficient d of Equation (5.55)	0.3355	0.3664	0.3856	0.3863	0.3623	0.3456

5.5.5 Determining a hydraulic diameter of open cell foams based on pore density

As described in Chapter 5.3, Equation (5.35) has a universal form for all designed foam structures, independent of material and geometrical factors. Therefore, it is possible to obtain the hydraulic diameter for new open cell foams with unknown geometric parameters, e.g., specific surface area, strut diameter, pore diameter and window diameter, based on pressure drop results. Then it is not necessary to perform expensive and complicated magnetic resonance imaging experiments to find the specific surface area for calculation of the hydraulic diameter according to Equation (5.20). Figure 5.36 shows the comparison of the hydraulic diameter calculated from the specific surface area $d_h(S_V)$ and from the pressure drop $d_h(P)$ simulation for open cell foams designed in present work. The data of Figure 5.36 are listed in Table 5.25. It can be seen that these two hydraulic diameters correspond satisfactorily to each other.

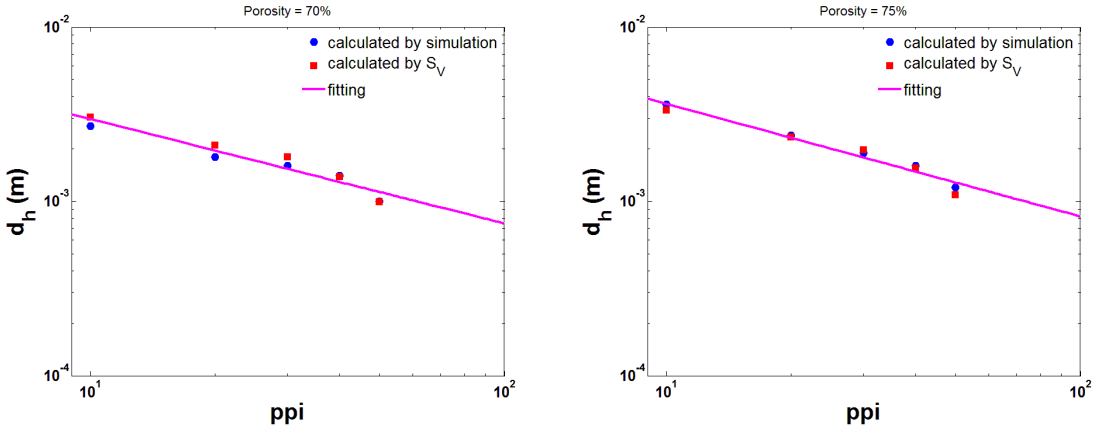

(a) (b)

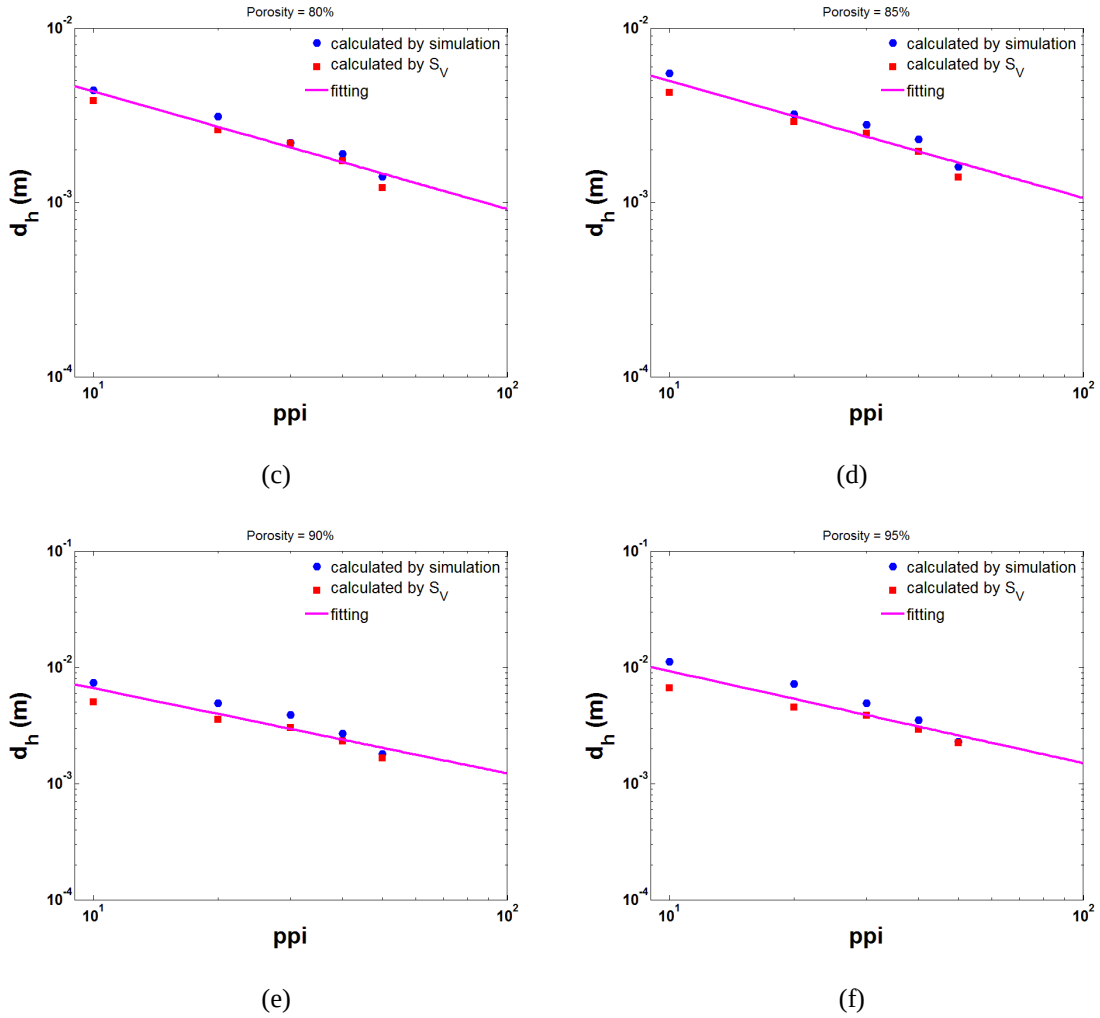

Figure 5.36 Comparison of hydraulic diameters calculated from pressure drop simulations with those calculated from the specific surface area for (a) 70%, (b) 75%, (c) 80%, (d) 85%, (e) 90%, and (f) 95%

Table 5.25 Hydraulic diameters calculated from the specific surface area $d_h(S_V)$ (mm) and from pressure drop simulation $d_h(P)$ (mm)

ε	10 ppi		20 ppi		30 ppi		40 ppi		50 ppi	
(%)	$d_h(S_V)$	$d_h(P)$	$d_h(S_V)$	$d_h(P)$	$d_h(S_V)$	$d_h(P)$	$d_h(S_V)$	$d_h(P)$	$d_h(S_V)$	$d_h(P)$
70	3.04	2.80	2.10	1.89	1.80	1.69	1.39	1.40	0.99	1.00
75	3.34	3.56	2.34	2.37	1.97	1.93	1.55	1.55	1.09	1.16
80	3.84	4.37	2.60	3.05	2.18	2.20	1.73	1.86	1.22	1.39
85	4.28	4.45	2.90	3.18	2.48	2.75	1.96	2.27	1.39	1.58
90	4.99	5.36	3.54	4.85	3.02	3.86	2.31	2.65	1.65	1.76
95	6.63	7.08	4.54	6.16	3.86	4.84	2.92	3.47	2.23	2.28

Furthermore, Figure 5.36 presents the fitting correlations between the nominal ppi number and the hydraulic diameter determined by pressure drop simulations. The ppi number is provided by the foams manufacturer and therefore a well-known parameter for each foam sample. The correlations are the fitting function of the simulation values for all type of investigated open cell foams with the porosity of from 70% to 95% and they are described by

$$d_h = H \cdot ppi^N \tag{5.56}$$

The values of coefficients H and N are shown in Table 5.26. Thus, it is possible to obtain the hydraulic diameter, which is an important characteristic parameter of open cell foams, based on the ppi number. The hydraulic diameter calculated from Equation (5.56) can be used as the first estimation for the open cell foams designed in present work.

Table 5.26 Values of the coefficients H and N of Equation (5.56)

Porosity	70%	75%	80%	85%	90%	95%
Coefficient H of Equation (5.56)	0.012	0.016	0.021	0.024	0.036	0.056
Coefficient N of Equation (5.56)	-0.599	-0.645	-0.675	-0.673	-0.733	-0.793

5.5.6 Methods of fabrication for designed open cell foams

The open cell foams designed in this work can be produced by rapid prototyping using different additive manufacturing techniques, e.g., selective laser melting (SLM), selective electron beam melting (SEBM), selective laser sintering (SLS), digital light processing (DLP), stereolithography (SLA), 3D printing, and electron beam melting (EBM), etc. Thus, with these techniques it is possible to control the morphological and geometrical parameters of foam structures with a high degree of reproducibility and vary

these properties in a controlled manner and it is possible to perform computational design for open cell foams with defined flow properties using the Laguerre-Voronoi model developed in Chapter 3 and 4 of this work. Figure 5.37 shows the copper and aluminum foams fabricated by EBM technology. EBM is especially suited to direct digital manufacturing in metal and is a leading candidate to replace forging and casting as a means of producing spares, offering lead times measured in hours or days, not months or years. This emerging manufacturing process is capable of producing fully dense, functional metal parts without the need for molds, dies, or complex fixtures [71].

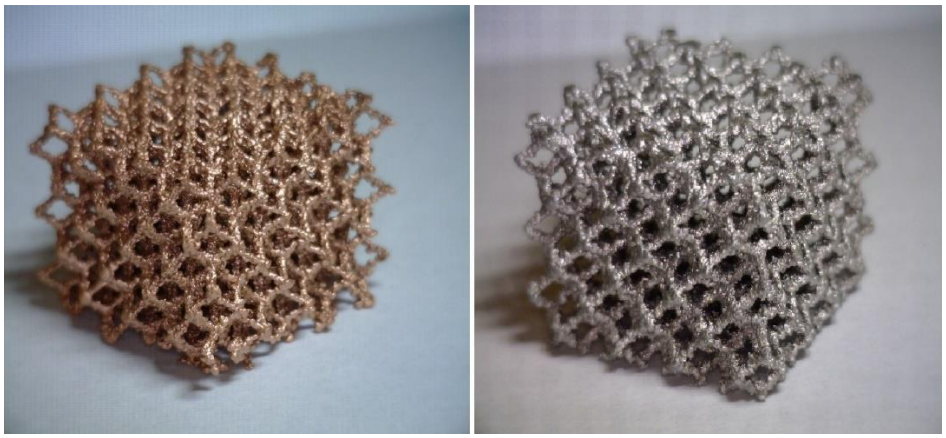

Figure 5.37 Copper foam (left) and aluminum foam (right) fabricated by EBM [72]

5.6 Conclusions

A pressure drop correlation with a universal form is developed based on theoretical grounds and the tortuosity of open cell foams is taken into account for the pressure drop. The developed correlation then is validated using numerical simulations on pressure drop properties of aluminum foam structures of pore densities between 10 ppi and 50 ppi and porosities from 70% to 95%, with the commercial CFD analysis package: ANSYS Fluent. The numerical results for pressure drop are compared with the prediction by the theoretical

correlation. The results show that the pressure drop of foams increases with increasing pore density and decreasing porosity. The numerical results are consistent with the prediction of the theoretical correlation.

Permeability and friction factor of foams are also evaluated. For the low Reynolds number range, friction factor scales as $1/Re$ at lower Reynolds numbers, while at higher Reynolds numbers, the non-linear term begins to dominate because of the inertial effects. When Re is equal to 0.1, viscosity accounts for around 99% of the pressure drop, while for Re is equal to 3000, kinetic effects account for 97% of the pressure drop. Then the computed interstitial heat transfer coefficients are investigated. The heat transfer coefficient increases with the air velocity and the heat transfer coefficient increases when the porosity increases at constant pore density. At constant porosity the heat transfer coefficient increases when increasing the pore density. Furthermore, a correlation is given to derive the hydraulic diameter from the ppi number so that performing expensive and complicated magnetic resonance imaging experiments to find the specific surface area for calculation of the hydraulic diameter is not necessary anymore.

Finally, with additive manufacturing techniques, e.g., SLS, DLP, and EBM, it is possible to control the morphological and geometrical parameters of foam structures with a high degree of reproducibility and vary these properties in a controlled manner and it is possible to perform computational design for open cell foams with defined flow properties using the Laguerre-Voronoi model developed in Chapter 3 and Chapter 4 of this work.

REFERENCE

[1] Diani, A., et al., *Numerical investigation of pressure drop and heat transfer through reconstructed metal foams and comparison against experiments.* International Journal of Heat and Mass Transfer, 2015. **88**: p. 508-515.

[2] de Carvalho, T.P., et al. *Experimental and Tomography-Based CFD Investigations of the Flow in Open Cell Metal Foams With Application to Aero Engine Separators*. in *ASME Turbo Expo 2015: Turbine Technical Conference and Exposition*. 2015. American Society of Mechanical Engineers.

[3] Inayat, A., et al., *Development of a new pressure drop correlation for open-cell foams based completely on theoretical grounds: Taking into account strut shape and geometric tortuosity.* Chemical Engineering Journal, 2016. **287**: p. 704-719.

[4] Ambrosio, G., et al., *The effect of open-cell metal foams strut shape on convection heat transfer and pressure drop.* Applied Thermal Engineering, 2016. **103**: p. 333-343.

[5] Ghosh, I., *Heat transfer correlation for high-porosity open-cell foam.* International Journal of Heat and Mass Transfer, 2009. **52**(5-6): p. 1488-1494.

[6] Mancin, S., et al., *Heat transfer during air flow in aluminum foams.* International Journal of Heat and Mass Transfer, 2010. **53**(21-22): p. 4976-4984.

[7] Mancin, S., et al., *Heat Transfer Performance of Aluminum Foams.* Journal of Heat Transfer, 2011. **133**(6): p. 060904.

[8] Dietrich, B., *Heat transfer coefficients for solid ceramic sponges–Experimental results and correlation.* International Journal of Heat and Mass Transfer, 2013. **61**: p. 627-637.

[9] Mancin, S., et al., *Experimental air heat transfer and pressure drop through copper foams.* Experimental Thermal and Fluid Science, 2012. **36**: p. 224-232.

[10] Dietrich, B., *Pressure drop correlation for ceramic and metal sponges.* Chemical Engineering Science, 2012. **74**: p. 192-199.

[11] Zhao, C.Y., *Review on thermal transport in high porosity cellular metal foams with open cells.* International Journal of Heat and Mass Transfer, 2012. **55**(13-14): p. 3618-3632.

[12] Dietrich, B., *Heat transfer coefficients for solid ceramic sponges – Experimental results and correlation.* International Journal of Heat and Mass Transfer, 2013. **61**: p. 627-637.

[13] Mancin, S., et al., *Pressure drop during air flow in aluminum foams.* International Journal of Heat and Mass Transfer, 2010. **53**(15-16): p. 3121-3130.

[14] Bhattacharya, A., V. Calmidi, and R. Mahajan, *Thermophysical properties of high porosity metal foams.* International Journal of Heat and Mass Transfer, 2002. **45**(5): p. 1017-1031.

[15] Kim, S., J. Paek, and B. Kang, *Flow and heat transfer correlations for porous fin in a plate-fin heat exchanger.* Journal of heat transfer, 2000. **122**(3): p. 572-578.

[16] Paek, J., et al., *Effective thermal conductivity and permeability of aluminum foam materials1.* International Journal of Thermophysics, 2000. **21**(2): p. 453-464.

[17] Dukhan, N., *Correlations for the pressure drop for flow through metal foam.* Experiments in fluids, 2006. **41**(4): p. 665-672.

[18] Dukhan, N. and P. Patel, *Equivalent particle diameter and length scale for pressure drop in porous metals.* Experimental Thermal and Fluid Science, 2008. **32**(5): p. 1059-1067.

[19] Crosnier, S., et al. *Modeling of gas flow through metallic foams*. in *1st European Hydrogen Energy Conference*. 2003.

[20] Khayargoli, P., et al. *The impact of microstructure on the permeability of metal foams*. in *CSME forum*. 2004.

[21] Topin, F., et al., *Experimental analysis of multiphase flow in metallic foam: flow laws, heat transfer and convective boiling.* Advanced Engineering Materials, 2006. **8**(9): p. 890-899.

[22] Tadrist, L., et al., *About the use of fibrous materials in compact heat exchangers.* Experimental thermal and fluid science, 2004. **28**(2): p. 193-199.

[23] Liu, J., et al., *Measurement and correlation of friction characteristic of flow through foam matrixes.* Experimental thermal and fluid science, 2006. **30**(4): p. 329-336.

[24] Richardson, J., Y. Peng, and D. Remue, *Properties of ceramic foam catalyst supports: pressure drop.* Applied Catalysis A: General, 2000. **204**(1): p. 19-32.

[25] Hwang, J.-J., et al., *Measurement of interstitial convective heat transfer and frictional drag for flow across metal foams.* Journal of Heat Transfer, 2002. **124**(1): p. 120-129.

[26] Kim, T., et al., *An experimental study on thermal transport in lightweight metal foams at high Reynolds numbers.* Proceedings of Compact Heat Exchangers; A Festschrift on the 60th Birthday of Ramesh K. Shah, 2002: p. 227-232.

[27] Boomsma, K. and D. Poulikakos, *The effects of compression and pore size variations on the liquid flow characteristics in metal foams.* Journal of fluids engineering, 2002. **124**(1): p. 263-272.

[28] Boomsma, K., D. Poulikakos, and F. Zwick, *Metal foams as compact high performance heat exchangers.* Mechanics of materials, 2003. **35**(12): p. 1161-1176.

[29] Edouard, D., et al., *Pressure drop modeling on SOLID foam: State-of-the art correlation.* Chemical Engineering Journal, 2008. **144**(2): p. 299-311.

[30] Mahjoob, S. and K. Vafai, *A synthesis of fluid and thermal transport models for metal foam heat exchangers.* International Journal of Heat and Mass Transfer, 2008. **51**(15-16): p. 3701-3711.

[31] Lacroix, M., et al., *Pressure drop measurements and modeling on SiC foams.* Chemical Engineering Science, 2007. **62**(12): p. 3259-3267.

[32] Du Plessis, P., et al., *Pressure drop prediction for flow through high porosity metallic foams.* Chemical Engineering Science, 1994. **49**(21): p. 3545-3553.

[33] Fourie, J.G. and J.P. Du Plessis, *Pressure drop modelling in cellular metallic foams.* Chemical Engineering Science, 2002. **57**(14): p. 2781-2789.

[34] Incera Garrido, G., et al., *Mass transfer and pressure drop in ceramic foams: A description for different pore sizes and porosities.* Chemical Engineering Science, 2008. **63**(21): p. 5202-5217.

[35] Moreira, E.A., M.D.M. Innocentini, and J.R. Coury, *Permeability of ceramic foams to compressible and incompressible flow.* Journal of the European Ceramic Society, 2004. **24**(10-11): p. 3209-3218.

[36] Beavers, G.S. and E.M. Sparrow, *Non-Darcy flow through fibrous porous media.* Journal of Applied Mechanics, 1969. **36**(4): p. 711-714.

[37] Hamaguchi, K., S. Takahashi, and H. Miyabe, *Flow friction and heat transfer characteristics of a regenerator matrix (case of foamed metal).* Trans. Jpn. Soc. Mech. Eng, 1983. **49**: p. 1991-2000.

[38] Vafai, K. and C. Tien, *Boundary and inertia effects on convective mass transfer in porous media.* International Journal of Heat and Mass Transfer, 1982. **25**(8): p. 1183-1190.

[39] Lin, Y., et al., *Experimental study on heat transfer and pressure drop of recuperative heat exchangers using carbon foam.* Journal of Heat Transfer, 2010. **132**(9): p. 091902.

[40] Calmidi, V. and R. Mahajan, *Forced convection in high porosity metal foams.* Journal of Heat Transfer, 2000. **122**(3): p. 557-565.

[41] Calmidi, V.V., *Transport phenomena in high porosity fibrous metal foams*. 2008: UMI.

[42] Hsieh, W., et al., *Experimental investigation of heat-transfer characteristics of aluminum-foam heat sinks.* International Journal of Heat and Mass Transfer, 2004. **47**(23): p. 5149-5157.

[43] Kim, S.Y., B.H. Kang, and J.-H. Kim, *Forced convection from aluminum foam materials in an asymmetrically heated channel.* International Journal of Heat and Mass Transfer, 2001. **44**(7): p. 1451-1454.

[44] Younis, L. and R. Viskanta, *Experimental determination of the volumetric heat transfer coefficient between stream of air and ceramic foam.* International Journal of Heat and Mass Transfer, 1993. **36**(6): p. 1425-1434.

[45] Dukhan, N. and K.-C. Chen, *Heat transfer measurements in metal foam subjected to constant heat flux.* Experimental Thermal and Fluid Science, 2007. **32**(2): p. 624-631.

[46] Garrido, G.I., et al., *Mass transfer and pressure drop in ceramic foams: a description for different pore sizes and porosities.* Chemical Engineering Science, 2008. **63**(21): p. 5202-5217.

[47] Garrido, G.I. and B. Kraushaar-Czarnetzki, *A general correlation for mass transfer in isotropic and anisotropic solid foams.* Chemical Engineering Science, 2010. **65**(6): p. 2255-2257.

[48] Ergun, S. and A.A. Orning, *Fluid flow through randomly packed columns and fluidized beds.* Industrial & Engineering Chemistry, 1949. **41**(6): p. 1179-1184.

[49] Ergun, S., *Fluid flow through packed columns.* Chem. Eng. Prog., 1952. **48**: p. 89-94.

[50] Bird, R.B., et al., *Transport phenomena*. 2007: John Wiley & Sons.

[51] Gibson, L.J. and M.F. Ashby, *Cellular solids: structure and properties*. 1999: Cambridge university press.

[52] Kozeny, J., *About capillaries conducting water in the earth.* Sitzber. Akd. Wiss. Wien, Math. Naurv. Kasse, 1927. **136**: p. 271-306.

[53] Loudon, C. and K. McCulloh, *Application of the Hagen—Poiseuille Equation to Fluid Feeding through Short Tubes.* Annals of the Entomological Society of America, 1999. **92**(1): p. 153-158.

[54] Carman, P.C., *Fluid flow through granular beds.* Transactions-Institution of Chemical Engineeres, 1937. **15**: p. 150-166.

[55] Sobieski, W., Q. Zhang, and C. Liu, *Predicting Tortuosity for Airflow Through Porous Beds Consisting of Randomly Packed Spherical Particles.* Transport in Porous Media, 2012. **93**(3): p. 431-451.

[56] Inayat, A., et al., *Predicting the Specific Surface Area and Pressure Drop of Reticulated Ceramic Foams Used as Catalyst Support.* Advanced Engineering Materials, 2011. **13**(11): p. 990-995.

[57] Inayat, A., et al., *Periodic open-cell foams: Pressure drop measurements and modeling of an ideal tetrakaidecahedra packing.* Chemical Engineering Science, 2011. **66**(12): p. 2758-2763.

[58] Huu, T.T., et al., *Towards a more realistic modeling of solid foam: use of the pentagonal dodecahedron geometry.* Chemical Engineering Science, 2009. **64**(24): p. 5131-5142.

[59] Ahmed, J., C. Pham-Huu, and D. Edouard, *A predictive model based on tortuosity for pressure drop estimation in 'slim'and 'fat'foams.* Chemical engineering science, 2011. **66**(20): p. 4771-4779.

[60] Inayat, A., et al., *Determining the specific surface area of ceramic foams: The tetrakaidecahedra model revisited.* Chemical Engineering Science, 2011. **66**(6): p. 1179-1188.

[61] Bianchi, E., et al., *An appraisal of the heat transfer properties of metallic open-cell foams for strongly exo-/endo-thermic catalytic processes in tubular reactors.* Chemical engineering journal, 2012. **198**: p. 512-528.

[62] Woudberg, S. and F. Smit, *Comparative Analysis of Geometric Models for Predicting the Dynamic Specific Surface of Foamlike Media.* 2014.

[63] Diani, A., et al., *Numerical Analysis of Air Flow through Metal Foams.* Energy Procedia, 2014. **45**: p. 645-652.

[64] Wikipedia. *Turbulence*. 2016; Available from: https://en.wikipedia.org/wiki/Turbulence.

[65] Dietrich, B., et al., *Pressure drop measurements of ceramic sponges—Determining the hydraulic diameter.* Chemical Engineering Science, 2009. **64**(16): p. 3633-3640.

[66] Bear, J., *Dynamics of fluids in porous media*. 2013: Courier Corporation.

[67] Bodla, K.K., J.Y. Murthy, and S.V. Garimella, *Microtomography-Based Simulation of Transport through Open-Cell Metal Foams.* Numerical Heat Transfer, Part A: Applications, 2010. **58**(7): p. 527-544.

[68] Kamath, P.M., C. Balaji, and S. Venkateshan, *Experimental investigation of flow assisted mixed convection in high porosity foams in vertical channels.* International Journal of Heat and Mass Transfer, 2011. **54**(25): p. 5231-5241.

[69] Kurtbaş, İ., N. Celik, and İ. Dinçer, *Exergy transfer in a porous rectangular channel.* Energy, 2010. **35**(1): p. 451-460.

[70] Bird, R.B., *Transport phenomena.* Applied Mechanics Reviews, 2002. **55**(1): p. R1-R4.

[71] L-IMST. *NEXT GENERATION MANUFACTURING: BUILDING NEAR-NET-SHAPE PARTS ON DEMAND*. 2016; Available from: http://www.mse.ncsu.edu/imst/manufacturing.

[72] CAMAL. *EBM Produced Copper & Aluminum Network Structures*. 2016; Available from: https://camal.ncsu.edu/ebm-produced-copper-aluminum-network-structures/.

CHAPTER 6 CONCLUSIONS AND FUTURE WORK

6.1 Conclusions

In this dissertation, the effect of V_2O_5 as the sintering aid on the density and hardness of ZnO–TiO_2 ceramics and cermets made of ZnO–TiO_2 ceramics and copper were investigated as shown in Chapter 1. The density of ZnO–TiO_2 ceramics was increased up to 95% of theoretical density with an additive of 2 wt.% V_2O_5 at low sintering temperatures 900–920 ℃ for 4 hours. The hardness of ZnO–TiO_2 ceramics added 2 wt.% V_2O_5 addition sintered at a 920 ℃ for 4 hours could reach to 560 HV. For the cermets made of ZnO–TiO_2 ceramics and copper, up to 90% of theoretical density can be obtained when the sintering temperature is 960 ℃ for 4 hours. The hardness of cermets made of ZnO–TiO_2 ceramics and 80 wt.% Cu can reach 130 HV. The prospective applications using ZnO–TiO_2 ceramics and cermets made of ZnO–TiO_2 ceramics and copper as raw materials of 3D printing would be very attractive.

In Chapter 2, porous alumina ceramics with different porosity were fabricated by two different methods: one combined the starch consolidation process with the gel-casting process using corn starch as the pore-forming agent and also as the binder. The other used hollow microspheres as the pore-forming agent. For both of two methods, the bulk density, porosity, and microstructure of the obtained alumina ceramics were studied. It was found that the total porosity range of sintered samples with different amount of starch contents from 10 to 50 vol% is 14.8–55.3% and the total porosity increased with the increase of starch content. The relationship between the linear shrinkage of porous alumina ceramics and the starch content also was discussed. The compressive strength of the sintered samples

varied within the range of 5.89–24.16 MPa, corresponding to the starch content of 50–10 vol%. Meanwhile, it was found that the total porosity range of specimens prepared by the second method with the different amount of hollow microsphere contents from 2.0 wt.% to 4.0 wt.% was 69.3–75.6% and the total porosity increased with the increase of hollow microsphere contents. The interconnected and spherical cell morphology was obtained with 3.0 wt.% hollow microsphere content. The resulting ceramics consists of a hierarchical structure. The hierarchical structure consists of large-sized cells with diameters of 20–60 μm, small-sized pores in cell walls averaging about 10 μm. Moreover, the compressive strength of the sintered samples varied within the range of 8.31–11.50 MPa, corresponding to hollow microsphere contents of 2.0–4.0 wt.%.

From Chapter 3 to Chapter 5, this dissertation studied the open cell foam structures, including the structure modeling of open cell foams, the computation of the elastic properties of three dimensional structures, and numerical investigation of pressure drop and heat transfer through open cell foams. Chapter 3 proposed an original geometrical model based on randomly packed spheres using Laguerre-Voronoi tessellations to simulate geometrical and topological characteristics in the microstructure of open cell foams. The statistical data of the generated foam structures, including volume, face and edge number distributions, F, E and $CV(V)_{\text{cell}}$, were very close to those of real materials. Further analysis showed that the porosity of foam structures, ε, decreased with the ratio of strut diameter to the average diameter of randomly packed spheres, $d_s/E(d)$, while the specific surface area of foams, S_V, increased with $d_s/E(d)$. Another issue undertaken in Chapter 3 was the model verification using commercial foams. The results showed that the proposed model provided more accurate results compared with other models available in

the literature. The proposed model could give a better inside into understanding interrelationships between statistical geometry parameters and the properties of isotropic foam structures.

Three-dimensional random Laguerre-Voronoi models were developed in Chapter 4. The proposed method can generate accurate foam models having randomly distributed parameter values. The developed foam models were used to simulate the macroscopic elastic properties of open cell foams under uni-axial and bi-axial loading and were compared with the existing open cell foam models in the literature. In the high porosity regime, it was found that the elastic properties predicted by random Laguerre-Voronoi foam models were almost the same as those by perfect Kelvin foam models while in the low porosity regime the results of present work deviated significantly from those of other models in the literature. However, the results of current work generally were in a better agreement with experimental data than other models. The Laguerre-Voronoi foam models generated in this work were quite close to real foam topology and yielded more accurate results than other open cell foam models.

Chapter 5 investigated the pressure drop and heat transfer through open cell foams. A pressure drop correlation with a universal form was developed based on theoretical grounds and the tortuosity of open cell foams was taken into account for the pressure drop. The developed correlation then was validated using numerical simulations on pressure drop properties of aluminum foam structures of pore densities between 10 ppi and 50 ppi and porosities from 70% to 95%, with the commercial CFD analysis package: ANSYS Fluent. The numerical results for pressure drop were compared with the prediction by the theoretical correlation. The results showed that the pressure drop of foams increased with

increasing pore density and decreasing porosity. The numerical results were consistent with the prediction of the theoretical correlation. Permeability and friction factor of foams were also evaluated. For the low Reynolds number range, friction factor scaled as $1/Re$ at lower Reynolds numbers, while at higher Reynolds numbers, the non-linear term began to dominate because of the inertial effects. Then the computed interstitial heat transfer coefficients were investigated. The heat transfer coefficient increased with the air velocity and the heat transfer coefficient increased when the porosity increases at constant pore density. At constant porosity the heat transfer coefficient increased when increasing the pore density. Furthermore, a correlation was given to derive the hydraulic diameter from the ppi number.

Finally, this dissertation stated that with additive manufacturing techniques, e.g., SLS and EBM, it is possible to control the morphological and geometrical parameters of foam structures with a high degree of reproducibility and vary these properties in a controlled manner and it is possible to perform computational design for open cell foams with defined flow properties using the Laguerre-Voronoi model developed in Chapter 3 and Chapter 4 of this work.

6.2 Future work

The prospective applications using ZnO–TiO_2 ceramics and cermets made of ZnO–TiO_2 ceramics and copper as raw materials of 3D printing is very attractive. The authors will attempt to use the ZnO–TiO_2 ceramics and cermets made in this study as a raw material for a further study on three dimensional printing: what will happen to 3D printing products

when going through sintering and how the machining properties of the products can be improved after sintering.

As for the porous alumina ceramics with high porosity fabricated in this work the authors would use them as preforms for pressure filtration to fabricate a new composite material, which is made of ceramic and metal. The interfacial phenomenon would be the critical issue in the pressure filtration. The ultimate goal of this work is to obtain a material with properties of high strength, high toughness, and light weight, etc.

Computational design of foams with certain geometric parameters, e.g., porosity, specific surface area, mechanical properties, flow properties, and thermal properties, would be performed based on the results of Chapter 3, Chapter 4 and Chapter 5. Moreover, another alternative three dimensional model for open cell foams can be developed by changing the cross-section shape of struts to a triangle or a curved triangle or changing the cylindrical struts to cylindrical struts with triangle prism cavity or triangular struts with a cylindrical cavity. In addition, the experimental studies would be performed to verify and modify the conclusions of Chapter 4 and Chapter 5 in future work.

Fabrication of lightweight and flexible materials, e.g., ceramics and metals, is a promising research topic. It is possible to obtain open cell polymer preforms for lightweight and flexible ceramics using the three dimensional model developed in this work. Then the open cell polymer preforms would be electroless plated with a conformal thin metal film, or be impregnated with a ceramic slurry, followed by etch removal of polymer preforms. The so-called lightweight and flexible materials would be obtained.

The flow mode inside the open cell foams is still very challenging so far. The pressure drop correlation discussed in this work does not consider the turbulent effect. To

predict mass transfer properties and heat transfer properties of open cell foams more accurately, developing a turbulent model for flow inside open cell foams becomes to another important research topic in future work.

APPENDIX A

```
### LAMMPS code for randomly packed spheres
atom_style sphere
boundary fm fm fm
newton off
comm_modify vel yes
### units
### molecule object myspheres.txt offset 0 1 1 1 1

region reg block -7.5 7.5 -7.5 7.5 0 15 units box
create_box 1 reg

neighbor 0.2 bin
neigh_modify delay 0

#pair_style gran/hertz/history Kn Kt gamma_n gamma_t xmu dampflag

pair_style gran/hooke/history 20000.0 NULL 50.0 NULL 0.5 0
pair_coeff * *

timestep 0.001

fix 1 all nve/sphere
fix 2 all gravity 50.0 spherical 0.0 -180.0

fix zlower all wall/gran 20000.0 NULL 50.0 NULL 0.5 0 &
zplane 0.0 15.0
fix xlower all wall/gran 20000.0 NULL 50.0 NULL 0.5 0 &
xplane -7.5 7.5
fix ylower all wall/gran 20000.0 NULL 50.0 NULL 0.5 0 &
yplane -7.5 7.5


region slab block -7.5 7.5 -7.5 7.5 7.5 15 units box

#fix ins1 all pour 500 1 12345 region slab diam one 0.2

#fix insl all pour 120 1 56789 region slab diam range 4 8

fix ins1 all pour 5000 1 133349 region slab diam poly 76
1.0 0.0011 1.1 0.0014 1.2 0.0023 1.3 0.0037 1.4 0.0055 1.5 0.0077 1.6 0.0102 1.7 0.0129
1.8 0.0158 1.9 0.0187 2.0 0.0215 2.1 0.0241 2.2 0.0265 2.3 0.0286 2.4 0.0304 2.5 0.0318
2.6 0.0329 2.7 0.0336 2.8 0.034  2.9 0.0341 3.0 0.0339 3.1 0.0334 3.2 0.0329 3.3 0.0320
3.4 0.0310 3.5 0.0299 3.6 0.0287 3.7 0.0275 3.8 0.0262 3.9 0.0247 4.0 0.0234 4.1 0.0221
```

4.2 0.0208 4.3 0.0195 4.4 0.0183 4.5 0.0171 4.6 0.0159 4.7 0.0148 4.8 0.0138 4.9 0.0128
5.0 0.0119 5.1 0.011 5.2 0.0102 5.3 0.0094 5.4 0.0087 5.5 0.008 5.6 0.0074 5.7 0.0068
5.8 0.0063 5.9 0.0058 6.0 0.0053 6.1 0.0049 6.2 0.0045 6.3 0.0042 6.4 0.0038 6.5 0.0035
6.6 0.0032 6.7 0.003 6.8 0.0027 6.9 0.0025 7.0 0.0023 7.1 0.0021 7.2 0.002 7.3 0.0018
7.4 0.0017 7.5 0.0015 7.6 0.0014 7.7 0.0013 7.8 0.0012 7.9 0.0011 8.0 0.001 8.1 0.0009
8.2 0.0009 8.3 0.0008 8.4 0.0007 8.5 0.0007

#Compute voronoi/atom
#compute 1 all voronoi/atom peratom yes neighbors yes

#dump to cfg for Ovito postprocessing
#dump 1 all custom 100 dump.comp.* id type xs ys zs c_csym #c_peratom fx fy fz

dump 1 all custom 100 dump.lmp type id x y z radius diameter
dump_modify 1 sort id
run 300000

VITA

Zhengwei Andrew Nie was born in May 1987 in Yongcheng, Henan, China. He received his Bachelor's degree in Process Equipment and Control Engineering from Beifang University of Nationalities, China in 2010. Then he started his graduate study at School of Energy and Power Engineering, Xi'an Jiaotong University, China from September 2010. He got his Master's degree in Power Engineering and Engineering Thermophysics from Xi'an Jiaotong University in July 2013. He enrolled at Department of Mechanical and Aerospace Engineering, University of Missouri-Columbia to pursue his Ph.D. degree in Mechanical Engineering in August 2013.

Zhengwei Andrew Nie is a member of American Society of Mechanical Engineering (ASME) and American Society for Engineering Education (ASEE). As of October 2016, he has published 9 journal papers and 2 conference papers in total and is a reviewer of ASME and ASEE conferences.